Magnetic Microrobotics for Biomedical Applications

David Folio

UNIVERSITÉ D'ORLÉANS

ÉCOLE DOCTORALES MATHÉMATIQUES, INFORMATIQUE, PHYSIQUE THÉORIQUE ET INGÉNIERIE DES SYSTÈMES

LABORATOIRE PRISME

MÉMOIRE

Par

David FOLIO

Soutenu le 03 décembre 2021

pour obtenir le grade d'Habilitation à Diriger des Recherches

Discipline: **Robotique**

Magnetic Microrobotics for Biomedical Applications: Modeling, Simulation, Control and Validations

Jury:

Michaël Gauthier	Directeur de Recherche, CNRS, FEMTO-ST, Besançon	Rapporteur
Sylvain Martel	Professeur, Polytechnique Montréal, Canada	Rapporteur
Philippe Poignet	Professeur des Universités, Univ. Montpellier	Rapporteur
Chantal Pichon	Professeur des Universités, Univ. Orléans	Examinatrice
Christine Prelle	Professeur des Universités, UTC	Examinatrice
Mohammed Samer	Professeur des Universités, Univ. Paris-Est Creteil Val de Marne	Examinateur
Li Zhang	Professeur, Dept. MAE, CUHK, Hong Kong	Examinateur
Antoine Ferreira	Professeur des Universités, INSA Centre Val de Loire	Garant

Contents

List of Tables

List of Figures

Avant Propos (Forewords)

Avant de commencer, il est à noter que bien que cet avant-propos soit rédigé en langue française, le reste de ce mémoire est quant à lui écrit en langue anglaise.

Ce mémoire, rédigé en vue de l'obtention d'une Habilitation à Diriger des Recherches (HDR), décrit mes activités d'enseignement, de recherche, d'encadrement et de collaborations. Ce manuscrit doit donc présenter une synthèse (non exhaustive) de ces activités effectuées depuis ma prise de fonction en qualité de maître de conférences en septembre 2008 à l'ENSI de Bourges (aujourd'hui INSA Centre Val de Loire) et au sein de l'équipe Robotique du laboratoire PRISME. Ce qui est présenté ici est avant tout le résultat d'un travail collectif, issu des interactions avec des collègues enseignant-chercheurs, administratifs et techniques, et aussi d'échange avec des étudiants, avec des scientifiques de divers établissements et des opportunités de projets dans lesquels je me suis investi. Notamment, ce travail n'aurait pas été possible sans l'enthousiasme et l'implication des jeunes chercheurs que j'ai eu l'opportunité de co-encadrer ou de superviser. Leur contribution est mentionnée tout au long de ce mémoire.
Depuis mon recrutement, mes travaux de recherche concernent d'une manière générale l'étude de systèmes robotiques, en vue de proposer des solutions innovantes pour réaliser des tâches avancées et fiables pour des applications essentiellement biomédicales. Même si j'ai travaillé dans différents domaines de la robotique, la grande partie de mes contributions concernent l'étude du comportement de ces systèmes aux échelles microscopiques. Cette thématique originale est un domaine de recherche en pleine expansion et fortement pluridisciplinaire, associant entre autre la robotique, le biomédical, la mécanique du solide et des fluides, l'électromagnétisme, les microsystèmes… Les applications et les retombés socio-économiques sont potentiellement très prometteuses. Les futurs robots qu'inspirent ces travaux pourraient transformer significativement la médecine par la possibilité d'aider le diagnostic *in situ* ou de réaliser des thérapies localisées dans des zones aujourd'hui difficiles d'accès autrement que par une chirurgie invasive. Je me suis ainsi fortement investi dans ce nouvel axe de recherche, ayant ainsi un positionnement scientifique original. Je me suis plus particulièrement intéressé à des problématiques, au sens large, de *"modélisation et de commande"* de microrobots magnétiques évoluant dans le corps humain pour du ciblage thérapeutique. L'émergence au sein du laboratoire PRISME de cette thématique coïncide avec le démarrage du projet européen NANOMA dont le laboratoire était coordinateur. Plusieurs enseignants-chercheurs du laboratoire PRISME des groupes de recherche de Robotique et d'Automatique se sont impliqués dans cette thématique autour des aspects de modélisation et de commande.

Ce mémoire est organisé en huit chapitres répartis dans deux parties. Comme tout maître de conférences, mes travaux englobent deux composantes principales qui sont liées aux activités d'enseignement et de recherche. Dans la première partie, quatre chapitres présentent le résumé de ces activités. Ainsi dans le Chapitre I, je présente un bref aperçu de ma carrière et du contexte de mes activités. Le Chapitre II résume mes responsabilités pédagogiques et administratives. La synthèse de mes activités de recherche est introduite au Chapitre III, avec une brève présentation des projets de recherche, des encadrements d'étudiants, des collaborations scientifiques et des actions de rayonnement. La liste complète de mes publications est indiquée dans le Chapitre IV.

Dans la deuxième partie de ce manuscrit, mes principales contributions scientifiques sont présentées. Dans un souci de cohérence, j'ai choisi de ne présenter que les réalisations concernant le développement des microrobots magnétiques pour des thérapies ciblées, en navigant à travers le système cardiovasculaire. Cette problématique, fondamentalement pluridisciplinaire, est globalement abordée selon une approche ascendante (dite "bottom-up"), à savoir de la compréhension et de la modélisation du micromonde à la définition de stratégies de navigation de haut niveau. C'est notamment en suivant cette approche que la présentation de mes contributions scientifiques est organisée.
Le Chapitre V décrit alors le contexte scientifique de mes travaux de recherche. Comme mes principales contributions concernent la microrobotique pour les applications biomédicales, ce thème y est introduit. Puis la manière dont mes activités se sont structurées est présentée.
Dans le Chapitre VI, les fondements théoriques qui permettent de décrire et de modéliser les microrobots sont introduis. En effet, pour concevoir un système microrobotique efficace et fiable pour une application biomédicale, une bonne compréhension de leur comportement est une étape importante. Il est nécessaire de bien caractériser la manière dont les microrobots évoluent suivant le type d'environnement biologique et des stimuli externes. Pour cela, nous avons exploré en profondeur les différents éléments qui contribuent majoritairement aux dynamiques dominantes.
Sur cette base, dans le Chapitre VII, nous sommes en mesure de pouvoir simuler le comportement des microrobots. Ces simulations ont pour objectif de bien appréhender les spécificités des systèmes microrobotiques considérés et de tenter d'anticiper les contraintes et difficultés susceptibles de les impacter. Nous avons aussi proposé des stratégies de planification pouvant prendre en compte les contraintes de l'application. Cela nous permet d'obtenir une référence qui est effectivement réalisable par le système microrobotique. Nous avons pu alors définir des stratégies de navigations en fonction des spécificités du système microrobotique et de l'application visée.
Pour tester et valider les modèles et stratégies choisis, nous avons développé différentes plateformes démontrant les preuves-de-concept. Ces réalistions décrites au Chapitre VIII ont été développées essentiellement au sein du laboratoire PRISME, mais ont bénéficié également de collaborations scientifiques avec de nombreux partenaires internationaux (ETH Zurich-Suisse, University of Oldenburgh-Allemagne, KAIST-Corée du Sud…). Notamment, pour évaluer nos stratégies de navigation dans un environnement de type cardiovasculaire, nous avons développé un simulateur qui reproduit au mieux les conditions physiologiques. Puis, pour guider magnétiquement les microbots développés, différentes plateformes d'actionnement magnétiques ont été considérées. Tout cela nous a permis d'évaluer et de démontrer expérimentalement les différents concepts et stratégies que nous avons développés.

En plus des contributions décrites dans ce mémoire, les perspectives que j'ambitionne d'explorer à l'avenir sont également présentées en conclusion de ce mémoire.

Part I

Activities Background

Chapter I

Presentation

I.1 Curriculum Vitæ

I.1.1 Identity

David Folio

Born September 17, 1979; French nationality

Associate Professor

Main topic: Microrobotics for biomedical applications.

- Contact information
  INSA Centre Val de Loire,
  Campus de Bourges, 88 bd Lahitolle;
  CS 60013; F-18022 Bourges cedex; France
  – Mobile:+33(0)6 71 30 06 88
  – Tel.:+33(0)2 48 48 40 75
  – Fax: +33(0)2 48 48 40 50
  – email: david.folio@insa-cvl.fr
- Public profiles
  – Google Scholar: XQVc6JMAAAAJ
  – Orcid: 0000-0001-9430-6091
  – ResearchGate: David_Folio
  – ResearcherID: D-5808-2013
  – Scopus: 15924858900
  – Linkedin: david-folio-5b8b43a7

I.1.2 Current situation

Since 2008 **Associate Professor** (maître de conférences), 61st CNU section

Affiliation: INSA Centre Val de Loire, University of Orléans, PRISME Laboratory EA4229, Bourges, France.

Teaching: member of the teaching team of the Industrial Risk Control (MRI), of the Energy, Risks, and Environment (ERE), and of the Sciences and Techniques for Engineers (STPI) departments on the Bourges campus of INSA Centre Val de Loire.

Research: member of the Robotics team of the Images, Robotics, Automatic control and Signal (IRAuS) unit of the PRISME Laboratory.

Supervision: 5 Master students (M2) and 6 PhD students, and 3 externals PhD students.

Publications: a total of 47 publications, including 15 articles (ACL), 1 guest editorial (DO), 3 books chapter (OS) and 23 proceedings (ACT).

Since 2014

- in charge of the Nuclear Energy option of the 5th year of the Industrial Risk Control (MRI) department.
- French outstanding research award (PEDR)

Since 2020 elected member of the council of the Industrial Risk Control (MRI) department.

I.1.3 Experience and Graduate Education

Oct.2007 – Aug.2008 Post-Doctorate at Inria Rennes-Bretagne-Atlantique, Rennes, France. Research on sensory control for unmanned aerial vehicles conducted in Lagadic team, supervised by François Chaumette.

Feb.2007 – Aug.2007 Teaching assistant (ATER), at Paul Sabatier University of Toulouse, France.

Feb.2004 – Aug.2007 Doctorate degree at Laboratory for Analysis and Architecture of Systems (LAAS), CNRS, Toulouse, France. "Multi-sensor-based control strategies and visual signal loss management for mobile robots navigation", PhD thesis in Robotic control, of Paul Sabatier University of Toulouse,
directed by Viviane Cadenat

Jury
- Michel Devy, Senior Research Scientist[1] LAAS-CNRS, President
- François Chaumette, Senior Research Scientist Inria, Reviewer
- Seth Hutchinson, Professor of University of Illinois, Reviewer
- Bernard Bayle, Associate Professor of University of Strasbourg, Examiner
- Michel Couredesse, Professor of University of Toulouse, Examiner
- Viviane Cadenat, Associate Professor of University of Toulouse, Director
- Philippe Souères, Senior Research Scientist LAAS-CNRS, Guest

2003 – 2004 Master of Science (DESS) on Intelligent Systems at Paul Sabatier University of Toulouse, France.

2002 – 2003 Master of Advanced Studies (DEA) on Computer Sciences at Paul Sabatier University of Toulouse, France.

1999 – 2002 Scholarship (IUP[2], L2-M1) on Intelligent Systems at Paul Sabatier University of Toulouse, France.

1997 – 1999 Bachelor's degree (L1-L2) in Science and Technology for the Engineer, at University of Reunion Island, France.

I.2 Background and Career Overview

I.2.1 Doctorate degree and post-doctorate

I have defended my PhD in Robotics in 2007 within the Robotics, Action, and Perception (RAP) group of the Laboratory for Analysis and Architecture of Systems[3] (LAAS), CNRS[4], under the supervision of Viviane Cadenat, Associate Professor at the Paul Sabatier University of Toulouse, France. Specifically, my PhD thesis was entitled "*Multi-sensor-based control strategies and visual signal loss management for mobile robots' navigation*". My thesis subject was to design multi-sensor-based control strategies allowing a mobile robot to perform vision-based tasks amidst possibly occluding obstacles. Indeed, the improvement of sensors gave rise to the sensor-based control which allows defining the robotic task in the sensor space rather than in the configuration space. As cameras provide high-rate meaningful data, visual servoing has been particularly investigated, and can be used to perform various and accurate navigation tasks [1–3]. My PhD objectives were then to perform reliable navigation tasks,

[1] Senior Research Scientist refers to in French " Directeur de Recherche".
[2] From French "Institut Universitaire Professionnalisé" (IUP)
[3] LAAS is a laboratory depending on the CNRS, http://www.laas.fr
[4] CNRS is the French National Center for Scientific Research, http://www.cnrs.fr

despite the presence of obstacles. Thereby, it is necessary to preserve not only the robot safety (i.e. ensuring non-collision), but also the visibility of visual features to ensure the vision-based task feasibility. To achieve these aims, we have first proposed techniques able to fulfill simultaneously the mentioned objectives [ACT1,ACT2,ACT3]. However, avoiding both collisions and occlusions often over-strained the robotic navigation task, reducing the range of realizable missions. This is the reason why we have developed a second approach which let occurs the loss of the visual features if it is necessary for the success of the task. Using the link between vision and motion, we have proposed different methods (analytical and numerical) to compute the visual signal as soon it becomes unavailable [ACT4]. We have then applied them to perform vision-based tasks in cluttered environments, before highlighting their interest to deal with a camera failure during the mission [ACT4,ACT5].

In addition, during my doctorate degree, I also had the opportunity to perform teaching activities, first as temporary teacher (3 years), and then as teaching assistant, specifically in French as "Attaché Temporaire d'Enseignement et de Recherche" (ATER, 1 year), both for the Paul Sabatier University of Toulouse. These global teaching experiences have led to a total volume of 308 hETD[5].

Between 2007 and 2008, I joined the Lagadic team at Inria[6] Rennes-Bretagne Atlantique as a post-doctoral fellow on sensory control for unmanned aerial vehicles. My postdoctoral fellow has been supported by *Sensory Control for Unmanned Aerial Vehicles* (SCUAV) ANR project[7]. The main objective was to improve multi-sensor-based servoing tasks for unmanned aerial vehicles. The idea was to design robust control law that combine different sensory data directly at the control level. Especially, I have contributed to the design of a new online sensor self-calibration based on the sensor/robot interaction links [ACT6].

I.2.2 Tenured as associate professor

In 2008, I was recruited as Associate Professor for the 61st CNU section[8] at the Graduate Engineering School (ENSI) of Bourges, which is since 2014 the INSA Centre Val de Loire. The INSA Centre Val de Loire was established following the merger of the Val de Loire National Engineering School (ENIVL), Blois and ENSI of Bourges. The Institute was extended in 2015, when it absorbed the National Graduate School for Nature and Landscape, Blois. Like any INSA engineering school, the first two years are a preparatory cycle (L1 and L2) embedded in the Sciences and Techniques for Engineers (STPI) department. From the third to the fifth year, students are enrolled in one of the INSA Centre Val de Loire specialties to became engineer.

[5]Equivalent TD hours that is in French heures équivalentes TD (hETD), are the reference hours to calculate the teaching duties. (see also the index of terms and notations for further definition)

[6]From French: Institut national de recherche en informatique et en automatique. https://www.inria.fr/centre/rennes

[7]From French "Agence Nationale de la Recherche" (ANR), which is the French National Research Agency, http://www.agence-nationale-recherche.fr

[8]From French "Conseil National des Université" (CNU), comprises 57 sections covering different scientific disciplines. The 61st section involves IT engineering, automation and signal processing. https://www.conseil-national-des-universites.fr

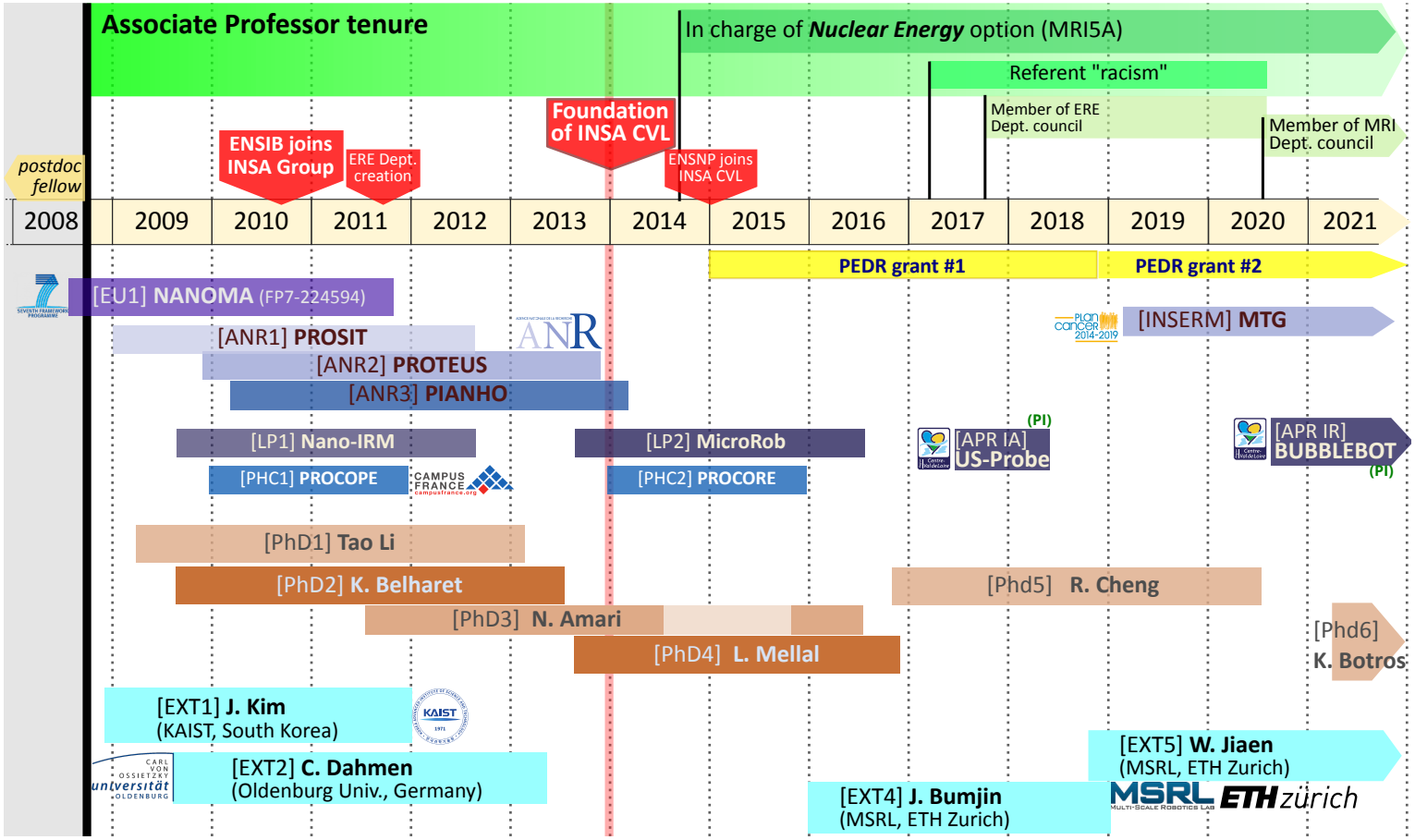

Figure I.1: Timeline of main events and activities since tenure as Associate Professor. Further information on the different projects, and the supervisions are given in Chapter III.

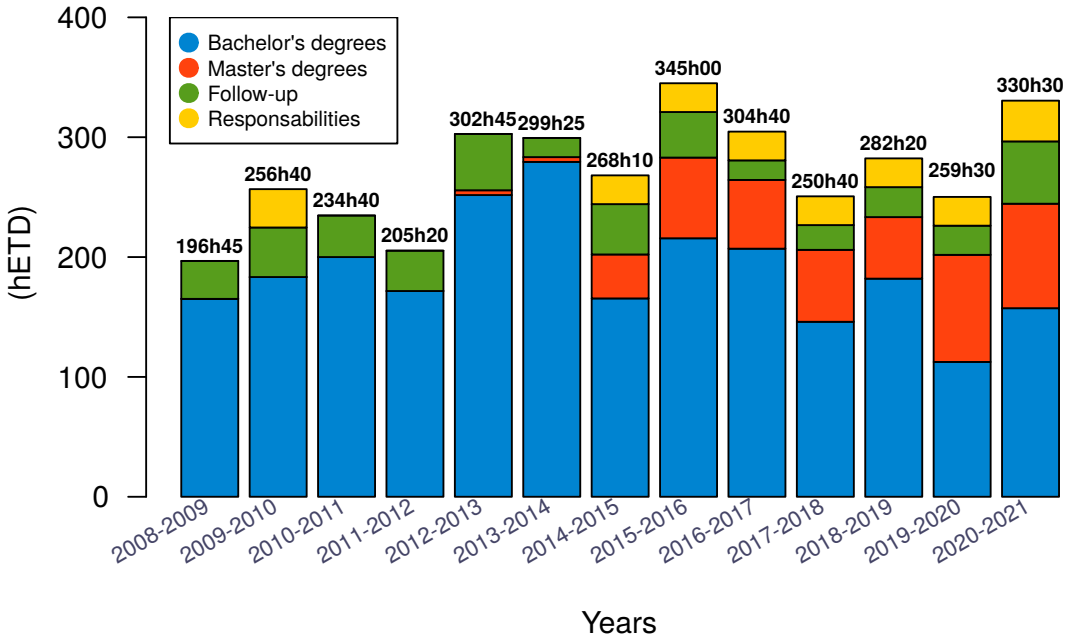

Figure I.2: Teaching activities progress expressed in *equivalent TD hours* (hETD).

Since my tenure, I have been regularly involved in the life of the Institute. I contribute at a local level to the scientific animations (e.g. organization of laboratory visits), transfer and training-research relationship. For instance, I regularly attend the international relations division by accompanying the different delegations of schools and universities partners during their visits. In March 2017, the direction of the INSA Centre Val de Loire given to me the mission of referent *racism and antisemitism*. Figure I.1 shows the relevant events related with my activities since tenured as associate professor.

As a lecturer, I am involved, among others, in the development of electronics and electrical sciences teaching activities within the Institute. In particular, I helped to develop all the teaching materials for these courses, tutorials and practices. Since tenured as associate professor, my average teaching load is about 272 hETD per year. Figure I.2 presents the evolution of my teaching duty since 2008. These teaching loads varied depending on the recruitment and the choice of engineering students in the different departments in which I teach. Furthermore, some key events in the life of the Institute have also influenced my teaching loads, as shown in Figure I.1. For instance, since 2012, after the ERE department creation, I have also started to form the apprentices engineers to electrical engineering. In parallel, I took part in the electronics training for the new preparatory cycle which became the Sciences and Techniques for Engineers (STPI) department.
Similarly, various responsibilities entrusted to me have also influenced my teaching duties. Since September 2014, I am in charge of the option entitled *Nuclear Energy* of the 5^{th} year (engineer's degree, M2) of the Industrial Risk Control (MRI) department. Between 2017 and 2020, I have been elected as member of the council department of the Energy, Risks and Environment (ERE); and since November 2020 I am an elected member of the council department of Industrial Risk Control (MRI). Further information on my teaching activities and responsibilities are provided in Chapter II.

Furthermore, I carry out my research activities with the PRISME Laboratory in the Robotics team belonging to the Images, Robotics, Automatic control and Signal (IRAuS) department. The INSA Centre Val de Loire and University of Orléans are jointly responsible for PRISME Laboratory. The laboratory also has hosting agreement with the private School of High Studies in Engineering (HEI) located in Châteauroux. PRISME Laboratory seeks to carry out multidisciplinary research in the general domain of engineering sciences over a broad range of subject areas, including combustion in engines, energy engineering, aerodynamics, mechanics, image and signal processing, control and **robotics**. One of the specificity of the PRISME Laboratory is that it is spread over 3 departments of the administrative Region Centre Val de Loire, within a total of 7 sites. Within the IRAuS department, the Robotic team is mainly involved in robotics for biomedical and healthcare applications. Specifically, the Robotics team contributes to the development of methods, tools and techniques for the design and control of innovative robotic systems. To achieve these goals, the team comprised 10 researchers. The members of the Robotics team are spread over 3 cities: Bourges (5 with IUT and 2 with INSA Centre Val de Loire), Châteauroux (2) and Orléans (1).

Since I have been an associate professor, my field of scientific research mainly focused on the modeling and control for nano and micro-robots in a biomedical context. It should be noticed that since my PhD degree and post-doctoral fellow, I had to apply a slight evolution on my research topics to address the specificity of the microworld. Hence, during the first years of taking up my position, I deepened my understanding of microrobotics with a particular attention to their biomedical applications. Indeed, one of my first research activities have been mainly related with the European project NANOMA (see also Sections III.1.1 for further detail on projects). This project consisted of designing microrobotic system for targeted drug delivery through the cardiovascular system. Globally, my main contributions focus on the study of **magnetic medical microrobots** for targeted therapies, and this topic will be the common thread in the second part of this manuscript.
Meanwhile, I have also contributed to the development of micromanipulation activities of the laboratory. Firstly, the micromanipulation tasks have been devoted to intracytoplasmic applications [ACT10,ACL5]. Next, these research activities have evolved to micromanipulation of object to be placed in the focus of a light beam within the ANR project PIANHO and the PhD thesis of **Nabil Amari** [PhD3]. In parallel, I also contributed to projects more related to common robotics topic. Specifically, I have helped the Robotic team in the field of medical robotics with the development of a tele-echographic platform with the ANR project PROSIT [ACL8]; and in the field of mobile robotics with the ANR project PROTEUS. Thanks to the experience acquired in participating in these projects, I subsequently obtained the funding of the **US-Probe** and **BUBBLEBOT** project for which I am the principal investigator (PI). These different research projects in which I have been involved are reported in Figure I.1, and are presented in Section III.1. In addition, I have directly supervised the works of 5 Master and 6 PhD students, and I also had the opportunity to follow the research works of 3 external PhD students. Further information about these supervisions are given in Section III.2.

Since tenured in 2008, these various scientific activities have led to 47 publications, including[9] 15 articles (ACL), 1 guest editorial (DO), 3 books chapter (OS) and 23 proceedings (ACT). Figure I.3 illustrates the timeline progress of my publishing activities and the detailed list

[9]The bibliography categories follows the nomenclature proposed by the Hcéres which is an independent administrative authority for evaluation of research and higher education. http://www.hceres.fr

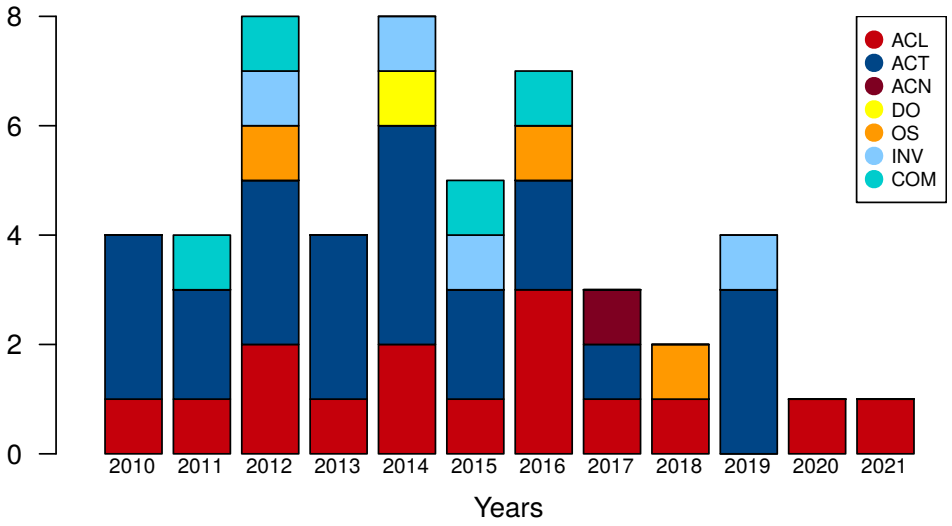

Figure I.3: Personal references progress since tenure (see detail in Chapter IV).

of my publications are given in the Chapter IV. My H-index is around 15 based on Google Scholar Citations[10] (2021).

[10]See also my Google Scholar profile: http://scholar.google.com/citations?user=XQVc6JMAAAAJ

Chapter II

Teaching and Administrative Responsibilities

In this chapter, the different aspects related to my teaching activities are summarized. My overall teaching activities have been solely related with the 61st CNU section which regroups scientific disciplines from control, IT engineering and signal processing. I taught these teaching activities as a temporary teacher (3 years), teaching assistant (ATER, 1 year), and then as associate professor (since 2008). These different teaching experiences are presented in the following sections.

II.1 Before Tenure

I have started teaching as a temporary teacher at the Paul Sabatier University of Toulouse, France, during my doctorate (2004 – 2006). Next, I have pursued as teaching assistant, specifically in French as Attaché Temporaire d'Enseignement et de Recherche (ATER, 2007), at the Paul Sabatier University of Toulouse. My teachings were mainly in the fields of robotics, control theory, image processing and real-time systems for students from bachelor's to master degrees. These global teaching experiences have led to a total volume of 308 hETD.

These activities were my first experience in high-graduate education. Those opportunities highlighted my interest in the scientific knowledge transmission. They also allowed me to be familiarized with the different forms of teachings. Indeed, I had then the opportunity to supervise not only tutorials (TD), practical work (TP), and long-term projects (BE); but also few courses. Especially, I also helped the teaching team by writing some TP contents, and in the students' evaluation. This first experience confirmed my interest in teaching, leading me logically to apply for an associate professor position.

II.2 Since Tenured

Until now, my teaching activities have been mainly held at INSA Centre Val de Loire on the Bourges campus. Thus, I am mainly involved in the students' formation of the MRI, ERE, and STPI departments. After having started with teaching of electronics and electrical engineering, I have participated or organized lessons on signal processing, sensors, control and robotics. These various teaching experiences imply very different pedagogical tasks. Especially, those tasks depend on the type of intervention: courses (C), tutorials (TD), practical works (TP), or tutored projects (P); but also according to the different degrees of scientific maturity and specialization of the concerned students: from bachelor's (L1) to

Table II.1: Overview of the various teaching disciplines as associate professor.

			Face time				
Disciplines	LMD[a]	Students[b]	C[c]	TD	TP	Dept.	Years
Electrokinetics	L1	100	18h00	24h00		STPI	2012-2014
Analog Electronics (I)	L2	80	8h00	32h00		STPI	2015-present
Analog Electronics (II)	L3	70	21h20	21h20	6h00	MRI	2008-2016
Analog Electronics (III)	L3	70	10h40	10h40		MRI	2015-present
Electrical engineering	L3	70	10h40	10h40		MRI	2008-2016
Electricity - Electrical engineering	L3	78	8h00	14h00		ERE	2016-present
Electricity - Electrical engineering	M1	78	8h00	14h00		ERE	2012-2016
Control and Sensors	M1	78	6h	9h		ERE	2014-2016
Control and Diagnostic	M1	20	10h40	10h40		MRI	2015-present
Signals and Systems	M1	20	10h40	10h40		MRI	2014-present
Perception for robotic	M2	25	4h			MARSS	2012-2018
Robotic	M2	50	9h	9h		MRI/3EA	2019-present
Students Projects (SA)	M1	2				MRI	2008-present
Students Projects (PSI)	M1	10				MRI	2008-present

[a] LMD is the bachelor's, master's, doctorate system (in French License-Master-Doctorat) designed by the Bologna process, with L1-L3: from the 1st to the 3rd year bachelor's degree; M1-M2: from the 1st to the 2nd year master's degree.
[b] the average number of students per year.
[c] refer to face time hours for courses (C), tutorials (TD) and practical works (TP).

master's (M2) degree level. For instance, it can be noticed, that the ERE department trains engineers through an apprenticeship training. Table II.1 illustrates a synthetic overview of the different teaching disciplines for which I am in charge. These responsibilities imply the implementation of teaching materials and the students evaluations, but also the support of teaching assistants (e.g. for the TD). As needed, I also intervened to support the teaching activities of some of my colleagues (e.g. for their TD).

A description of some of these disciplines are summarized hereafter.

Analog electronics (I), (II) and (III): The aim is to provide from basic to high level view of the elementary components that are the heart of electronic circuits. It deal with passive components such as resistors, capacitors and inductors as well as an introduction to diodes, transistors and operational amplifiers, and their use in filters, amplifiers, power supply circuits.
First taught to engineering students (L3) of ENSI of Bourges, this discipline has evolved since the creation of INSA Centre Val de Loire and is provided to the STPI (L2) and MRI (L3) departments. This allowed me to develop the teaching of analog electronics from the L3 level to more advanced electronics.

Electrical engineering: After an introduction to fundamental concepts (e.g. electricity, single-phase and three-phase electric power, etc.), this teaching is supplemented by case studies. This allows engineering students to understand the use of tools and models to evaluate the performance of an electrical system, for diagnosis and help in the choice of more efficient and sustainable solutions.

Robotics: This course is intended for engineering students from the MRI department (M2) together with the international master degree on Electronics, Electrical Energy and Automatics (3EA) jointly with the University of Tours. This teaching, in English language, allows students to discover new fields of research and to take an interest in the modeling and control of mobile robots.

Student Projects:

- Advanced systems projects (SA): a pair have to work over a semester to study an advanced system, such as a microrobotic system, an electromagnetic actuation platform, etc.
- Industrial synthesis projects (PSI): a group of about ten students must divide the workload to study complex processes, such as the viscous flow in channels, the modeling of magnetic fields induced by electromagnetic coils…

II.3 Responsibilities

In addition to teaching tasks, various duties are related to associate professor position. First, I am involved in the life and the scientific animation of the Institute. I also participate in the juries of our engineering students. Similarly, since our establishment have joint the INSA group in 2014, I contribute to select and interview the applying students (about 15 students per year).

Between 2009 and 2013, I have been member of the Hygiene and Security committee of the of ENSI Bourges.

Since September 2014, I am in charge of the Nuclear Energy option of the 5 year (engineer's degree) of the Industrial Risk Control (MRI) department. As such, I coordinate the specific lessons of the option by selecting and recruiting external professional contractors. I also organize visits (nuclear power plant, simulator, etc.) for the engineering students of the option. Since 2018, I took part to panel discussions "support for nuclear training" and "nuclear-jobs-training" which have enabled participants to better understand issues about nuclear energy in France.

Between November 2017 and 2020, I have been an elected member of the ERE department council. Next, since 2020, I am an elected member of the Industrial Risk Control (MRI) department council.

In March 2017, the direction of the INSA Centre Val de Loire given to me the mission of referent "racism and antisemitism".

Chapter III

Summary of Research Activities

This chapter summarizes the different research activities in which I have been involved. This includes research projects, student supervision, scientific collaborations, and outreach.

III.1 Scientific Projects

My research activities regularly lead me to contribute to scientific projects. These projects aim to obtain funds to either recruit young researchers, to design or improve our experimental platforms, as well as to help to enhance scientific cooperation. Below are listed the different projects in which I have been strongly involved, both in their implementation and in their achievements. Let us notice that all of these projects have been subject to a process with deep scientific reviews. The list of unsuccessful applications is equally important.

III.1.1 European Union (EU) and national funding projects

NANOMA Nano-Actuators and Nano-Sensors for Medical Applications

Date 06/2008 – 10/2011

Funding 3.3M€, supported by the European Commission under FP7 ICT 2007.3.6, Micro/nanosystems

Summary The NANOMA was coordinated by Professor Antoine Ferreira, University of Orléans, PRISME Laboratory. This project aimed at proposing novel controlled nanorobotic delivery systems to improve the diagnosis and the administration of drugs in the treatment of breast cancer.

Role co-responsible of the workpackage: "object tracking, planning and control in MRI".

PROSIT Robotic Platform for an Interactive Tele-echographic Systems

Date 01/2009 – 09/2012

Funding 230k€, supported by ANR Contint program

Summary The PROSIT project was coordinated by Professor Pierre Vieyres, University of Orléans, PRISME Laboratory. The goal was to develop an interactive and complex master-slave robotic platform for a medical diagnosis application (i.e. tele-echography) based on a well-defined modular control architecture.

Role co-responsible of the workpackage: "visual servoing".

PROTEUS Robotic platform to facilitate transfer between industries

Date 12/2009 – 12/2013

Funding 2.1M€, supported by ANR ARPEGE program

Summary The PROTEUS project motivation was to help to organize interactions between academic and industrial partners of the French robotic community by

providing suitable tools and models. One goal was to create a portal for the French robotic community as embodied by the GDR Robotique and its affiliated industrial partners, in order to facilitate transfer of knowledge and problems among this community. To achieve the PROTEUS project 12 partners have been involved.

Role co-responsible of the workpackage: "young challenge".

PIANHO Innovative haptic instrumental platform for 3D nano-manipulation

Date 03/2010 – 03/2014

Funding 761k€, supported by ANR P3N program.

Summary The PIANHO project motivation is to create a nanomanipulation platform capable of pick, hold and place nano-objects in the synchrotron radiation beam of the ESRF[1] (Grenoble, France) via tuneable tool-object interaction.

Role co-responsible of the workpackage: "control of a two-fingered AFM-based nano-manipulation system".

MTG Microrobots Targeting Glioblastoma (MTG)

Date 03/2019 – 03/2022

Funding 511.4k€, supported by French National Institute of Health and Medical Research[2] (Inserm) "plan cancer" program

Summary The MTG objective is to functionalize magnetic microrobot with NFL peptide[3] to target glioblastoma (GBM).

Role co-responsible of the workpackage: "*in vitro* and *in vivo* distribution and tracking studies using IVIS imaging system to test the capacity of MTG to target glioblastoma cells versus healthy cells of the nervous system".

III.1.2 Cooperation projects

PHC PROCOPE Franco-German Hubert Curien[4] partnership (PHC)

Date 2010 – 2011

Summary Supervision and control of an improved platform for targeted administration of therapeutic Nanorobots.

Partnership Division of Microrobotics and Control Engineering[5] (AMiR), university of Oldenburg, Germany.

PHC PROCORE Franco–Hong-Kong Hubert Curien partnership

Date 2014 – 2015

Summary Design, fabrication and characterization of the swim of enhanced helical microrobots.

Partnership Department of Mechanical and Automation Engineering[6] (MAE), Chinese university of Hong-Kong (CUHK).

[1] European Synchrotron Radiation Facility (ESRF), https://www.esrf.eu

[2] from French: Institut national de la santé et de la recherche médicale (INSERM), https://www.inserm.fr

[3] NeuroFilament Light subunit that is binding Tubulin (NFL peptide) is capable to penetrate in GBM, block and inhibit cell division.

[4] PHC, from French Partenariats Hubert Curien, provides support for international scientific and technological exchange of the Ministry of Foreign Affairs. https://www.campusfrance.org

[5] AMiR, that is from German Abteilung für Mikrorobotik und Regelungstechnik, is a department of the University of Oldenburg, Germany, headed by Prof. Dr.-Ing. Sergej Fatikov. http://www.amir.uni-oldenburg.de

[6] MAE is a department of the Chinese University of Hong Kong, with A.Prof. Li Zhang. http://www.mae.cuhk.edu.hk

III.1.3 Regional projects

Nano-IRM

Date 09/2009 – 08/2012

Funding 110k€, supported by Région Centre Val de Loire, the Cher (18) departmental councils and the agglomeration comity of Bourges.

Summary Supervision and control of an improved platform for targeted administration of therapeutic nanorobots. This project supports the above project NANOMA, by providing the funding for the PhD thesis of **Karim Belharet**.

Role co-supervision of the PhD thesis of **Karim Belharet**.

MicroRob

Date 10/2013 – 09/2016

Funding 110k€, supported by Région Centre Val de Loire and the agglomeration comity of Bourges.

Summary Modeling and control of magnetic microcarrier for targeted cancer therapy.

Role co-supervision of the PhD thesis of **Lyes Mellal**.

US-Probe High Definition Echograph

Date 03/2017 – 03/2018

Funding 50k€, supported by Région Centre Val de Loire (APR-IA)

Summary Design of novel microrobotic platform with ultrasound imaging.

Role **Principal Investigator** (PI).

BUBBLEBOT Magnetic microbubbles for the targeted delivery of therapeutic agent in the brain

Date 10/2020 – 10/2023

Funding 210k€, supported by Région Centre Val de Loire (APR-IR)

Summary The aim is to combine the progress made in microrobotics with those made with microbubbles in order to improve the therapeutic targeting of glioblastoma.

Role **Principal Investigator** (PI).

III.2 Student Supervision

My research work was carried out with the contributions of young researchers whose works I supervised. I had directly supervised 5 Master (M2) and 6 PhD students. The total rate of supervision of defended PhD theses is 200%. In addition, I also had the opportunity to follow the research works of 3 externals PhD students. These different students are listed hereafter, as well as the joint publications.

III.2.1 Master students (M2)

Kamel Ncir

Date 03/2010 – 08/2010

Title Commande robuste pour le nano-positionnement d'une plateforme instrumentale.

Situation Technician at Jubilant HollisterStier LLC, Montréal, Québec, Canada

Nabil Amari

Date 03/2011 – 08/2011

Title Modélisation et Commande d'une plateforme de nano positionnement

Situation Associate Professor HEI, Châteauroux, France

Bruno Sarkis

Date 03/2015 – 08/2015

Title Modélisation des microjets catalytiques dans des canaux micro-fluidiques

References [ACT22,ACL14]

Hadjila Mahfoufi

Date 03/2018 – 08/2018

Title Modélisation, Simulation et Commande de Microrobot Catalytique

Situation Engineer at Alstom, Paris, France

Oumarou HABOU SOULE

Date 03/2019 – 09/2019

Title Suivi de Microrobot par Imagerie Echographique

III.2.2 Doctoral students

III.2.2.1 Defended theses

[PhD1] Tao Li

Date 03/2009 – 02/2013

Title Commande d'un robot de télé-échographie par asservissement visuel. Thesis of university of Rennes 1

Supervision 37.5% with Prof. Pierre Vieyres (12.5%), François Chaumette (12.5%) and Alexandre Krupa (37.5%)

References [ACL8]

Situation Engineer at Another Brain, Paris, France

[PhD2] Karim Belharet

Date 10/2009 – 07/2013

Title Navigation prédictive d'un microrobot magnétique : Instrumentation, commande et validation. Thesis of university of Orléans

Supervision 50% with Prof. Antoine Ferreira

References [ACT8,ACT9,ACT12,ACT14,ACT17,ACT19,ACT21,ACL2,ACL3, ACL6,OS2]

Situation Associate Professor HEI, Châteauroux, France

[PhD3] Nabil Amari

Date 10/2011 – 07/2016

Title Développement et Commande d'une Plateforme Microrobotique pour la Synchronisation d'un Faisceau de Lumière. Thesis of university of Orléans

Supervision 30% with Prof. Antoine Ferreira

References [ACT15,ACT16,ACT18,ACT20,ACL7,OS3]

Situation Associate Professor HEI, Châteauroux, France

[PhD4] Lyès Mellal

Date 10/2013 – 12/2016

Title Modélisation et commande de microrobots magnétiques pour le traitement ciblé du cancer. Thesis of university of Orléans

Supervision 40% with Prof. Antoine Ferreira (30%) and Karim Belharet (30%)

References [ACT23,ACT24,ACT25,ACT27,ACL9,ACL12]

Situation Teaching assistant at ISEN, Lille, France

[PhD5] Ruipeng Chen

Date 11/2016 – 07/2020

Title Design Methodology for Electromagnetic Microrobotic Platforms. Thesis of INSA Centre Val de Loire

Supervision 50% with Prof. Antoine Ferreira

References [ACT27,ACT28,ACT29,ACL15]

Situation Post Doctorate, INSA CVL, Bourges, France

III.2.2.2 Ongoing thesis

[PhD6]Karim Botros

Date 04/2021 – 03/2024

Title Magnetic Micro-robotic Platform Guided by Robotic Ultrasound for Brain Tumor Targeting. Thesis of INSA Centre Val de Loire

Supervision 50% with Prof. Antoine Ferreira

III.2.2.3 External PhD students

[Ext1] Junsig Kim

Date 2008 – 2012

Title A Study of Oocyte/Embryo Manipulation Using Microfluidics and Robotics. Thesis of Korea Advanced Institute of Science and Technology (KAIST), South Korea

References [ACT10,ACL5]

Situation Senior Research Engineer at LG Electronics, South Korea

[Ext2] Christian Dahmen

Date 2009 – 2013

Title Robust Object Tracking for Micro- and Nanorobotics. Thesis of Carl von Ossietzky Universität Oldenburg

References [ACT11,ACT13,ACL11]

Situation Dr. Ing. at Carmeq GmbH, Berlin, Germany

[Ext3] Jang Bumjin

Date 2015 – 2016

Title Magnetic Nano Actuators for Quantitative Analysis. Thesis of ETH Zurich, Switzerland

References [ACL10]

Situation Engineer at Samsung Electronics, South Korea

III.3 Scientific Collaborations

My research works have led to various international and national collaborations. These cooperations have made possible to investigate complementary approaches to those I have studied, helping me to benefit from supplementary skills. These exchanges were important in view of the strong multidisciplinary of the achieved works, the variety of physical principles used, and the technologies involved. Hereafter some significant collaborations and partnerships that have resulted in either joint publications or that are still ongoing.

III.3.1 International relationships

- Department of Mechanical Engineering at Korea Advanced Institute of Science and Technology (KAIST), South Korea
  - Team of Prof. Jung Kim
  - References: [ACT10,ACL5]
- Division of Microrobotics and Control Engineering (AMiR), university of Oldenburg, Germany
  - Team of Prof. Sergej Fatikow
  - References: [ACT11,ACT13,ACL11]
- Multi-Scale Robotics Laboratory[7] (MSRL), ETH[8] Zurich, Switzerland
  - Team of Prof. Bradley Nelson and Prof. Salvador Pané Vidal
  - References: [ACT11,ACL10]
- Mechanical and Automation Engineering (MAE) Department of Chinese University of Hong Kong (CUHK), Hong-Kong.
  - Team of Prof. Li Zhang

III.3.2 National relationships

- Inria Rennes–Bretagne Atlantique, IRISA, University of Rennes, France
  - Team of senior researcher François Chaumette
  - Co-supervision of the PhD thesis of **Tao Li**.
  - Reference: [ACL8]
- Translational micro and nanomedicines[9] (MINT) Laboratory, University of Angers, France
  - Team of senior researcher Joël Eyer
- Center for Molecular Biophysics[10] (CBM), CNRS, Orleans, France
  - Team "Innovative therapies and nanomedicine" with Prof. Chantal Pichon
- Vermon[11] SA, Tours, France
  - R&D work on development and industrialization to enhance micro-object perception through ultrasound transducers.

III.4 Scientific Dissemination and Outreach

The appreciation of my research works have been effective through various actions that are reported hereafter.

[7] Multi-Scale Robotics Lab (MSRL) is part of Institute of Robotics and Intelligent Systems (IRIS), ETH Zurich, Switzerland. https://msrl.ethz.ch, https://www.iris.ethz.ch

[8] ETH Zurich is the Swiss Federal Institute of Technology in Zurich, from German "Eidgenössische Technische Hochschule". https://ethz.ch

[9] From French "Laboratoire Micro et Nanomédecines translationnelles", is funded by the University of Angers, as well as Inserm and the CNRS. http://mint.univ-angers.fr

[10] CBM is a research unit of the CNRS affiliate with the University of Orléans.http://cbm.cnrs-orleans.fr

[11] Vermon is a society involved in the design, manufacturing of composite piezoelectric transducer. https://www.vermon.com

III.4.1 Invitations

June 2010 scientific visit in the AMiR division, university of Oldenburg, Germany

March 2015 scientific visit in MAE Department of Chinese University of Hong Kong (CUHK), Hong-Kong.

Others I have also been invited as a speaker in international or national conferences, [INV1,INV2,INV3] which are reported in Section IV.4.1.

III.4.2 Scientific expertise

- I have took part in the evaluation process of Generic Call (2019,2020) for the French National Research Agency (ANR).
- I have been member of the recruitment selection committee:
  - 2013: associate professor position at University of Orléans;
  - 2015: associate professor position at INSA Centre Val de Loire;
  - 2021: associate professor position at INSA Centre Val de Loire;
- In addition to the PhD works that I co-supervised, I was also invited as an examiner member of the PhD thesis defense of:
  1. Adrien Durand Petiteville, *Navigation référencée multi-capteurs d'un robot mobile dans un environnement encombré*, university of Toulouse, December, 2011.
  2. Moahmed Dkhil, *Modélisation, caractérisation et commande d'un système micro-robotique magnétique à l'interface air/liquide*, University of Pierre and Marie Curie, Paris, April, 2016

III.4.3 Editorial activities

Since 2005 IEEE member (SM'05, AM'08, M'12).

Since 2013 Editorial Board member of the *International Journal of Advanced Robotic Systems* (IJARS).

Since 2015 Member of the program committee of the *International Conference on Robotics, Manipulation, and Automation at Small Scales* (MARSS)

2012 Oct. Session chairman of the *IEEE/RSJ International Conference on Intelligent Robots and Systems*, Vilamoura, Algarve, Portugal, October 2012

2021 Associate Editor of the *18th International Conference on Ubiquitous Robots*, Gangneung-si, Gangwon-do, Korea, 2021.

Regular Reviewer (non-exhaustive list)

- *IEEE Transactions on Robotics* (TRO);
- *IEEE robotics and automation letters* (RAL);
- *IEEE Transactions on Biomedical Engineering* (TBME);
- *IEEE/ASME Transactions on Mechatronics* (TMECH);
- *IEEE Transactions on Automation Science and Engineering* (TASE);
- *International Journal of Advanced Robotic Systems* (IJARS);
- *IEEE International Conference on Robotics and Automation* (ICRA);
- *IEEE/RSJ International Conference on Intelligent Robots and Systems* (IROS);
- *IEEE International Conference on Biomedical Robotics and Biomechatronics* (BioRob), ...

III.4.4 Awards

French outstanding research award (PEDR) for the periods 2014-2018 and 2018-2022.

Chapter IV

Personal References

My research activities have led to scientific publications that are listed in this chapter. The names of the people for whom I have supervised their works are in **bold face**. Furthermore, the publications list follows the Hcéres proposed nomenclature.

IV.1 Articles

IV.1.1 Articles in International peer-reviewed and referenced journals (ACL)

Remark **(Remark) —** \iffalse{} Remark (Metrics). Two journal metrics are reported here: journal quartile (Qn) and impact factor (IF). Journal metrics are based on Scopus® data as of April 2020. The reported quartile is the metric of the journal in the year of publishing.

[ACL1] David FOLIO, and Viviane Cadenat. "Dealing with visual features loss during a vision-based task for a mobile robot", *International Journal of Optomechatronics*, 2 (3): pp. 185–204, June 2008. doi:10.1080/15599610802301110. Special issue on Visual Servoing. (Q2, IF:0.81)

[ACL2] **Karim Belharet**, David FOLIO, and Antoine Ferreira. "MRI-based microrobotic system for the propulsion and navigation of ferromagnetic microcapsules", *Minimally Invasive Therapy & Allied Technologies*, 19 (3): pp. 157–169, June 2010. doi:10.3109/13645706.2010.481402. (Q2, IF:1.0)

[ACL3] **Karim Belharet**, David FOLIO, and Antoine Ferreira. "Three-dimensional controlled motion of a microrobot using magnetic gradients", *Advanced Robotics*, 25 (8): pp. 1069–1083(15), May 2011. doi:10.1163/016918611X568657. (Q2, IF:1.24)

In 2013 one of the Advanced Robotics most cited articles from 2011 publications.

[ACL4] Viviane Cadenat, David FOLIO, and Adrien Durand Petiteville. "A comparison of two sequencing techniques to perform a vision-based navigation task in a cluttered environment", *Advanced Robotics*, 26 (5-6): pp. 487–514, March 2012. doi:10.1163/156855311X617470. (Q2, IF:1.24)

[ACL5] **Jungsik Kim**, Hamid Ladjal, David FOLIO, Antoine Ferreira, and Jung Kim. "Evaluation of telerobotic shared control strategy for efficient single-cell manipulation", *IEEE Transactions on Automation Science and Engineering*, 9 (2): pp. 402–406, April 2012. doi:10.1109/TASE.2011.2174357 (**Q1**, IF:4.93)

[ACL6] **Karim Belharet**, David FOLIO, and Antoine Ferreira. "Simulation and planning of a magnetically actuated microrobot navigating in arteries", *IEEE Transactions on Biomedical Engineering*, 60 (4): pp. 994–1001, April 2013. doi:10.1109/TBME.2012.2236092. (**Q1**, IF:4.42)

[ACL7] **Nabil Amari**, David FOLIO, and Antoine Ferreira. "Motion of a micro/nanomanipulator using a laser beam tracking system", *International Journal of Optomechatronics*, 8 (1): pp. 30–46, April 2014. doi:10.1080/15599612.2014.890813 (Q3, IF:0.81)

[ACL8] Alexandre Kruba, David FOLIO, Cyril Novales, Pierre Vieyres, and **Tao Li**. "Robotized tele-echography: an assisting visibility tool to support expert diagnostic", *IEEE Systems Journal*, 10 (3): pp. 974–983, April 2014. doi:10.1109/JSYST.2014.2314773 (Q2, IF:3.98)

[ACL9] **Lyes Mellal**, Karim Belharet, David FOLIO, and Antoine Ferreira. "Optimal structure of particles-based superparamagnetic microrobots: application to MRI guided targeted drug therapy", *Journal of Nanoparticle Research*, 17 (2): 64, February 2015. doi:10.1007/s11051-014-2733-3 (Q2, IF:2.13)

[ACL10] **Bumjin Jang**, Wei Wang, Samuel Wiget, Andrew Petruska, Xiangzhong Chen, Chengzhi Hu, Ayoung Hong, David FOLIO, Antoine Ferreira, Salvador Pané, and Bradley Nelson. "Catalytic locomotion of core-shell nanowire motors", *ACS Nano*, 10 (11): pp. 9983–9991, November 2016. doi:10.1021/acsnano.6b04224 (**Q1**, IF:14.58)

[ACL11] **Christian Dahmen**, **Karim Belharet**, David FOLIO, Antoine Ferreira, and Sergej Fatikow. "MRI-based dynamic tracking of an untethered ferromagnetic microcapsule navigating in liquid", *International Journal of Optomechatronics*, 10 (2): pp. 73–96, April 2016. doi:10.1080/15599612.2016.1166305 (Q3, IF:0.81)

[ACL12] **Lyes Mellal**, David FOLIO, Karim Belharet, and Antoine Ferreira. "Modeling of optimal targeted therapies using drug-loaded magnetic nanoparticles for the liver cancer", *IEEE Transactions on Nano-Bioscience*, 15 (3): pp. 265–274, April 2016. doi:10.1109/TNB.2016.2535380 (Q2, IF:2.79)

[ACL13] David FOLIO and Antoine Ferreira. "2D robust magnetic resonance navigation of a ferromagnetic microrobot using pareto optimality", *IEEE Transactions on Robotics*, 33 (3): pp. 583–593, 2017. doi:10.1109/TRO.2016.2638446 (**Q1**, IF:6.12)

[ACL14] **Bruno Sarkis**, David FOLIO and Antoine Ferreira. Catalytic "Tubular Microjet Navigating in Confined Microfluidic Channels: Modeling and Optimization". *IEEE/ASME Journal of Microelectromechanical Systems*, 27 (2): pp.333–343, April 2018. doi:10.1109/JMEMS.2018.2803803 (**Q1**, IF:2.53)

[ACL15] **Ruipeng Chen**, David FOLIO, and Antoine Ferreira. "Mathematical Approach for the Design Configuration of Magnetic System with Multiple Electromagnets". *Robotic and Autonomous Systems*, 135: p. 103674, 2020. doi:10.1016/j.robot.2020.103674 (**Q1**, IF:2.82)

[ACL16] **Lyes Mellal**, David FOLIO, Karim Belharet, and Antoine Ferreira. "Modeling and Characterization of Deformable Soft Magnetic Microrobot for Targeted Therapy", *IEEE Robotics and Automation Letters*, vol. 6, no. 4, pp. 8293–8300, Oct. 2021, doi:10.1109/LRA.2021.3107102 (**Q1**, IF:3.74)

IV.1.2 Articles in unreferenced journals (ACLN)

[ACLN1] David FOLIO. Les innovations en microrobotique pour le biomédical. *Prospective et Stratégie*, APORS Éditions, 7 (1): pp. 69–78, 2017. doi:10.3917/pstrat.007.0069

IV.2 Books

IV.2.1 Guest Editor (DO)

[DO1] Ashis Banerjee, David FOLIO, Sarthak Misra and Quan Zhou. Guest editors of the Special Issue: "*Design, Fabrication, Control, and Planning of Multiple Mobile Microrobots*". *International Journal of Advanced Robotic Systems*, 2014. doi:10.5772/1

IV.2.2 Book Chapter (OS)

[OS1] David FOLIO and Viviane Cadenat. *Treating Image Loss by using the Vision/Motion Link: Generic Framework*, chapter 4, page 538. I-Tech, Vienna, Austria, November 2008. ISBN 978-953-7619-21-3.

[OS2] **Karim Belharet**, David FOLIO, and Antoine Ferreira. *Real-time software platform for in vivo navigation of magnetic micro-carriers using MRI system*, chapter 11. Number 51 in Biomaterials. Woodhead Publishing, Cambridge, October 2012. ISBN:780857091307.

[OS3] **Nabil Amari**, David FOLIO, and Antoine Ferreira. *Encyclopedia of Nanotechnology*, chapter Nanorobotics for Synchrotron Radiation Applications, pp. 1–19. Springer Netherlands, Dordrecht, 2nd edition, 2016. doi:10.1007/978-94-007-6178-1009270-1

[OS4] **Lyès Mellal**, Karim Belharet, David FOLIO, and Antoine Ferreira. *Modeling Approach of Transcatheter Arterial Delivery of Drug-Loaded Magnetic Nanoparticles*, chapter 10. in The Encyclopedia of Medical Robotics. World Scientific, October 2018. ISBN: 780857091307. doi:10.1142/9789813232280_0010

IV.3 Proceedings in International Conferences (ACT)

[ACT1] David FOLIO and Viviane Cadenat. Using redundancy to avoid simultaneously occlusions and collisions while performing a vision-based task amidst obstacles. In *European Conference on Mobile Robots (ECMR'05)*, Ancona, Italy, September 2005.

[ACT2] David FOLIO and Viviane Cadenat. A controller to avoid both occlusions and obstacles during a vision-based navigation task in a cluttered environment. In *European Control Conference (ECC'05)*, pages 3898–3903, Seville, Spain, December 2005.

[ACT3] David FOLIO and Viviane Cadenat. A redundancy-based scheme to perform safe vision-based tasks amidst obstacles. In *IEEE/RSJ International Conference on Robotics and Biomimetics (ROBIO'06)*, pages 13–18, Kunming, Yunnan, China, December 2006. doi:10.1109/ROBIO.2006.340252.

Finalist to the T.J. Tarn best paper in Robotics.

[ACT4] David FOLIO and Viviane Cadenat. A new controller to perform safe vision-based navigation tasks amidst possibly occluding obstacles. In *European Control Conference (ECC'07)*, Kos, Greece, July 2007.

[ACT5] David FOLIO and Viviane Cadenat. Using simple numerical schemes to compute visual features whenever unavailable. In *IFAC International Conference on Informatics in Control, Automation and Robotics (ICINCO'07)*, May 2007.

[ACT6] David FOLIO and Viviane Cadenat. A sensor-based controller able to treat total image loss and to guarantee non-collision during a vision-based navigation task. In *IEEE/RSJ International Conference on Intelligent Robots and Systems (IROS'2008)*, pages 3052–3057, Nice, France, September 2008. doi:10.1109/IROS.2008.4650743.

[ACT7] Olivier Kermorgant, David FOLIO, and François Chaumette. A new sensor self-calibration framework from velocity measurements. In *IEEE International Conference on Robotics and Automation (ICRA'2010)*, pp. 1524–1529, Anchorage, Alaska, May 2010. doi:10.1109/ROBOT.2010.5509219

[ACT8] **Karim Belharet**, David FOLIO, and Antoine Ferreira. 3D MRI-based predictive control of a ferromagnetic microrobot navigating in blood vessels. In *IEEE RAS and EMBS International Conference on Biomedical Robotics and Biomechatronics (BioRob'2010)*, pp. 808–813, Tokyo, Japan, September 2010. doi:10.1109/BIOROB.2010.5628063

[ACT9] **Karim Belharet**, David FOLIO, and Antoine Ferreira. Endovascular navigation of a ferromagnetic microrobot using MRI-based predictive control. In *IEEE/RSJ International Conference on Intelligent Robots and Systems (IROS'2010)*, pp. 2804–2809, Taipei, Taiwan, October 2010. doi:10.1109/IROS.2010.5650803

[ACT10] **Jungsik Kim**, Dongjune Chang, Hamid Ladjal, David FOLIO, and Antoine Ferreira and Jung Kim. Evaluation of telerobotic shared control for efficient manipulation of single cells in microinjection. In *IEEE International Conference on Robotics and Automation (ICRA'2011)*, pp. 3382–3387, Shanghai, China, May 2011. doi:10.1109/ICRA.2011.5979868

[ACT11] David FOLIO, **Christian Dahmen**, Tim Wortmann, M. Arif Zeeshan, Kaiyu Shou, Salvador Pane, Bradley J. Nelson, Antoine Ferreira, and Sergej Fatikow. MRI magnetic signature imaging, tracking and navigation for targeted micro/nano-capsule therapeutics. In *IEEE/RSJ International Conference on Intelligent Robots and Systems (IROS'2011)*, pp. 1297–1303, San Fransisco, CA, USA, September 2011. doi:10.1109/IROS.2011.6048651

[ACT12] **Karim Belharet**, David FOLIO, and Antoine Ferreira. Control of a magnetic microrobot navigating in microfluidic arterial bifurcations through pulsatile and viscous flow. In *IEEE/RSJ International Conference on Intelligent Robots and Systems (IROS'2012)*, pp. 2559–2564, Vilamoura, Algarve, Portugal, October 2012. doi:10.1109/IROS.2012.6386030

[ACT13] **Christian Dahmen**, David FOLIO, Tim Wortmann, Alexander Kluge, Antoine Ferreira, and Sergej Fatikow. Evaluation of a MRI based propulsion/control system aiming at targeted micro/nano-capsule therapeutics. In *IEEE/RSJ International Conference on Intelligent Robots and Systems (IROS'2012)*, pp. 2565–2570, Vilamoura, Algarve, Portugal, October 2012. doi:10.1109/IROS.2012.6386244

[ACT14] **Karim Belharet**, David FOLIO, and Antoine Ferreira. Untethered microrobot control in fluidic environment using magnetic gradients. In *International Symposium on Optomechatronic Technologies (ISOT'2012)*, pp. 1–5, October 2012.

[ACT15] **Nabil Amari**, David FOLIO, and Antoine Ferreira. Robust laser beam tracking control using micro/nano dual-stage manipulators. In *IEEE/RSJ International Conference on Intelligent Robots and Systems (IROS'2013)*, pp. 1543–1548, Tokyo Big Sight, Japan, November 2013. doi:10.1109/IROS.2013.6696554

[ACT16] **Nabil Amari**, David FOLIO, **Karim Belharet**, and Antoine Ferreira. Motion of a micro/nanomanipulator using a laser beam tracking system. In *International Symposium on Optomechatronic Technologies (ISOT'2013)*, Jeju Island, Korea, October 2013.

[ACT17] **Karim Belharet**, Yang Chunbo, David FOLIO, and Antoine Ferreira. Model characterization of magnetic microrobot navigating in viscous environment. In *International*

Symposium on Optomechatronic Technologies (ISOT'2013), Jeju Island, Korea, October 2013.

[ACT18] **Nabil Amari**, David FOLIO, and Antoine Ferreira. Robust tracking of a two-fingered micromanipulation system working through the focus of an optical beam. In *American Control Conference (ACC'2014)*, pp. 1613–1618, Portland, OR, USA, June 2014. doi:10.1109/ACC.2014.6859244

[ACT19] **Karim Belharet**, David FOLIO, and Antoine Ferreira. Vision-based forces characterization of magnetic microrobot in a viscous environment. In *IEEE International Conference on Robotics and Automation (ICRA'2014)*, pp. 2065–2070, Hong Kong, China, May 2014. doi:10.1109/ICRA.2014.6907133

[ACT20] **Nabil Amari**, David FOLIO, and Antoine Ferreira. Robust nanomanipulation control based on laser beam feedback. In *IEEE/RSJ International Conference on Intelligent Robots and Systems (IROS'2014)*, pp. 4674–4679, Chicago, IL, USA, September 2014. doi:10.1109/IROS.2014.6943226

[ACT21] **Karim Belharet**, David FOLIO, and Antoine Ferreira. Study on rotational and unclogging motions of magnetic chain-like microrobot. In *IEEE/RSJ International Conference on Intelligent Robots and Systems (IROS'2014)*, pp. 834–839, Chicago, IL, USA, September 2014. doi:10.1109/IROS.2014.6942656

[ACT22] **Bruno Sarkis**, David FOLIO, and Antoine Ferreira. Catalytic tubular microjet propulsion model for endovascular navigation. In *IEEE International Conference on Robotics and Automation (ICRA'2015)*, pp. 3537–3542, Seattle, Washington, USA, May 2015. doi:10.1109/ICRA.2015.7139689

[ACT23] **Lyes Mellal**, David FOLIO, Karim Belharet, and Antoine Ferreira. Magnetic microbot design framework for antiangiogenic tumor therapy. In *IEEE/RSJ International Conference on Intelligent Robots and Systems (IROS'2015)*, pp. 1397–1402, Hamburg, Germany, September 2015. doi:10.1109/IROS.2015.7353550

[ACT24] **Lyes Mellal**, David FOLIO, Karim Belharet, and Antoine Ferreira. Optimal control of multiple magnetic microbeads navigating in microfluidic channels. In *IEEE International Conference on Robotics and Automation (ICRA'2016)*, pp. 1921–1926, Stockholm, Sweden, May 2016. doi:10.1109/ICRA.2016.7487338

[ACT25] **Lyes Mellal**, David FOLIO, Karim Belharet, and Antoine Ferreira. Estimation of interaction forces between two magnetic bolus-like microrobots. In *International Conference on Manipulation, Automation and Robotics at Small Scales (MARSS'2016)*, pp. 1–6, Paris, France, July 2016. doi:10.1109/MARSS.2016.7561740

[ACT26] **Lyes Mellal**, David FOLIO, Karim Belharet, and Antoine Ferreira. Motion control analysis of two magnetic microrobots using the combination of magnetic gradient and oscillatory magnetic field. In *International Conference on Manipulation, Automation and Robotics at Small Scales (MARSS'2017)*, pp. 1–6, Montreal, QC, Canada, July 2017. doi:10.1109/MARSS.2017.8001917

[ACT27] **Ruipeng Chen**, David FOLIO, and Antoine Ferreira Study of robotized electromagnetic actuation system for magnetic microrobots devoted to minimally invasive ophthalmic surgery, in *International Symposium on Medical Robotics (ISMR'2019)*, pp. 1–7, Atlanta, GA, USA, April 2019. doi:10.1109/ISMR.2019.8710208

[ACT28] **Ruipeng Chen**, David FOLIO, and Antoine Ferreira Computational Electromagnetics Performances of Magnetic Microrobotics Systems, in *International Conference on Robotics and Automation (ICRA'2019)*, Montreal, QC, Canada, May 2019. doi:10.1109/ICRA.2019.8794092

[ACT29] **Ruipeng Chen**, David FOLIO, and Antoine Ferreira Performance Metrics for a Robotic Actuation System using Static and Mobile Electromagnets, in *IEEE International Conference on Computational Electromagnetics (ICCEM'2019)*, pp. 1–3, Shanghai, China, July 2019. doi:10.1109/COMPEM.2019.8778897

IV.4 Oral Communications

IV.4.1 Invited Speaker in International or National Conferences (INV)

[INV1] David FOLIO. Bio-nanorobotics: A reality for tomorrow? Invited speaker in International R&D Symposium: "biology and communications", Madrid, Spain, March 2012. Fundación Ramón Areces.

[INV2] David FOLIO. Micro/nano-robots thérapeutique pour le traitement cibler du cancer. Invited speaker in Colloque International: " Quelles nanotechnologies pour la médecine", Rabat, Morocco, November 2014.

[INV3] David FOLIO. Innovation en microrobotique pour le biomédical. Invited speaker in Colloque " les futurs de l'innovation", Bourges, France, June 2015. Prospective et Stratégie.

IV.4.2 Communications in International or National Conferences (COM)

[COM1] David FOLIO and Viviane Cadenat. A method to safely perform a visually guided navigation task amidst occluding obstacles. Presented in the *7th International Workshop on Electronics, Control, Modelling, Measurement and Signals* (ECMS'2005), May 2005.

[COM2] David FOLIO évitement d'obstacles et gestion des occultations durant une tâche de navigation référencée vision. Presented in the *6ème Congrès des doctorants EDSYS (EDSYS'05)*, May 2005.

[COM3] David FOLIO and Viviane Cadenat. Gestion des problèmes d'occultation et de collision durant une tâche référencée vision. Poster presentes in *Journées Nationales de la Recherche en Robotique (JNRR'05)*, October 2005.

[COM4] David FOLIO and Viviane Cadenat. Dealing with visual features occlusions and collisions during a vision-based navigation task in cluttered environments. Presented in the *8th International Workshop on Electronics, Control, Modelling, Measurement and Signals* (ECMS'2007), May 2007.

[COM5] **Nabil Amari**, David FOLIO, and Antoine Ferreira. Robust tracking of a two-fingered nanomanipulation system working through the focus of a X-ray beam. Presented in the *Workshop on Automation of Assembly and Packaging at the Micro/Nano-scale*, Trieste, Italy, August 2011.

[COM6] David FOLIO and Antoine Ferreira. Endovascular navigation of magnetic microcarriers using a MRI system. Presented in the *Workshop on Magnetically Actuated Multiscale Medical Robots*, Vilamoura, Algarve, Portugal, October 2012.

[COM7] David FOLIO. Dynamic Modeling Of Self-phoretic Magnetic Janus Microrobot. Presented in the *Special session Control of bio-hybrid & bio-inspired microrobotic systems* of the *International Conference on Manipulation, Automation and Robotics at Small Scales (MARSS'2019)*, Helsinki, Finland, June 2019.

Appendix

Appendix A

Three-dimensional controlled motion of a microrobot using magnetic gradients (ACL3)

Three-Dimensional Controlled Motion of a Microrobot using Magnetic Gradients

Karim Belharet, David Folio, Antoine Ferreira

3D Controlled Motion of a Microrobot using Magnetic Gradients

Karim Belharet, David Folio and Antoine Ferreira

Institut PRISME, ENSI de Bourges, 88 boulevard Lahitolle, 18020 Bourges, FRANCE;

{karim.belharet, david.folio, antoine.ferreira} @ensi-bourges.fr

Abstract

This paper presents an endovascular navigation of a ferromagnetic microdevice using MRI-based predictive control. The concept was studied for future development of microrobot designed to perform minimally invasive interventions in remote sites accessible through the human cardiovascular system. A system software architecture is presented illustrating the different software modules to allow 3D navigation of a microdevice in blood vessels, namely: (i) vessel path extraction, (ii) magnetic gradient steering, (iii) tracking and (iv) closed-loop navigation control. First, the navigation path of the microrobot into the blood vessel is extracted using Fast Marching Method from the pre-operation images (3D MRI imaging) to guide the microrobot from the injection point to the tumor area through the anarchic vessel network. Based on the pre-computed path, a Model Predictive Controller is proposed for robust time-multiplexed navigation along a 3D path in presence of pulsative flow. The simulation results suggest the validation of the proposed image processing and control algorithms.

keywords: Microrobot, gradient controlled motion, endovascular navigation

1 INTRODUCTION

Microrobots designed to perform targeted therapy by navigating in the cardiovascular system are a prolific research area for minimally invasive surgeries [1][2] and treatments efficiency through early diagnosis of diseases [3]. When microrobots are propelled in the body fluids, especially in the blood circulatory system, a very large number of remote locations in the human body become accessible. Because the method of propulsion should allow such a microrobot to navigate through the cardiovascular system, the use of the normal blood flow itself must be considered only as a complementary means of propulsion when the travel path is along the direction of the blood flow. These untethered microrobots have been mainly developed according to three different designs: magnetic bead pulling [2], biomimetic flagellated robot [4] and magnetotactic bacteria [5]. Furthermore, navigation requires observation of the scene in order either to plan the trajectory by off-line mapping, or to correct on-line the microrobot's pose error between the planned and the observed trajectory. Recently, magnetic resonance imaging (MRI)-based medical microrobotic platforms are investigated to reach locations deep in the human body while enhancing targeting efficacy using real-time navigational and trajectory control [6]. For the position recognition of the microrobot in the blood vessels, from the pre-operation images, 3D path planning and route optimization

solutions have been proposed. The authors in [7] proposed an endovascular path-planning method based on 3D potential fields and enhanced breath-first search algorithms based on MR-imaging. Based on these path-planning techniques, only explorative 2D control strategies have been adopted so far using simple proportional-integral-derivative (PID) controller [8]. However, stability and robustness are not ensured against important perturbations. First, pulsatile flow should be taken into account since variations in waveform, amplitude, and frequency exists from vessels. Second, variation of time-multiplexed sequence parameters (duty cycle of the propulsion gradients, and repetition time of the tracking sequence) produce important trajectory errors during real-time navigation. Finally, random imaging signal noise degrades the localization of the microrobot during tracking.

The main objective of this paper is to propose an automated technique based on image processing and control algorithms for path finding, reconstruction and navigation control of a ferromagnetic microrobot using the MRI system. The MRI-based control of a ferromagnetic microcapsule presented here is dedicated to macroscale navigation, which focuses in conveying a microsphere radius of 300 μm in vessels, such as arteries and arterioles (eg, around 10 to 0.5 mm), as close as possible to the tumor area. Based on slice images provided by an MRI system, relevant information related to detection of blood vessels is extracted using robust Frangi vesselness filtering from the pre-operation images. Then, a set of minimal path is predefined, using Fast Marching Method (FMM), to guide the ferromagnetic microrobot from the injection point to a targeted area through the anarchic vessel network. Based on the precomputed path, a Model Predictive Controller (MPC) is designed. Hence, we proposed a control strategy for robust time-multiplexed navigation along a 3D path even in presence of pulsative flow. The simulation results suggest the validation of the proposed image processing and control algorithms against perturbations.

2 MRI-based NAVIGATION SYSTEM

2.1 System Overview

The Magnetic Resonant Imaging (MRI)-based microrobotic system is used here for propulsion and navigation of the microdevice. The propulsion of the ferromagnetic microcapsule in the cardiovascular system is realized through the induction of force from magnetic gradients provided by the MRI. This MRI system will guide the microcapsule *in vivo* through vascular networks to a targeted area. The overview of the software system architecture is given in Fig. 1.

(i) The graphical user interface module, which comprises input command prompt, 3D-visualization, and process supervision tools. (ii) The control module, which comprises (a) the high-level controller responsible for the microcapsule navigation tasks and for the generation of the magnetic field gradients and (b) the low-level controller (manufacturer MRI controller) responsible for the generation of the desired field gradients and for the image acquisition tasks. Then, (iii) the controlled hardware, which comprises (a) the MRI hardware and software systems and (b) the microcapsules that have been injected within the vasculature and are steered by the magnetic gradients. Finally, (iv) the image processing module, which comprises the MRI data rendering, the navigation path extraction, and the microdevice recognition/tracking algorithm. In particular, the tracking

procedure, presented in [9], allows to estimate the position and accumulation of the microdevices within the vasculature, the tissues, and the organs of the human. However as MR-imaging is too slow to gather position of the microrobot and special MR-tracking algorithm, such as MR-SET, must considered to ensure real time control.

2.2 Navigation in blood vessels

In our context, the problem of navigation in blood vessels within the MRI data can be formulated as finding the correct way through the data that follows the vessel of interest between its start and end points. Finding a navigation path within the endovascular network is then an essential, primary, and important step that must be addressed prior to the control procedure. The problem of vessels extraction has received considerable attention in the computer vision and medical imaging communities [10]. Hence, several class of methods have been proposed to find a path from a set of medical imaging, such as using tracking methods [11] [6] [12], path extraction methods [13][14][15], and so on. Most works based on *in vivo* MR-tracking methods usually need many user-defined way points as the input of a controller module for the navigation computation. A major drawback in general remains when the user must define many points (e.g. way or fiducial points) manually. Hence, for a complex structure (e.g. colon, small vessels...) the required interactivity can be very tedious. The path extraction is useful for a range of application domains including medical image analysis, robot navigation, and artificial intelligence. The path extraction technique needs a very simple initialisation and leads to global minimum of a snake-like energy, thus avoiding local minima. Moreover, it is fast and accurate. This path finding problem has been studied for ages by mathematicians, and has been solved numerically using graph theory or dynamic programming. Cohen and Kimmel [16] solved the minimal path problem in 2D with a front propagation equation between the two fixed end points, using the Eikonal equation (that physically models wave-light propagation), with a given initial front. Wink *et al.*[14] explored different methods to determine the minimum cost path through a pre-defined cost image, for extraction of vessel centrelines from medical image data. Among them are Dijikstra's algorithm, the $A^\star$ algorithm, which makes use of additional heuristics to steer the search process, and wave front propagation analysis [15]. Early, Sethian [17] explored the use of Fast Marching Method (FMM) to extract minimal paths. This method relies on the fact that the gradient of the FMM arrival function has only one local minimum, which is guaranteed to be global minimum [13]. Therefore, the minimal path can be extracted by back-propagating from given seeds (e.g. the end point of the desired path) to the starting point implicitly embedded in the arrival function.

In this work the FMM is adopted to design a set of paths to guide the microdevice from the injection point to the tumor area through the vessel network. Our aim is to focus on the automation of the path construction, reducing the need of interaction and improving performance, in a robust way.

3 MRI-BASED PREDICTIVE CONTROL

3.1 Problem formulation

Navigation in blood vessel requires observation of the scene in order either to plan the path by offline mapping, or to correct online the microrobot pose error between the planned and the observed path. To insure a smooth conveyance of the microcapsule to destination, collisions and the risk to be trapped by the endothelium, optimal navigation performance will be affected by external perturbations and MRI technological constraints:

- Nonnegligible pulsatile flow, whose variations in waveform, amplitude, and frequency exist from one vessel to another (such as arteries and arterioles).
- Magnetic gradients are used both for observation and control purposes in a time-multiplexed sequence. It requires different trade-offs in terms of refresh rate, duty cycle of the propulsion gradients, and repetition time of the tracking sequence.
- MRI overheating avoidance leading to limitations on the MRI duty cycle, tends to increase the disproportional scaling between magnetic forces used for control purpose and perturbation forces (drag forces and net buoyancy forces).
- Limitations on the magnetic gradient amplitude in available MRI devices.
- Proper delay in the image processing algorithms that renders the navigation control unstable.

3.2 Real-Time Sequence Design

The overall concept of the in-vivo MRI-tracking system is based on the fact that both tracking and propulsion is possible with the gradient coils of the MRI system. Software based upgrading of a clinical MRI system is the least expensive approach to convert a platform that is used for imaging to an effective interventional platform. At any instant only one of the functions could be applied (i.e. either tracking or propulsion), but both will be executed over the same MRI interface. The MRI interface has therefore to be shared and a time-division-multiple-access scheme for it has to be developed. Fig. 2 shows an overview of the real-time sequence with time-multiplexed positioning and propulsion phases introduced by Martel *et al.* [6]. The main aspect relevant to the controller's performance is (i) the duty cycle $T_{\text{Prop}}/T_{\text{s}}$ that stands for the ratio between the propulsion time and the time between two successive position requests, and (ii) the synchronization event delay T_{Sync} that stands for the minimum time allowed for image processing and real-time control feedback. First, the duty cycle should be adapted to apply sufficient magnetic propulsion gradients during a predefined propulsion time T_{Prop} to prevent the microrobot from drifting away from the path. Second, a large time delay T_{Sync} produces oscillations as the microrobot approaches the reference path w leading to position instabilities. Such limitations have been pointed out by Mathieu et al. [8] when implementing simple proportional-integral-derivative (PID) controller. We proposed a Model Predictive Controller (MPC) including microrobot's motion and dynamics with estimation of the pulsative blood flow and time-multiplexed positioning. A predictive path-tracking control consider a prediction window (cf. Fig. 2). The

propulsion phase starts during T_{Prop} seconds at the same initial condition as the prediction phase, recording the performance of the system according to a prediction horizon. After this phase the system ends after a imaging-propulsion sequence at a final position Y which is set as the new initial condition of the next prediction output $\widehat{Y}$. The proposed navigation based predictive controller offers stability by design and allows the designer to trade-off performance for (computation) speed, stability margins according to the MRI application and technological requirements outlined in section 3.1.

3.3 Model description

The linear model used in this work is derived from the nonlinear model developed in a previous study [18]. The authors used this model to combine the backstepping controller and high-gain observer in order to control the path of the microrobot inside a vessel using the MRI gradients.

The different forces acting on the microrobot are (see Fig. 3): drag force $\overrightarrow{F}_d$, apparent weight $\overrightarrow{W}_a$ and magnetic force $\overrightarrow{F}_m$. The application of Newton's third law and the projection on the $(\overrightarrow{x}, \overrightarrow{y}, \overrightarrow{z})$ axes leads to:

$$\left\{\begin{array}{lcl} m\ddot{x} &=& \overrightarrow{F}_{dx} + \overrightarrow{F}_{mx} \\ m\ddot{y} &=& \overrightarrow{F}_{dy} + \overrightarrow{F}_{my} \\ m\ddot{z} &=& \overrightarrow{F}_{dz} + \overrightarrow{F}_{mz} + \overrightarrow{W}_a \end{array}\right. \tag{1}$$

where m is the mass of the microrobot modeled by a ferromagnetic sphere with a high saturation magnetization.

Let $\overrightarrow{\mathbf{v}} = (v_{f_x}, v_{f_y}, v_{f_z})$ denotes the blood flow velocity, and (x,y,z) the robot location in the blood vessel wrt. to a given frame $\mathscr{F}(O, \overrightarrow{x}, \overrightarrow{y}, \overrightarrow{z})$. Taking the drag coefficient $C_d = \frac{24}{Re}$, the linear model can be written as follow:

$$\left\{\begin{array}{lcl} \ddot{x} &=& \alpha_1 \left(\dot{x} - v_{f_x}\right) + \alpha_2 u_x \\ \ddot{y} &=& \beta_1 \left(\dot{y} - v_{f_y}\right) + \beta_2 u_y \\ \ddot{z} &=& \gamma_1 \left(\dot{z} - v_{f_z}\right) + \gamma_2 u_z \end{array}\right. \tag{2}$$

with the following parameters α_i, β_i and γ_i, and the magnetic gradients considered as control inputs u_x, u_y and u_z, that is:

$$\left\{\begin{array}{lclcl} \alpha_1 &=& -4.5\frac{\eta\cos\varphi\cos\theta}{r^2\rho}, & u_x &=& \left\|\overrightarrow{\nabla} B_x\right\| \\ \beta_1 &=& -4.5\frac{\eta\cos\varphi\sin\theta}{r^2\rho}, & u_y &=& \left\|\overrightarrow{\nabla} B_y\right\| \\ \gamma_1 &=& -4.5\frac{\eta\sin\varphi}{r^2\rho}, & u_z &=& \left\|\overrightarrow{\nabla} B_z\right\| \\ \alpha_1 &=& \beta_2 = \gamma_2 = \frac{m}{\rho} & & & \end{array}\right. \tag{3}$$

where ρ is the density of the fluid; η is the fluid viscosity; r is the spherical radius of the microrobot; and $\mathbf{B} = (B_x, B_y, B_z)^T$ is the magnetic field generated by the MRI system.

Finally, the state-space representation is deduced from (2):

$$(S)\left\{\begin{array}{lcl} \dot{x} &=& v_x \\ \dot{v_x} &=& \alpha_1 v_x - \alpha_1 v_{f_x} + \alpha_2 u_x \end{array}\right\} (S_x)$$
$$\left\{\begin{array}{lcl} \dot{y} &=& v_y \\ \dot{v_y} &=& \beta_1 v_y - \beta_1 v_{f_y} + \beta_2 u_y \end{array}\right\} (S_y)$$
$$\left\{\begin{array}{lcl} \dot{z} &=& v_z \\ \dot{v_z} &=& \gamma_1 v_z - \beta_1 v_{f_z} + \gamma_2 u_z \end{array}\right\} (S_z) \tag{4}$$

where $(v_x, v_y, v_z)^T$ denotes the robot velocity along $\overrightarrow{x}$-axis, $\overrightarrow{y}$-axis and $\overrightarrow{z}$-axis. Assuming that the microrobot location (x,y,z) can be measured thanks to the MRI system, we denote by $Y = (x,y,z)^T$ the process measure. We can notice that system (S) can be divided into three subsystems (S_x), (S_y) and (S_z), which allow us to define three independents MPC schemes to track the reference path w in 3D MRI data.

In this paper, we aim to use the system model defined in (4) in a high level MPC scheme in order to follow efficiently a pre-planed path extracted with the method proposed in section 2.2. The proposed MPC controller is intended to embed the low level *robust controller* designed in [18][19] (see Fig. 4). Let us notice that the low level controller provides[1] robustness performances against MRI system constraints (as pulsatile flow, limited gradient amplitude, and image noise) while the MPC controller is designed to tradeoff time-multiplexed sequence constraints in terms of refresh-rate, duty cycle of the propulsion gradients, and repetition time of the tracking sequence.

3.4 Predictive Control

Model Predictive Control (MPC) has become an area of significant research interest over the last past twenty years. This interest has been powered by a stream of successful industrial applications [21]. When focusing on linear (and unconstrained) discrete time transfer function models and quadratic cost functions, some of the best known approaches include the Generalized Predictive Control (GPC) introduced by Clarck *et al.*[22], and the inner loop stabilizing Stable Predictive Control [23].

MPC refers to a class of computer control algorithms which use an explicit process model to predict the future response of the system. One way to design MPC is to use an extended state-space representation, which is given by:

$$\begin{cases} \dot{X}_{k+1} &= AX_k + B\Delta u_k \\ Y_k &= CX_k \end{cases} \tag{5}$$

where $\Delta u_k = u_k - u_{k-1}$ is the discrete difference operator. The predicted state vector at time $k+i$ is then computed from [24]:

$$\widehat{X}_{k+i|k} = A^i X_{k|k-1} + \sum_{j=0}^{i-1} A^j B u_{k-j-1} \tag{6}$$

Then, the future outputs $Y_{k+j|k}$ can be computed based on the plant for future times starting at time k using a recursion procedure, defined by:

$$\widehat{Y}_{k+i|k} = C\left(A^i X_k + \sum_{j=1}^{i} A^{i-j-1} B u_{k+i-j|k}\right) \tag{7}$$

Design criterion is defined for certain interval of predictions (several steps to future). It includes the part of control error, in which the model of system is covered (insertion of equations of prediction (7)) and the part of control actions, where the input energy (control actions) is weighted. This part redistributes control errors to individual steps of predictions and provides coupling within intervals of predictions. Usual form of the criterion

[1]The interested reader is invited to refer to [18][19][20].

for predictive design is written as follows:

$$J_k = \sum_{j=N_1+1}^{N_2} \left[Y_{k+j} W_{k+j}^T Q_Y Y_{k+j} W_{k+j} \right] + \sum_{j=1}^{N_u} \left[u_{k+j-1}^T Q_u u_{k+j-1} \right] \tag{8}$$

The criterion is expressed in step k. $N = N_2 - N_1$ is a horizon of prediction, N_u is the control horizon. Q_Y and Q_u are output and input penalizations. Y_{k+j} and u_{k+j-1} are output and input (full or incremental) values.

Finally, let us note how to construct real control actions at incremental algorithm: after computing a vector for whole horizon, only first control u_k is used; then to obtain the full control actions the second line of equation (5) is applied.

When using MPC in the state-space formulation, and generally at the use of whichever stat-space control, it is necessary to solve the question of availability of the state of the system (state vector). If it is not available, and only system output from the measurement are known, then some state-space estimation has to be considered. Suitable well-known solution of such estimation is the state-space observer based on Kalman filter.

4 Results

4.1 Navigation Path Extraction

The FMM algorithm, introduced by Sethian [17] is applied here to extract a targeted navigation path within the vessel network. From the set of 3D MRI data, a speed map is computed (ie. a weighting image map) in order to enhance the relevant intravascular network. Choosing an appropriate and efficient image cost function is the most difficult part of the entire process.

We describe in the sequel presented in Fig. 5, the process used to extract the navigation path. First, we need a relevant cost function which allow to enhance vessel in the image. To this aim, we used some *a priori* knowledge about vessel shape and intensity in MRI data (cf. Fig. 5). Vessels are expected to appear as bright tubular structures in a darker environment. One way to account for the varying size of vessels is by multiscale analysis. It allows us to detect structures of different sizes according to the scale at which they give maximal response. In this context, a typical speed image is produced by using a Frangi vesselness filter [25] which uses the eigenvectors of the Hessian matrix at each voxel of the image to compute the likeliness of an image region to vessels. This mapping is selected in such a way that vessels regions will have higher speed (high level in speed image, see Fig. 5). Once the speed map is generated, the user has to select a start and end points (ie. seed points) in the viewer of the input original image. The FFM will then propagate a front from the start seed and traveling to the targeted area, thanks to the speed map. Thus, this approach allow to find a minimal navigation path between the start and targeted seed (cf. Fig. 5).

4.2 Microdevice Navigation using Predictive Control

Simulations conducted here are performed within the scope of actual commonly spread MRI system abilities. Actually, MRI systems are able to generate magnetic gradients with an intensity of some tens of $\mathrm{mT.m^{-1}}$. Let us note that this limitation is additionally affected by the gradient coils duty-cycle and by the time-multiplexing

sequence ($T_{\text{Prop}}/T_{\text{s}}$) needed both for controlling and observing sequences. In order to make sure that the amplitude of the control inputs remains bounded by physical actuators limits $u_{i,\max}$, and to protect the system, we applied a simple time-scaling factor defined by $\frac{u_i}{k(t)}$, with $k(t)$ =max $\left\{1, \frac{u_i}{u_{i,\max}}\right\}$. The following set of simulations corresponds to a microcapsule radius of $r = 300\ \mu$m and a time scaling settled at $k(t) = 0.55$. Different situations are considered to illustrate and to validate the performance of the proposed MRI-based predictive controller.

We validated the proposed control strategy on a 3D endovascular navigation path w extracted from MRI-data with the previously presented method without any disturbance. Then, to evaluate the efficiency of the proposed MRI-based predictive controller, we performed some tests with a white Gaussian noise on the system output measure Y. The noise is about 10 % of the measured signal which is motivated by the common precision of clinical MRI devices.

Fig. 6 describes the navigation path followed by the microrobot, and Fig. 7 presents the relative error norm between the current position Y and the reference w, for a time horizon $N = 5$. As shown, the system output Y follows perfectly the reference path w. In particular, the microdevice is able to reach quickly the navigation path, in spite of a gap between the initial position Y and the reference w. Let us notice that the 3D tracking is not too much affected by the Gaussian noise since position standard deviation (STD) and root mean square (RMS) error are quite satisfactory.

Fig. 8 simulates the impact of the time horizon N on the system tracking error for optimized time horizon values between 3 $\leq$N$\leq$ 10. Comparing the error statistics, the nature of anticipation of the MPC scheme is well illustrated - important values of N improve greatly the anticipation nature of the path behavior but increases at the same time the path tracking error-. Hence, a great value of N does not necessarily guarantee good performances, and classically increase the complexity of the scheme.

To evaluate the robustness of our control strategies, we have also applied an external disturbance which represent the pulsatile blood flow behavior.

Hence, we have modeled the blow flow as a time-sinusoidal profile with spatial parabolic form $\sigma_{\text{flow}}(t)$. In case of an artery, to model the action of flow (positive) and reflux of blood (negative) $\sigma_{\text{flow}}(t)$ were shifted up, leading to:

$$\sigma_{\text{flow}}(t) = 0.025\left(1 + 1.15\sin\left(2\pi t + \frac{\pi}{8}\right)\right) \tag{9}$$

where amplitude of 0.025 is representative of maximum blood flow speed. In the following, the performance and stability of the predictive controller with respect to physiological parameters variations are demonstrated in Fig. 9. It appears that the system is robust to uncertain physiological parameters (disturbance applied at $t = 13$ seconds) since the 3D position tracking error norm is bounded to 0.2 %.

Finally, we have evaluated the robustness of our controller for different duty cycle values: 25 %, 50 % and 75 %, respectively. The error curves and statistics for the three scenario are illustrated on Fig. 10. As one can see for a duty cycle of 50 %, that is the MRI system propels during the first half-period, and acquires 3D images on the other half-period, the path tracking is quite satisfactory. It corresponds to the real-time navigational and trajectory control constraints reported in [8]. Nevertheless for a duty cycle of 25 % (ie. the MRI propels during $1/4$ period, and image during $3/4$ period) the microrobot can not properly track the reference path w leading

to great tracking error. The time-multiplexing duty cycle is optimized for a value around 40 %. In the optimal case, the simulated predictive behavior of the MPC controller suggests better tracking results compared to those obtained by [8] that should be confirmed by experimentation.

5 CONCLUSIONS

The proposed MRI-based ferromagnetic microcapsule steering and navigation strategy has been developed at milli and microscale, where endovascular navigation path extraction and predictive controller have been designed. The main drawback of MRI-based navigation stems from the strong limitations on the magnetic gradient amplitude of available MRI devices. As magnetic forces used for propelling are volumetric, whereas the drag force is at best dependent on the microcapsule's area, the smaller the capsule, the higher the required control forces with respect to hydrodynamic perturbations. Consequently, this approach is well conditioned for beads whose radius is up to a few dozen micrometers with actual MRI devices. Targeting aims at focusing these microcarriers and stopping them through embolization at the arterioles entry close to the occluded blood vessels. Possible releasing mechanisms could rely on biodegradable polymer and techniques used in hyperthermia where aggregates of nanocapsules can be heated to melt polymer. Such a solution is actually under experimentation for validation of the proposed minimally invasive MRI-based microrobotic system.

6 ACKNOWLEDGMENTS

This work was supported by European Union's 7th Framework Program and its research area ICT-2007.3.6 Micro/nanosystems under the project NANOMA (Nano-Actuactors and Nano-Sensors for Medical Applications). The PhD student K. Belharet is supported by the Nano-IRM project, funded by Conseil Gnral du Cher and Agglomeration de Bourges.

References

[1] K. Ishiyama, M. Sendoh, and K. I. Arai, "Magnetic micromachines for medical applications," *J. of Magnetism and Magnetic Materials*, vol. 242-245, pp. 41–46, 2002.

[2] J. Abbott, Z. Nagy, F. Beyeler, and B. Nelson, "Robotics in the Small," *IEEE Robot. Automat. Mag.*, p. 92, 2007.

[3] T. A. Cavalcanti, B. Shirinzadeh and S. Ikeda, "Nanorobot for Brain Aneurysm," *Int. J. of Robotic Research*, vol. 28, no. 4, pp. 558–570, 2009.

[4] B. Behkam and M. Sitti, "Design methodology for biomimetic propulsion of miniature swimming robots," *ASME J. Dyn. Syst. Meas. Control*, pp. 36–43, 2006.

[5] S. Martel, M. Mohammadi, O. Felfoul, Z. Lu, and P. Pouponneau, "Flagellated magnetotactic bacteria as controlled MRItrackable propulsion and steering systems for medical nanorobots operating in the human microvasculature," *Int. J. Robot. Res.*, vol. 28, no. 4, pp. 571–582, 2009.

[6] O. Felfoul, J. Mathieu, G. Beaudoin, and S. Martel, "In vivo MR-tracking based on magnetic signature selective excitation," *IEEE Trans. Med. Imag.*, vol. 27, no. 1, pp. 28–35, Jan. 2008.

[7] W. Sabra, M. Khousam, and S. Martel, "Use of 3D potential field and an enhanced breath-first search algorithms for path-planning of microdevices propelled in the cardiovascular system," in *27th IEEE EMBS Annual Int. Conf.*, Shangai, China, 2005, pp. 91 – 100.

[8] S. Tamaz, A. Chanu, J.-B. Mathieu, R. Gourdeau, and S. Martel, "Real-time mri-based control of a ferromagnetic core for endovascular navigation," *IEEE Trans. Bio-Med. Eng.*, vol. 55, no. 7, pp. 1854–1863, July 2008.

[9] T. Wortmann, C. Dahmen, and S. Fatikow, "Study of MRI susceptibility artifacts for nanomedical applications," *Journal of Nanotechnology in Engineering and Medicine*, vol. 1, no. 4, p. 041002, 2010.

[10] C. Kirbas and F. Quek, "A review of vessel extraction techniques and algorithms," *ACM Comput. Surv.*, vol. 36, no. 2, pp. 81–121, 2004.

[11] P. Reuzé, J. Coatrieux, L. Luo, and J. Dillenseger, "A 3D moment based approach for blood vessel detection and quantification in MRA," *Technology and Health Care*, vol. 1, pp. 181–188, 1993.

[12] J. Tokuda, G. S. Fischer, S. P. DiMaio, D. G. Gobbi, C. Csoma, P. W. Mewes, G. Fichtinger, C. M. Tempany, and N. Hata, "Integrated navigation and control software system for mri-guided robotic prostate interventions," *Computerized Medical Imaging and Graphics*, vol. 34, no. 1, pp. 3–8, 2010.

[13] T. Deschamps, "Curve and shape extraction with minimal path and level-sets techniques: Applications to 3d medical imaging," Ph.D. dissertation, University of Paris Dauphine, 2001.

[14] O. Wink, W. J. Niessen, and M. A. Viergever, "Minimum cost path determination using a simple heuristic function," *Int. Conf. on Pattern Recognition*, vol. 3, p. 7010, 2000.

[15] O. Wink, W. Niessen, B. Verdonck, and M. Viergever, "Vessel axis determination using wave front propagation analysis," *Medical Image Computing and Computer-Assisted Intervention*, vol. 2208, pp. 845–853, 2001, lecture Notes in Computer Science.

[16] L. Cohen and R. Kimmel, "Global minimum for active contour models: A minimal path approach," *Int. J. of Computer Vision*, vol. 24, no. 1, pp. 57–78, 1997.

[17] J. A. Sethian, *Level set methods and fast marching methods*. Cambridge University Press, 1999.

[18] L. Arcèse, M. Fruchard, and A. Ferreira, "Nonlinear modeling and robust controller-observer for a magnetic microrobot in a fluidic environment using MRI gradients," in *IEEE/RSJ Int. Conf. on Intel. Robots and Systems*, St. Louis, MO, USA, Oct. 2009, pp. 534–539.

[19] L. Arcese, A. Cherry, M. Fruchard, and A. Ferreira, "High gain observer for backstepping control of a mri-guided therapeutic microrobot in blood vessels," in *IEEE/RAS-EMBS Int. Conf. on Biomedical Robotics and Biomechatronics*, Tokyo, Japan, Sep. 2010, pp. 349 –354.

[20] L. Arcese, A. Cherry, M. Fruchard, and A. Ferreira, "Dynamic behavior investigation for trajectory control of a microrobot in blood vessels," in *IEEE/RSJ Int. Conf. on Intel. Robots and Systems*, Taipei, Taiwan, Oct. 2010, pp. 5774 –5779.

[21] S. Qin and T. Badgwell, "A survey of industrial model predictive control technology," *Control engineering practice*, vol. 11, no. 7, pp. 733–764, 2003.

[22] D. Clarke, C. Mohtadi, and P. Tuffs, "Generalized predictive control – Part I & II," *Automatica*, vol. 23, pp. 137–160, 1987.

[23] B. Kouvaritakis, J. Rossiter, and A. Chang, "Stable generalised predictive control: an algorithm with guaranteed stability," *IEE Proceedings Part D Control Theory and Applications*, vol. 139, no. 4, pp. 349–362, 1992.

[24] E. Camacho and C. Bordons, *Model predictive control*. Springer Verlag, 2004.

[25] A. Frangi, W. Niessen, K. Vincken, and M. Viergever, "Multiscale vessel enhancement filtering," *Lecture Notes in Computer Science*, pp. 130–137, 1998.

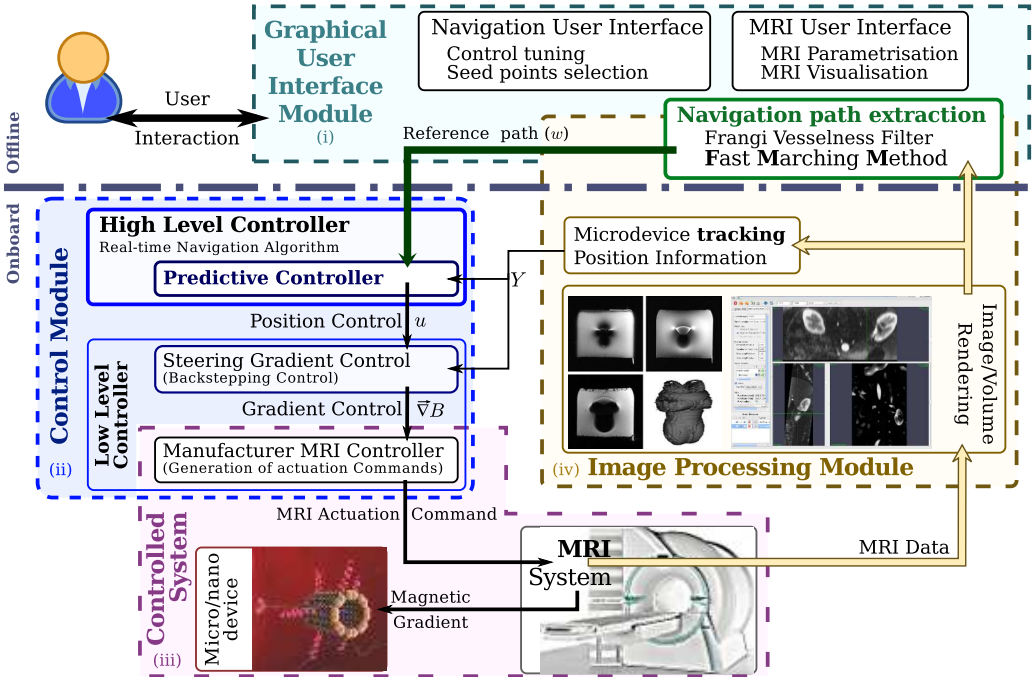

Figure 1: Overall system overview.

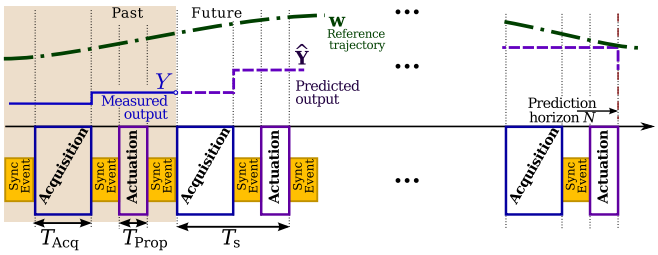

Figure 2: Timeline of acquisition and control prediction.

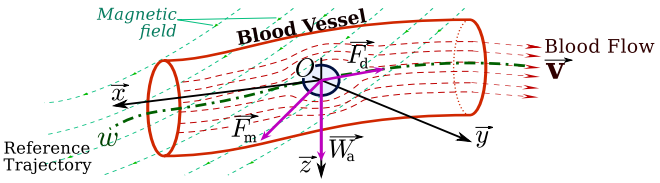

Figure 3: Forces applied on microrobot navigating in blood vessel.

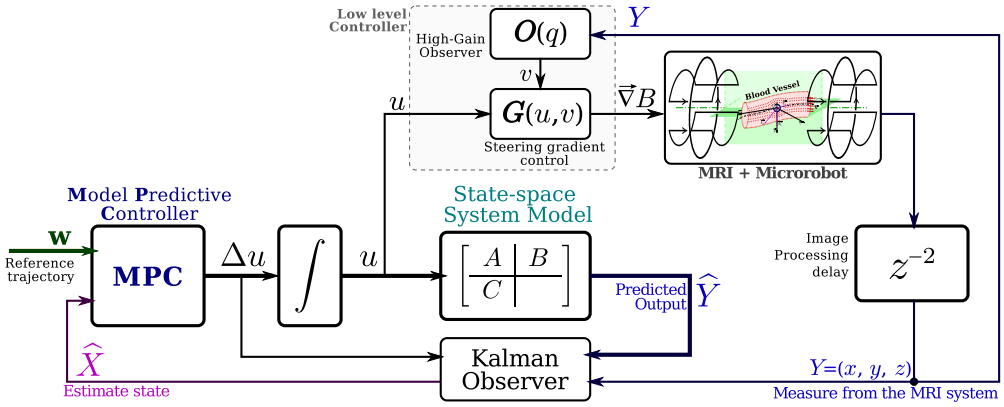

Figure 4: MRI-based Predictive Control strategy.

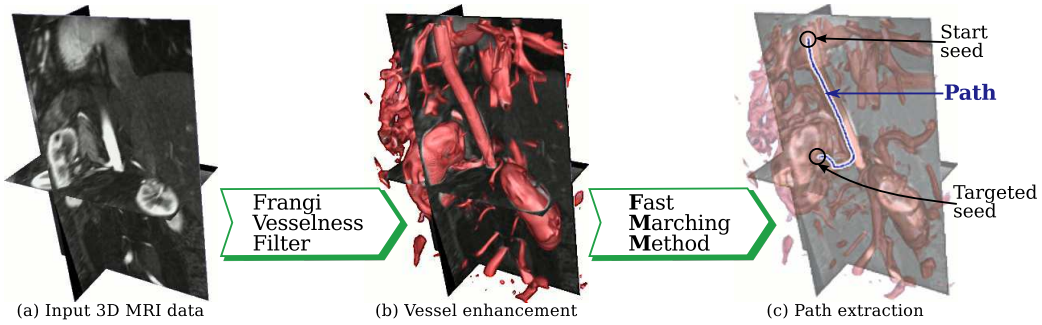

Figure 5: 3D Navigation path extraction processing: a) Original MRI data; b) Computed cost function using Frangi filter (here displayed in red volume); c) Extracted navigation path between the start and end seeds using FFM.

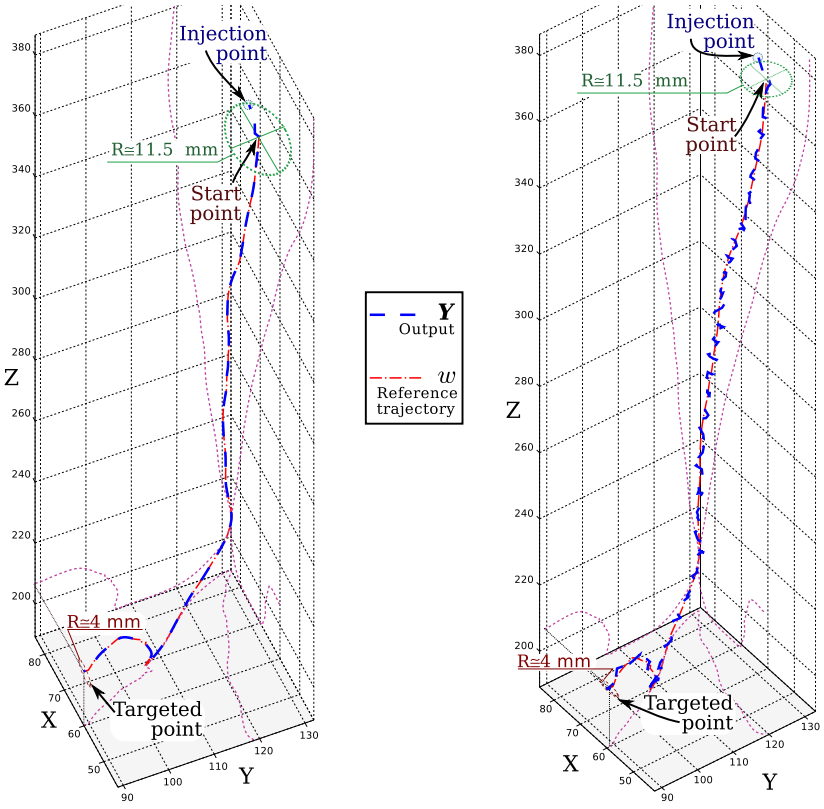

(a) 3D trajectories. (b) with a white noise.

Figure 6: 3D MRI-based microrobot endovascular navigation ($N = 5$, in mm).

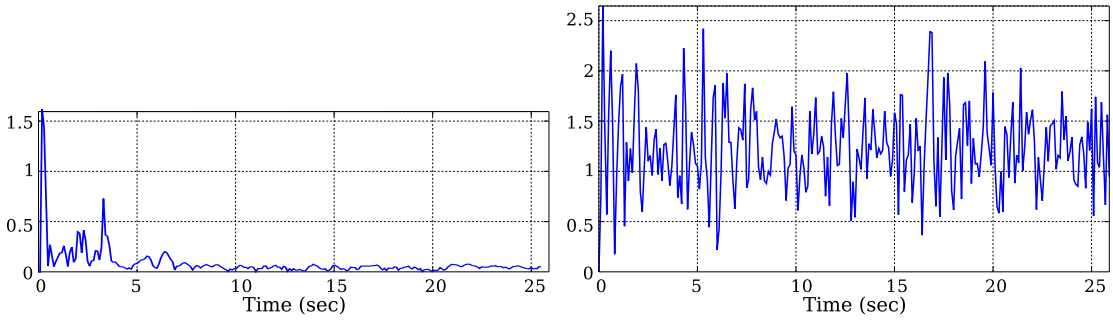

(a) Without noise (b) With white noise

Figure 7: 3D tracking error: $\|Y - w\|$ for $N = 5$.

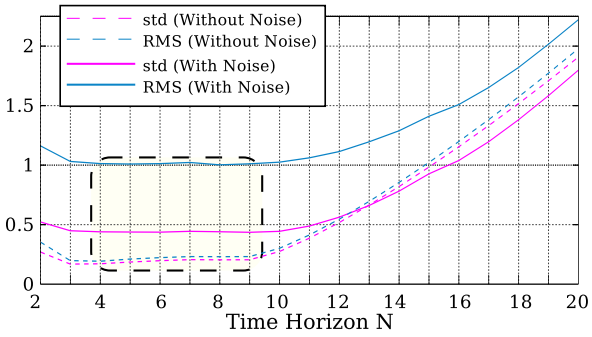

Figure 8: Tracking error statistics for different time horizons N.

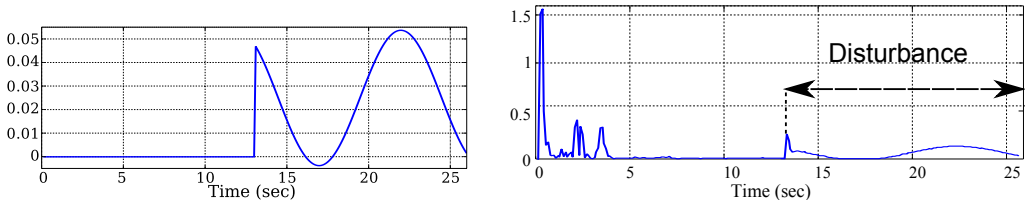

(a) Blood flow disturbance $\sigma_{\text{flow}}(t)$.

(b) Tracking error.

Figure 9: MRI-based navigation with blood flow disturbance.

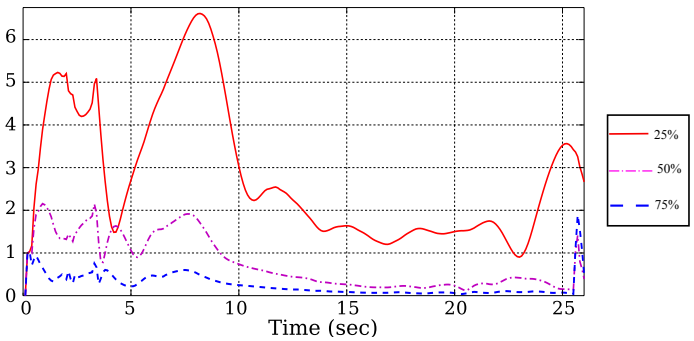

	25%	50%	75%
std	1.5871	0.6860	0.2563
RMS	3.2023	0.9697	0.3628

Figure 10: Tracking error with different values of duty cycle.

Appendix B

Simulation and planning of a magnetically actuated microrobot navigating in arteries (ACL6)

Simulation and Planning of a Magnetically Actuated Microrobot Navigating in Arteries

Karim Belharet, David Folio, Antoine Ferreira

Simulation and Planning of a Magnetically Actuated Microrobot Navigating in the Arteries

Karim Belharet, David Folio, *Member, IEEE,* and Antoine Ferreira, *Member, IEEE*

***Abstract*—This work presents a preoperative microrobotic surgical simulation and planning application. The main contribution is to support computer-aided minimally invasive surgery (MIS) procedure using untethered microrobots that have to navigate within the arterial networks. We first propose a fast interactive application (with endovascular tissues) able to simulate the blood flow and microrobot interaction. Secondly, we also propose a microrobotic surgical planning framework, based on the anisotropic Fast Marching Method (FMM), that provides a feasible pathway robust to biomedical navigation constraints. We demonstrate the framework performance in a case study of the treatment of peripheral arterial diseases (PAD).**

***Index Terms*—Microrobotics, minimally invasive surgery, blood flow simulation, anisotropic path planning.**

I. Introduction

PREOPERATIVE surgical simulation and planning is a critical stage in medical decision-making and in the design of novel microrobotic minimally invasive surgery (MIS) techniques [1,2]. Due to the lack of anatomic consistency, preoperative planning with virtual and physical models of the system could improve the chances of achieving predictable intraoperative results. To this aim, it is mandatory to cope with potential conflicts between the intervention purposes of the microrobotic surgical system and the biological laws governing the patient body. To improve microrobotic MIS procedure significant progress has been made in three dimensional (3D) imagers [3]; modeling software for anatomy and vascular networks representation [4]; and biomechanical modeling of interactions between tissues and MIS tools. These advances have been mainly developed for catheter or guidewire-based operations [5,6], or gastrointestinal endoscopic capsules [7,8]. In contrast, there has been fewer works in the area of untethered microrobots for cardiovascular interventions [1,9]. To date, even in the case of a successfully performed procedure, the choice of a microrobot's design (shape, size, materials, locomotion abilities…) plays a key role. Indeed, these factors affect the microrobot propulsion that depends mainly on the motile, fluidic and friction forces between the endovascular device and the vessel. Therefore, the development of training applications or interactive planning systems, where the robotician or physician is able to design different microrobots and then test their behaviors in a patient-specific context, will be very helpful. A few applications focusing on interventional MIS have been developed or commercialized [10,11] until now. These applications include interactive models of catheters [5], endoscopic capsules [7], but do not address the challenging topic of modeling untethered microrobots [12] and their complex interactions with the blood flow and vessels walls [1]. Most proposed solutions use finite element modeling (FEM)-based representations, or computational fluid dynamics (CFD) simulations. Such approaches are suitable when accurate modeling or simulation are a primary concern. However, they usually rely on commercial software (such as Fluents or Comsol), and the computation time (usually in hours) is incompatible with interactive simulation or clinical practice. Moreover, planning a reliable and feasible path against the blood flow and vessel networks constraints is an important issue to be addressed for innovative microrobot-aided MIS applications. For instance, S. Martel et al. propose to use potential fields and the breadth-first search algorithm to find a pre-planned path [13] which are then delimited by waypoints [9]. A first drawback in such discrete graph-search algorithms is that they suffer from metrication errors [14]. Moreover, it is difficult to cope explicitly with the anisotropy. Finally, most untethered microrobot propulsion schemes based on magnetic pulling have to face important constraints related to coils technology. The planned path has to reduce the maximum pulling gradients being applied to the coils, the operation time and to maintain the rising temperature of the coils within operating limits. It actually impacts different endovascular magnetic actuation systems based on Magnetic Resonance Navigation (MRN) [9], or Octomag system [15]. Thus, the planned pathway must satisfy these considerations to be reliable.

This work aims to propose a preoperative microrobotic surgical planning application with blood flow simulation that may use patient-specific data. In particular, the computer-aided optimization of the untethered microrobots for innovative MIS procedure is the main focus of our work. First, in Section II, after introducing the system model used by the microrobotic surgical simulation, we present the surgical planning framework. The proposed framework is based on the Fast Marching Method (FMM) [16]. In our previous work [17,18], the classical FMM with isotropic cost function has been proposed to extract the vessel centerline path. This first solution is suitable mainly to navigate far away from the vessel wall. However, as navigation in real vascular networks is directionally constrained by the biological environment, a new framework based on the *anisotropic* FMM [19] is proposed in this paper. Furthermore, the proposed method allows a multi-parameter optimization of the navigation path that takes into account: i) the technology of the magnetic system; ii) the microrobot design; and iii) the physiology of the patient. Finally, our approach ensures a smooth conveyance of the microrobot to destination robust to cardiovascular navigation

The authors are with Laboratoire PRISME, ENSI de Bourges, 88 boulevard Lahitolle, 18020 Bourges, France.
E-mail: firstname.name@ensi-bourges.fr

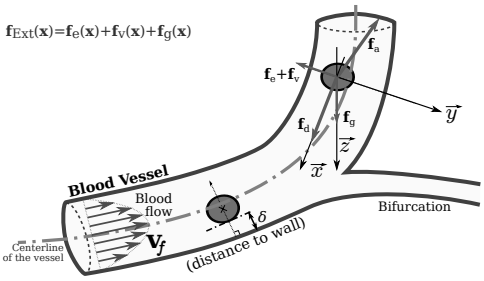

Fig. 1. Modeling scheme example in case of bead pulled microrobot.

constraints while minimizing the energy expenditure, to reduce the gradient pulling and system overheating. Specifically, we aim to get a *feasible path* by finding the min-energy pathway (which is not necessarily the shortest). Section III briefly describes our developed microrobotic surgical simulation and planning application, before illustrating its performance. As an illustration, we consider the treatment of peripheral arterial diseases (PAD), such as artery narrowing (stenosis). For instance, one possible surgical application is to target atherosclerotic plaques in stenosed arteries. One of the most common strategies is angioplasty, occasionally with stent implantation. Despite the high success rate, these solutions are not satisfactory, as vessel damage, infection and restenosis can appear at a later stage. Otherwise, a surgical microrobot for such vascular applications offers some novel solutions [1]. Specifically, microrobotic intervention based on chemical, mechanical or mechano-chemical could be achieved to treat vascular obstructions [2]. Finally, we discuss some open issues, evaluate the computational efficiency, and outline some future extends in Section IV. This study is concluded in Section V.

II. Methods

A. A modeling overview

Different types of devices could be used for MIS interventions from catheter and guidewires, to wireless microcapsules or microcarriers [1]. In this framework, any kind of untethered microdevice (termed as *microrobot* throughout the text) that has to perform endovascular navigation within blood flow is considered. More precisely, we consider any microsystem that could be modeled as:

$$m\dot{\mathbf{v}} = \mathbf{f}_{\mathrm{a}}(\mathbf{a}) + \mathbf{f}_{\mathrm{d}}(\mathbf{v}) + \mathbf{f}_{\mathrm{Ext}}(\mathbf{x}) \tag{1}$$

where $\mathbf{v}$ is the velocity of the device; m its mass; $\mathbf{f}_{\mathrm{a}}(\mathbf{a})$ is the *controlled* force, that is related to the control action $\mathbf{a} \in \mathcal{A}$, with $\mathcal{A}$ the *admissible controls* set; $\mathbf{f}_{\mathrm{d}}(\mathbf{v})$ denotes the fluid flow hydrodynamic drag force; and $\mathbf{f}_{\mathrm{Ext}}(\mathbf{x})$ are all other external forces, as depicted Fig. 1. Different external forces could be added to the model (1), such as the weight ($\mathbf{f}_g$), electrostatic ($\mathbf{f}_{\mathrm{e}}$), van der Waals ($\mathbf{f}_{\mathrm{v}}$), contact or steric forces. The interested reader may refer to [20] for detailed formulation of microforces. Fig.2 illustrates the evolution of these microforces with varying microrobot radius r and wrt. its distance to vessel wall δ. In particular, Fig. 2(f) shows that close to the centerline of the vessel ($\delta = R$) the electrostatic

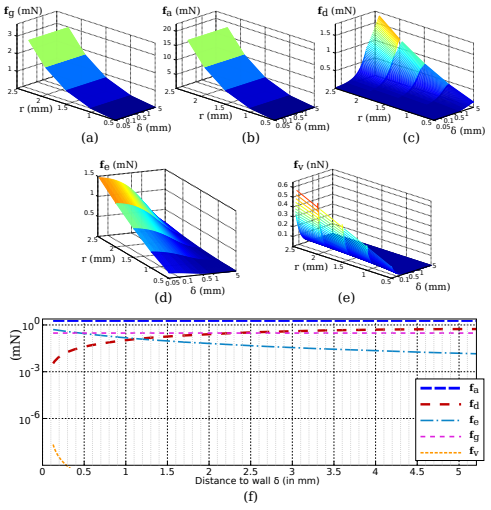

Fig. 2. Microforces evolution: (a) apparent weight $\mathbf{f}_g$ (b) magnetic force $\mathbf{f}_{\mathrm{a}}$ (with $\nabla B = 200\,\mathrm{mT/m}$), (c) drag force $\mathbf{f}_{\mathrm{d}}$ (with $\|\overline{\mathbf{v}}_{\mathrm{f}}\| = 400\,\mathrm{mm/s}$), (d) electrostatic force $\mathbf{f}_{\mathrm{e}}$, (e) van der Waals force $\mathbf{f}_{\mathrm{v}}$, as function of the distance to the vessel wall δ in artery ($R = 5\,\mathrm{mm}$) and wrt. the microrobot radius r. (f) Microforces acting on a microrobot with $r = 1\,\mathrm{mm}$ wrt. the distance to the vessel wall δ in artery ($R = 5\,\mathrm{mm}$).

and the van der Waals microforces are negligible compared to the other relevant forces. In addition, if the microrobot is never in contact with the vessel wall, the contact force could be omitted. Finally, most of the time because of the size of the microsphere, the effect of Brownian motion is also neglected.

B. Navigation Planning in Flow

1) Minimal Path Planning: Classically, a navigation pathway could be defined as a curve $\mathcal{P}$ linking a starting point $\mathbf{x}_0$ to any point $\mathbf{x}$. In the general case, a curve is a *minimal path*, also called a *geodesic*, wrt. the metric ϖ, if it globally minimizes the energy functional:

$$\mathcal{E}_{\varpi}(\mathcal{P}) = \int_{\mathcal{P}} \varpi(\mathcal{P}(l), \dot{\mathcal{P}}(l))dl, \tag{2}$$

with l the arclength parameter. The solution to the minimum path finding problem (2) could be obtained through the computation of the distance map $\mathcal{U} : \mathcal{C} \mapsto \mathbb{R}^+$, defined as: $\mathcal{U}(\mathbf{x}) = \min_{\mathcal{P}} \mathcal{E}(\mathcal{P})$, for any $\mathcal{P}$ linking $\mathbf{x}$ to $\mathbf{x}_0$ in the domain $\mathcal{C} \subset \mathbb{R}^d$ (with $d = 2, 3, 4\ldots$). In this context, Sethian [16] has proposed the Fast Marching Method (FMM). Indeed, the FMM converges to a smooth solution in the **continuous domain** even when it is implemented on a sampled environment, contrary to discrete graph-search algorithms. Especially, in the isotropic case, the FMM satisfies the Eikonal equation:

$$\begin{cases} \|\nabla \mathcal{U}(\mathbf{x})\| &= w(\mathbf{x}), \qquad \forall \mathbf{x} \in \mathcal{C} \\ \mathcal{U}(\mathbf{x}_0) &= 0 \end{cases} \tag{3}$$

where the isotropic cost function $w : \mathbf{x} \in \mathcal{C} \mapsto w(\mathbf{x}) \in \mathbb{R}^+$ is the metric. As the map $\mathcal{U}$ has a single local minimum, the geodesic can be retrieved with a simple gradient descent on $\mathcal{U}$ from a targeted seed $\mathbf{x}_{\mathrm{g}}$ to $\mathbf{x}_0$. The FMM provides a continuous solution to the minimum path problem by employing upwind differences and a causality condition [16]. The key issue of

the FMM is then to get an appropriate metric $w(\mathbf{x})$ which drives the front expansion efficiently to find a geodesic $\mathcal{P}$. In previous works [17,18], we have proposed to design such a metric on spatial consideration:

$$w : \mathbf{x} \in \mathcal{C} \mapsto \texttt{Vesselness}(\mathbf{x}) \in \mathbb{R}^+ \tag{4}$$

where $\texttt{Vesselness}(\mathbf{x})$ is a vesselness enhancement function. A typical $\texttt{Vesselness}(\mathbf{x})$ function could be designed using a multi-scale analysis of the Hessian matrix, as proposed by Frangi [21] or Sato [22]. This approach then allows to find the vessel centerline geodesic $\mathcal{P}_c$, as the considered vesselness filter gives their maximal response in the vessel center. We have applied this procedure to different sets of data, in 2D [17] as well as in 3D [18].

As mentioned previously the contact, electrostatic and van der Waals microforces are negligible when the microrobot navigates close to the centerline $\mathcal{P}_c$ (cf. Fig. 2). $\mathcal{P}_c$ is then the best solution to navigate far away from the vessels wall. However, navigation in real vascular networks is constrained by the biological environment, and can strongly modify the system behavior, leading to incompleteness in real intra-operative applications.

2) Anisotropic Path Planning: Navigating in blood flow implies some directional constraints. When the path finding problem has some preferred directions of travel it becomes *anisotropic*, i.e. the solutions depend on the configuration and directional constraints. In [19], the authors noticed that the FMM could be applied to isotropic or anisotropic problems, and they provided a numerical scheme to solve static Hamilton-Jacobi equations of the form:

$$\begin{cases} \|\nabla \mathcal{U}(\mathbf{x})\| &= \varpi(\mathbf{x}, \frac{\nabla \mathcal{U}(\mathbf{x})}{\|\nabla \mathcal{U}(\mathbf{x})\|}), \quad \forall \mathbf{x} \in \mathcal{C} \\ \mathcal{U}(\mathbf{x}_0) &= 0 \end{cases} \tag{5}$$

where the anisotropy expansion is the result of the dependence of ϖ on $\nabla \mathcal{U}(\mathbf{x})$. Nevertheless, the computational complexity of the FMM in the anisotropic case is growing significantly with the amount of anisotropy. The literature provides different variants of the FMM to deal with anisotropy, such as using a recursive approach [23], or iterative schemes [24]. Furthermore, in [14] anisotropic cost functions have been also proposed. The proposed basic idea is to take advantage of the original FMM efficiency, and to model the anisotropy thanks to a vector $\mathbf{f}$ of a field of force $\mathcal{F}$, leading to the following anisotropic metric:

$$\varpi : (\mathbf{x}, \mathbf{f}) \in \mathcal{C} \times \mathcal{F} \mapsto \varpi(\mathbf{x}, \mathbf{f}) \in \mathbb{R}^+ \tag{6}$$

Such an anisotropic cost function leads to anisotropic front-propagation, and gives better geodesic than isotropic FMM. To embed the directional constraints $\mathbf{f}$ within such an anisotropic FMM different specific cost functions have been proposed mainly for autonomous underwater vehicles (AUVs) [14,25]. The drag and flow forces have a significant effect on the motion of the AUV, which is a common problem with our microrobot planning problem. However, the proposed solution mainly deals with either the *min*-distance or the *min*-time path finding problem, and not minimizing directly neither the dynamics nor the motion applied to the system. Moreover, most existing approaches classically simplify the problem by assuming constant vehicle speed, or only spatially varying flow fields without time variation. Such limitations can generate physically unfeasible paths. Especially, in the presence of strong flows, incompleteness or incorrectness issues are reported [25].

3) Minimum-feasible-energy Planning: Most microrobot propulsion schemes usually require a limitation of the power consumption, and have a maximum available power. Moreover, considering only either the *min*-time or *min*-distance problem usually leads to compute high motion forces, that is reach the goal as fast as possible. But in our context, high motion implies high drag forces, and then high motion force $\mathbf{f}_\text{a}$ (limited by the maximum available magnetic forces) to be able to reach the targeted area. To minimize the energy expenditure, a basic idea is to use a classical power functional expression, that is:

$$p(\mathbf{x}, \mathbf{a}) = \langle \mathbf{f}(\mathbf{x}, \mathbf{a}) \cdot \mathbf{v}(\mathbf{x}) \rangle \tag{7}$$

where $\langle \cdot \rangle$ is the inner product of $\mathbb{R}^d$; $\mathbf{v}$ is a velocity; and $\mathbf{f}(\mathbf{x}, \mathbf{a})$ is the applied resultant force that embeds the controlled action $\mathbf{a} \in \mathcal{A}$. Using the optimal control approach, we propose the following anisotropic cost function:

$$\varpi(\mathbf{x}, \mathbf{f}) = \max_{\mathbf{a} \in \mathcal{A}} \langle \mathbf{f}(\mathbf{x}, \mathbf{a}) \cdot \mathbf{v}(\mathbf{x}) \rangle \tag{8}$$

This anisotropic cost formulation, as in [14,25], naturally incites the device to move in the direction of the force $\mathbf{f}$. Especially, $\varpi(\mathbf{x}, \mathbf{f})$ will imply that the FMM propagation (5) follows the force field constraints, that is $\frac{\nabla \mathcal{U}(\mathbf{x})}{\|\nabla \mathcal{U}(\mathbf{x})\|} \propto \mathbf{f}$. Finally, this new anisotropic formulation (8) using optimal control aspects embeds the system motion wrt. a finite defined admissible control set $\mathcal{A}$. This ensures that the given geodesic $\mathcal{P}$ is *really feasible* by the system and minimizes energy expenditure. Indeed, the metric $\varpi(\mathbf{x}, \mathbf{f})$ allows to consider both the biological constraints and the microrobot capabilities.

III. Results

A. Simulation and Planning Tool

The proposed framework has been integrated in a dedicated interactive microrobot surgical simulation and planning application. This application, depicted on Fig. 3, is based on the Visualization Toolkit (VTK) [26], the Insight Segmentation and Registration Toolkit (ITK) [27], and the Qt Toolkit [28]. Through the user interface (Fig. 3(b)), the surgeon realizes the following operating mode iteratively:

a) *Specifications:* The surgeon provides different parameters in the software (in the left panel on Fig. 3(b)) related to: i) the physiology of the patient (blood flow and viscosity, vessel's size and topology); ii) the technology of the magnetic system (coil's slew rate, maximum magnetic gradients, power limitations); and iii) the microrobot design (size, density, magnetic saturation).

b) *Simulations:* The surgeon initiates the simulation and planning process wrt. the specification constraints.

c) *Data analysis:* The surgeon analyses the power functional mapping and force field wrt. microrobot specifications.

This iterative process is conducted until the preoperative planning of plaque removal specifications are satisfied. We

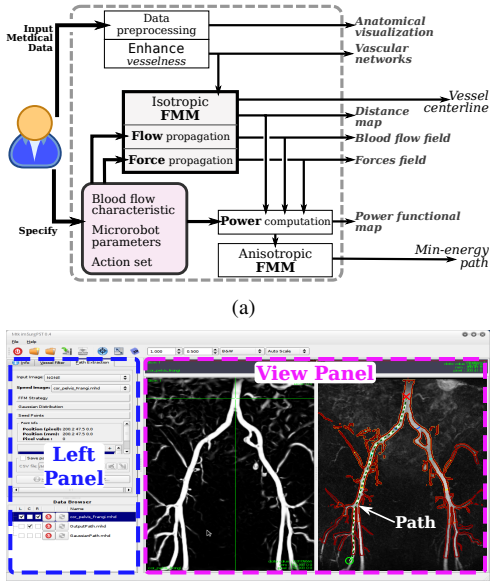

Fig. 3. Preoperative microrobot surgical simulation and planning application: (a) application workflow; (b) vessel centerline extraction example.

focus in the sequel on the main contributions of this paper that is the simulation and reliable vascular navigation planning.

B. Case study: peripheral arterial diseases

To assess the overall framework, we have performed a series of tests for both the microrobot within blood vessel model simulation and preoperative microrobotic MIS planning. We illustrate the proposed application for the treatment of peripheral arterial diseases (PAD). One possible application is to locate atherosclerotic plaque in stenosed arteries. In particular, stenosis implies an abnormal narrowing of the vessel which causes a decrease in blood flow. Different plaque removal tasks have already been realized by magnetically actuated microrobots navigating in occluded blood vessels [2]. In [29], shear-targeting of a thrombolytic drug in a mouse arterial thrombosis model using a microcarrier has been successfully tested. In [30], the rotation of the magnetic microrobot is at the origin of a drilling action through an occlusion in a vessel. In the following, we propose a preoperative planning of a magnetic microrobot navigating within the vasculature to the stenosed artery for plaque removal. We will consider here as case study the real Magnetic Resonance Angiogram (MRA) clinical dataset depicted on Fig. 4. As the proposed framework works in $\mathcal{C} \subset \mathbb{R}^d$ (with $d = 2, 3\ldots$), for the sake of clarity of the representation, we will only show here a Maximum Intensity Projection (MIP) image of the MRA. Here, the patient has a single level disease represented by an isolated stenosis in the iliac artery. As it is still a challenging issue to identify automatically the patient pathology and its location, the PAD is manually defined by the user.

C. Simulation Results

As previously mentioned, the simulation is based on a physics-based model (presented in details in [20]). When

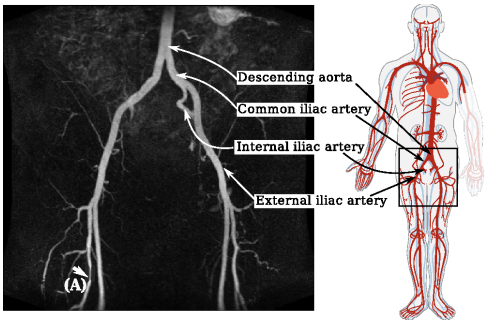

Fig. 4. Real MIP image from MRA (resolution of $N = 384 \times 384$ nodes) obtained in a patient with an isolated stenosis in the iliac artery (the white (A)-arrow), used to illustrate microrobotic MIS treatment simulation and planning.

interactive simulation is required (for training, intervention planning, etc.), a trade-off between computation time and accuracy has to be found. In our application, computational efficiency is more important than small-scale details, as we aim to increase the users interaction capabilities, whereas precision could be achieved using FEM or CFD simulation. To speed-up either the blood flow velocity or the force fields simulation computation, the basic FMM is extended to be able to compute these vector fields during the front propagation (see Fig. 3(a)). Indeed, using $\texttt{Vesselness}(\mathbf{x})$ isotropic cost function, the FMM front will extend only within the vascular structure. This allows to take advantage of the FMM efficiency, without using the whole dataset grids, and significantly reduce the overall computational time.

The blood flow velocity field simulation of the considered case study is illustrated on Fig.5. The interactive simulation tool takes into account that blood flow velocity intensity $\overline{\mathbf{v}}_\mathrm{f}$ on the vessel centerline decreases wrt. vessels radii, that is from about $\|\overline{\mathbf{v}}_\mathrm{f}^\mathrm{ad}\| \approx 400$ mm/s in descending aorta with a radius $R \approx 6.5$ mm, to $\|\overline{\mathbf{v}}_\mathrm{f}^\mathrm{ei}\| \approx 250$ mm/s in external iliac artery with a radius $R \approx 3.5$ mm. As one can see, the blood flow velocity field is modified in the considered stenosis case (narrowed vessel on Fig.5). The corresponding force field that will act on a neodymium microrobot with a radius $r = 500\ \mu$m is shown on Fig.6. In this simulation, only the weight $\mathbf{f}_g$ (in the $\overrightarrow{g}$-axis direction), drag $\mathbf{f}_\mathrm{d}$ and electrostatic $\mathbf{f}_\mathrm{e}$ forces are calculated. Let us notice that any force that can have an analytical expression and can be embedded in (1) can easily be added to the application. Finally, the realized interactive simulation application is also able to deal with periodic time-varying pulsatile blood flows, as presented on Fig. 7. The user defines the periodic pulsatile blood flow parameters [20], a number of time-steps, and can then browse the time-frame of either the blood flow velocity or the applied force field. Fig. 7(a) illustrates a typical periodic time-varying pulsatile blood flow that takes place in the descending aorta, and the row 7(b) describes the corresponding velocity field. Fig. 7(c) and 7(d) show the resulting force fields applied on the microrobot for two case studies, a microrobot of radius of $r = 250\,\mu$m and $r = 1.5$ mm, respectively. This demonstrates that when the microrobot's radius r or weight $\mathbf{f}_g$ increases, the resultant force becomes more important.

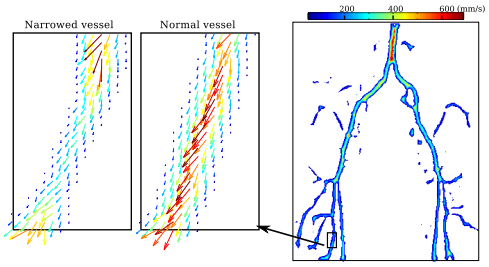

Fig. 5. Simulation results of the blood flow velocity field computation.

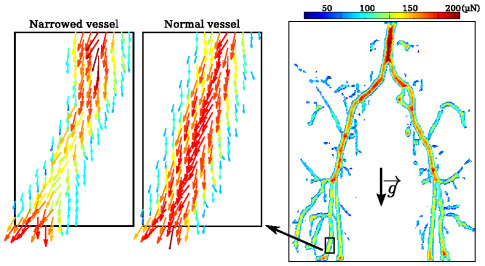

Fig. 6. Simulation results of the force field: $\mathbf{f} = \mathbf{f}_{\mathrm{d}}(\mathbf{v}) + \mathbf{f}_{\mathrm{e}}(\mathbf{x}) + \mathbf{f}_g$, applied on a microrobot of $r = 500$ μm radius.

D. Microrobotic surgical planning demonstration

Once the microrobot is specified (size, materials, etc.), the system's planning step only requires as user's input the starting $\mathbf{x}_0$ and ending points $\mathbf{x}_{\mathrm{g}}$. Next, to deal with the anisotropy of the media, the blood flow and force fields simulation results are used to compute the power functional map (7). The key issue is then to generate the controlled force field $\mathbf{f}_{\mathrm{a}}(\mathbf{a}), \forall \mathbf{a} \in \mathcal{A}$. First, the action magnitude has to be defined wrt. available actuation command. The action magnitude is usually the controlled magnetic gradient ($\mathbf{a} = \nabla B$), which implies the following magnetic force on a spherical device:

$$\mathbf{f}_{\mathrm{a}}(\nabla B) = D\tau_m \frac{4}{3}\pi r^3 \left(\mathbf{M}.\nabla\right)\nabla B, \tag{9}$$

where r is the microsphere radius; $\tau_m \in [0;1]$ is the volume ratio of the magnetic material; $\mathbf{M}$ its magnetization; and $D \in [0;1]$ is the duty-cycle, i.e., the ratio between the duration of the applied magnetic gradient for propulsion to the total period T.

The magnetic gradient used to propel a magnetic microrobot is assumed to be generated from various medical magnetic steering systems: ElectroMagnetic based Actuation (EMA) systems such as the Magnetic Catheter Steering System (a larger version of the Octomag system [15]) or the one developed in [30]; and Magnetic Resonance Navigation (MRN). The EMA systems are capable of generating maximum magnetic gradient fields up to $\mathbf{a}_{\max} = 350$ mT/m in closed-loop navigation control. In this case, the duty cycle is considered equal to $D = 1$ since the imaging modality is provided by either optical microscopy or X-ray imaging. These systems are more suitable for the navigation of millimeter-sized hard magnetic microrobots. The MRN system is based on clinical MRI systems, without any hardware upgrades. Such magnetic systems are usually limited to maximum values to $\mathbf{a}_{\max} = 80$ mT/m in closed-loop navigation control. Generally, the duty cycle is $D < 1$, since MR-imaging sequences and MR-tracking are provided by the same scanner to gather feedback positional information during MRN [9]. The MRN approach is more suitable for micrometer-sized soft magnetic microrobots. However, it should be noticed that experimental results have shown that therapeutic particles (known as TMMC), 50-60 μm diameter were navigated in arteries (rabbit models) and that MRN was done with gradient coils (capable of 450 mT/m with inner diameter suitable for limbs or head interventions) installed in the tunnel of clinical MRI scanners [31].

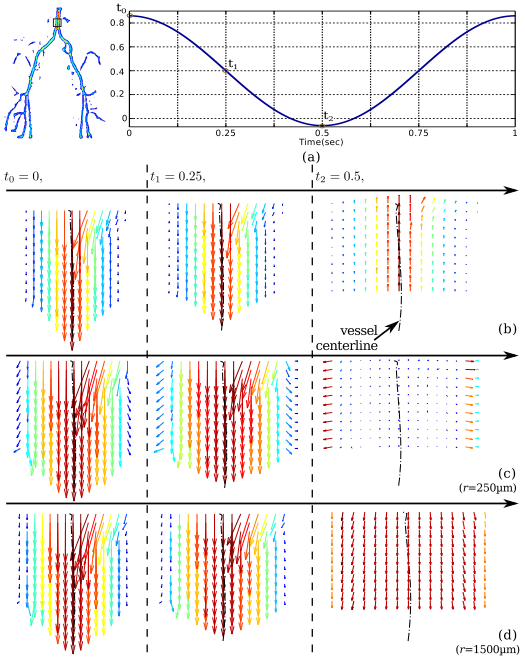

Fig. 7. Pulsatile blood flow simulation: (a) the periodic time-varying velocity in the descending aorta; (b) zoomed view of the blood flow velocity field; (c-d) zoomed view of the force field $\mathbf{f} = \mathbf{f}_{\mathrm{d}} + \mathbf{f}_{\mathrm{e}} + \mathbf{f}_g$ acting on a microrobot of: (c) $r = 250\,\mu$m, and (d) $r = 1500\,\mu$m for different time instants.

Our proposed FMM strategy can be adapted to each specific case by taking into account the duty-cycle D, the slew rate of the magnetic coils, and the maximum temperature coils. Secondly, the action direction should be defined. To this aim, we used some a priori knowledge about the goal direction, defined between $\mathbf{x}_0$ and $\mathbf{x}_{\mathrm{g}}$, provided by the isotropic FMM using $\mathtt{Vesselness}(\mathbf{x})$ cost function (see Fig. 3(a)). Indeed, this FMM step provides the distance map $\mathcal{U}_c$ between $\mathbf{x}_0$ and $\mathbf{x}_{\mathrm{g}}$ (or reciprocally), and then the goal direction field $\nabla\mathcal{U}_c(\mathbf{x})$. This helps to define the appropriate *guidance field* $G(\mathbf{x}) \propto \nabla\mathcal{U}_c(\mathbf{x})$. Some variations could be added on the goal direction field to enlarge the guidance field set. The admissible control set $\mathcal{A}$ can then be defined as:

$$\mathcal{A} = \{\mathbf{A} \times \mathbf{G}\}, \tag{10}$$

where $\mathbf{A} \subset]0; \mathbf{a}_{\max}]$ is a finite set of action magnitudes, and $\mathbf{G} = \{G(\mathbf{x}) \sim [0; \frac{\pi}{2}]\}$ is the guidance field set. Let us recall that $\mathcal{A}$ could be filtered to consider some technological constraints (such as the duty-cycle, or the magnetic slew rate).

This planning framework has been validated on the case study dataset considering different microrobot sizes navigating within arteries. First, Fig. 8 demonstrates the influence of the

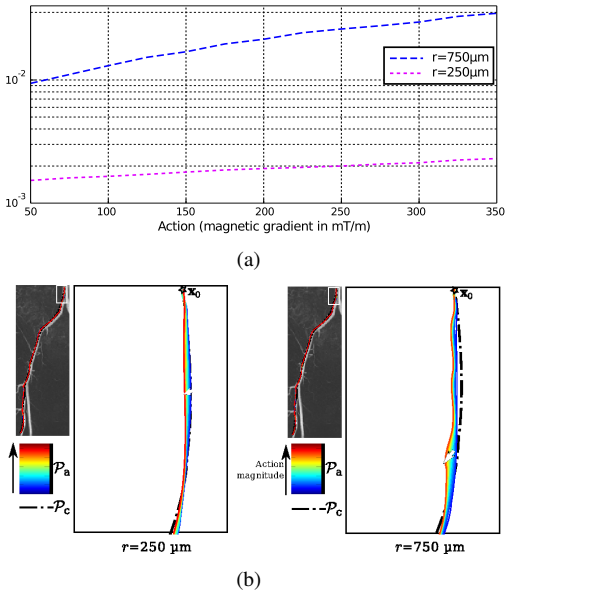

Fig. 8. Planning results on varying control action influence for a neodymium microrobot of size 250 μm and 750 μm: (a) the energy functional $\mathcal{E}_{\varpi}(\mathcal{P})$ wrt. the action magnitude (i.e. the magnetic gradient) and (b) zoomed view of the corresponding geodesics: $\mathcal{P}_c$ the vessel centerline and $\mathcal{P}_a$ the min-energy path for the varying action magnitude.

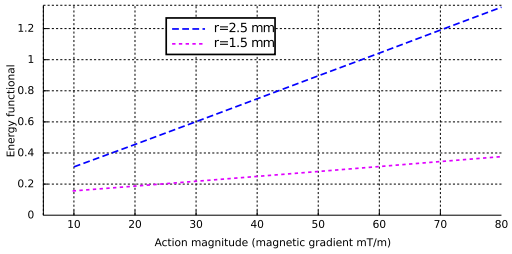

Fig. 9. Planning results on varying control action influence for a neodymium microrobot of size 1.5 mm and 2.5 mm in clinical MRI context.

motion force magnitude on finding the minimum-feasible-energy path. We noticed that as the motion force magnitude increased, the required energy $\mathcal{E}_{\varpi}(\mathcal{P})$ increased exponentially. This is significant for important microrobot size ($r = 750$ μm on Fig. 8(a)). Indeed, Fig. 8(b) shows that with much power the microrobot is more able to leave the vessel's centerline $\mathcal{P}_c$ (provided by the isotropic FMM) to reach the goal faster. If limited magnetic gradient magnitudes are available to propel the microrobot, such as in clinical MRI, Fig. 9 shows that increasing its size should overcome the power limitation. Therefore, the proposed *min*-energy path planning has been evaluated for various microrobot sizes and for EMA and MRN systems, as reported on Fig. 10. We can notice that for a microrobot radius bigger than 1.5 mm the curve length increases slightly, and starts to decrease significantly below 1 mm (cf. Fig. 10(a)). Furthermore, Fig. 10(b) depicts that the energy functional decreases significantly with the microrobot radius. In fact, the action force $\mathbf{f}_{\mathrm{a}}(\mathbf{a})$ decreases following a cubic power (L^3), minimizing the power budget. Therefore, it is more difficult for neodymium microrobots with a size below 750 μm to overcome the blood flow constraints that take place in the artery. Finally, as an illustration of the blood flow

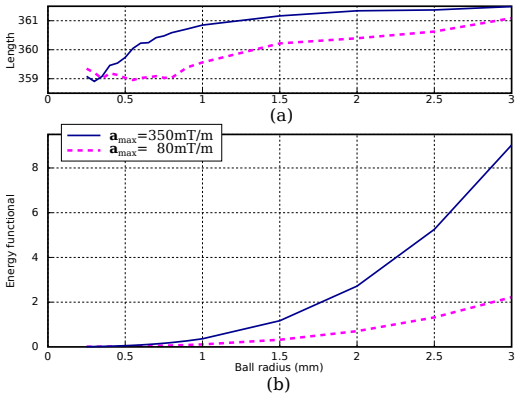

Fig. 10. Planning results with varying microrobot radii, for an EMA system ($\mathbf{a}_{\max} = 350\,\mathrm{mT/m}$) and a MRN ($\mathbf{a}_{\max} = 80\,\mathrm{mT/m}$): (a) the geodesic curvature length (in mm); and (b) the energy functional.

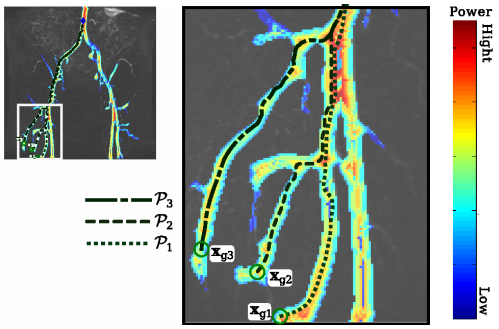

Fig. 11. Planning results using the proposed anisotropic cost function for a neodymium microrobot with $r = 1.5$ mm: three targeted point are specified ($\mathbf{x}_{\mathrm{g}1}$, $\mathbf{x}_{\mathrm{g}2}$ and $\mathbf{x}_{\mathrm{g}3}$). The colored map depicted the power functional level.

TABLE I
PLANNING RESULTS OF MINIMUM-FEASIBLE-PATH FOR THREE TARGETED POINT ($\mathbf{x}_{\mathrm{g}1}$, $\mathbf{x}_{\mathrm{g}2}$ AND $\mathbf{x}_{\mathrm{g}3}$) DEPICTED ON FIG.11

Geodesic #	Length (mm)	Energy $\mathcal{E}_{\varpi}(\mathcal{P})$
$\mathcal{P}_1$	360.086	0.6765
$\mathcal{P}_2$	**359.612**	0.5118
$\mathcal{P}_3$	361.735	**0.4879**

influence, Fig. 11 shows the planning results of our minimum-feasible-path finder for three targeted points ($\mathbf{x}_{\mathrm{g}1}$, $\mathbf{x}_{\mathrm{g}2}$ and $\mathbf{x}_{\mathrm{g}3}$), and Table I lists the curve lengths of their geodesic ($\mathcal{P}_1$, $\mathcal{P}_2$ and $\mathcal{P}_3$) and the energy functional $\mathcal{E}_{\varpi}(\mathcal{P})$. The *min*-energy geodesic is curve $\mathcal{P}_3$, while the shortest length is $\mathcal{P}_2$. This means that although $\mathcal{P}_3$ is longer than $\mathcal{P}_2$, $\mathcal{P}_3$ consumes less energy.

IV. DISCUSSION

The most computationally intensive part of the microrobotic surgical application is the vesselness filter (that provides $\texttt{Vesselness}(\mathbf{x})$ cost function) based on a multiscale analysis of the Hessian matrix [21]. This multiscale interpretation of eigenvalues of the Hessian matrix could be improved thanks to parallelization through GPU implementation. Furthermore, as mentioned, instead of using the overall dataset grid (in the case study $N = 147\,456$), the vector fields simulations are performed on only 18 941 nodes corresponding to the vasculature. Thus, on an Intel Core2 3Ghz processor, one simulation time

takes less than 150 ms. For the periodic pulsatile blood flow, this allows to compute one cardiac cycle with 50 time-steps in less than 8 s. Therefore, the combination of the microrobot and the caradiovascular model together with the FMM may become accurate enough to support interactive microrobotic surgical planning applications. Finally, in the planning step, the main computational aspect remains on action set $\mathcal{A}$ generation. This set $\mathcal{A}$ is related to the dimension of the action magnitude set $\mathbf{A}$ and guidance field set $\mathbf{G}$, specified by the users. For the case study with $\dim \mathcal{A} = \{10 \times 10\}$, the overall planning procedure needs a calculation time of about 36 s. This computational efficiency ensures a high level of interactivity for preoperative simulation, planning and navigation.

In the simulation process we have chosen to focus on computational efficiency, rather than on accurate blood flow simulations. Nonetheless, the vasculature and blood flow modeling are still strongly investigated by the communities, and remain an open issue. In future extends, we will use some analytical modeling of vessel bifurcation as in [20], to improve the blood flow simulation accuracy. Although the visualization of vector fields is still a challenging issue (especially in 3D), more intuitive flow rendering (such as streamline, streamribbon, etc.) could also be helpful for the microrobotic surgery applications.

V. Conclusion

In this study, a microrobotic surgical simulation and planning has been presented for the treatment of peripheral arterial diseases. However, the proposed framework could also be applied to other regions of the body, different therapy and various MIS microrobots. Especially, the results shows that interactive applications can be helpful to design the suitable microrobot design (e.g. shape, size, materials, etc.) wrt. anatomic consistency to improve microrobotic surgical applications. Hence, preoperative surgical planning with blood flow simulation provides useful information for understanding cardiovascular pathologies, predicting their onset and choosing an optimal therapy strategy for innovative microrobotic MIS procedure.

Acknowledgment

The PhD student K. Belharet is supported by the Nano-IRM project, founded by Region Centre and City of Bourges.

References

[1] B. J. Nelson, I. K. Kaliakatsos, and J. J. Abbott, "Microrobots for minimally invasive medicine," *Annual Review of Bio.med. Eng.*, vol. 12, no. 1, pp. 55–85, 2010.

[2] P. Miloro, E. Sinibaldi, A. Menciassi, and P. Dario, "Removing vascular obstructions: a challenge, yet an opportunity for interventional microdevices," *Bio.med. Microdevices*, vol. 14, pp. 511–532, 2012.

[3] R. M. Satava, "Virtual reality, telesurgery, and the new world order of medicine," *Computer Aided Surgery*, vol. 1, no. 1, pp. 12–16, 1995.

[4] K. Sun, Z. Chen, and S. Jiang, "Local morphology fitting active contour for automatic vascular segmentation," *IEEE Trans. Biomed. Eng.*, vol. 59, no. 2, pp. 464–473, Feb. 2012.

[5] Y. Ganji and F. Janabi-Sharifi, "Catheter kinematics for intracardiac navigation," *IEEE Trans. Biomed. Eng.*, vol. 56, no. 3, pp. 621–632, Mar. 2009.

[6] W. Tang, T. R. Wan, D. A. Gould, T. How, and N. W. John, "A stable and real-time nonlinear elastic approach to simulating guide-wire and catheter insertions based on cosserat rod," *IEEE Trans. Biomed. Eng.*, vol. PP, no. 99, p. 1, 2012.

[7] F. Carpi, N. Kastelein, M. Talcott, and C. Pappone, "Magnetically controllable gastrointestinal steering of video capsules," *IEEE Trans. Biomed. Eng.*, vol. 58, no. 2, pp. 231–234, Feb. 2011.

[8] G. Ciuti, M. Salerno, G. Lucarini, P. Valdastri, A. Arezzo, A. Menciassi, M. Morino, and P. Dario, "A comparative evaluation of control interfaces for a robotic-aided endoscopic capsule platform," *IEEE Trans. Robot.*, vol. 28, no. 2, pp. 534–538, Apr. 2012.

[9] S. Tamaz, A. Chanu, J.-B. Mathieu, R. Gourdeau, and S. Martel, "Real-time MRI-based control of a ferromagnetic core for endovascular navigation," *IEEE Trans. Biomed. Eng.*, vol. 55, no. 7, pp. 1854–1863, Jul. 2008.

[10] (2012) Stereotaxis Inc. [Online]. Available: http://www.stereotaxis.com

[11] (2012) Sensei(r) x robotic catheter system. Hansen Medical. [Online]. Available: http://www.hansenmedical.com

[12] C. Pawashe, S. Floyd, and M. Sitti, "Modeling and experimental characterization of an untethered magnetic micro-robot," *The Int. J. of Robot. Research*, vol. 28, no. 8, pp. 1077–1094, 2009.

[13] W. Sabra, M. Khouzam, and S. Martel, "Use of 3D potential field and an enhanced breadth-first search algorithms for the path planning of microdevices propelled in the cardiovascular system," in *IEEE Int. Conf. of the Eng. in Med. and Bio. Soc.*, Apr. 2005.

[14] C. Pêtrès, Y. Pailhas, P. Patron, Y. Petillot, J. Evans, and D. Lane, "Path planning for autonomous underwater vehicles," *IEEE Trans. Robot.*, vol. 23, no. 2, pp. 331–341, 2007.

[15] M. Kummer, J. J. Abbott, B. E. Kratochvil, R. Borer, A. Sengul, and B. J. Nelson, "Octomag: An electromagnetic system for 5-dof wireless micromanipulation," *IEEE Trans. Robot.*, vol. 26, no. 6, pp. 1006–1017, Sep. 2010.

[16] J. A. Sethian, *Level set methods and fast marching methods: evolving interfaces in computational geometry, fluid mechanics, computer vision, and materials science*. Cambridge University Press, 1999.

[17] K. Belharet, D. Folio, and A. Ferreira, "Endovascular navigation of a ferromagnetic microrobot using MRI-based predictive control," in *IEEE/RSJ Int. Conf. on Intel. Robots and Syst.*, Taiwan, Oct. 2010.

[18] ——, "3D MRI-based predictive control of a ferromagnetic microrobot navigating in blood vessels," in *IEEE RAS & EMBS Int. Conf. on BioMed. Robot. and BioMechatron.*, Tokyo, Japan, Sep. 2010.

[19] J. A. Sethian and A. Vladimirsky, "Ordered upwind methods for static hamilton-jacobi equations: theory and algorithms," *SIAM J. on Numerical Analysis*, vol. 41, no. 1, pp. 325–363, 2003.

[20] L. Arcèse, M. Fruchard, and A. Ferreira, "Endovascular Magnetically-Guided Robots: Navigation Modeling and Optimization," *IEEE Trans. Biomed. Eng.*, no. 99, pp. 1–12, Sep. 2011.

[21] A. Frangi, W. Niessen, K. Vincken, and M. Viergever, "Multiscale vessel enhancement filtering," *Lect. Notes in Comp. Scie.*, pp. 130–137, 1998.

[22] Y. Sato, S. Nakajima, H. Atsumi, T. Koller, G. Gerig, S. Yoshida, and R. Kikinis, "Three-dimensional multi-scale line filter for segmentation and visualization of curvilinear structures in medical images," *Med. Imag. Anal.*, vol. 2, no. 2, pp. 143–168, 1998.

[23] E. Konukoglu, M. Sermesant, O. Clatz, J.-M. Peyrat, H. Delingette, and N. Ayache, "A recursive anisotropic fast marching approach to reaction diffusion equation: Application to tumor growth modeling," in *Inf. Processing in Med. Imag.*, N. Karssemeijer and B. Lelieveldt, Eds., vol. 4584. Springer, 2007, pp. 687–699.

[24] F. Bornemann and C. Rasch, "Finite-element discretization of static hamilton-jacobi equations based on a local variational principle," *Computing and Visualization in Science*, vol. 9, pp. 57–69, 2006.

[25] M. Soulignac, "Feasible and optimal path planning in strong current fields," *IEEE Trans. Robot.*, no. 99, pp. 1–10, Feb. 2011.

[26] (2012) The visualization toolkit (VTK). Kitware. [Online]. Available: http://www.vtk.org

[27] (2012) Insight segmentation and registration toolkit (ITK). Kitware. [Online]. Available: http://www.itk.org

[28] (2012) Qt-a cross-platform application and UI framework. Nokia. [Online]. Available: http://qt.nokia.com/

[29] N. Korin, M. Kanapathipillai, B. Matthews, M. Crescente, A. Brill, T. Mammoto, K. Ghosh, S. Jurek, S. Bencherif, D. Bhatta *et al.*, "Shear-activated nanotherapeutics for drug targeting to obstructed blood vessels," *Science*, vol. 337, no. 6095, pp. 738–742, 2012.

[30] C. Yu, J. Kim, H. Choi, J. Choi, S. Jeong, K. Cha, J. oh Park, and S. Park, "Novel electromagnetic actuation system for three-dimensional locomotion and drilling of intravascular microrobot," *Sensors and Actuators A: Physical*, vol. 161, no. 1-2, pp. 297–304, 2010.

[31] P. Pouponneau, J.-C. Leroux, G. Soulez, L. Gaboury, and S. Martel, "Co-encapsulation of magnetic nanoparticles and doxorubicin into biodegradable microcarriers for deep tissue targeting by vascular MRI navigation," *Biomaterials*, vol. 32, no. 13, pp. 3481–3486, 2011.

Appendix C

Catalytic locomotion of core-shell nanowire motors (ACL10

Catalytic locomotion of Au/Ru core-shell nanowire motors

Bumjin Jang„ Wang Wei, Samuel Wiget„ Petruska Andrew, Xiangzhong Chen„ Chengzhi Hu„ Ayoung Hong„ David Folio, Antoine Ferreira, Salvador Pané, et al.

Catalytic locomotion of Au/Ru core-shell nanowire motors

Bumjin Jang,*,† Wei Wang,‡ Samuel Wiget,† Andrew J. Petruska,† Xiang-Zhong Chen,† Chenzhi Hu,† David Folio,§ Antoine Ferreira,§ Salvador Pané,*,† and Bradley J. Nelson*,†*

†Institute of Robotics and Intelligent Systems, ETH Zurich, Zurich, CH-8092, Switzerland

‡Shenzhen Key Laboratory for Advanced Materials, School of Material Sciences and Engineering, Shenzhen Graduate School, Harbin Institute of Technology, University Town, Shenzhen 518055, China

§ INSA Centre Val de Loire, Universite d'Orléans, PRISME EA 4229, Bourges, France.

KEYWORDS: *core-shell nanowires, catalytic micro-nanomotors, self-electroosmosis, self-diffusiophoresis, net propulsive force*

Fifteen years ago, Whitesides et al. pioneered a work on self-propelled catalytic millimeter-scale ships,[1] triggering a mighty development of synthetic micro- and nanomotors. These devices move autonomously in the presence of a fuel solution by converting chemical to mechanical energy.[2] Most of reported catalytic micro- and nanomotors are driven by the decomposition of hydrogen peroxide, although there are other recent examples using glucose and urea as fuels.[3-5] Several applications for these miniaturized motors have been demonstrated such

as electronic circuit healing,[6] biosensing,[4, 7] nanolithography,[8] microfluidic pumping,[9] nanocargo transport[10], or environmental remediation (for details, see recent review articles[11-16]). Most of these applications require a precise control over the speed and directionality of the motors.[17], which are highly dependent on the motor design parameters, such as its geometry, size and composition. Understanding the mechanisms involved in the propulsion of catalytic micro- and nanomotors as a function of their design is crucial for controlling their motion. Different propulsion mechanisms have been identified, such as bubble propulsion, self-electroosmosis, self-diffusiophoresis or interfacial tension.[16] In the first mechanism, bubbles are formed on the catalytic surface and impart momentum to the motor. For example, tubular microjets[18, 19] are driven by oxygen bubble propulsion, caused by the decomposition of H_2O_2 at the inner catalytic surface. While bubble propulsion seems at first glance the most intuitive way to explain the motion of these motors, this mechanism cannot be used to rationalize, for instance, the motion of bimetallic structures such as Pt/Au or Cu/Pt nanowires (NWs) in H_2O_2 and I_2 solutions respectively.[20, 21] For bimetallic NWs, self-electroosmosis [22, 23] is generally the most accepted mechanism compared to others[21],[24]. In this case, a self-induced electric field is generated by redox reactions occurring on the two different metallic segments. The motion of other micro- and nanomotors has been explained in terms of self-diffusiophoresis. Several works suggest that micro- and nanoparticles asymmetrically coated with Pt move due to an O_2 concentration gradient, caused by the asymmetric decomposition of H_2O_2 along the body of the motor.[25-27] [28, 29] Recent investigations evaluating more complex motor architectures are pointing towards a concomitant occurrence of mechanisms.[30, 31]

Among all micro- and nanomotors' structures, NWs are particularly appealing due to their unique physical properties.[32] Additionally, NWs can be compartmentalized in several functional modules by means of segmentation[33] or coaxial lithography[34] to increase their capabilities and functionalities. For instance, the trajectory of catalytic NW motor consisting of Pt/Ni/Au/Ni/Au segments can be controlled by means of magnetic fields.[35] However, interfacing certain building blocks can be detrimental for several applications. For example, the combination of two dissimilar metallic segments such as Au and Ni can lead to an increase of the corrosion rate of the magnetic part due to galvanic coupling.[36] Also, the interaction of certain materials (e.g. Ni) with the surrounding environment (e.g.biological or aquatic media) must be avoided to prevent undesired leakage of toxic ions. Alternatively, core-shell arrangements can provide an inert housing to prevent certain components to be in direct contact to the surrounding environment. Core-shell NWs have been manufactured using a wide variety of methods, and usually they imply two or more steps.[37-42]

In this work, we capitalize on a recently developed method, which allows for the batch fabrication of freestanding NWs based on template-assisted electrodeposition and wafer bonding. As the NWs are self-supported on the wafer after template removal, a second electrodeposition step can be realized to produce a core-shell architecture. This newly developed method can be adopted to fabricate core-shell NWs with various material combinations. Here, we have produced different types of bimetallic core-shell NWs such as Au/Ru, Rh/Au, Au/Rh and we have investigated for the first time their motion in H_2O_2 solutions. We observed abnormal behaviors of these core-shell devices including a speed increase with the length of Au/Ru core-shell NWs and a large speed difference among Au/Ru, Rh/Au and Au/Rh, which have not been

observed for the segmented (conventional bimetallic) NWs. The experimental results suggest that self-electroosmosis cannot be the sole mechanism for the locomotion of these architectures. Indeed, we suggest that self-diffusiophoresis is additionally playing a role as well. Additionally, magnetically guided motion of a (Au-Ni)/Ru core-shell NW is demonstrated. In this configuration, the magnetic component is enclosed within the shell, thus preventing the Ni core to be in contact with the surrounding solution.

Results

Numerical model of electroosmotic mechanism on core-shell NWs. It has previously been established that the electroosmotic force is the main driving force for locomotion of nanomotors based on surface redox reactions.[43, 44] The redox reaction consists of an oxidation reaction and reduction reaction as illustrated in Figure 1a. Protons, oxygen molecules, and electrons are generated in the oxidation process at the anode (Au) by decomposing H_2O_2. The generated protons travel by convection, diffusion, and migration to the cathode (Ru), where they react with electrons, oxygen and H_2O_2 molecules to produce H_2O in the reduction process. As a consequence of this redox reaction, protons are asymmetrically distributed around the nanomotor and, accordingly, an asymmetric electric field is developed. This self-generated electric field causes protons to migrate inside the electrical double layer that naturally formed when the nanomotor is immerged in a water solution. The proton migration leads to an electroosmotic flow, which eventually causes the motion of the nanomotor. The influence of the electroosmotic mechanism on the locomotion of our newly designed nanomotor is simulated using commercial multiphysics simulation package COMSOL (5.1). Figure S1a shows that the proton concentration around the Au/Ru core-shell NW is highly asymmetric, as expected. The protons are highly concentrated at the Au (anode) end the NW, where they are generated, and have a low

concentration at the Ru (cathode) end, where they are consumed. As expected, Figure S1b shows that the electric potential is also asymmetric because of the asymmetric distribution of protons. Figure 1b shows that the fluid flows from the anode to the cathode, translating to a directional motion of the Au/Ru core-shell NW with the anode forward. The simulation also reveals that the fluid speed is highest at the interface between the cathode and anode of the core-shell NW, where the majority of the electroosmosis flow occurs.

We notice in our simulation (Figure 1b) that near the opposite tip to the anode there is a convergent flow loop on each side of the rod due to the coupling between the electrosmotic flow moving from the anode to the cathode, and a flow from the surrounding solution due to the electric field pointing towards the cathode. We further investigate how the length of Au/Ru core-shell NW affects the convergent flow. When the length is small enough (~ 500 nm, Figure 1b (i)), the electric field generated at the anode dominates the overall electroosmotic flow (Figure S1c), and the disturbance to the fluid flow at the tip of the cathode is negligible. At approximately 1.5 μm, a flow reversal at the tip occurs, which is caused by the migration of protons from the surrounding solution to the cathode (Figure 1b (ii)). The reverse flow gains enough strength to create vortices near the surface of the NW tip. Further increase in length increase the size of vortices (Figure 1b (iii), (iv)). These vortices represent a local increase in the fluidic drag at the tail of the NW, according to the observed negative fluidic speed at the tip of the cathode as seen from the fluid profile along the NW long axis (Figure S1d).

The nanomotor speeds are calculated from the fluid velocities around the core-shell NWs using the Solomentsev and Anderson model.[45] Figure 1c shows the speed as a function of length of the core-shell NW. The decreased speed with length in the numerical simulation can be

attributed to the increase in drag force of the nanomotor as its length increases, since no-slip boundary condition was chosen for the nanomotor surface in the simulation.

Design and fabrication of the Au/Ru core shell NWs. The fabrication process is illustrated in Figure 2a. First, an anodic aluminium oxide (AAO) membrane was transferred onto a Si substrate via the Au/Au compressive bonding technique previously developed in our group.[46] Next, Au was electrodeposited into the pores of the AAO. The AAO was then chemically etched to obtain a freestanding Au NW array on the Si substrate. Ru was then electrochemically deposited on the freestanding Au NW array, hence the formation of a core-shell structure. The strong adhesion between the freestanding array and the Si substrate is able to withstand the electrophoretic and fluidic forces exerted on the NWs during Ru electrodeposition. We importantly note that the freestanding NWs must be kept in solution to prevent drying, because the surface tension forces during drying will cause severe NW aggregation [47] and result in a non-uniform deposition of the Ru shell. After the Ru deposition, the NWs are released by sonication.

A scanning electron microscope (SEM) image obtained using a back-scattered electron (BSE) detector in Figure 2b shows a typical Au/Ru core-shell NW with an approximate diameter and a length of 350 nm and 2.5 μm, respectively, where the length varies with the deposition time of the Au core. Since the intensity of the BSE signal is proportional to the atomic number, the bright area and the dark area can be assigned to Au and Ru, respectively. The Au core appears only at the base (left end) as a consequence of being released from the Si substrate. No obvious defects are observed in the Au/Ru core-shell NW structure as is seen in the high-angle annular dark field (HAADF) scanning transmission electron microscopy (STEM) image (Figure 2c). The corresponding energy dispersive X-ray (EDX) mapping verifies that the core-shell NW is

composed of Au and Ru (Figure 2d). For a better understanding of the Ru distribution, we further selectively etched the Au core in Au etchant. Representative SEM and STEM images (Figure 2e,f) show that the remaining structure after etching is a Ru shell. The Ru shell has an approximate diameter of 350 nm, which is similar to that of a Au/Ru core-shell NW. A smooth surface of the nanoshell without holes or cracks on the rod is observed and confirms the uniform distribution and the conformal growth of the Ru shell. Subsequent EDX mapping verifies that the nanoshell solely consists of Ru (Figure 2g).

Catalytic propulsion of the Au/Ru core-shell NWs. The catalytic locomotion of the Au/Ru core-shell NWs (approximate length of 2.5 μm) in H_2O_2 solution was investigated at various concentrations (0, 0.1, 0.3, 2.5, 5, 10 and 20 wt %). As expected, the speed of the core-shell NW increases with the concentration of H_2O_2 (Figure 3a), showing the maximum speed of 41 ± 7.6 μm/s at 20 wt % H_2O_2. The positive correlation between the speed of the motor and the concentration of H_2O_2 is in accordance with previous findings.[48-51] A representative core-shell-NW trajectory is shown in Figure 3a (i). A large displacement is observed over 4.55 sec in the presence of H_2O_2 (5 wt %) in contrast to the control experiment, conducted in the absence of H_2O_2, which shows Brownian motion and a very small displacement (Figure 3a (ii)).

To systematically understand the locomotion, we studied the dynamic motion behavior of the core-shell NW with different lengths (1.8, 2.6 and 3.4 μm). We calculated the mean-square displacement (MSD) from the recorded motion trajectory (see also supporting movie1) using:

$$\Delta L^2(t) \equiv \left\langle \left[r(t) - r(0) \right]^2 \right\rangle \qquad (1)$$

where $r(t) = (x(t), y(t))$.

Similar to catalytic motors of other shapes, the MSD curves in Figure 3b and S2a,b show sinusoidal oscillations, which indicate that our motors exhibit a circular motion.[48, 52, 53] The translational velocity *(v)*, rotational velocity (ω), translational diffusivity (*D*) and rotational diffusivity (D_r) for a moving particle can be extracted by fitting the MSD curves with[53]:

$$\Delta L^2(t) = 4D_t + \frac{2v^2 D_r t}{D_r^2+\omega^2} + \frac{2v^2\left(\omega^2 - D_r^2\right)}{D_r^2+\omega^2} + \frac{2v^2 e^{D_r t}}{\left(D_r^2+\omega^2\right)^2}\left[\left(D_r^2-\omega^2\right)\cos\omega t - 2\omega D_r \sin\omega t\right]$$

For comparison, the translational diffusivity $D_{t,b}$ and the rotational diffusivity $D_{r,b}$ of passive Brownian motion (i.e. in the absence of H_2O_2) of our core-shell NW are calculated by the Einstein relation:

$$D_{t,b} = \frac{k_B T}{f_{t,}^{\parallel}} \tag{3}$$

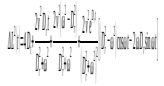

(4)

where k_B is the Boltzmann constant, *T* is the absolute temperature, $f_t^{\parallel}$ is the translational frictional drag force and $f_r^{\parallel}$ is the rotational frictional drag force parallel to the long axis of NW with a length (*L*) and a diameter (*d*) in a viscous media $D_{t,b} = \frac{k_B T}{f_t^{\parallel}}$. $D_{r,b} = \frac{k_B T}{f_r^{\parallel}}$ are defined as:[54]

$$f_t^{\parallel} = \frac{2\pi\eta L}{\ln(L/d) - 0.207 + \frac{0.980}{(L/d)} - \frac{0.133}{(L/d)^2}} \tag{5}$$

$$K_B \tag{6}$$

All of the values, as summarized in Table 1, vary as the length changes. The translational diffusivity D_t, rotational diffusivity D_r, and rotational velocity decrease with increasing length

which are easy to understood by the Einstein law; as the length increases, both translational and rotational drag forces increase, which results in a decrease in both the diffusivity and velocity. However, while D_t is quite close to $D_{t,b}$, a discrepancy of several orders of magnitude is observed between D_r and $D_{r,b}$ for longer core-shell NWs. The vortices at the tail of the cathode, found in the numerical modelling (see again Figure 1b) may explain the observed discrepancy between D_r and $D_{r,b}$ for a longer NW. This additional fluidic drag caused by the vortices, electrochemically formed contributes to the large reduction in the rotational diffusivity, hence reducing its tendency to rotate and, therefore, increasing its motion stability (or directionality.) For a detailed elucidation, we example macro-scaled flying objects, such as rockets or airplanes. For those flying objects, it is commonly known that the center of drag force should locate behind the center of thrust for a directional stability, and the stability further increases with the distance of the two centers. In our case, the center of thrust locates at the tip of the anode, while the center of drag force, supposed to be at the center for this rectangular shaped-nanomotor is actually shifted to the side of the cathode tip due to the additional drag force. The distance of the two centers further increases with the size of vortex as the length increases.

In addition, the increase in translational velocity (v) with increasing length is unexpected and somewhat counter-intuitive. Previous study conducted on Cu/Pt nanomotors show a decrease in velocity with increasing nanomotor length, most likely due to the increased drag force for a longer length.[20] However, in our experiments the speed of Au-Ru core-shell nanomotor increased with the nanomotor length, as shown by the averaged measured velocities in Figure 3c for lengths of 1.5, 2.5 and 3.5 μm (N>8 for each length). Our experimental values show a dissimilar trend with the numerical simulations (Figure 1c). The increase in speed with length in the experimental data implies that there might be an extra driving force that increases with length.

This extra driving force superimposes on the main driving force (electroosmotic force), resulting in increase in the net propulsive force of the nanomotor (Figure 3d). We can assume that the extra driving force can be related to a self-diffusiophoresis mechanism because O_2 concentration gradient around the motor surface is reinforced as the catalytically reactive surface area (Ru) increases with length. Although it is intuitively compelling that self-diffusiophoresis due to the generated O_2 concentration on the Ru surface leads to a speed enhancement, the exact magnitude of such enhancement remains unknown, and it is therefore difficult to directly compare the relative contribution from the enhanced force due to O_2 generation, and the larger viscous drag that a longer rod would experience slowing down the motor.

Catalytic propulsion of the core-shell NWs with various material combinations and the prediction of their propulsive force. In order to further investigate the role of diffusiophoresis in the catalytic propulsion of core-shell naonomtors, we fabricated Au/Rh and Rh/Au core-shell NWs with a length of 2.5 um. Their motion in the presence of 20 wt% H_2O_2 were compared with that of Au/Ru core-shell NW. We note that Ru/Au core-shell NW was not fabricated due to the growth limit of Ru cores beyond 200 nm in a length. The trajectories of the core-shell NWs are represented in Figure 4. The speed comparison of these three types of nanomotors was Au/Ru >> Rh/Au > Au/Rh (See the Supplementary movie2).

Such a trend cannot be explained by existing theory on self-electroosmosis, and we reason as follows. The speed of a self-electroosmotic nanomotor is in general correlated to a combination of the surface charge of the nanomotor (zeta potential), and the self-generated electric field as a result of surface electrochemical reactions. To understand the effects of these two factors, we first measured the zeta potential of Au/Ru, Rh/Au and Au/Rh core-shell NWs, all

yielding results around ~ -26 mV. This indicates that the observed speed difference among these three samples cannot be explained solely by the differences in their zeta potential. Secondly, as far as self-generated electric field is concerned, we believe that the difference among these three samples are to be insignificant, supported by a previous study by Wang et al.[22] showing similar speed of Au-Ru, Rh-Au and Au-Rh segmented NW motors. To briefly summarize, self-electroosmosis mechanism would predict similar speeds for these three samples, which is in clear contrast to what we have experimentally observed.

Given the inadequacy of self-electroosmosis in explaining the observed speed trend, we attempt to reconcile our results with self-diffusiophoresis. The magnitude of the self-diffusiophoretic force (extra driving force) depends on the O_2 concentration gradient, developed by the decomposition of H_2O_2 on the catalytically active layer. According to the previous studies, the decomposition rate of H_2O_2 on Ru is twice as high as Rh, while it is 10 times slower on Au than on Rh.[55] This implies that the predicted magnitude of the self-diffusiophoretic forces on the core-shell NWs are in the order of Au/Rh >> Rh/Au > Au/Ru core-shell NWs, provided that the total number of H_2O_2 decomposition is defined as the product of the decomposition rate and the reactive surface area. With the regards, diffusiophoretic force directions on Au/Rh, Rh/Au, Au/Ru core-shell nanomotors can be predicted as $\mathrm{Au} \rightarrow \mathrm{Rh}$, $\mathrm{Rh} \rightarrow \mathrm{Au}$ and $\mathrm{Au} \rightarrow \mathrm{Ru}$ respectively. The predicted force magnitudes and directions are illustrated in the left column of Figure 4. We note that the arrow sizes are relative among three core-shell samples.

To this end,, the relative speeds among three nanomotors are predicted by comparing the magnitudes of the propulsive forces that is the sum of the self-electroosmotic force and self-diffusiophoretic force. Since the Au/Ru and Au/Rh core-shell NW exhibits the highest and lowest propulsive force respectively, the expected speeds for the core-shell NWs decrease in the

following order: Au/Ru > Rh/Au > Au/Rh. This prediction is in accordance with our experimental observation, confirming our propulsion mechanism.

Magnetic guided motion of (Au-Ni)/Ru core-shell NWs.

In this section, we demonstrate that the trajectory of our core-shell NWs can be controlled under an applied magnetic field in H_2O_2 solution. For a magnetically guided motion, a Ni segment was additionally deposited on a Au segment, and subsequently coated with a Ru shell (see Figure S3 for SEM images and EDX mapping of the (Au-Ni)/Ru core-shell NWs). A magnetic guided motion was performed under the magnetic field ($\vec{B}$) of 1mT with a negligible magnetic field gradient. Supplementary movie 3 shows rectangular trajectories of two (Au-Ni)/Ru core-shell NWs when the field orientation is switched counterclockwise with a step of 90°. Interestingly, the magnetic field only serves to align the motors parallel to the magnetic field lines, but it does not determine the heading direction along them.

In conclusion, core-shell NWs composed Au/Ru have been fabricated and studied as a potential catalytic nanomotor when submerged in H_2O_2. Their maximum speed was observed to be 41±7.6 μm/s at a 20% H_2O_2 concentration. Moreover, decreased rotational diffusivity or, equivalently, enhanced directionality is observed with increased length, which results from the formation of vortices at the end of the cathode as revealed by the electroosmotic mechanism based numerical simulation. Experimentally, this nanomotor design exhibits a positive length-speed correlation, which is contrary to what occurs in other designs or in our simulation. In the case of our core-shell nanostructures, we assume that the propulsion comes from two simultaneous mechanisms: self-diffusiophoresis and self-electroosmosis. When the catalytic

active surface area (Ru) increases with length, the self-diffusiophoretic force increases due to a higher O_2 concentration gradient. For a core-shell Au/Ru NW, the generated self-diffusiophoretic force is superimposed to the self-electroosmotic force with the same force direction. Therefore, the net propulsion force is reinforced. The suggested propulsion mechanism also justifies the large difference in speed among Au/Rh, Rh/Au and Au/Ru core-shell NWs, which has not been observed for conventional bimetallic NWs. Finally, we have successfully demonstrated magnetically guided motion of core-shell NWs by inserting a Ni segment in the core-shell architecture as a magnetic responsive material. The core-shell fabrication method presented here also allows for the integration of materials within the shell such as magnetic parts, and prevent them to be in direct contact with the surrounding environment.

Figures

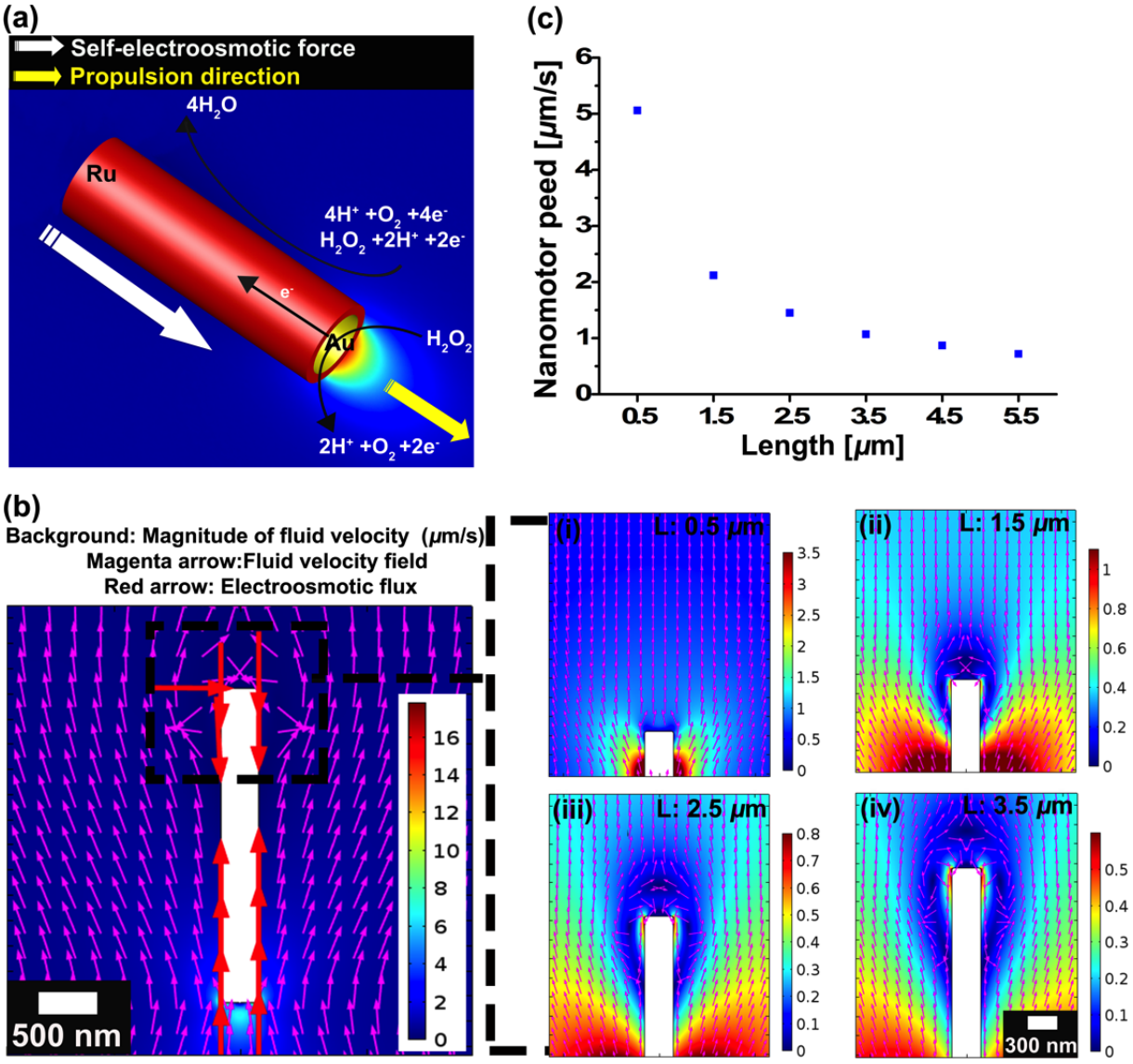

Figure 1. Numerical modeling of Au/Ru core-shell NW in the presence of H_2O_2: (a) A schematic drawing of the self-electroosmotic model for our Au/Ru core-shell NW. We note the force arrow is represented from the point of view of the nanomotor, rather than fluid. b) Magnitude of fluid velocity (background), fluid velocity (magenta arrows) and electroosmotic flux (red arrows) of Au/Ru core-shell NW with a length of 2.5 um; the inserts are the magnified images of the magnitude of fluid velocity (background) and fluid velocity field (magenta arrows) for the length of (i) 0.5 um, (ii) 1.5 um, (iii) 2.5 um and (iv) 3.5 um; the diameter of NWs are fixed to 300 nm, and (c) Speed as a function of lengths.

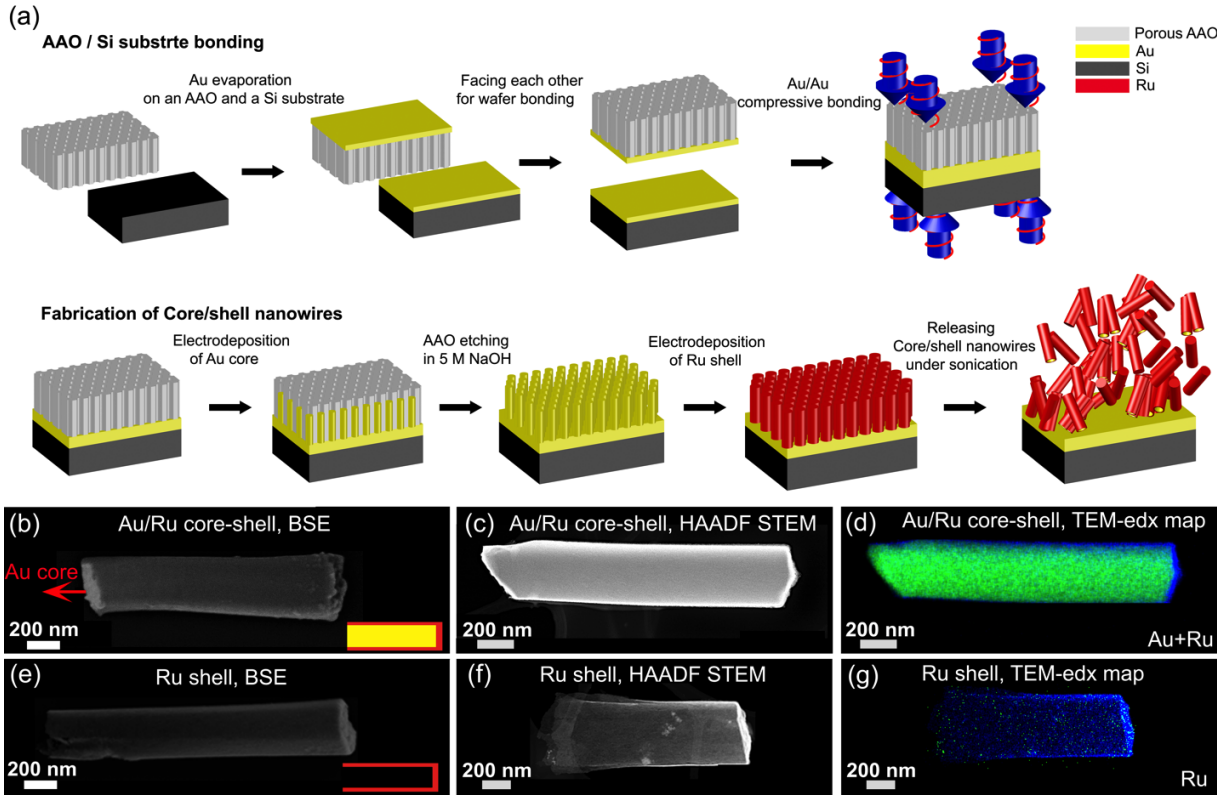

Figure 2. (a) A schematic drawing of the fabrication of core-shell NWs: the fabrication process includes AAO/Si substrate bonding and electrodeposition. BSE images of (b) a Au/Ru core-shell NW and (e) a Ru shell. *Insets in (b) and (e) are schematic drawings of Au/Ru core-shell NW and Ru shell, respectively. HAADF STEM images of (c) a Au/Ru core-shell NW and (f) a Ru shell. TEM-edx maps of (d) a Au/Ru core-shell NW and (g) a Ru shell, respectively.

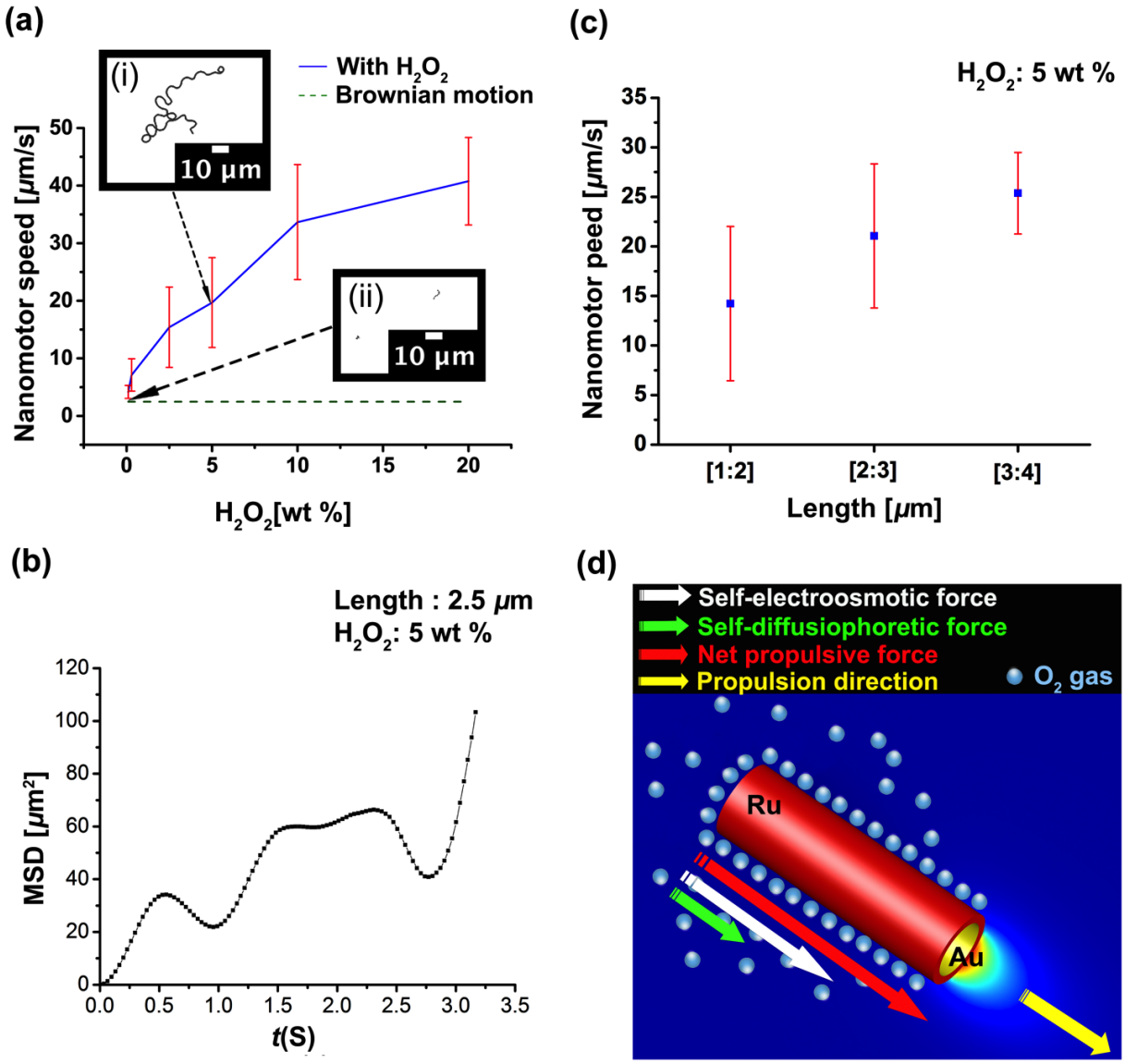

Figure3. Experimental data of Au/Ru core-shell NW in the presence of H_2O_2. (a) Averaged speed as a function of the concentration of H_2O_2. Speed was averaged from at least 11 samples with an approximate length of 2.5 μm. Inset (i): A tracked path of a core-shell NW at 5 wt % H_2O_2. And inset (ii): A tracked path of a core-shell NW at 0 wt % H_2O_2. (b) a MSD curve of Au/Ru core-shell NWs at the approximate length of 2.5 μm. (c) Speed of Au/Ru core-shell NWs as a function of a length of NWs in the presence of 5 wt % H_2O_2. *The length of core-shell NWs ranges from 1 to 2 μm, 2 to 3 μm and 3 to 4 μm. Averaged speed from at least eight samples for each range. (d) A schematic drawing of our proposed mechanism for the propulsion of the Au/Ru core-shell NWs. We note the force arrows are represented from the point of view of the nanomotor, rather than fluid.

Table 1. Measured parameters (D_t, v, D_r and ω) and theoretical values ($D_{t,b}$ and $D_{r,b}$) of Au/Ru core-shell NWs

Parameters Length	D_t (μm²/s)	$D_{t,b}$ (μm²/s)	v (μm/s)	D_r (μm²/rad)	$D_{r,b}$ (μm²/rad)	Ω (rad/s)
1.8 μm	0.97	0.71	9.83	1.84	2.13	6.97
2.6 μm	0.58	0.58	16.35	0.44	1.52	5.73
3.4 μm	0.31	0.50	27.88	0.0015	1.18	1.43

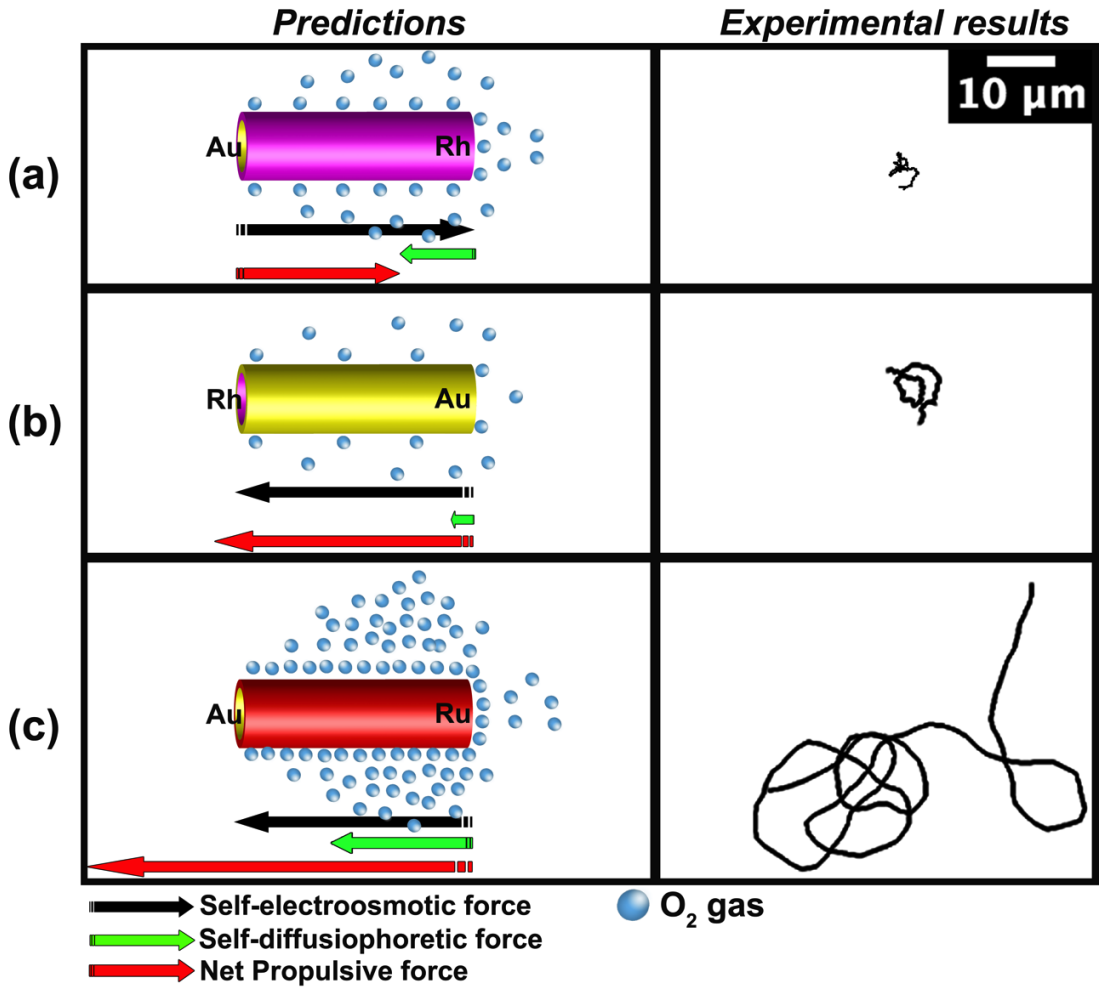

Figure 4. The predictions of the magnitude and direction of self-electroosmotic and self-diffusiophoretic forces, and the experimentally observed tracked paths of (a) Au/Rh, (b) Rh/Au and (c) Au/Ru core-shell NWs over 4.8 sec. * The arrow size are relatively predicted in three samples and force arrows are represented from the point of view of the nanomotor, rather than fluid.

TOC

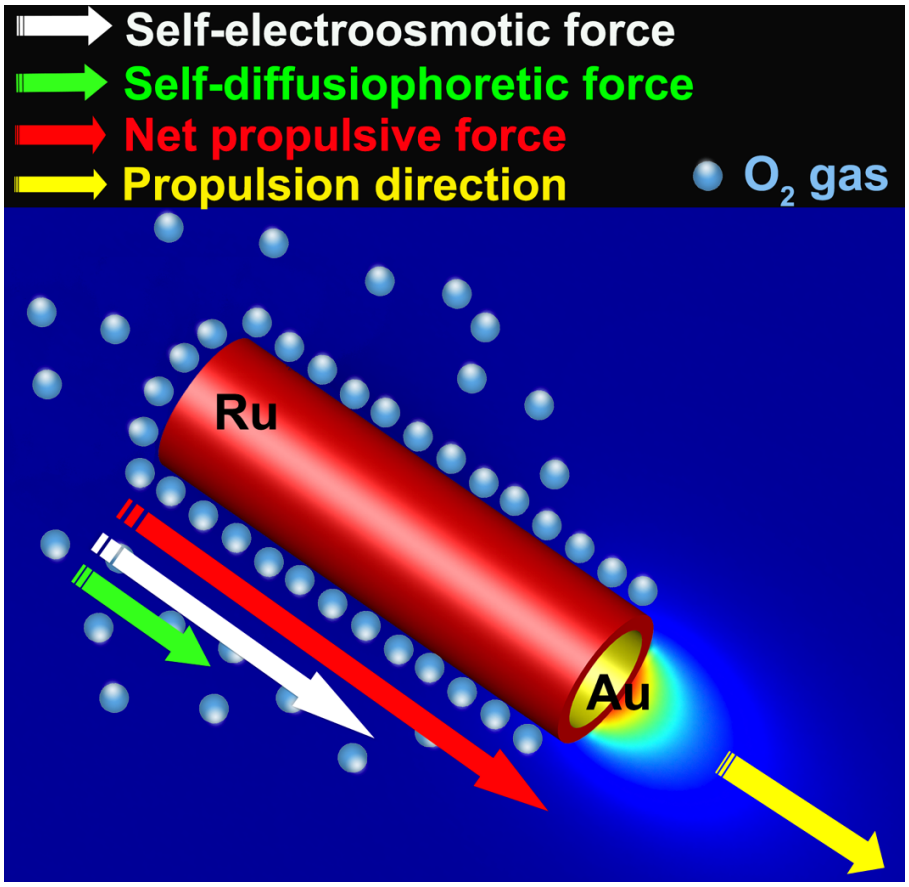
Self-electroosmotic force
Self-diffusiophoretic force
Net propulsive force
Propulsion direction
O2 gas
Ru
Au

REFERENCES

(1) Ismagilov, R. F.; Schwartz, A.; Bowden, N.; Whitesides, G. M. Autonomous Movement and Self-Assembly. *Angew. Chem. Int. Ed. Engl.* 2002, 41, 652-654.

(2) Wang, W.; Duan, W.; Ahmed, S.; Mallouk, T. E.; Sen, A. Small power: Autonomous nano- and micromotors propelled by self-generated gradients. *Nano Today* 2013, 8, 531-554.

(3) Mano, N.; Heller, A. Bioelectrochemical Propulsion. *J. Am. Chem. Soc.* 2005, 127, 11574-11575.

(4) Ma, X.; Jannasch, A.; Albrecht, U. R.; Hahn, K.; Miguel-Lopez, A.; Schaffer, E.; Sanchez, S. Enzyme-Powered Hollow Mesoporous Janus Nanomotors. *Nano Lett.* 2015, 15, 7043-7050.

(5) Gaspar, S. Enzymatically induced motion at nano- and micro-scales. *Nanoscale* 2014, 6, 7757-7763.

(6) Li, J.; Shklyaev, O. E.; Li, T.; Liu, W.; Shum, H.; Rozen, I.; Balazs, A. C.; Wang, J. Self-Propelled Nanomotors Autonomously Seek and Repair Cracks. *Nano Lett.* 2015, 15, 7077-7085.

(7) Dey, K. K.; Zhao, X.; Tansi, B. M.; Mendez-Ortiz, W. J.; Cordova-Figueroa, U. M.; Golestanian, R.; Sen, A. Micromotors Powered by Enzyme Catalysis. *Nano Lett.* 2015, 15, 8311-8315.

(8) Li, J.; Gao, W.; Dong, R.; Pei, A.; Sattayasamitsathit, S.; Wang, J. Nanomotor lithography. *Nat. Commun.* 2014, 5, 5026.

(9) Kline, T. R.; Paxton, W. F.; Wang, Y.; Velegol, D.; Mallouk, T. E.; Sen, A. Catalytic Micropumps: Microscopic Convective Fluid Flow and Pattern Formation. *J. Am. Chem. Soc.* 2005, 127, 17150-17151.

(10) Sundararajan, S.; Lammert, P. E.; Zudans, A. W.; Crespi, V. H.; Sen, A. Catalytic Motors for Transport of Colloidal Cargo. *Nano Lett.* 2008, 8, 1271-1276.

(11) Dey, K. K.; Wong, F.; Altemose, A.; Sen, A. Catalytic Motors—Quo Vadimus? *Curr. Opin. Colloid Interface Sci.* 2016, 21, 4-13.

(12) Yadav, V.; Duan, W.; Butler, P. J.; Sen, A. Anatomy of Nanoscale Propulsion. *Annu. Rev. Biophys.* 2015, 44, 77-100.

(13) Sanchez, S.; Soler, L.; Katuri, J. Chemically powered micro- and nanomotors. *Angew. Chem. Int. Ed. Engl.* 2015, 54, 1414-1444.

(14) Wang, W.; Duan, W.; Ahmed, S.; Sen, A.; Mallouk, T. E. From one to many: dynamic assembly and collective behavior of self-propelled colloidal motors. *Acc. Chem. Res.* 2015, 48, 1938-1946.

(15) Guix, M.; Mayorga-Martinez, C. C.; Merkoci, A. Nano/micromotors in (bio)chemical science applications. *Chem. Rev.* 2014, 114, 6285-6322.

(16) Zhou, C.; Zhang, H.; Li, Z.; Wang, W. Chemistry pumps: a review of chemically powered micropumps. *Lab Chip* 2016, 16, 1791-1811.

(17) Colberg, P. H.; Reigh, S. Y.; Robertson, B.; Kapral, R. Chemistry in motion: tiny synthetic motors. *Acc. Chem. Res.* 2014, 47, 3504-3511.

(18) Solovev, A. A.; Mei, Y.; Bermudez Urena, E.; Huang, G.; Schmidt, O. G. Catalytic microtubular jet engines self-propelled by accumulated gas bubbles. *Small* 2009, 5, 1688-1692.

(19) Huang, W.; Manjare, M.; Zhao, Y. Catalytic Nanoshell Micromotors. *J. Phys. Chem. C* 2013, 117, 21590-21596.

(20) Liu, R.; Sen, A. Autonomous nanomotor based on copper-platinum segmented nanobattery. *J. Am. Chem. Soc.* 2011, 133, 20064-20067.

(21) Paxton, W. F.; Kistler, K. C.; Olmeda, C. C.; Sen, A.; St. Angelo, S. K.; Cao, Y.; Mallouk, T. E.; Lammert, P. E.; Crespi, V. H. Catalytic Nanomotors: Autonomous Movement of Striped Nanorods. *J. Am. Chem. Soc.* 2004, 126, 13424-13431.

(22) Wang, Y.; Hernandez, R. M.; Bartlett, D. J.; Bingham, J. M.; Kline, T. R.; Sen, A.; Mallouk, T. E. Bipolar Electrochemical Mechanism for the Propulsion of Catalytic Nanomotors in Hydrogen Peroxide Solutions†. *Langmuir* 2006, 22, 10451-10456.

(23) Pumera, M. Electrochemically powered self-propelled electrophoretic nanosubmarines. *Nanoscale* 2010, 2, 1643-1649.

(24) Fournier-Bidoz, S.; Arsenault, A. C.; Manners, I.; Ozin, G. A. Synthetic self-propelled nanorotors. *Chem. Commun.* 2005, 4, 441-443.

(25) Ma, X.; Hahn, K.; Sanchez, S. Catalytic mesoporous Janus nanomotors for active cargo delivery. *J. Am. Chem. Soc.* 2015, 137, 4976-4979.

(26) Yamamoto, D.; Takada, T.; Tachibana, M.; Iijima, Y.; Shioi, A.; Yoshikawa, K. Micromotors working in water through artificial aerobic metabolism. *Nanoscale* 2015, 7, 13186-13190.

(27) Howse, J. R.; Jones, R. A.; Ryan, A. J.; Gough, T.; Vafabakhsh, R.; Golestanian, R. Self-motile colloidal particles: from directed propulsion to random walk. *Phys. Rev. Lett.* 2007, 99, 048102.

(28) Frankel, A. E.; Khair, A. S. Dynamics of a self-diffusiophoretic particle in shear flow. *Phys. Rev. E: Stat., Nonlinear, Soft Matter Phys.* 2014, 90, 013030.

(29) Golestanian, R.; Liverpool, T. B.; Ajdari, A. Propulsion of a molecular machine by asymmetric distribution of reaction products. *Phys. Rev. Lett.* 2005, 94, 220801.

(30) Wilson, D. A.; Nolte, R. J.; van Hest, J. C. Autonomous movement of platinum-loaded stomatocytes. *Nat. Chem.* 2012, 4, 268-274.

(31) Wang, S.; Wu, N. Selecting the swimming mechanisms of colloidal particles: bubble propulsion versus self-diffusiophoresis. *Langmuir* 2014, 30, 3477-3486.

(32) Hu, J.; Odom, T. W.; Lieber, C. M. Chemistry and Physics in One Dimension: Synthesis and Properties of Nanowires and Nanotubes. *Acc. Chem. Res.* 1999, 32, 435-445.

(33) Nicewarner-Pena, S. R.; Freeman, R. G.; Reiss, B. D.; He, L.; Pena, D. J.; Walton, I. D.; Cromer, R.; Keating, C. D.; Natan, M. J. Submicrometer metallic barcodes. *Science* 2001, 294, 137-141.

(34) Ozel, T.; Bourret, G. R.; Mirkin, C. A. Coaxial lithography. *Nat. Nanotechnol.* 2015, 10, 319-324.

(35) Kline, T. R.; Paxton, W. F.; Mallouk, T. E.; Sen, A. Catalytic Nanomotors: Remote-Controlled Autonomous Movement of Striped Metallic Nanorods. *Angew. Chem. Int. Ed. Engl.* 2005, 117, 754-756.

(36) Hangarter, C. M.; Lee, Y. I.; Hernandez, S. C.; Choa, Y. H.; Myung, N. V. Nanopeapods by galvanic displacement reaction. *Angew. Chem. Int. Ed. Engl.* 2010, 49, 7081-7085.

(37) Lauhon, L. J.; Gudiksen, M. S.; Wang, D.; Lieber, C. M. Epitaxial core-shell and core-multishell nanowire heterostructures. *Nature* 2002, 420, 57-61.

(38) Hwang, J.; Min, B.; Lee, J. S.; Keem, K.; Cho, K.; Sung, M. Y.; Lee, M. S.; Kim, S. Al2O3 Nanotubes Fabricated by Wet Etching of ZnO/Al2O3 Core/Shell Nanofibers. *Adv. Mater.* 2004, 16, 422-425.

(39) Yin, Y.; Lu, Y.; Sun, Y.; Xia, Y. Silver Nanowires Can Be Directly Coated with Amorphous Silica To Generate Well-Controlled Coaxial Nanocables of Silver/Silica. *Nano Lett.* 2002, 2, 427-430.

(40) Kong, X. Y.; Ding, Y.; Wang, Z. L. Metal−Semiconductor Zn−ZnO Core−Shell Nanobelts and Nanotubes. *J. Phys. Chem. B* 2004, 108, 570-574.

(41) Cao, H. Q.; Xu, Z.; Sang, H.; Sheng, D.; Tie, C. Y. Template Synthesis and Magnetic Behavior of an Array of Cobalt Nanowires Encapsulated in Polyaniline Nanotubules. *Adv. Mater.* 2001, 13, 121-123.

(42) Hu, J. Q.; Meng, X. M.; Jiang, Y.; Lee, C. S.; Lee, S. T. Fabrication of Germanium-Filled Silica Nanotubes and Aligned Silica Nanofibers. *Adv. Mater.* 2003, 15, 70-73.

(43) Moran, J. L.; Wheat, P. M.; Posner, J. D. Locomotion of electrocatalytic nanomotors due to reaction induced charge autoelectrophoresis. *Phys. Rev. Lett. E* 2010, 81, 065302.

(44) Moran, J. L.; Posner, J. D. Electrokinetic locomotion due to reaction-induced charge auto-electrophoresis. *J. Fluid Mech.* 2011, 680, 31-66.

(45) Wang, W.; Chiang, T. Y.; Velegol, D.; Mallouk, T. E. Understanding the efficiency of autonomous nano- and microscale motors. *J .Am. Chem. Soc.* 2013, 135, 10557-10565.

(46) Jang, B.; Chen, X.-Z.; Siegfried, R.; Montero Moreno, J. M.; Özkale, B.; Nielsch, K.; Nelson, B. J.; Pané, S. Silicon-supported aluminum oxide membranes with ultrahigh aspect ratio nanopores. *RSC Adv.* 2015, 5, 94283-94289.

(47) Hill, J. J.; Haller, K.; Gelfand, B.; Ziegler, K. J. Eliminating capillary coalescence of nanowire arrays with applied electric fields. *ACS Appl. Mater. Interfaces* 2010, 2, 1992-1998.

(48) Marine, N. A.; Wheat, P. M.; Ault, J.; Posner, J. D. Diffusive behaviors of circle-swimming motors. *Phys. Rev. Lett. E* 2013, 87.

(49) Lee, T. C.; Alarcon-Correa, M.; Miksch, C.; Hahn, K.; Gibbs, J. G.; Fischer, P. Self-propelling nanomotors in the presence of strong Brownian forces. *Nano Lett.* 2014, 14, 2407-2412.

(50) Demirok, U. K.; Laocharoensuk, R.; Manesh, K. M.; Wang, J. Ultrafast catalytic alloy nanomotors. *Angew. Chem. Int. Ed. Engl.* 2008, 47, 9349-9351.

(51) Laocharoensuk, R.; Burdick, J.; Wang, J. Carbon-Nanotube-Induced Acceleration of Catalytic Nanomotors. *ACS Nano* 2008, 2, 1069-1075.

(52) Teeffelen, S. V.; Lowen, H. Dynamics of a Brownian circle swimmer. *Phys. Rev. E: Stat., Nonlinear, Soft Matter Phys.* 2008, 78, 020101.

(53) Ebbens, S.; Jones, R. A.; Ryan, A. J.; Golestanian, R.; Howse, J. R. Self-assembled autonomous runners and tumblers. *Phys. Rev. E: Stat., Nonlinear, Soft Matter Phys.* 2010, 82, 015304.

(54) Charsooghi, M. A.; Akhlaghi, E. A.; Tavaddod, S.; Khalesifard, H. R. A MATLAB program to calculate translational and rotational diffusion coefficients of a single particle. *Comput. Phys. Commun.* 2011, 182, 400-408.

(55) McKee, D. W. Catalytic decomposition of hydrogen peroxide by metals and alloys of the platinum group. *J. Catal.* 1969, 14, 355-364.

ASSOCIATED CONTENT

Supporting Information.

Experimental procedures, numerical modelling procedures, supplementary figures and supplementary movies are included.

This material is available free of charge via the Internet at http://pubs.acs.org.

AUTHOR INFORMATION

Corresponding Author

*E-mail: bjang@ethz.ch, vidalp@ethz.ch

Author Contributions

S.P. and B.J.N. initiated the project. S.P. and B.J. designed the fabrication experiments. B.J. and S.W. fabricated the magnetic nanoswimmers and analyzed their motion. W.W. and B.J. conducted the simulation experiments. B.J., W.W., A.P., X.C., B.J.N., D.F. and A.F. performed the analysis of the swimmers and provided theoretical discussion. B.J., W.W., A.P., X.C., S.P., and B.J.N. supervised the work and gave critical input. All authors contributed to discussions.

Notes

The authors declare no competing financial interests.

ACKNOWLEDGMENT

Funding support from the European Community's Seventh Framework Programme (FP7/2007-2013) under grant agreement 296679 (MANAQA) is acknowledged. S.P. acknowledges financial support by the European Research Council Starting Grant "Magnetoelectric Chemonanomotorics for Chemical and Biomedical Applications (ELECTROCHEMBOTS)", by the ERC grant agreement n. 336456. W.W. is grateful for the financial support from National Natural Science Foundation of China (Grant No. 11402069) and the city government of Shenzhen (Grant No. KQCX20140521144102503). We especially thank Prof. Mahmut Selman Sakar from the Mechanical Engineering (School of Engineering, EPFL), and Carlos C.J. Alcantara and Ayoung Hong from the Multi-Scale Robotics Lab (ETH Zürich) for constructive discussions.

Appendix D

Modeling of optimal targeted therapies using drug-loaded magnetic nanoparticles for the liver cancer (ACL12)

Modeling of Optimal Targeted Therapies using Drug-Loaded Magnetic Nanoparticles for the Liver Cancer

Lyès Mellal, David Folio, Karim Belharet, Antoine Ferreira

This article has been accepted for publication in a future issue of this journal, but has not been fully edited. Content may change prior to final publication. Citation information: DOI 10.1109/TNB.2016.2535380, IEEE Transactions on NanoBioscience

Modeling of Optimal Targeted Therapies using Drug-Loaded Magnetic Nanoparticles for the Liver Cancer

Lyès Mellal, David Folio, Karim Belharet and Antoine Ferreira

***Abstract*—To enhance locoregional therapies for liver cancer treatment, we propose in this study a mathematical model to optimize the transcatheter arterial delivery of therapeutical agents. To maximize the effect of the treatment and minimize adverse effects on the patient, different mathematical models of the tumor growth are considered in this study to find the optimal number of the therapeutic drug-loaded magnetic nanoparticles to be administered. Three types of therapy models are considered, e.g. angiogenesis inhibition therapy, chemotherapy and radiotherapy. We use state-dependent Riccati equations (SDRE) as an optimal control methodology framework to the Hahnfeldt's tumor growth formulation. Based on this, design optimal rules are derived for each therapy to reduce the growth of a tumor through the administration of appropriate dose of anti-angiogenic, radio- and chemo-therapeutic agents. Simulation results demonstrate the validity of the proposed optimal delivery approach, leading to reduced intervention time, low drug administration rates and optimal targeted delivery.**

***Index Terms*—Magnetic Resonance Navigation; Tumor Growth model; Optimal Tumor Control; Optimal drug delivery; Locoregional therapies.**

I. Introduction

Cancer is known as one of the major causes of morbidity and death worldwide. Especially, the liver cancer continues to be a major cause of mortality, and its incidence is still increasing [1]. Due to a lack of donors, it is even more rarely possible to perform a liver transplantation or to consider surgical procedures [2], [3]. Therefore, transarterial locoregional interventions, such as transcatheter arterial chemoembolization (TACE) or radioembolization (TARE), are procedures that provide a significant survival benefit [2]–[4]. These minimally invasive procedures aim to restrict a tumor's blood supply (embolization) together with a drug delivery (radioembolization or chemoembolization) into an artery supplying a tumor. In particular, the use of drug eluting beads (microspheres) that carry the chemotherapeutic agent ensures the delivery a lower side-effect than systemic chemotherapy [5], [6]. The success of both TACE or TARE procedures requires a critical mass of drug eluting beads or radioactive Yttrium-90 microspheres to implant in vessels at the tumor periphery, as illustrated in Fig. 1. Due to anatomical size constraints the delivery catheter is limited in terms of accessibility, improper catheter placement and insufficient extrahepatic artery embolization. As a consequence, the current procedures demonstrated insufficient deposition results close to the tumor vessels promoting tumor growth. Furthermore, some therapeutic agents end up in the systemic flow, and destroy healthy liver tissue via ischemia, radiation damage and/or drug inflammation [7], [8] .

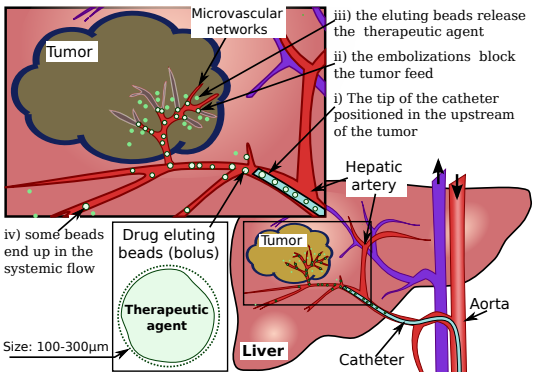

Fig. 1. Schematic representation of the principle locoregional therapy for the liver cancer. Access is gained from the femoral artery, and the catheter is passing through the abdominal aorta to the hepatic (liver) artery for delivering the therapeutic agents (drug eluting beads) close to the tumor. Then, the beads are cutting off the blood supply (embolization), as well as delivering the drugs to the tumor (chemo- or radio-therapy). Without proper control some therapeutic agents could end up in the systemic flow and cause injuries.

Recently, magnetic navigation using a clinical magnetic resonance imaging (MRI) scanner has been introduced as a novel technique to improve the above mentioned loco regional procedures. It consists to serially steer single magnetic agents (delivered through the catheter tip) to the disease site to reach a given drug dose or radioactive isotope concentration (Fig. 1). As example, radioactive magnetic biodegradable nanoparticles that incorporate both magnetite and the β-emitter ^{90}Y have demonstrated efficient tumor targeting by using the superconducting magnet provided by MRI scanner [9]. In the same way, Martel *et al.* have proposed the use of an upgraded clinical MRI scanner to enable magnetic resonance navigation (MRN) of therapeutic agents to realize direct tumor targeting [10]–[12]. In their experiments, the authors have used FeCo magnetic particles to carry doxorubicin (cytotoxic drug) coated with a biodegradable polymer (PLGA) [11]. These preliminary trials point out the need to know precisely the number, the size, the shape and the steering properties of the therapeutic agents to be injected with respect to the developmental stage of the tumor [13]. In this study, to maximize the effect of the treatment and to minimize adverse

This paper extends the work presented at the IEEE International Conference on Intelligent Robotics and Systems, Hamburg, Germany, 2015. L. Mellal, D. Folio and A. Ferreira is with the INSA Centre Val de Loire, Univ. Orléans, K. Belharet is with the HEI Centre, PRISME Laboratory EA 4229, Bourges, F-18020, France. E-mail: antoine.ferreira@insa-cvl.fr.

This article has been accepted for publication in a future issue of this journal, but has not been fully edited. Content may change prior to final publication. Citation information: DOI 10.1109/TNB.2016.2535380, IEEE Transactions on NanoBioscience

effects on the patient, mathematical models of the tumor growth are considered to find the number of magnetic agents to be administered. Indeed, an ultimate goal in the clinical setting is to use models to help design optimal therapeutic strategies. Actually, mathematical modeling offers interesting tools that could give insights into a better understanding and control of these open clinical problems. In particular, modeling of cancer behavior is an active research field for biologists, mathematicians and engineers. Different approaches are used in the mathematical modeling of cancer and its control [14]–[23]. For instance, some researchers investigated the tumor growth model by using cellular automata which can include very specific characteristics of the tumor, patient and drug effectively in the model [24], [25]. Most of mathematical formulations are mainly constructed using ordinary differential equations (ODE) to exhibit the cancer dynamics and their response to the therapeutic agents [15]–[22]. Therefore, the modeling of tumor treatment is realized for chemotherapy [20], [21], immunotherapy [22], anti-angiogenic therapy [15]–[17], radiotherapy [17] as well as a combination of the above [17]–[19]. For example, de Pillis and Radunskaya [22] set out an ODE system to depict the dynamics of tumor growth by means of the populations of tumor, normal and immune cells. To the best of the author's knowledge, no studies have investigated the mathematical modeling of locoregional procedures. This is mainly due to modeling difficulties. First, as the tumor behavior (avascular, vascular, and metastatic stages) and medication level are highly patient-dependent, different therapeutical materials may be considered as navigable agents, e.g. drug eluting microspheres, biologically active agents, chemical mediators of cell function, viral vectors or genetic material. Second, a large dispersion of the therapeutic agents occurs along the feeding vessels to the tumor(s) that endup in the systemic flow. It renders difficult the estimation of drug concentration deposited within the tumor. Third, the tolerability of conventional locoregional therapies seems to be affected by the type of regimen and the frequency of the treatment. The model should take into account constraints on drug delivery rates and state of the patient by solving an optimization problem at regular time intervals. This work aims to fill this gap by extending conventional therapy models for the transcatheter tumor therapy using MRN procedure for hepatocellular carcinoma (HCC). This paper is organized as follows: first, Section 2 presents the mathematical model framework for cancer therapy. Then, Section 3 proposes an optimal direct targeting therapy optimization problem. Section 4 demonstrates the applicability of the design framework in the context of MRN-assisted procedures. Finally, Section 5 discusses the main limitations when translating the theoretical results to practical experiments.

II. Mathematical Modeling of Cancer

A. Background

Cancer is a group of diseases involving basically abnormal cell growth (neoplasia). With over 100 different known forms that could affect all human organs, cancer is not a unique pathology. Hence, cancers are classified by the type of malignant cell, such as blastoma, carcinoma, sarcoma, lymphoma and leukemia. Therefore, many treatments against cancer exist, including surgery, chemotherapy, radiation therapy, or palliative care. The chosen treatment(s) depends on the type, location, and grade of the cancer as well as the person's states.

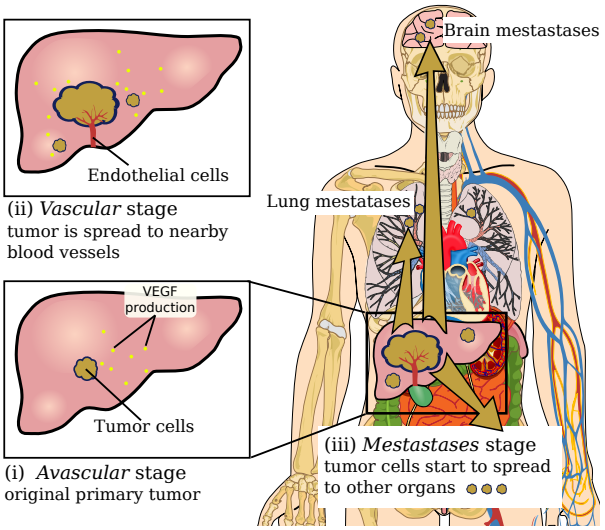

Fig. 2. Representation of the liver cancer stages: (i)avascular stage: the tumor is small and found in one part of the liver without connection with the blood vessels or lymph nodes; (ii) vascular stage: tumor has grown into the blood vessels of the liver; (iii) metastases stage: tumor has spread into other organs.

Thus, the understanding of the cancer evolution is a main issue in its fight. To this aim, it is mandatory to investigate the neoplasia process. Actually, neoplasia commonly forms a mass that is referred as *tumor*. Basically, a tumor evolution could be described in three stages, as illustrated in Fig. 2. First, a tumor appears and starts to grow to obtain its nutriments from its immediate environment. At this step, known as *avascular growth*, it is usually difficult to detect it through medical screening. The tumor could then continue to expand by seeking additional resources that allows it entering to the second stage: the *vascular growth*. At this step, the body provides new nutriments, and endothelial cells migrate to the tumor to form new microvascular networks. This process, referred as angiogenesis, allows the tumor to continue its development. In this vascular stage, symptoms may appear and the tumor becomes detectable on medical images. Finally, the tumor could evolve to the third step: the *metastasis stage*. In this step, the tumor cells are spread to other organs, and it becomes more difficult to treat them.

B. Tumor Growth Models

Different cancer models have been proposed [14]–[23]. One key aspect in the cancer evolution is the angiogenesis process. Commonly, in this context, the Hahnfeldt's tumor growth model [15] is considered, as it could be applied for different cancer therapies [17]–[19]. Specifically, the underlying diffusion of tumor and endothelial cells that stimulate and inhibit angionesis are incorporated into a system of ordinary differential equation (ODE). Different extensions of the original Hahnfeldt's model have been proposed [16]–[19].

This article has been accepted for publication in a future issue of this journal, but has not been fully edited. Content may change prior to final publication. Citation information: DOI 10.1109/TNB.2016.2535380, IEEE Transactions on NanoBioscience

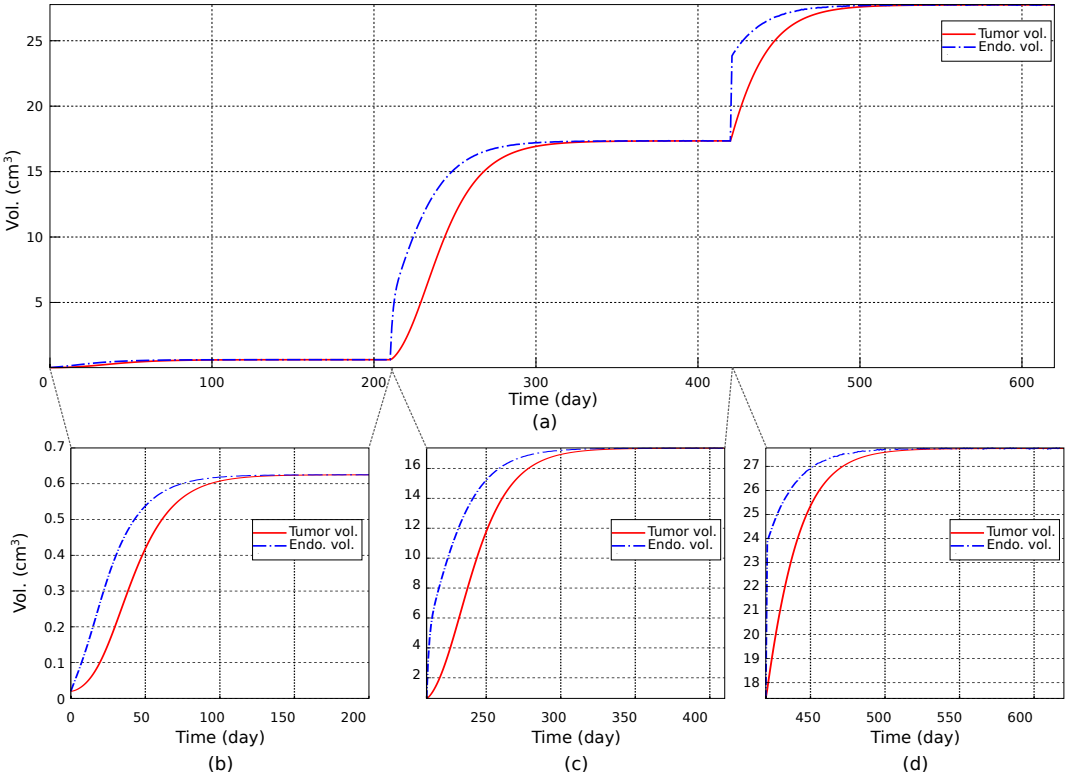

Fig. 3. (a) Tumor growth rate changes at different stages of the liver cancer. Evolution of the tumor and endothelial volumes without drug administered: (b) vascular growth from $c_0 = 20\,\mathrm{mm}^3$ and $e_0 = 20\,\mathrm{mm}^3$; (c) vascular step from the avascular equilibrium point $c_{\mathrm{avasc.},\infty} = e_{\mathrm{avasc.},\infty} = 625\,\mathrm{mm}^3$; and (d) metastasis stage simulation from the vascular equilibrium point $c_{\mathrm{vasc.},\infty} = e_{\mathrm{vasc.},\infty} = 17\,346.5\,\mathrm{mm}^3$.

Let c denotes the volume of cancer cells, and e the volume of endothelial cells that supplies the tumor with nutriments. The tumor angiogenesis evolution could be then described by the following ODE system:

$$\dot{c}(t) = -\lambda_c c(t) \log\left(\frac{c(t)}{e(t)}\right) \quad (1)$$

$$\dot{e}(t) = bc(t) - dc(t)^{2/3} e(t) \quad (2)$$

with λ_c the tumor growth rate; b the vascular endothelial cells birth rate; and d the vascular endothelial cells death rate.

Especially, the tumor follows a Gompertzian law [15]: its growth saturates at a maximal volume, and we get the following steady-state:

$$c_\infty = e_\infty = \left(\frac{b}{d}\right)^{3/2} \quad (3)$$

The endothelial cell birth (b) and death (d) rate depend mainly on the type of tumor and the patient. Obviously, the system model states that the tumor cannot increase over c_∞ volume, and then does not take into account the evolution to the metastasis stage. As the system model (1)-(2) is mainly devoted to the vascular stage, to take into account the other stages the endothelial birth rate b could be considered as piece-wise continuous. To understand the tumor dynamics, it is important to analyze its growth. The growth parameters set $\{\lambda_c, b, d\}$ has been identified by Hahnfeldt *et al.* [15] from experimental data with mice diseased with lung cancer (Lewis lung-carcinoma, LLC) for the vascular stage, and the corresponding values are reported in Table I. Fig. 3a shows the evolution of the tumor and endothelial volume growth for each stage. First, we consider that a malignant neoplasm appears with an initial volume $c_0 = 20\,\mathrm{mm}^3$. We assume that nutriments sought by the tumor from its immediate environment could be equivalent to an initial volume of endothelial cells of $e_0 = 20\,\mathrm{mm}^3$. Hence, in the avascular stage the endothelial state simulates the resources absorbed by the tumor (see Fig. 3b). The tumor volume increases with a Gompertzian curve, and after 100 days reaches the equilibrium value: $c_{\mathrm{avasc.},\infty} = e_{\mathrm{avasc.},\infty} = 625\,\mathrm{mm}^3$, predicted by (3). After 200 days, endothelial cell migrates to the tumor to form a microvasculature networks around the tumor. The avascular equilibrium values is used as the initial condition of the vascular stage (cf. Fig. 3c). Once again, an equilibrium is

TABLE I
ANGIOGENESIS TUMOR GROWTH PARAMETERS SET.

Param.	Value [15]	Units
λ_c	$0.192/\log(10)$	day^{-1}
d	8.73×10^{-3}	$\mathrm{day}^{-1}\,\mathrm{mm}^{-2}$
b	0.638	day^{-1}

(a)

Stage	Avasc.	Vasc. [15]	Met.	Units
b	0.638	5.85	8	day^{-1}

(b)

This article has been accepted for publication in a future issue of this journal, but has not been fully edited. Content may change prior to final publication. Citation information: DOI 10.1109/TNB.2016.2535380, IEEE Transactions on NanoBioscience

reached: $c_{\text{vasc.},\infty} = e_{\text{vasc.},\infty} = 17\,346.5\,\text{mm}^3$. If no treatment is administered or it fails to block the growth of the tumor, the metastasis stage could occur (cf. Fig. 3d).

C. Cancer Therapy Modeling

This section addresses the mathematical modeling of targeted therapy for optimal administration of drug-loaded magnetic nanoparticles, namely *therapeutic vectors*. When a therapeutic vector is delivered to a host, two different types of processes are involved: pharmacokinetics (PK) and pharmacodynamics (PD). The PK model characterizes what the body does with the agent, and is commonly modeled through the concentration of the therapeutic agents $\delta(t)$, in the sampled fluid (e.g. plasma or blood). The agent concentration expression is [15]:

$$\delta(t) = \int_0^t u(s) \exp\left(-\lambda_\delta\,(t-s)\right) ds \tag{4}$$

where u is the rate of administration of the therapeutic agent, and λ_δ is the elimination rate. The PD describes the effects of the agent to the body, and is related to the concentration $\delta(t)$ provided by the PK model. The classic PD model is the log-kill effect [15], [22]. The following presents how the PK and PD are related to the tumor growth, according to considered cancer therapy.

1) Angiogenesis Inhibition Treatment: Basically, for such treatment only the endothelial growth (2) will be antagonized by an anti-angiogenic agent, such as endostatin, whose plasma concentration is $\delta_a(t)$, leading to its new formulation [15]:

$$\dot{e}(t) = bc(t) - dc(t)^{2/3}e(t) - k_a\delta_a(t)e(t) \tag{5}$$

with k_a the angiogenic drug killing parameter. Table III shows the PK parameters of the endostatin.

2) Chemotherapy Treatment: The literature provides different mathematical formulations of the tumor functioning and response to chemotherapy [19]–[21]. Here, to model the effect of a cytotoxic chemotherapeutic agent of concentration $\delta_x(t)$ the angiogenesis model is used [19], and is extended as:

$$\dot{c}(t) = -\lambda_c c(t) \log\left(\frac{c(t)}{e(t)}\right) - k_{cx}\ c(t)\delta_x(t) \tag{6}$$

$$\dot{e}(t) = bc(t) - dc(t)^{2/3}e(t) - k_{ex}\ e(t)\delta_x(t) \tag{7}$$

with k_{cx} and k_{ex} the PD log-kill parameters. The case $k_{ex} = 0$ means that the cytotoxic drug does not have any effects on the endothelial cells. Contrarily to angiogenesis inhibition model, no PK-PD parameters $\{k_{cx}, k_{ex}, \lambda_\delta\}$ characterized from experimental data are available in the literature.

3) Radiotherapy Treatment: Classically, the so-called tumor linear-quadratic (LQ) model [17], [18], [26] is used to characterize the effects of ionizing radiation on the tumor and endothelial cells. Thus, the damage of radiation on a cell x is modeled in the following form [17], [18], [26]:

$$-x(t)\left(\alpha_x + \beta_x \int_0^t \left(u(s)\exp\left(-\mu(t-s)\right) ds\right)\right) u(t) \tag{8}$$

where $u(t)$ represents the fractionation schedule of radiation; α_x and β_x are positive gains related to the tumor-LQ parameters; and μ is the cell repair rate. As the radiation damage the tumor and the endothelial cells, the model for radiotherapy could be expressed with the following ODE set [18]:

$$\dot{c} = -c\left(\lambda_c \log\left(\frac{c}{e}\right) + (\alpha_c + \beta_c r)\, u\right) \tag{9}$$

$$\dot{e} = bc - e\left(dc^{2/3} + (\alpha_e + \beta_e r)\, u\right) \tag{10}$$

with $r(t)$ the concentration of the radiation.

III. Optimal Direct Targeting Therapy

In traditional treatment regimes the amount of administered therapeutic agents is very important for patient's survival. Actually, the therapy does not treat only the tumor, it often kills some healthy tissues or causes them serious damage. Hence, the dosage of the therapy must be carefully adjusted to minimize side-effects, while maximizing the capability to destroy the tumor. To address this issue, control theory is basically employed [27]. In particular, optimal control techniques have been applied for antiangiogenic therapy [16], [17], chemotherapy [21], [22], [28] or radiotherapy [17] to define the optimal treatment and drug dose. This section presents an adaptation of conventional therapies [15]–[19] to the case of magnetically controlled drug-loaded nanoparticles.

A. Optimal Control Design

Optimal control deals with the problem of finding a regulator such that a certain optimality criterion is achieved [29], [30]. Given cancer models presented in Section II, the issue is to find an optimal control input u to decrease the tumor size while minimizing total drug administered. However, the different therapy models exhibit a highly nonlinear and complex nature. Thus, different optimization techniques have been used for stabilizing tumor growth while minimizing the administered therapeutic agent [19], [21], [23], [28]. One of these approaches consider the state-dependent Riccati equations (SDRE) framework [28], [30], [31]. Actually, SDRE has emerged as an interesting strategy for direct synthesis of nonlinear controllers [30], [31]. This optimal control methodology has been applied with the de Pillis *et al.* cancer model [22] in [28]. However, to the authors' knowledge, this optimal framework has not been applied to the Hahnfeldt's tumor growth formulation [15] or its extension [16]–[19].

1) SDRE Optimal Regulation: Let us consider a system represented by the following pseudo-linear equations in state-depend coefficient (SDC) form:

$$\dot{\mathbf{x}} = \mathbf{A}(\mathbf{x})\mathbf{x} + \mathbf{B}(\mathbf{x})u \tag{11}$$

where $\mathbf{x} \in \mathbb{R}^n$ is the time-dependent state vector, with n the number of states; $u \in \mathbb{R}^m$ is the (drug) control input ($m = 1$ for monotherapy); $\mathbf{A}(\mathbf{x}) \in \mathbb{R}^{n\times n}$ and $\mathbf{B}(\mathbf{x}) \in \mathbb{R}^{n\times m}$ are state-dependent matrices. In infinite horizon, the continuous-time SDRE optimization problem is then to minimize the following quadratic cost functional [29], [30]:

$$\mathbf{J} = \int \left(\mathbf{x}^T\mathbf{Q}\mathbf{x} + u^T\mathbf{R}u\right) \mathrm{d}t \tag{12}$$

where the weights (design parameters) are state-dependent, such that $\mathbf{Q} \in \mathbb{R}^{n\times n}$ is positive-definite and $\mathbf{R} \in \mathbb{R}^{m\times m}$.

This article has been accepted for publication in a future issue of this journal, but has not been fully edited. Content may change prior to final publication. Citation information: DOI 10.1109/TNB.2016.2535380, IEEE Transactions on NanoBioscience

Thus, the optimal control law that minimizes this criterion is given by:

$$u = -\mathbf{R}^{-1}(\mathbf{x})\mathbf{B}^{\top}(\mathbf{x})\mathbf{P}(\mathbf{x})\ \mathbf{x} \tag{13}$$

with $\mathbf{P}(\mathbf{x})$ is the unique, symmetric, positive-definite solution of the algebraic state-dependent Riccati equation (SDRE) [30], [31]:

$$\mathbf{PA} + \mathbf{A}^{\top}\mathbf{P} - \mathbf{PBR}^{-1}\mathbf{B}^{\top}\mathbf{P} + \mathbf{Q} = 0 \tag{14}$$

Let us notice that the SDRE control design is similar to the well known linear quadratic regulator (LQR), where each of the above matrices are state-dependent.

2) Pseudolinearization: The nonlinear ordinary differential equation (ODE) of the considered cancer therapy could be expressed in the following general nonlinear dynamical system:

$$\dot{\mathbf{x}}(t) = f(\mathbf{x}) + g(\mathbf{x})u(t) \tag{15}$$

To apply the above SDRE methodology, the so-called pseudo-linearized form (11) of the nonlinear system (15) has to be computed. More precisely, the state matrix is obtained from $f(\mathbf{x}) = \mathbf{A}(\mathbf{x})\mathbf{x}$ by mathematical factorization. This state-dependent parametrization of the nonlinear system is not unique [30]. Among the alternatives, the chosen pseudo-linearization should ensure point-wise controllability condition, where the so-called state-dependent controllability matrix has full rank, that is:

$$\mathcal{C} = \left[\mathbf{B}(\mathbf{x})\ \mathbf{A}(\mathbf{x})\mathbf{B}(\mathbf{x}) \dots \mathbf{A}^{n-1}(\mathbf{x})\mathbf{B}(\mathbf{x})\right] \tag{16}$$

$$\text{rank}(\mathcal{C}) = n \tag{17}$$

B. Control of Angiogenesis Inhibitor

The objective here is to apply the SDRE optimal control strategy to reduce the growth of a tumor through the administration of appropriate dose of anti-angiogenic agents. As mentioned, the drug-free equilibrium is given by (3). Thus, the state vector $\mathbf{x}$ is designed to shift the equilibrium point to the origin, that is:

$$\mathbf{x} = (x_1 = (c - c_\infty);\quad x_2 = (e - e_\infty);\quad x_3 = \delta_a)^{\top} \tag{18}$$

where $c_\infty = e_\infty = x_\infty$ are the drug-free volume steady-state (3). A state-dependent parametrization of the angiogenesis inhibition treatment could be then written as:

$$\mathbf{A}(\mathbf{x}) = \begin{bmatrix} a_{11} & \lambda_c \frac{x_1}{x_2} & a_{13} \\ a_{21} & a_{22} & a_{23} \\ 0 & 0 & -\lambda_\delta \end{bmatrix},\ \text{and}\ \mathbf{B}(\mathbf{x}) = \begin{bmatrix} 0 \\ 0 \\ 1 \end{bmatrix} \tag{19}$$

with

$$a_{11} = -\lambda_c \left(1 + \log\left(\frac{x_1 + x_\infty}{x_2 + x_\infty}\right)\left(1 + \frac{x_\infty}{x_1}\right)\right) \tag{20}$$

$$a_{13} = 0 \tag{21}$$

$$a_{21} = b\left(1 + \frac{x_\infty}{x_1}\right) - \frac{x_\infty}{x_1} d\,(x_1 + x_\infty)^{2/3} \tag{22}$$

$$a_{22} = -d\,(x_1 + x_\infty)^{2/3} - k_a x_3 \tag{23}$$

$$a_{23} = -k_a x_\infty \tag{24}$$

This pseudolinearization is used to apply the SDRE control of the amount of anti-angiogenetic agent by considering $R = 10^3$ and $Q = \text{diag}\,(50, 0, 0)$. This Q and R values are chosen to take into account the volume of the tumor, while preventing high doses. Especially, the drug intake u has to be saturated to an upper limit $u_{\max}$.

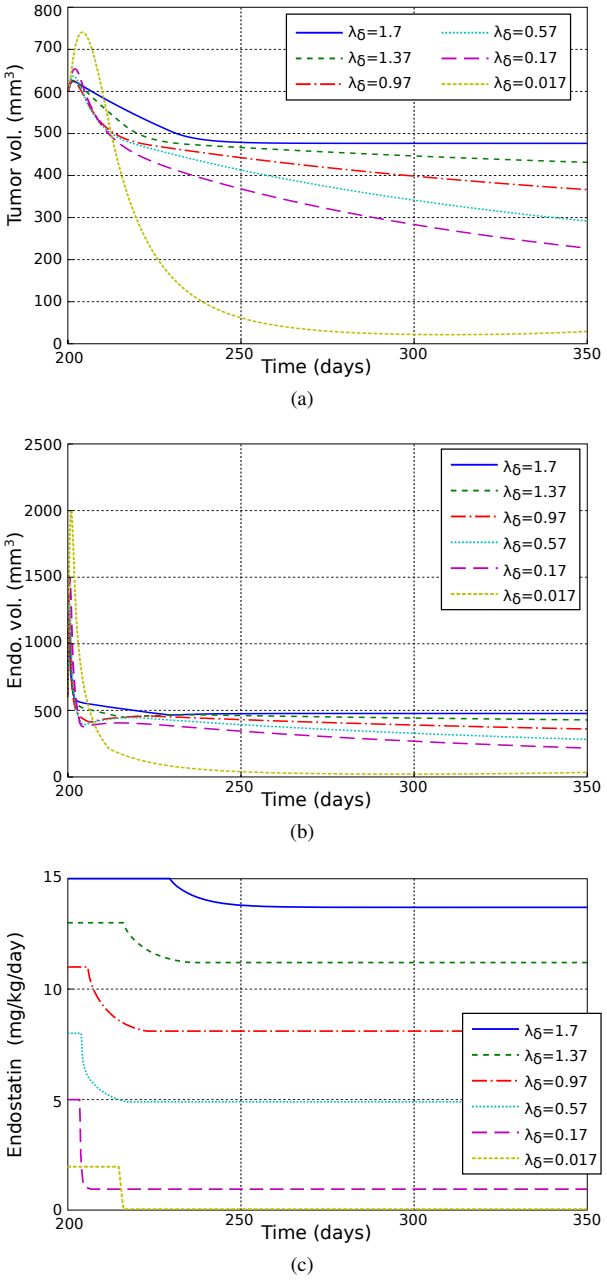

Fig. 4. Continuous infusion angiogenesis inhibition therapies: decreasing of (a) tumor volume and (b) endothelial over time with (c) optimal input drug.

TABLE III
ENDOSTATIN PK-PD PARAMETERS [15], [32].

Param.	Unit						
k_a	$\text{day}^{-1}\,\text{conc}^{-1}$	0.66					
λ_g	day^{-1}	1.7	1.37	0.97	0.57	0.17	0.017
$u_{\max}$	$\text{conc}\,\text{day}^{-1}$	15	13	11	8	5	2

Fig. 4 illustrates optimal angiogenesis inhibition therapies of a tumor at a vascular stage. Actually, tumors could be

This article has been accepted for publication in a future issue of this journal, but has not been fully edited. Content may change prior to final publication. Citation information: DOI 10.1109/TNB.2016.2535380, IEEE Transactions on NanoBioscience

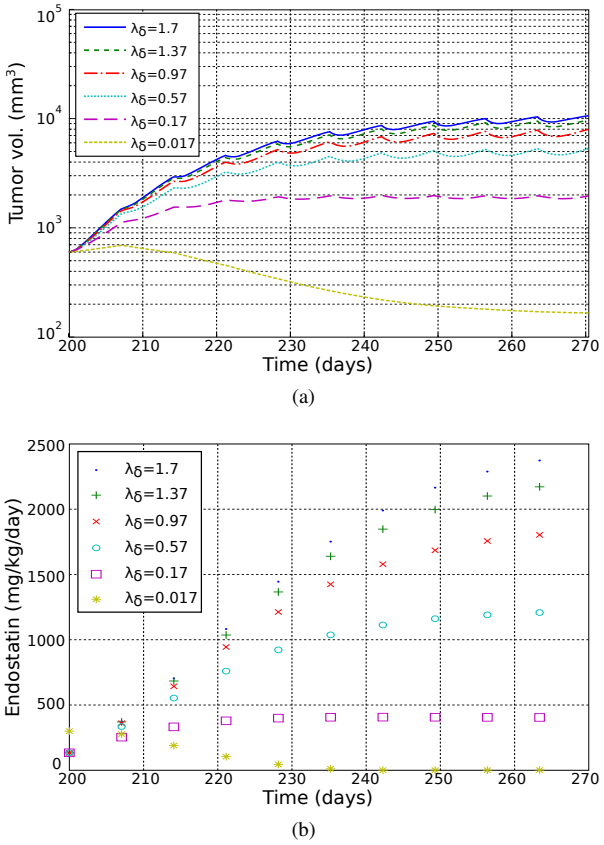

Fig. 5. Angiogenesis inhibition therapies with a session of 30 min every 7 days: (a) evolution of the tumor volume with (b) an optimal input drug.

detected mainly from this step, and the treatment is applied at the beginning of this stage (Fig. 3). Let us recall that our main motivation is to propose a direct targeted drug delivery using magnetic boluses. Therefore, our drug intake approach differs significantly than the original subcutaneous injection technique investigated by Hahnfeldt *et al.* [15]. The direct targeting could be modeled through the drug clearance rate λ_δ. Obviously, by varying λ_δ the amount of drug that is not filtered out of the blood and delivered to the tumor can be modeled. Similarly to the works achieved in [15]–[17], endostatin antiangiogenic agents is considered here. The elimination rate of endostatin is varying from $1.7\,\text{day}^{-1}$ for a subcutaneous injection [15] to $0.017\,\text{day}^{-1}$ [32], which corresponds to the efficiency of the drug in targeted treatment. The different values of PK-PD models parameters of endostatin are summarized in the Table III based on the results given in [15], [32]. The Fig. 4a and 4b show that for a clearance of $\lambda_\delta = 0.017\,\text{day}^{-1}$ the tumor and the endothelial volumes vanish in about 60 days. In contrast, for $\lambda_\delta = 1.7\,\text{day}^{-1}$ the volumes reach a steady-state of $c_\infty = e_\infty = 476.5\,\text{mm}^3$.

However, the Fig. 4c illustrates that a continuous administration of endostatin has to be realized. For instance, a reliable therapy procedure would be a session of 30 min every 7 days. Nevertheless, due to the endostatin limit $u_{\max}$, it is not possible to treat the tumor with such treatment sequence. Indeed, Fig. 5 shows the evolution of the tumor and the corresponding endostatin intake (without the upper bound). As one can see, only a low elimination rate λ_δ enables a noticeable decrease of the tumor volume. These results exhibit that the angiogenesis inhibition could be significantly improved thanks to direct targeting.

C. Chemotherapeutic Agents Direct Delivery

The same reasoning as above is used here to design optimal chemotherapy. Especially, the chemotherapy treatment model is similar to the angiogenesis inhibition model. Hence, the same state vector (18) and state-dependent parametrization (19) could be considered, where only $\{a_{13}, a_{22}, a_{23}\}$ parameters are modified as follows:

$$a_{13} = -k_{cx}\left(x_1 + x_\infty\right) \tag{25}$$

$$a_{22} = -d\left(x_1 + x_\infty\right)^{2/3} - k_{ex}x_3 \tag{26}$$

$$a_{23} = -k_{ex}x_\infty \tag{27}$$

SDRE method is then applied to control the amount of cytotoxic drug. The optimal controller parameters are defined here as: $R = 10^4$ and $Q = \text{diag}\,(1, 0, 0)$.

Contrarily to the anti-angiogenetic model, there are not PK-PD parameters based on experimental data for the model presented in paragraph II-C2. Actually, most previous works [16], [17], [19] have considered experiments only. In this work the PK-PD parameters reported in Table IV are proposed based on d'Onofrio *et al.* analysis [19] to fit the DEB-TACE procedure pharmacokinetics [6]. This choice allows to address direct targeting (low clearance) with a highly cytotoxic drug (e.g. doxorubicin) combined with embolization of the microvascular network feeding in nutriments the tumor ($k_{ex} > 0$).

TABLE IV
CYTOTOXIC AGENT PK-PD PARAMETERS.

Param.	Value	Units
λ_δ	0.009	day^{-1}
k_{cx}	2	$\text{day}^{-1}\,\text{conc}^{-1}$
k_{ex}	1	$\text{day}^{-1}\,\text{conc}^{-1}$

A tumor at vascular stage is then treated thanks to the cytotoxic agent (e.g. doxorubicin), and the results are depicted in Fig. 6. Here, the sampling time is settled to 1 h. In particular, the therapy schedule is a session of 30 min every 7 days. To limit the amount of cytotoxic drug, the intake is saturated to $u_{\max} = 2.5\,\text{conc/day}$, that is $0.0417\,\text{(mg/kg)/day}$ per session. Hence, after 6 sessions of drug administration the tumor vanish under a volume of $c_\infty = 12.67\,\text{mm}^3$. demonstrating the efficiency of cytotoxic agents.

D. Direct Delivery of Radioisotope

Based on the same modeling, the optimal control of radiotherapy is designed on the same previous formulation. Hence, the same state vector (18) and the state matrix $\mathbf{A}(\mathbf{x})$ proposed in (19) could be considered, where only $\{a_{13}, a_{22}, a_{23}\}$ parameters are modified as follows:

$$a_{13} = 0 \tag{28}$$

$$a_{22} = -d\left(x_1 + x_\infty\right)^{2/3} \tag{29}$$

$$a_{23} = 0 \tag{30}$$

This article has been accepted for publication in a future issue of this journal, but has not been fully edited. Content may change prior to final publication. Citation information: DOI 10.1109/TNB.2016.2535380, IEEE Transactions on NanoBioscience

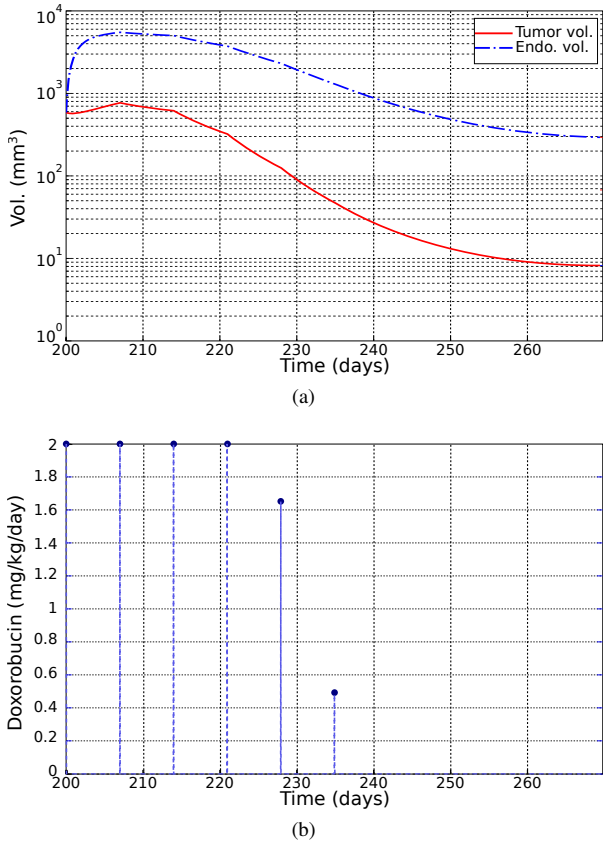

Fig. 6. Cytotoxic agent direct delivery: decreasing of (a) tumor volume and endothelial over time with optimal input drug (b).

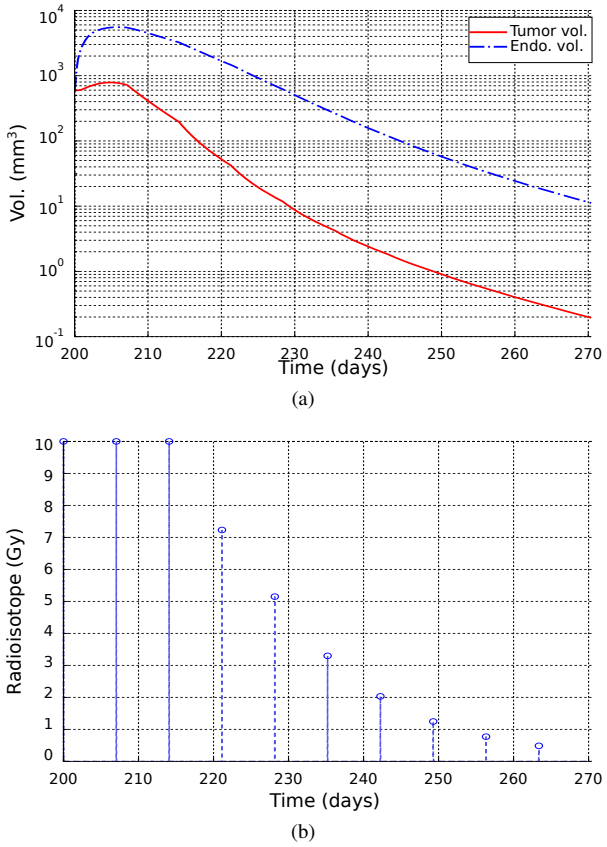

Fig. 7. Radioisotope direct delivery: decreasing of (a) tumor volume and endothelial over time with optimal input drug (b).

However, the state-dependent input matrix is now given by:

$$\mathbf{B}(\mathbf{x}) = \begin{bmatrix} -(\alpha_c + \beta_c r)(x_1 + x_\infty) \\ -(\alpha_e + \beta_e r)(x_2 + x_\infty) \\ 1 \end{bmatrix} \tag{31}$$

The optimal amount of radioisotope is computed using the following SDRE controller parameters: $Q = \mathrm{diag}\,(1, 0, 1)$ and $R = 10^3$. The tumor-LQ model is used to characterize the effects of radiation on the tumor and endothelial cells [17], [18], [26]. For the sake of simplicity, similar numerical values of the tumor-LQ parameters proposed in [17] are considered, and summarized in Table V. As previously, we consider a cancer at vascular stage. Fig. 6 illustrates the corresponding radiotherapy treatment. To limit the amount of radiation, the radioisotope dose is saturated to $u_{\max} = 10\,\mathrm{Gy}$. Once again, the radiotherapy schedule is a session of 30 min every 7 days. Thus, after 10 sessions the tumor vanish under a volume of $c_\infty = 0.195\,\mathrm{mm}^3$. As expected, radiotherapy is able to cure efficiently the cancer but the required number of sessions is higher compared to chemotherapy.

TABLE V
RADIOISOTOPE TUMOR-LQ MODEL PARAMETERS.

Param.	Value	Units	Param.	Value	Units
α_c	0.7	Gy^{-1}	β_c	$\alpha_c/10$	Gy^{-2}
α_e	0.136	Gy^{-1}	β_e	$\alpha_e/2.5$	Gy^{-2}
μ	11.09	day^{-1}			

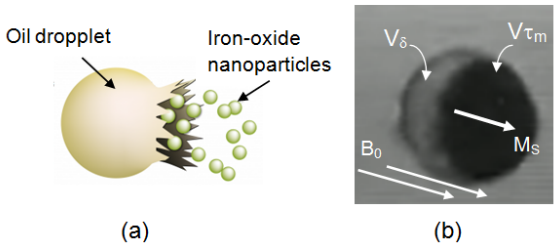

Fig. 8. Magnetic bolus model embedding aggregates of iron-oxides microparticles. (a) General design and (b) oil-based ferrofluid bolus.

IV. Optimal Delivery of Therapeutic Agents

A. Structure

In standard transcatheter tumor delivery using MRN, the therapeutic agents are constituted by magnetic boluses of microagglomerations of iron-oxide nanoparticles and drug loadings (shown in Fig. 8). The optimal size and shape of the magnetic magnetic microcarriers have been determined in [13] through simulations and experiments. Spherical boluses of 500 μm of diameter composed of SPIO particles (BioMag BM547, Bang Laboratories, Inc.) of 8 μm in size were chosen. To be controllable, the bolus has its optimal nondimensional magnetophoretic number C_{mt} ratio greater than 1. The reader may refer to [13] for optimal size selection.

The effective drug load V_δ of a single bolus is a fraction of the total volume defined as $V_\delta = (1 - \tau_m)V$ with τ_m the

This article has been accepted for publication in a future issue of this journal, but has not been fully edited. Content may change prior to final publication. Citation information: DOI 10.1109/TNB.2016.2535380, IEEE Transactions on NanoBioscience

so-called magnetization rate. When injected in the vascular phantom placed in the tunnel of the MRI scanner, the magnetic bolus will take the form of a prolate sphere due to the strong dipole-to-dipole interactions between the nanoparticles. Due to the B_0 field of the scanner, the equivalent magnetization M_s of the aggregates is aligned with the B_0 field. We consider here that the magnetic material (Vm) is saturated to its maximal value M_s = 56 emu/g under a magnetic field B_0 = 3.0 Tesla. The injected magnetic volume $\tau_m V$ is computed as a tradeoff between the encapsulated drug volume and the necessary steering force. Finally, the number of magnetic boluses is estimated from

$$N_b = \left\lceil \frac{u\ m}{V_\delta \rho_\delta} \right\rceil \tag{32}$$

where u is the rate of administration of the therapeutic agent; m is the patient weight (considered as $m = 60\,\text{kg}$ hereafter); and ρ_δ is the agent load density.

B. Endostatin Angiogenesis Inhibitor

The objective is to determine the amount N_b of required boluses to reduce the tumor size by administrating an anti-angiogenic agent. In paragraph III-B endostatin agent is used as angiogenesis inhibitor. Endostatin is a naturally occurring 20 kDa polypeptide, identified as a C-terminal fragment of collagen (type 18). Commonly, endostatin agent is available in solution concentration of $1\,\text{mg ml}^{-1}$. Hence, considering the upper limit $u_{\max}$ given in Table III, the Table VI presents the maximum of required number of magnetic boluses that have been to be conveyed continuously. Even in the low clearance case with $\lambda_\delta = 0.017\,\text{day}^{-1}$ where the endostatin administration rate is lower ($u_{\max} = 2\,\text{conc day}^{-1}$), $N_b = 4661$ magnetic boluses have to be injected continuously to administrate the daily dose.

TABLE VI
REQUIRED MAGNETIC BOLUSES THAT CARRY ENDOSTATIN TO TREAT A PATIENT OF AVERAGE WEIGHT $m = 60\,\text{kg}$.

Param.	Unit						
$u_{\max}$	conc day^{-1}	15	13	11	8	5	2
Dose	mg day^{-1}	750	650	550	400	250	100
N_b	1×10^3	34.95	30.29	25.63	18.64	11.65	4.66

Similarly, if the considered scheduling of one session every week is applied (cf. Fig. 5), $N_b = 1.398 \times 10^4$ boluses have to be administered at the first session.

C. Cytotoxic Drug (doxorubicin)

Chemotherapy is achieved by direct targeting of highly cytotoxic drug, such as doxorubicin. Doxorubicin is an anthracycline tumor antibiotic that works by intercalating DNA. This drug has already shown its efficiency in DEB-TACE procedure since a decade [5], [6]. The drug eluting beads (DEB) have been easily loaded with doxorubicin to a recommended level of $25\,\text{mg ml}^{-1}$, with a maximum loading of $45\,\text{mg ml}^{-1}$ [5]. Here, we assume that the doxorubicin PK-PD model parameters is close to the cytotoxic agent given in Table IV. For a patient of average weight $m = 60\,\text{kg}$ a maximum dose of 120 mg has to be conveyed per session (cf. Fig. 6). Therefore, a maximum of $N_b = 1036$ magnetic boluses have to be administered.

D. Radioisotope (Yttrium)

The radiotherapy consists to administrate microspheres containing a radioisotope. Usually, yttrium-90 (^{90}Y) microspheres are administered in directed cancer radiotherapy [4]. ^{90}Y is a high-energy beta-emitting isotope with no primary gamma emission and a half-life of 2.67 days. For instance, TheraSphere (MDS Nordion, Canada) are biocompatible and nonabsorbable glass microspheres loaded with ^{90}Y. The radius of TheraSphere beads is about $r_p = 12.5 \pm 2.5\mu\text{m}$, and then one magnetic bolus could embed up to 3147 radioisotope microspheres. Each ^{90}Y bead contains an activity of 2500 Bq, leading to 7.8675×10^{-3} GBq per bolus. Assuming an uniform distribution, the radiation dose intake is computed from [4] $u = \dfrac{49.67A}{m_l}$ with A the radioisotope activity (in GBq), and m_l the mass of the liver (in kg). Therefore, the number of magnetic boluses that carries ^{90}Y beads is obtained from:

$$N_b = \left\lceil \frac{u \cdot m_l}{49.67 \times 3147 \times 2.5 \times 10^{-6}} \right\rceil \tag{33}$$

We consider that the radioisotope tumor-LQ model parameters given in Table V corresponds to TheraSphere. For a typical patient with a liver mass of $m_l = 2\,\text{kg}$, a maximum of $N_b = 52$ boluses have to be administered in one session to carry the upper limit of 10 Gy (cf. Fig. 7).

V. DISCUSSION

Locoregional therapies are considered as the best treatments in patients with unresectable hepatocellular carcinoma (HCC). The various mathematical models of cancer therapies for HCC that have been evaluated so far describe some interactions between tumor cells and blood vessels. However, the internal cell behavior is not explicitly expressed, whereas further sources of complexity arise from its internal cell-to-cell cooperative and competitive interactions [17]. Especially, due to the use of ODE system the model also does not include the spatial characteristic of the tumor growth along the surrounding tissue. Particularly, this work considers medically reasonable parameters set given in Table I-to-V taken from the literature. Actually, only few data are available to estimate the parameter sets, especially in the case of human models [16], [17], [22]. Mathematically modeling the dynamics of a tumor allows us to better understand tumor activity by considering critical biological influences, time delays, human intervention and tumor adaptation. Our model parameters are computed on the basis of experimental data given in [15]. The environmental factors such as habits, smoking, alcohol consumption, and infections, have a profound influence on cancer development. As example, it is possible to regulate the nuclear transcription factor, NF-kB, by controlling the vascular endothelial cells birth rate, b, expressed in the model [33]. Furthermore, the control of the drug input u offers the possibility to model the drug overdose and/or toxicity.

In the proposed direct targeting therapy, the drug input is saturated to u_{max} values which should be related to the upper bound of the drug concentration u_{max}. For instance, the most commonly used dosage of doxorubicin is to not exceed δ_{max} = 2 mg/kg to have a very low risk of overdose. Finally, the theoretical simulation results point out some benefits when considering MRN-assisted locoregional therapy. At an earlier-stage disease, TACE and TARE treatments are commonly used. Actual TACE treatments with doxorubicin at baseline (cTACE) or doxorubicin-loaded eluting beads (DEB-TACE) deliver a high dose of drug over a longer period of time (3 months) into the tumor. The schedule of treatment is settled to 3 months, 6 months, and then every 6 months thereafter. The size of DEB is chosen according to the particular study, usually with smaller particles (100-to-300 μm) being selected first, followed by larger particles (500-to-700 μm). When performing MRN-assisted procedure using embolic magnetic boluses releasing doxorubicin, similar benefits (drug rate and frequency of treatment) are found but the technique may prevent bile duct injury by avoiding overembolization that will relentlessly lead to nontarget embolization. In the case of embolic radioembolization in TARE treatment, glass or resine microspheres of 20-to-30 μm in size are used. A high number of aggregated spheres (glass: 1.2 million microspheres/3 GBq; resin: 40-to-60 millions of microspheres/3 GBq) are required leading to deposition in the liver as a large number of discrete clusters. The use of MRN could significantly improve the technique by reducing the number and the timeless of sequences, and most importantly, by providing heterogeneous radiation dose distribution patterns. At an advanced-stage disease, Sorafenib, a multikinase inhibitor with antiangiogenic properties of Sorafenib, in combination with locoregional therapy if of increased interest to specialists who care for patients with unresectable hepatocellular carcinoma [18]. To demonstrate the feasibility of MRN-assisted procedure, Bigot *et al.* [12] have demonstrated that the propulsion of $N_b = 1530$ magnetic boluses inside a multi-bifurcation phantom required 33 min of duration. These experiments are in agreement with our simulation results concerning TACE and TARE treatments since only 1036 and 52 magnetic boluses are required.

VI. Conclusion

The paper described an optimal design strategy for innovative transcatheter arterial magnetic bolus delivery using MRN procedure. To maximize the effect of the treatment and minimize adverse effects on the patient, a mathematical model has been developed to find the number of magnetic boluses with respect to the growth of a tumor and the carried therapeutic agent. The application of such mathematical design framework is the optimization of anti-cancer treatment modalities by its optimal use with locoregional tumor therapies. Indeed, the preliminary results demonstrate that MRN may improve the conventional TACE and TARE treatments by increasing the local drug concentration, reducing the number and duration of treatment sequences, and decreasing the side-effects related to toxicity in healthy tissues. Undergoing work considers the locoregional magnetic bolus delivery of various sizes of aggregates in small animals.

References

[1] R. L. Siegel, K. D. Miller, and A. Jemal, "Cancer statistics, 2015," *CA: a cancer journal for clinicians*, vol. 65, no. 1, pp. 5–29, 2015.

[2] J. M. Llovet, M. I. Real, X. Montaa, R. Planas, S. Coll, J. Aponte, C. Ayuso, M. Sala, J. Muchart, R. Sol, J. Rods, and J. Bruix, "Arterial embolisation or chemoembolisation versus symptomatic treatment in patients with unresectable hepatocellular carcinoma: a randomised controlled trial," *The Lancet*, vol. 359, no. 9319, pp. 1734–1739, 2002.

[3] A. Forner, J. M. Llovet, and J. Bruix, "Hepatocellular carcinoma," *The Lancet*, vol. 379, no. 9822, pp. 1245–1255, 2012.

[4] A. Kennedy, S. Nag, R. Salem, R. Murthy, A. J. McEwan, C. Nutting, A. Benson III, J. Espat, J. I. Bilbao, R. A. Sharma *et al.*, "Recommendations for radioembolization of hepatic malignancies using yttrium-90 microsphere brachytherapy: a consensus panel report from the radioembolization brachytherapy oncology consortium," *International Journal of Radiation Oncology* Biology* Physics*, vol. 68, no. 1, pp. 13–23, 2007.

[5] A. L. Lewis, M. V. Gonzalez, A. W. Lloyd, B. Hall, Y. Tang, S. L. Willis, S. W. Leppard, L. C. Wolfenden, R. R. Palmer, and P. W. Stratford, "DC bead: in vitro characterization of a drug-delivery device for transarterial chemoembolization," *Journal of vascular and interventional radiology*, vol. 17, no. 2, pp. 335–342, 2006.

[6] M. Varela, M. I. Real, M. Burrel, A. Forner, M. Sala, M. Brunet, C. Ayuso, L. Castells, X. Montañá, J. M. Llovet *et al.*, "Chemoembolization of hepatocellular carcinoma with drug eluting beads: efficacy and doxorubicin pharmacokinetics," *Journal of hepatology*, vol. 46, no. 3, pp. 474–481, 2007.

[7] T. Matsumoto, J. Endo, K. Hashida, H. Ichikawa, S. Kojima, S. Takashimizu, N. Watanabe, T. Yamagami, and T. Hasabe, "Balloon-occluded transarterial chemoembolization using a 1.8-french coaxial microballoon catheter for hcc: Tehnical and safety considerations," *Minimally Invasive Therapy Allied Technologies*, vol. 24, no. 2, pp. 94–100, 2015.

[8] R. Salem and K. Thurston, "Radioembolization with 90yttrium microspheres: A state-of-the-art brachyterapy treatment for primary and secondary liver malignancies- part 1: Technical and methodologic considerations," *Journal of Vascular Interventional Radiology*, vol. 17, pp. 1251–1278, 2006.

[9] U. Hafeli, S. Sweeney, B. Beresford, J. Humm, and R. Macklis, "Effective targeting of magnetic radioactive y-microspheres to tumor cells by an externally applied magnetic field. preliminary in-vitro and in-vivo resuls," *Nuclear Medecina and Biology*, vol. 22, no. 2, pp. 147–155, 1995.

[10] J.-B. Mathieu, G. Beaudoin, and S. Martel, "Method of propulsion of a ferromagnetic core in the cardiovascular system through magnetic gradients generated by an MRI system," *IEEE Trans. Biomed. Eng.*, vol. 53, no. 2, pp. 292–299, 2006.

[11] P. Pouponneau, J.-C. Leroux, G. Soulez, L. Gaboury, and S. Martel, "Co-encapsulation of magnetic nanoparticles and doxorubicin into biodegradable microcarriers for deep tissue targeting by vascular MRI navigation," *Biomaterials*, vol. 32, no. 13, pp. 3481–3486, 2011.

[12] A. Bigot, C. Tremblay, G. Soulez, and S. Martel, "Magnetic resonance navigation of a bead inside a three-bifurcation pmma phantom using an imaging gradient coil insert," *navigation (MRN)*, vol. 5, p. 7, 2014.

[13] L. Mellal, K. Belharet, D. Folio, and A. Ferreira, "Optimal structure of particles-based superparamagnetic microrobots: application to mri guided targeted drug therapy," *Journal of Nanoparticle Research*, vol. 17, no. 2, pp. 1–18, 2015.

[14] B. Ribba, N. Holford, P. Magni, I. Trocóniz, I. Gueorguieva, P. Girard, C. Sarr, M. Elishmereni, C. Kloft, and L. Friberg, "A review of mixed-effects models of tumor growth and effects of anticancer drug treatment used in population analysis," *CPT: pharmacometrics & systems pharmacology*, vol. 3, no. 5, p. e113, 2014.

[15] P. Hahnfeldt, D. Panigrahy, J. Folkman, and L. Hlatky, "Tumor development under angiogenic signaling a dynamical theory of tumor growth, treatment response, and postvascular dormancy," *Cancer research*, vol. 59, no. 19, pp. 4770–4775, 1999.

[16] A. d'Onofrio and A. Gandolfi, "Tumour eradication by antiangiogenic therapy: analysis and extensions of the model by hahnfeldt *et al.* (1999)," *Mathematical biosciences*, vol. 191, no. 2, pp. 159–184, 2004.

[17] A. Ergun, K. Camphausen, and L. M. Wein, "Optimal scheduling of radiotherapy and angiogenic inhibitors," *Bulletin of mathematical biology*, vol. 65, no. 3, pp. 407–424, 2003.

[18] U. Ledzewicz, A. dOnofrio, and H. Schttler, "Tumor development under combination treatments with anti-angiogenic therapies," in *Mathematical*

Methods and Models in Biomedicine, ser. Lecture Notes on Mathematical Modelling in the Life Sciences, U. Ledzewicz, H. Schttler, A. Friedman, and E. Kashdan, Eds. Springer New York, 2013, pp. 311–337.

[19] A. d'Onofrio, U. Ledzewicz, H. Maurer, and H. Schättler, "On optimal delivery of combination therapy for tumors," *Mathematical biosciences*, vol. 222, no. 1, pp. 13–26, 2009.

[20] S. Sanga, J. P. Sinek, H. B. Frieboes, M. Ferrari, J. P. Fruehauf, and V. Cristini, "Mathematical modeling of cancer progression and response to chemotherapy," *Expert Review of Anticancer Therapy*, vol. 6, no. 10, pp. 1361–1376, 2006.

[21] L. G. de Pillis, W. Gu, K. R. Fister, T. a. Head, K. Maples, A. Murugan, T. Neal, and K. Yoshida, "Chemotherapy for tumors: An analysis of the dynamics and a study of quadratic and linear optimal controls," *Mathematical Biosciences*, vol. 209, no. 1, pp. 292–315, 2007.

[22] L. G. De Pillis and A. Radunskaya, "The dynamics of an optimally controlled tumor model: A case study," *Mathematical and Computer Modelling*, vol. 37, no. 11, pp. 1221–1244, 2003.

[23] L. Kovács, A. Szeles, J. Sápi, D. A. Drexler, I. Rudas, I. Harmati, and Z. Sápi, "Model-based angiogenic inhibition of tumor growth using modern robust control method," *Computer methods and programs in biomedicine*, vol. 114, no. 3, pp. e98–e110, 2014.

[24] A. Kansal, S. Torquato, G. Harsh, E. Chiocca, and T. Deisboeck, "Simulated brain tumor growth dynamics using a three-dimensional cellular automaton," *Journal of theoretical biology*, vol. 203, no. 4, pp. 367–382, 2000.

[25] P. Gerlee and A. R. Anderson, "An evolutionary hybrid cellular automaton model of solid tumour growth," *Journal of theoretical biology*, vol. 246, no. 4, pp. 583–603, 2007.

[26] J. F. Fowler, "The linear-quadratic formula and progress in fractionated radiotherapy," *The British journal of radiology*, vol. 62, no. 740, pp. 679–694, 1989.

[27] G. W. Swan, "Role of optimal control theory in cancer chemotherapy," *Mathematical biosciences*, vol. 101, no. 2, pp. 237–284, 1990.

[28] Y. Batmani and H. Khaloozadeh, "Optimal chemotherapy in cancer treatment: state dependent riccati equation control and extended kalman filter," *Optimal Control Applications and Methods*, vol. 34, no. 5, pp. 562–577, 2013.

[29] K. Zhou, J. C. Doyle, K. Glover *et al.*, *Robust and optimal control*. Prentice Hall New Jersey, 1996, vol. 40.

[30] C. P. Mracek and J. R. Cloutier, "Control designs for the nonlinear benchmark problem via the state-dependent riccati equation method," *International Journal of robust and nonlinear control*, vol. 8, no. 4-5, pp. 401–433, 1998.

[31] T. Çimen, "Systematic and effective design of nonlinear feedback controllers via the state-dependent riccati equation (sdre) method," *Annual Reviews in Control*, vol. 34, no. 1, pp. 32–51, 2010.

[32] S.-U. Shin, H.-M. Cho, J. Merchan, J. Zhang, K. Kovacs, Y. Jing, S. Ramakrishnan, and J. D. Rosenblatt, "Targeted delivery of an antibody–mutant human endostatin fusion protein results in enhanced antitumor efficacy," *Molecular cancer therapeutics*, vol. 10, no. 4, pp. 603–614, 2011.

[33] P. Anand, A. B. Kunnumakara, C. Sundaram, K. B. Harikumar, S. T. Tharakan, O. S. Lai, and B. B. Aggarwal, "Cancer is a preventable disease that requires major lifestyle changes," *Pharmaceutical research*, vol. 25, no. 9, pp. 2097–2116, 2008.

Appendix E

Mathematical Approach for the Design Configuration of Magnetic System with Multiple Electromagnets (ACL15)

Mathematical approach for the design configuration of magnetic system with multiple electromagnets

Ruipeng Chen, David Folio, Antoine Ferreira*

INSA Centre Val de Loire, Université d'Orléans, PRISME EA 4229, Bourges, France

Abstract

Magnetic actuation techniques and microrobots have attracted great interest since they have potential in biomedicine applications. Interventional techniques have emerged as a tool to handle a wide range of minimally invasive surgeries (MIS). However, current MIS procedures are constrained by the limitation of manual operation by surgeon. Thus, various microrobotic solutions including magnetic navigation systems have been proposed for MIS, which carries many potential benefits such as reduced incision, less intraoperative hemorrhaging and postoperative pain, and faster recovery time. In recent decades, many electromagnetic actuation (EMA) systems have been reported and involved to general surgery. The EMA system allows to generate efficiently magnetic source for microrobot control when its specifications are further investigated and satisfied for the desired application. To precisely manipulate the biomedical microrobot, a key issue still relies on the design of a suitable EMA platform. In this paper, we demonstrate a mathematical approach for the design configuration of magnetic system with multiple electromagnets. Especially, the required magnetic coil number has been investigated where the heading motion control, magnetic force control and their combination control are discussed respectively. The singular cases of control are pre-evaluated by a mathematical analysis of the simulated electromagnetic field. In addition, the placed positions and tilted orientations of the applied electromagnets are investigated for the optimization regarding the six typical configurations of EMA platform with 4, 6 and 8 coils. The various configurations of EMA systems have been comprehensively analyzed. Therefore, with the number of electromagnets and their optimal configuration obtained by the proposed approach, the EMA system can be initially established.

Keywords: Electromagnetic actuation system, Magnetic microrobot, Design methodology, Robotic magnetic platform

1. Introduction

Minimally invasive surgery (MIS) encompasses surgical techniques that limit the size of incisions needed and so lessen wound healing time, associated pain and risk of infection. MIS procedures have been enabled by the advance of various medical technologies. In particular, several surgical robotics systems have been developed. Such robotic platforms already play a significant role to improve patient care, though it increases surgical preparation, cost and risk of the MIS approach compared with traditional open surgery[1, 2, 3, 4, 5, 6, 7, 8, 9, 10, 11]. For example, there are the well-known da Vinci surgical assistance robots[5, 7], developed by Intuitive Surgical1, which improves the surgeon technical skills. Moreover, unlike the dependence on using rigid instruments with dexterous distal wrists, it is commonly more attractive to use flexible or adaptive robotic tools that access internal anatomy with few skin incisions[10, 12, 13, 14, 15, 16, 17]. Especially, the mechanical parts of existing medical robotic devices are still relatively large and rigid to access and treat major inaccessible parts of the human body (e.g. in robot-assisted surgery). In parallel, the various medical robotics solutions have been developed to improve the acceptance of the use of robotics systems in clinical practices. In the meanwhile, mi-

*Corresponding author

Email addresses: david.folioinsa-cvl.fr (David Folio), antoine.ferreira@insa-cvl.fr (Antoine Ferreira)

crorobotics has also emerged as an attractive technology to introduce novel microsystems to further reduce trauma, create new diagnosis tools and therapeutic procedures.

Indeed, designing miniaturized and versatile microrobotic systems would allow accessing throughout the whole human body; leading to new procedures down to the cellular level; and offering localized diagnosis and treatment with greater precision and efficiency. For example, untethered microscopic devices, smaller than one millimeter, may navigate within the body for targeted therapies[18, 19, 20, 21]. Among the various actuation of microrobots, magnetic actuation is considered to be the most promising method[9, 18, 22, 23, 24, 25, 26, 27, 28, 29, 30, 31, 32, 33, 34]. To this aim, numerous electromagnetic actuation (EMA) systems have been proposed to control untethered magnetic microrobots for biomedical applications[18, 35, 36, 37, 38, 39, 40, 41, 42, 43, 44, 45, 46, 47]. The development of magnetic microrobotic systems circumvents the need to embed power within the microdevice[18, 19, 20]. Magnetic microrobot can be then remotely powered and actuated precisely by the use of external electromagnetic fields. This enables untethered microrobots to assist the surgeon to increase precision and dexterity of the MIS procedure[10, 18, 34, 42].

The paper aims to propose a mathematical approach for the design configuration of magnetic system using multiple electromagnets, that improves MIS procedures since the magnetic manipulation of microrobots is one of the most interesting method to assist researchers in many biomedical applications. To address this issue of designing a proper EMA system for a given application, the investigation of the appropriate design configuration carried out. The paper is then organized as follows. Section 2 presents the theoretical foundation of electromagnetism including the basic principles and necessary equations. From this basis, the electromagnetic manipulation of untethered microrobot with the magnetic torque and force control is discussed, and the necessary metrics are defined. In Section 3, the analysis of the minimum number of electromagnets for an EMA platform is investigated. In particular, singular cases are pointed out when magnetic field and gradient exhibit some linear dependencies. In Section 4, six typical configurations are simulated and evaluated for the efficient motion control of microrobot. The configuration of EMA system is optimized with respect to the considered magnetic

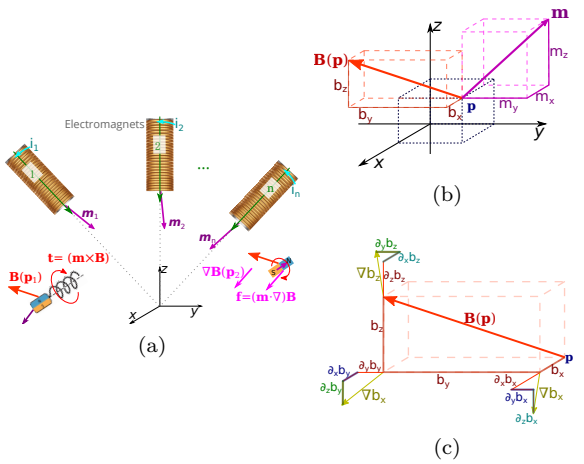

Figure 1: Electromagnetic manipulation: (a) illustration of the use of the magnetic force and torque on untethered magnetic microrobots; (b) composition of the magnetic field with the magnetic moment of the microrobot; and (c) the different components of the magnetic gradient.

control objectives. In Section 5, the comparison of configurations is performed when the magnetic performances are summarized regarding the arrangement parameters of magnetic system. The paper is concluded with the Section 6.

2. Theoretical foundation

The aim of this section is to recall the basic principles of electromagnetism that serve as a foundation of our research works.

2.1. Electromagnetic Manipulation

Starting from the Maxwell's equations, and assuming that charges are either fixed or move as a steady current J, the governing equation of a *quasi-static magnetic field* can be described by the two following relations [48]:

$$\nabla \cdot B = 0 \tag{1}$$

$$\nabla \times B = \mu_0 J \tag{2}$$

Next, assuming that the microrobot is a magnetized body described by its magnetic dipole moment M, that is placed in a magnetic flux B, the induced magnetic force and torque are basically expressed from [49]:

$$\mathbf{f} = (M \cdot \nabla)\, B \tag{3}$$

$$\mathbf{t} = (M \times B) \tag{4}$$

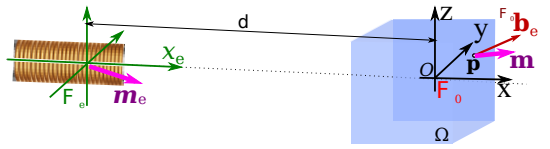

Figure 2: Schematic representation of a single electromagnet inducing a magnetic flux $B_e(P)$ within the workspace Ω (blue square box).

Obviously, $\mathbf{f}$ is related to the magnetic gradient ∇B, whereas the magnetic torque $\mathbf{t}$ is a function of the magnetic field B. Moreover, to actuate the microrobot, the magnetic field must undergo either a spatial change (i.e. exhibit a spatial field gradient), or a temporal change, such as through a rotating magnetic field, oscillation and so on. Fig. 1 illustrates these basic principles. Specifically, the magnetic field and its gradient are generated by a set of n electromagnets to control the motion of untethered microrobots. The orientation of microrobot tends to be aligned with the direction of magnetic field B, thus the microrobots are rotated by the magnetic torque $\mathbf{t}$. Moreover, the magnetic gradient ∇B induces the magnetic force $\mathbf{f}$ as propulsion force to move the microrobot. Hence, the magnetic object can be manipulated through the rotation and translation operations using magnetic field and gradient, respectively.

Secondly, if we assume there is no electric current flowing through the workspace occupied by the microrobot, Maxwell's equation implies that equation (2) becomes $\nabla \times B = 0$. The magnetic force (3) can be then rearranged using vector calculus into the following form:

$$\mathbf{f} = \begin{pmatrix} \frac{\partial B}{\partial x} \\ \frac{\partial B}{\partial y} \\ \frac{\partial B}{\partial z} \end{pmatrix} M = \begin{pmatrix} \frac{\partial b_x}{\partial x} & \frac{\partial b_y}{\partial x} & \frac{\partial b_z}{\partial x} \\ \frac{\partial b_x}{\partial y} & \frac{\partial b_y}{\partial y} & \frac{\partial b_z}{\partial y} \\ \frac{\partial b_x}{\partial z} & \frac{\partial b_y}{\partial z} & \frac{\partial b_z}{\partial z} \end{pmatrix} M = \mathbf{G}M \tag{5}$$

where $\mathbf{G} \in \mathbb{R}^{3\times 3}$ denotes the gradient matrix of the magnetic field $B = (b_x, b_y, b_z)$. Besides, the subscripts x, y and z explicitly refer to the basis directions of the Cartesian reference frame $\mathcal{F}_0(O : x, y, z)$ linked to the workspace Ω, in which all vectors are expressed (see Fig. 2).

The torque on microrobot tends to align the magnetization vector with the magnetic field. To represent vector cross products, the skew-symmetric matrix formed of a vector can be employed, that is:

$$\mathrm{Sk}(M) = \mathrm{Sk}\begin{pmatrix} m_x \\ m_y \\ m_z \end{pmatrix} = \begin{pmatrix} 0 & -m_z & m_y \\ m_z & 0 & -m_x \\ -m_y & m_x & 0 \end{pmatrix} \tag{6}$$

Therefore, the force (3) and torque (4) applied to magnetic microrobots can be rewritten as:

$$\begin{pmatrix} \mathbf{f} \\ \mathbf{t} \end{pmatrix} = \begin{pmatrix} (M \cdot \nabla) \\ \mathrm{Sk}(M) \end{pmatrix} B \tag{7}$$

2.2. Electromagnetic control

For multiple-coil configuration, the magnetic field is induced by an EMA system consisting of several electromagnets. Hence, with a given set of n electromagnets, each of them creates a magnetic field, $B_e(P)$, at any location of the workspace: $\forall P \in \Omega$. The magnetic fields and their spatial gradients depend linearly on the currents. When i_e flows through the coils e, the magnetic field can be expressed as: $B_e(P) = \widetilde{B}_e(P) i_e$. The superposition principle is commonly used to compute the overall magnetic field, that is:

$$\begin{aligned} B(P) &= \sum_{e=1}^{n} \widetilde{B}_e(P) i_e = \begin{pmatrix} \widetilde{b}_{x1} & \dots & \widetilde{b}_{xe} & \dots & \widetilde{b}_{xn} \\ \widetilde{b}_{y1} & \dots & \widetilde{b}_{ye} & \dots & \widetilde{b}_{yn} \\ \widetilde{b}_{z1} & \dots & \widetilde{b}_{ze} & \dots & \widetilde{b}_{zn} \end{pmatrix} \mathbf{i} \\ &= \begin{pmatrix} \mathcal{B}_x(P) \\ \mathcal{B}_y(P) \\ \mathcal{B}_z(P) \end{pmatrix} \mathbf{i} = \mathcal{B}(P)\mathbf{i} \end{aligned} \tag{8}$$

where $\mathbf{i} = (i_1 \dots i_n)^\intercal$ is the current vector, and $\mathcal{B}(P)$ is a $3 \times n$ matrix mapping the currents to the magnetic fields. Similarly, the magnetic gradient fields could be expressed as:

$$\frac{\partial B(P)}{\partial x} = \sum_{e=1}^{n} \frac{\partial \widetilde{B}_e(P)}{\partial x} i_e = \mathcal{G}_x(P)\mathbf{i} \tag{9}$$

$$\frac{\partial B(P)}{\partial y} = \sum_{e=1}^{n} \frac{\partial \widetilde{B}_e(P)}{\partial y} i_e = \mathcal{G}_y(P)\mathbf{i} \tag{10}$$

$$\frac{\partial B(P)}{\partial z} = \sum_{e=1}^{n} \frac{\partial \widetilde{B}_e(P)}{\partial z} i_e = \mathcal{G}_z(P)\mathbf{i} \tag{11}$$

where each $\mathcal{G}_{x,y,z}(P)$ is $3 \times n$ matrix mapping the current to the magnetic gradient field in the x, y, and z directions, respectively.

The different mapping matrices $\mathcal{B}(P)$ and $\mathcal{G}_{x,y,z}(P)$ expressions are related to the type and

geometry of each electromagnet (e.g. length, radius, numbers of turns). For instance, the mapping for Helmholtz or Maxwell coils could be easily carried out from the Biot-Savart's law. For the other types of electromagnets, especially with a magnetic core, the mapping matrices can be calculated either from measures of the magnetic field within the EMA system's workspace or from the simulations of magnetic field using FEM models [43].

Finally, the equations of magnetic force and torque can be rearranged as follows:

$$\begin{aligned}\begin{pmatrix}\mathbf{t}\\ \mathbf{f}\end{pmatrix} &= \begin{pmatrix}\mathrm{Sk}(M)\mathcal{B}\\ M^{\intercal}\mathcal{G}_x(P)\\ M^{\intercal}\mathcal{G}_y(P)\\ M^{\intercal}\mathcal{G}_z(P)\end{pmatrix}\mathbf{i} = \begin{pmatrix}\mathcal{A}_t(M,P)\\ \\ \mathcal{A}_f(M,P)\end{pmatrix}\mathbf{i} \\ &= \mathcal{A}(M,P)\mathbf{i}\end{aligned} \tag{12}$$

where $\mathcal{A}_t(M,P)$ and $\mathcal{A}_f(M,P)$ are the actuation matrices mapping the current vector $\mathbf{i}$ to the torque and force, respectively; and $\mathcal{A}(M,P)$ is the $6 \times n$ actuation matrix mapping to the applied magnetic wrench. These magnetic actuation matrices depend both on the position $P \in \Omega$, and on the orientation of the dipole moment M of the microrobot.

According to equations (3)-(4), each column of the matrix $\mathcal{A}(M,P)$ represents the wrench on the force and torque per current unit created by each electromagnet. If there are greater than $n > 6$ electromagnets, the actuation matrix $\mathcal{A}(M,P)$ leads to a better conditioned matrix, a more isotropic workspace Ω, a reduction of singularity configurations, and lower current requirements [50, 51]. In such cases, $n > 6$, the EMA system could be said "redundant" for the task. Especially, if $\mathcal{A}(M,P)$ is of full rank, for a desired force, $\mathbf{f}^\star$ and torque, $\mathbf{t}^\star$, the actuation currents $\mathbf{i}$ can be calculated from the pseudo-inverse:

$$\mathbf{i} = \mathcal{A}^{+}(M,P)\begin{pmatrix}\mathbf{t}^\star\\ \mathbf{f}^\star\end{pmatrix} \tag{13}$$

If $n < 6$, the pseudo-inverse would be a least-squares approximations. Hence, for a controlled force and torque, the input current can be obtained only if the pseudo-inverse of $\mathcal{A}(M,P)$ exists. This derivation on the controlled current $\mathbf{i}$ can be similarly extended for controllers that require torque and/or force control [52].

2.3. Indexes for Electromagnetic System

To be able to compare such various electromagnetic coils dispositions, it is necessary to define some metrics to get some quantitative assessments of their effectiveness. The basic idea is to set a *score* to a given EMA configuration to allow an effective comparative analysis. Indeed, with respect to the applications objectives, different indexes can be defined and considered.

2.3.1. Magnetic Field Indexes

First, the strength and homogeneity of either the magnetic field or its gradient in the workspace are the most significant metrics for medical applications. As example, a strong magnetic field strength leads to powerful torque $\mathbf{t}$ enabling reliable swimming of the helical microrobot. In the meantime, it should be homogeneous along the workspace to simplify the control strategy. Furthermore, the EMA system needs to avoid unexpected magnetic force when varying the orientation of microrobot along with the magnetic field. Similarly, a strong magnetic gradient provides an effective propulsion force $\mathbf{f}$, and its uniformity implies a homogeneous net force on microrobots. To this aim, various indexes can be used from statistical analysis of the fields distributions, such as its maximum, mean, RMS, STD, etc. To evaluate the quality of a magnetic field or its gradient, we have chosen to consider mainly the average and the uniformity indexes introduced hereafter.

Average index. In [40], the authors propose to characterize the strength of a sampled vector field φ by its average (i.e. the arithmetic mean) basically defined as:

$$\langle\varphi\rangle = \frac{1}{N}\sum_{P\in\Omega}^{N}\varphi(P) \tag{14}$$

with N the number of samples, and P the sampling location in the workspace Ω. This arithmetic mean value reflects the *strength* of a global vector field φ. It can be utilized to quantify the average of the magnitudes of a magnetic field or its gradient from the corresponding samples, and then to evaluate the strength of the torque or force in the workspace.

Uniformity index. The isotropy index measures and yields an intuitive value for the difference between each considered vector of a vector field φ distribution. To evaluate the isotropy, various indexes can be considered, such as the basic minimum-to-maximum ratio, or the coefficient of variation. For a vector field φ, the *uniformity index* γ is usually

considered, which is defined as:

$$\gamma(\varphi) = 1 - \frac{1}{2N\langle\varphi\rangle} \sum_{P\in\Omega}^{N} |\varphi(P) - \langle\varphi\rangle| \qquad \text{(in \%)} \tag{15}$$

where the isotropy index γ should be commonly bounded between 0% and 100%. Then, a uniformity index close to 100% indicates that every sample of the field φ is almost identical.

2.3.2. Magnetic Actuation Indexes

In the other hand, the EMA system has to actuate a magnetic microrobot in the workspace. Hence, the ability to perform or not certain motion at any location and direction is of prime importance. Basically, if there are some singularities, some motions cannot be achieved, and the DOFs of the microrobot is reduced. For an EMA system, this analysis can be performed through the examination of its magnetic actuation matrix $\mathcal{A}(M, P)$. As described in (12), $\mathcal{A}(M, P)$ allows mapping the input currents $\mathbf{i}$ to the magnetic torque and force that are applied to a microrobot possessing a magnetic moment M at the location $P \in \Omega$. Hence, the actuation matrix $\mathcal{A}(M, P)$ can be seen as a *Jacobian matrix*. Commonly, the Jacobian matrix of a system is used to characterize the control efficiency. Here, the columns of the actuation matrix $\mathcal{A}(M, P)$ represents the wrench on the magnetic microrobot. As long as $\mathcal{A}(M, P)$ is singularity-free or merely well-conditioned, the direct mapping will exist and full wrench control of the microrobot can be achieved in the workspace. Thus, the structure of $\mathcal{A}(M, P)$ has to be analyzed to determine the "wrench-kinematic" performance of the EMA system. Therefore, the magnetic actuation matrix provides a similar information as a classic Jacobian matrix in robotics.

There are numerous studies on the kinematic performance indexes of robotic mechanisms [53, 54, 55, 56]. Most of proposed metrics were derived from the definition of *manipulability index*, introduced by [54].

Manipulability index. From classic robotic kinematics, measuring the manipulability is a well-known technique for determining the ability to maneuver in workspace. Specifically, manipulability describes the degree to which a robot can freely apply forces and torques in arbitrary directions, and quantifies the ability to perform an action quickly and skillfully [54]. To do so, the manipulability index is defined as a quality measure describing the distance to singular configurations. The approach is based on analyzing the *manipulability ellipsoid* that is spanned by the singular vectors of the Jacobian. Similarly, we investigate the mapping efficiency between the current input $\mathbf{i}$ to the torque and force with this standard manipulability ellipsoid. Fig. 3 illustrates the manipulability ellipsoid, here in 2D, where the minor axis σ_2 represents the direction with the worse kinematic capacity, whereas the major axis σ_1 gives the easiest direction of force/torque transmission. Specifically, from the manipulability ellipsoid, the product of the ellipsoid's axes leads to the manipulability index which gives a measure of the maneuverability of the EMA system, and it is defined as [54]:

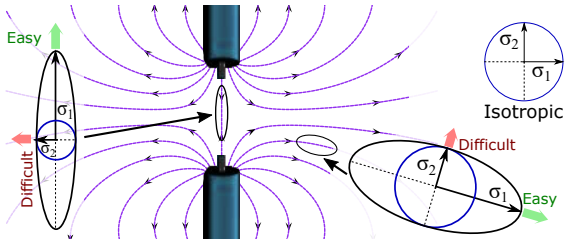

Figure 3: 2D illustration of the manipulability ellipsoid: microrobots have better kinematic capacity in the direction of the major axis σ_1 of the ellipsoid, whereas the minor axis σ_2 induces worse kinematic performance.

$$w(\mathcal{A}) = \sqrt{\det(\mathcal{A}\mathcal{A}^{\intercal})} \tag{16}$$

Commonly, the manipulability ellipsoids can be computed from SVD factorization. Let the SVD of a matrix $\mathcal{A}$ be:

$$\mathcal{A} = \mathbf{U}\Sigma\mathbf{V}^{\intercal} \tag{17}$$

where the $\mathbf{U}$ and $\mathbf{V}$ are orthogonal matrices, with $\mathbf{U}$ a 6×6 unitary matrix and $\mathbf{V}$ a $n \times n$ unitary matrix. In our considered system, Σ is a $6 \times n$ singular value matrix given as follows:

$$\Sigma = \begin{pmatrix} \sigma_1 & 0 & 0 & 0 & 0 & 0 & 0 & \cdots & 0 \\ 0 & \sigma_2 & 0 & 0 & 0 & 0 & 0 & \cdots & 0 \\ 0 & 0 & \sigma_3 & 0 & 0 & 0 & 0 & \cdots & 0 \\ 0 & 0 & 0 & \sigma_4 & 0 & 0 & 0 & \cdots & 0 \\ 0 & 0 & 0 & 0 & \sigma_5 & 0 & 0 & \cdots & 0 \\ 0 & 0 & 0 & 0 & 0 & \sigma_6 & 0 & \cdots & 0 \end{pmatrix} \tag{18}$$

where $\sigma_1 \geq \sigma_2 \geq \ldots \geq \sigma_6 \geq 0$ are the singular values of $\mathcal{A}$. The singular values are significant indexes for the evaluation of system and that can be

considered as a scalar gain by which each input is multiplied to produce the corresponding output.

Since the singular values give information about the quality of the workspace [54], the product of all singular values can be used to analyze the control capability of points or configurations in certain directions. Thereby, the measure of manipulability index w can be expressed as the product of the singular values:

$$w(\mathcal{A}) = \prod_{e=1}^{n} \sigma_e \tag{19}$$

It can be noticed that w is proportional to the volume of the manipulability ellipsoid. Generally, a larger measure of w indicates a better conditioning of the actuation matrix $\mathcal{A}(M, P)$, that means an effective control of the microrobot. Hence, the manipulability index w measures the "distance" from singularities, that represents the capability of the EMA system to control efficiently the magnetic microrobot.

Finally, as the above manipulability index (16) depends on the scale or units, the normalized manipulability can be preferred:

$$w_n = \frac{w(\mathcal{A}(M,P))}{\max\limits_{P\in\Omega} w(\mathcal{A}(M,P))} \tag{20}$$

Condition number. Another way to characterize the manipulability ellipsoid is to measure its isotropy. This is commonly achieved by computing the condition number of a matrix, which is defined as:

$$\kappa(\mathcal{A}) = \|\mathcal{A}\|\|\mathcal{A}^{\dagger}\| \in [1; +\infty) \tag{21}$$

where $\mathcal{A}^{\dagger}$ is the Moore-Penrose pseudo-inverse of $\mathcal{A}$, and $\|.\|$ denotes the Euclidean (or Frobenius) norm defined as:

$$\|\mathcal{A}\| = \sqrt{\mathrm{tr}\left(\mathcal{A}\mathbf{W}\mathcal{A}^{\intercal}\right)} \tag{22}$$

with $\mathbf{W}$ a weighting matrix, and especially, $\mathbf{W} = \mathbb{I}$ for the Euclidean norm.

To evaluate the control accuracy and isotropy of system, the inverse of the condition number of a matrix, also termed as *isotropic index*, was introduced by [53], and is defined as:

$$1/\kappa = \frac{\sigma_{\min}}{\sigma_{\max}} = \frac{\sigma_6}{\sigma_1} \in [0; 1] \tag{23}$$

The isotropic index indicates how well the microrobot can move in all directions, and characterizes in some sense the *dexterity* of the microrobot [56]. Therefore, when $1/\kappa\left(\mathcal{A}(M,P)\right)$ is close to 1, its manipulability ellipsoid is more close to be a sphere, which means the EMA system has more capacity to transmit the same force or torque in all directions (see also Fig. 3).

Let us notice that the previous indexes are only local metrics for a dedicated location $P \in \Omega$. To evaluate the system efficiency over the workspace Ω, many global performance indexes have been proposed [55, 56]. Classically, to define such global performance indexes, the integral of a local performance index ξ over a domain $\mathcal{W}$ is considered given by (24) or its sampled expression (25):

$$\Gamma_{\xi}(\mathcal{A}) = \frac{\int_{\mathcal{W}} \xi(\mathcal{A}) d\mathcal{W}}{\int_{\mathcal{W}} d\mathcal{W}} \tag{24}$$

$$\Gamma_{\xi}(\mathcal{A}) = \frac{1}{N} \sum_{x\in\mathcal{W}}^{N} \xi(\mathcal{A}, x) \tag{25}$$

When the domain is the workspace, that is $\mathcal{W} = \Omega \subset \mathbb{R}^3$ and $x = P$, and for $\xi = w_n$, $\Gamma_{w_n}(\mathcal{A})$ leads to the *global manipulability index*. Similarly, for $\xi = 1/\kappa$, $\Gamma_{1/\kappa}(\mathcal{A})$ denotes the *global isotropic index*, also termed as the *global conditioning index* [55, 56].

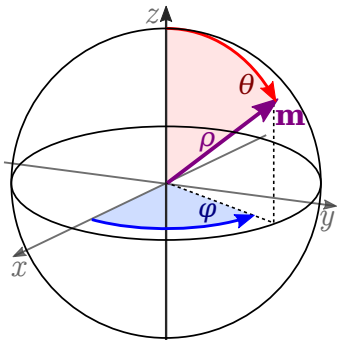

Figure 4: Spherical coordinates (ρ, θ, φ) with ρ the radial distance, θ the polar angle, and φ azimuthal angle.

Likewise, we can evaluate the performance indexes for any direction of the magnetic moment M by considering the 3D rotation group as domain, leading to: $\mathcal{W} = \mathrm{SO}(3)$, where it means the magnetic moment M has 3D orientations and can be aligned to x-, y- and z-directions. In the following, to express the orientation of the magnetic moment, we will consider the spherical coordinate representation, as shown in Fig. 4. Obviously, when both location $P \in \Omega$ of the microrobot and the orientation of its magnetic moment M are considered, the domain is defined accordingly, that is $\mathcal{W} = \Omega \times \mathrm{SO}(3)$.

In this work, the global performance metrics consisting of the average index (14), the uniformity index (15), the normalized manipulability index (20), and the (inverse) condition number (23) for EMA systems are proposed. The considered configuration of electromagnets is estimated in relation with these proposed performance metrics. Thereby, the various configurations can be quantitatively evaluated for their magnetic field distribution and actuation efficiency.

3. DESIGN AND MODELING

3.1. The estimation of magnetic coil number

One of the motivation of an EMA platform is to provide the necessary DOFs for the manipulation of microrobot, mainly depending on the configuration and the number n of constituting electromagnets. Intuitively, it can be shown that platforms with different arrangements of electromagnets exhibit a wide diversity of operating performances for various manipulation tasks [43, 57]. In this section, we will rigorously analyze the number of electromagnets that is required for different magnetic manipulations. Commonly, the manipulation of untethered magnetic microrobot includes the control of its orientation and position. As we mentioned in Fig. 1a, the orientation of microrobot can be simply controlled through the magnetic field. In addition, its position is reached using drilling force generated by rotating magnetic field or translating force generated by magnetic gradient. Thus, the efficient remote magnetic manipulation relies on the capability of generating proper magnetic field and gradient. Specifically, the DOFs of wireless microrobot can be evaluated through the magnetic field and its gradient that are generated by the EMA system with a given number of electromagnets.

As demonstrated in [58, 59, 60, 61], at least $n = 3$ electromagnets are required to achieve 3 DOFs pointing control. Besides, the position control can be effectively realized with at least $n = 4$ magnets in 3D workspace, but up to 5 coils are commonly used to improve the system stability [62]. As computed, 3 DOFs pointing control of the microrobot can be achieved by 2 DOFs torque manipulation. There is no torque that can be applied on the microrobot about its dipole moment main axis. Indeed, some articles have reports several methods to reach 3 DOFs torque control on the designed special microrobots[63, 64, 65]. For the minimum number of electromagnets, the non-magnetic restoring forces, such as gravity, play also an important role, and will be considered. Moreover, some unexpected singularities involving to force control lead to some holonomic constraints, that will be investigated in the follows.

3.1.1. Heading motion control

The quasi-static magnetic fields generated by electromagnets can be defined from the Maxwell's equations (1)-(2). The magnetic torque and force acting on a microrobot are described following (12). In current free space, (1) constraints the gradient matrix of the vector field B to have zero trace; and (2) constraints the gradient matrix of the vector field to be symmetric. Hence, the magnetic force (5) can be rearranged as:

$$\mathbf{f} = \begin{pmatrix} \frac{\partial b_x}{\partial x} & \frac{\partial b_x}{\partial y} & \frac{\partial b_x}{\partial z} \\ \frac{\partial b_x}{\partial y} & \frac{\partial b_y}{\partial y} & \frac{\partial b_y}{\partial z} \\ \frac{\partial b_x}{\partial z} & \frac{\partial b_y}{\partial z} & -\left(\frac{\partial b_x}{\partial x} + \frac{\partial b_y}{\partial y}\right) \end{pmatrix} \begin{pmatrix} m_x \\ m_y \\ m_z \end{pmatrix} \tag{26}$$

This rearrangement allows simplifying the number of magnetic gradient components from nine to five. It is obvious that the magnetic force relies on the applied magnetic gradient field and the magnetic dipole moment of the microrobot. Thus, for a given magnetic dipole, the induced magnetic force only depends on the magnetic gradient that is controlled by the currents flowing through the electromagnets. The magnetic force equations can be thereby expressed as the follows to highlight the magnetic gradients as the controllable parameters:

$$\begin{aligned} \mathbf{f} &= \begin{pmatrix} m_x & m_y & m_z & 0 & 0 \\ 0 & m_x & 0 & m_y & m_z \\ -m_z & 0 & m_x & -m_z & m_y \end{pmatrix} \begin{pmatrix} \frac{\partial b_x}{\partial x} \\ \frac{\partial b_x}{\partial y} \\ \frac{\partial b_x}{\partial z} \\ \frac{\partial b_y}{\partial y} \\ \frac{\partial b_y}{\partial z} \end{pmatrix} \\ &= \mathcal{F}(M)\mathbf{g} \end{aligned} \tag{27}$$

where $\mathcal{F}(M)$ indicates the matrix form of the dipole moment M of the microrobot; and the vector field $\mathbf{g}$ includes the five magnetic gradient components.

Similarly, the applied magnetic torque is dependent on the magnetic field when the dipole moment of the microrobot is determined. Using the skew matrix (6), the Eq. (7) can be rewritten as:

$$\begin{pmatrix}\mathbf{t}\\ \mathbf{f}\end{pmatrix} = \begin{pmatrix}\mathrm{Sk}(M)\\ \mathcal{F}(M)\end{pmatrix}\begin{pmatrix}B\\ \mathbf{g}\end{pmatrix} \tag{28}$$

Considering the current flowing through the n electromagnetic coils of the EMA system has a linearly mapping to the magnetic field (8) and gradient (9)-(11), it follows that the (12) can be then represented as:

$$\begin{aligned}\begin{pmatrix}\mathbf{t}\\ \mathbf{f}\end{pmatrix} &= \mathcal{A}(M,P)\mathbf{i} = \begin{pmatrix}\mathcal{A}_t(M,P)\\ \mathcal{A}_f(M,P)\end{pmatrix}\mathbf{i}\\ &= \begin{pmatrix}\mathrm{Sk}(M)\\ \mathcal{F}(M)\end{pmatrix}\begin{pmatrix}\mathcal{B}(P)\\ \mathcal{G}(P)\end{pmatrix}\mathbf{i}\end{aligned} \tag{29}$$

where $\mathcal{B}$ is a $3\times n$ matrix and $\mathcal{G}$ is a $5\times n$ matrix, that are defined as:

$$\begin{aligned}\mathbf{g} &= \mathcal{G}(P)\mathbf{i}\\ &= \begin{pmatrix}\frac{\partial \mathcal{B}_x}{\partial x} & \frac{\partial \mathcal{B}_x}{\partial y} & \frac{\partial \mathcal{B}_x}{\partial z} & \frac{\partial \mathcal{B}_y}{\partial y} & \frac{\partial \mathcal{B}_y}{\partial z}\end{pmatrix}^{\intercal}\mathbf{i}\end{aligned} \tag{30}$$

Besides, both $\mathcal{B}$ and $\mathcal{G}$ are a function of the location P of the microrobot in the workspace Ω. Through investigating the matrices $\mathcal{F}(M)$ and $\mathrm{Sk}(M)$, the conditioning of magnetic field and its gradient can be analyzed.

Since the orientation of microrobot tends to be aligned on the applied magnetic field, it is more convenient to linearize the system by specifying the desired field directly instead of magnetic torque. Hence, the magnetic field and inducing force can be obtained from:

$$\begin{pmatrix}B\\ \mathbf{f}\end{pmatrix} = \begin{pmatrix}\mathbb{I} & \mathbb{O}\\ \mathbb{O} & \mathcal{F}(M)\end{pmatrix}\begin{pmatrix}\mathcal{B}(P)\\ \mathcal{G}(P)\end{pmatrix}\mathbf{i} = \mathcal{A}_b(M,P)\ \mathbf{i} \tag{31}$$

where $\mathbb{I}$ is an identity matrix, and $\mathbb{O}$ is a zero matrix in an appropriately size.

If the microrobot is made of permanent magnet, magnetic torque is linear with the current. If the microrobot is composed of a soft magnetic material and it does not reach the magnetic saturation, there is a linear relation between the magnetic moment and the magnetic field. Consequently, the magnetic torque becomes quadratic with the current [66]. Thus, the capability of the EMA system, such as DOFs of manipulation of the microrobot, can be evaluated from the (31). Similarly to the (13), the input currents $\mathbf{i}$ can be also here computed using the pseudo-inverse of $\mathcal{A}_b(M,P)$ matrix when the matrix has full rank.

Furthermore, as the magnetic field and force are decoupled in (31), they can be first analyzed separately. As the magnetic field is linear with the current $\mathbf{i}$, the sole B field control relies on the properties of the matrix $\mathcal{B}(P)$. It can be easily shown that if the rank of $\mathcal{B}(P)$ is equal to the dimension of the workspace $\forall P\in\Omega$, that leads to a full control of B. In other words, the number of current inputs $\mathbf{i}$ should be equal or more than the dimension of the workspace Ω. In contrast, the force control requires more advanced investigations that are presented hereafter.

3.1.2. Magnetic force control

The matrix $\mathcal{F}(M)$ is a 3×5 non-square matrix, and it can be shown that its row rank is full. Thus, $\mathcal{F}(M)$ has a right Moore-Penrose inverse which is expressed by $\mathcal{F}(M)^{\dagger} = \mathcal{F}(M)^{\intercal}\left(\mathcal{F}(M)\mathcal{F}(M)^{\intercal}\right)^{-1}$. From (26), the desired magnetic gradient vectors $\mathbf{g}^{\star}$ are thereby obtained using the right inverse when the magnetic force is required. This leads to:

$$\begin{pmatrix}\frac{\partial b_x^{\star}}{\partial x}\\ \frac{\partial b_x^{\star}}{\partial y}\\ \frac{\partial b_x^{\star}}{\partial z}\\ \frac{\partial b_y^{\star}}{\partial y}\\ \frac{\partial b_y^{\star}}{\partial z}\end{pmatrix} = \begin{pmatrix}\frac{(m_n)\,m_x}{m_m} & \frac{-m_x^2 m_y}{m_m} & \frac{-m_z}{m_{nz}}\\ \frac{m_y^3+m_y m_z^2}{m_m} & \frac{m_x^3+m_x m_z^2}{m_m} & 0\\ \frac{(m_n)\,m_z}{m_m} & \frac{-m_x m_z^2}{m_m} & \frac{m_x}{m_{nz}}\\ \frac{-m_x m_y^2}{m_m} & \frac{(m_n)\,m_y}{m_m} & \frac{-m_z}{m_{nz}}\\ \frac{-m_x m_z^2}{m_m} & \frac{(m_n)\,m_z}{m_m} & \frac{m_y}{m_{nz}}\end{pmatrix}\mathbf{f}$$

$$\mathbf{g}^{\star} = \mathcal{F}(M)^{+}\mathbf{f} \tag{32}$$

where $m_n = m_x^2+m_y^2+m_z^2$, $m_m = (m_x^2+m_y^2+m_z^2)^2-(m_x m_y)^2$, and $m_{nz} = m_n+m_z^2$. As one can see, the matrix $\mathcal{F}(M)$ is a function of the dipole moment $M=(m_x,m_y,m_z)^{\intercal}$ of the microrobot. Hence, the pseudo-inverse matrix $\mathcal{F}(M)^{+}$ is also affected by the magnetic moment of microrobot.

If the magnetic moment M of the microrobot is fixed (e.g. when a uniform static magnetic field B_0 is applied), only three independent magnetic gradients of $\mathbf{g}$ are required to produce an arbitrary force $\mathbf{f}$. However, the all five magnetic gradient components are required for continuous force control if M

is changing. Therefore, there are ten linear relations between magnetic gradients.

For instance, linear dependence between $\frac{\partial b_x}{\partial x}$ and $\frac{\partial b_y}{\partial y}$ is considered. Let us express this linear dependence through adding a coefficient $\alpha \in \mathbb{R}^*$, that is: $\frac{\partial b_y}{\partial y} = \alpha \frac{\partial b_x}{\partial x}$. The Eq. (26) is written with the following $\mathbf{g}$ matrix:

$$\mathbf{g} = \begin{pmatrix} \frac{\partial b_x}{\partial x} & \frac{\partial b_x}{\partial y} & \frac{\partial b_x}{\partial z} & \alpha \cdot \frac{\partial b_x}{\partial x} & \frac{\partial b_y}{\partial z} \end{pmatrix}^T \quad (33)$$

If the magnetic microrobot is aligned along the z-axis, the magnetic force in z-axis direction is expressed as:

$$f_z = -(1+\alpha)\, m_z \frac{\partial b_x}{\partial x} \quad (34)$$

Obviously, f_z equals to zero when: $\alpha = -1$, that is for $\frac{\partial b_y}{\partial y} = -\frac{\partial b_x}{\partial x}$.

Let us now assume that the microrobot has a magnetic dipole moment defined by:

$$M = \{(m, \beta m, 0)^\intercal, (m, 0, \beta m)^\intercal, (0, m, \beta m)^\intercal\} \quad (35)$$

with $\beta \in \mathbb{R}^*$ a coefficient term. Then, these values have to be taken into the (32) to investigate the existence of a solution. The necessary and sufficient condition for a matrix reversibility is that the determinant is not equal to 0. Since the determinant of a matrix is equal to the product of all of their eigenvalues, all eigenvalues must be not equal to 0 in order to enable the existence of the inverse matrix. Thus, the singularly values of the system for the considered linear dependence can be mathematically analyzed by computing whether $\det(\mathcal{F}(M)\mathcal{F}(M)^\intercal) = 0$. The determinants with regard to the magnetic dipole moments of M are obtained as:

$$\det(m, \beta m, 0) = m\left(\alpha^2\beta^6 + \alpha^2\beta^4 + 2\alpha\beta^4 + 2\alpha\beta^2 + \beta^2 + 1\right) \quad (36)$$

$$\det(m, 0, \beta m) = m\left(\alpha^2\beta^6 + \alpha^2\beta^4 + 2\alpha\beta^6 + 4\alpha\beta^4 + 2\alpha\beta^2 + \beta^6 + 3\beta^4 + 3\beta^2 + 1\right) \quad (37)$$

$$\det(0, m, \beta m) = m\left(\alpha^2\beta^6 + 3\alpha^2\beta^4 + 3\alpha^2\beta^2 + \alpha^2 + 2\alpha\beta^6 + 4\alpha\beta^4 + 2\alpha\beta^2 + \beta^6 + \beta^4\right) \quad (38)$$

where det represents the determinant operator, such as $\det(M)$ is expressed as the determinant of $(\mathcal{F}(M)\mathcal{F}(M)^\intercal)$ for the given dipole moment.

When the determinant becomes 0, the rank of matrix $\mathcal{F}(M)$ is less than 3 and the inverse matrix does not exist, thereby, the system becomes singular. Thus, the system should avoid the relationship between β and α regarding the three dipole moments, respectively, meets the followings:

$$\beta = \pm\frac{1}{\sqrt{\alpha}} \quad (39)$$

$$\beta = \pm\frac{1}{\sqrt{-\alpha - 1}} \quad (40)$$

$$\beta = \pm\frac{\sqrt{-\alpha(\alpha+1)}}{\alpha+1} \quad (41)$$

When the above equations are satisfied, one of magnetic force components becomes linear dependent to one of the others. For instance, for a dipole moment $M = (m, \beta m, 0)^\intercal$, the basic condition is: $\alpha > 0$ and not satisfy (39), and then a singularity can be avoided. The other singular cases are summarized in Table. (1).

Table 1: The singular cases caused by the linear dependent between $\frac{\partial b_x}{\partial x}$ and $\frac{\partial b_y}{\partial y}$

$M^\intercal$	Relationship between β and α	Condition on α
$(m, \beta m, 0)$	$\beta = \pm\frac{1}{\sqrt{\alpha}}$	$\alpha > 0$
$(m, 0, \beta m)$	$\beta = \pm\frac{1}{\sqrt{-\alpha-1}}$	$\alpha < -1$
$(0, m, \beta m)$	$\beta = \pm\frac{\sqrt{-\alpha(\alpha+1)}}{\alpha+1}$	$\alpha \neq -1 \wedge \alpha(\alpha+1) \leq 0$

Similarly, other nine linearly dependent relations: $\frac{\partial b_x}{\partial y} = \alpha\frac{\partial b_x}{\partial x}$, $\frac{\partial b_x}{\partial x} = \alpha\frac{\partial b_x}{\partial z}$, $\frac{\partial b_x}{\partial x} = \alpha\frac{\partial b_y}{\partial z}$, $\frac{\partial b_x}{\partial y} = \alpha\frac{\partial b_x}{\partial z}$, $\frac{\partial b_x}{\partial y} = \alpha\frac{\partial b_y}{\partial y}$, $\frac{\partial b_x}{\partial y} = \alpha\frac{\partial b_y}{\partial z}$, $\frac{\partial b_x}{\partial z} = \alpha\frac{\partial b_y}{\partial y}$, $\frac{\partial b_x}{\partial y} = \alpha\frac{\partial b_y}{\partial z}$, and $\frac{\partial b_y}{\partial y} = \alpha\frac{\partial b_y}{\partial z}$ have also been investigated. The different conditions to enable a linear relationship between the magnetic gradients terms of $\mathbf{g}$ are summarized hereafter. If these conditions are fulfilled, the matrix $\mathcal{F}(M)$ is not always full rank. Thereby, the magnetic force control becomes singular because the matrix $\mathcal{F}(M)$ is not full rank when any two magnetic gradients exist linear dependence. It means that magnetic force $\mathbf{f}$ cannot be controlled in some orientations and positions where non-full rank happens. To apply an arbitrary force $\mathbf{f}$ on the microrobot in any position $P \in \Omega$ and orientation requires the all five magnetic gradients, whose

terms must be controlled independently.

It is obvious that the magnetic gradient is a variation in the magnetic field B with respect to position. Thus, when the magnetic gradients are applied on a microrobot for providing propulsion force, it is synchronously placed in a global magnetic field. According to (4), if the magnetic field B is changing, a magnetic torque $\mathbf{t}$ is simultaneously generated on the microrobot, which will change its magnetic moment orientation and then affect the applied magnetic force. For an EMA system to continuously apply a desired force, it must be capable of controlling the microrobot's orientation, and updating the magnetic gradients faster than the change of dipole-moment direction. Therefore, the control of magnetic field should be considered when applying magnetic gradient to the microrobot.

3.1.3. Combined torque and force control

Torque control can be analyzed directly through the magnetic field properties, as expressed in (31). Commonly, the three magnetic fields components are required to generate magnetic torque to align microrobot to any directions in the workspace Ω. As discussed above, the control of the five independent magnetic gradients is the necessary and sufficient condition for a singular-free force control. Hence, the (31) can be used to analyze the combined torque and force control. In addition, from equation (31), the matrix $\mathcal{B}$ and matrix $\mathcal{G}$ are combined as a 6×8 matrix defined as:

$$\mathbf{C}(M) = \begin{pmatrix} \mathbb{I} & \mathbb{O} \\ \mathbb{O} & \mathcal{F}(M) \end{pmatrix} \tag{42}$$

The first three columns are the expansion of the identity matrix $\mathbb{I}$, thus there is no singular case. The last five columns are relevant to force control. The above matrix $\mathbf{C}(M)$ can be reduced to $\mathcal{C}(M)$ that is a 6×7 matrix by replacing a linear combination between one of the first three columns and one of the last five columns. The obtained matrix $\mathcal{C}(M)$ describes an EMA system where there is a linear dependence between the magnetic field and its gradient.

Moreover, the all 10 singular cases have been already investigated regarding linearly dependent relations of magnetic gradients. There is always a singular case if any one of such 10 linear dependencies exists. Besides, there are 3 linear dependencies between magnetic fields. As discussed, these 3 linear relations will lead to singular case of field control. Thus, only the linear dependence between the first three columns and last five columns should be considered in the analysis of the matrix $\mathbf{C}$. In fact, there are totally 28 linear dependencies in the matrix $\mathbf{C}(M)$.

Consequently, there are 10 dependent relationships between each magnetic gradients, and 3 linear dependencies between the magnetic fields. Since, there is a total of 28 linear dependencies in the matrix $\mathcal{C}$, thereby, the linear combinations between fields and gradients are 15 that will be investigated hereafter.

Let us recall that an unrestrained magnetic microrobot will be aligned with the applied field direction for quasi-static manipulations. Specifically, we assume that the direction of magnetic moment changes slower compared to the rotational time of the alignment of the microrobot with the magnetic field B.

Once again, we will discuss linear dependencies on the magnetic gradient component $\frac{\partial b_x}{\partial x}$ as examples. These dependencies between $\frac{\partial b_x}{\partial x}$ and the magnetic field $B = (b_x, b_y, b_z)^\intercal$ are defined with the following formulas: a) $\frac{\partial b_x}{\partial x} = \alpha b_x$, b) $\frac{\partial b_x}{\partial x} = \alpha b_y$, and c) $\frac{\partial b_x}{\partial x} = \alpha b_z$, with $\alpha \in \mathbb{R}^*$ a coefficient. The corresponding matrices can be expressed respectively as follows:

$$\begin{aligned}
\mathcal{C}_a &= \begin{pmatrix} 1 & 0 & 0 & 0 & 0 & 0 & 0 \\ 0 & 1 & 0 & 0 & 0 & 0 & 0 \\ 0 & 0 & 1 & 0 & 0 & 0 & 0 \\ \alpha m_x & 0 & 0 & m_y & m_z & 0 & 0 \\ 0 & 0 & 0 & m_x & 0 & m_y & m_z \\ -\alpha m_z & 0 & 0 & 0 & m_x & -m_z & m_y \end{pmatrix} \\
\mathcal{C}_b &= \begin{pmatrix} 1 & 0 & 0 & 0 & 0 & 0 & 0 \\ 0 & 1 & 0 & 0 & 0 & 0 & 0 \\ 0 & 0 & 1 & 0 & 0 & 0 & 0 \\ 0 & \alpha m_x & 0 & m_y & m_z & 0 & 0 \\ 0 & 0 & 0 & m_x & 0 & m_y & m_z \\ 0 & -\alpha m_z & 0 & 0 & m_x & -m_z & m_y \end{pmatrix} \\
\mathcal{C}_c &= \begin{pmatrix} 1 & 0 & 0 & 0 & 0 & 0 & 0 \\ 0 & 1 & 0 & 0 & 0 & 0 & 0 \\ 0 & 0 & 1 & 0 & 0 & 0 & 0 \\ 0 & 0 & \alpha m_x & m_y & m_z & 0 & 0 \\ 0 & 0 & 0 & m_x & 0 & m_y & m_z \\ 0 & 0 & -\alpha m_z & 0 & m_x & -m_z & m_y \end{pmatrix}
\end{aligned} \tag{43}$$

When $\frac{\partial b_x}{\partial x}$ and b_x are linearly dependent, it is obvious that the matrix $\mathcal{C}_a$ is not full rank. The magnetic force on the x-direction is directly related to the magnetic field when the dipole moment is $M = (m_x, 0, 0)^\intercal$. That is the magnitude of magnetic field will be proportional to the magnetic force required in the dependent direction. However, when the force is applied to a direction, the orientation of the microrobot may be affected due to the

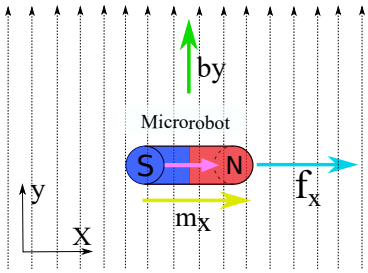

Figure 5: The illustration of the contradiction of microrobot orientation and magnetic field for generating magnetic force.

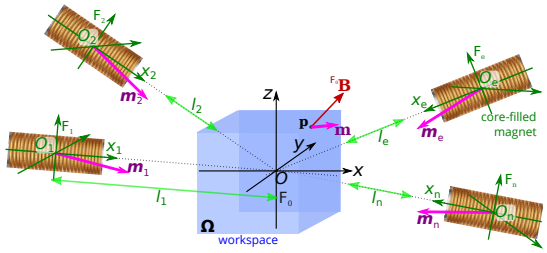

Figure 6: Schematic representation of a multiple electromagnets system inducing a magnetic flux $B(P)$ within the workspace Ω (blue square box). The length l_e represents the distance between the coil center O_e to the workspace center O.

linear dependence between the generated force and the applied field.

Moreover, there is still an issue on the sign of the force that can not be changed. Here, the magnetic field is used to align the microrobot magnetic moment along the same direction, that is: $m_x = \beta b_x$, with $\beta \in \mathbb{R}^*$ a coefficient. From the above analysis, the x-directed magnetic force is not linearly independent to the magnegtic field, which is expressed as: $f_x = \alpha b_x m_x = \alpha\beta b_x^2$. Hence, the sign of f_x can not be changed because the sign of dipole moment and the sign of field are always the same.

Therefore, such control system requires a non-magnetic restoring force in the x-direction. If a suitable nonmagnetic restoring force exists, the EMA system with the linear dependence between $\frac{\partial b_x}{\partial x}$ and b_x can be used to control the microrobot in the desired direction and position, thus, at least 7 inputs are required.

Some other linearly dependent relationships between magnetic field and its gradient can cause physical impossibility. For instance, a contradiction exists between the orientation of the microrobot and the direction of magnetic field. Indeed, the orientation of microrobot should be aligned along direction of magnetic field as we assumed.

When $\frac{\partial b_x}{\partial x}$ and b_y are linearly dependent, and if $M = (m_x, 0, 0)^\intercal$, it is impossible for any EMA system to apply a magnetic force in the x-direction. In this case, the force is expressed by $f_x = \alpha b_y m_x$. Obviously, it is impossible to apply a magnetic force in the x-direction . The reason is that it is not feasible to align the microrobot along the x-axis when the magnetic field is applied in the y-direction. As shown in the Fig. 5, the desired magnetic force requires that the orientation of the microrobot is aligned in x-direction that demands the applied magnetic field is aligned to x-direction. However, the magnetic field is applied to y-direction due to the assumed linear dependence. Hence, the desired magnetic force can not be produced in respect of such dependent relation. Similarly, when $\frac{\partial b_x}{\partial x}$ and b_z are in linear dependence, and dipole moment is $M = (m_x, 0, 0)^\intercal$, the magnetic force can be expressed as $f_x = \alpha b_z m_x$. This x-direction magnetic force can not be generated due to the constraint that the magnetic field aligns the microrobot to applied direction.

Other linearly dependent relations have also analyzed on $\frac{\partial b_x}{\partial y}$: d) $\frac{\partial b_x}{\partial y} = \alpha b_x$, e) $\frac{\partial b_x}{\partial y} = \alpha b_y$, and f) $\frac{\partial b_x}{\partial y} = \alpha b_z$; on $\frac{\partial b_x}{\partial z}$: g) $\frac{\partial b_x}{\partial z} = \alpha b_x$, h) $\frac{\partial b_x}{\partial z} = \alpha b_y$, and i) $\frac{\partial b_x}{\partial z} = \alpha b_z$; on $\frac{\partial b_y}{\partial y}$: j) $\frac{\partial b_y}{\partial y} = \alpha b_x$, k) $\frac{\partial b_y}{\partial y} = \alpha b_y$, and l) $\frac{\partial b_y}{\partial y} = \alpha b_z$; on $\frac{\partial b_y}{\partial z}$: m) $\frac{\partial b_y}{\partial z} = \alpha b_x$, n) $\frac{\partial b_y}{\partial z} = \alpha b_y$, and p) $\frac{\partial b_y}{\partial z} = \alpha b_z$. However, the possible linear relations only exist at following cases: $\frac{\partial b_x}{\partial x}$ and αb_x; $\frac{\partial b_y}{\partial y}$ and αb_y; or $\frac{\partial b_x}{\partial x} + \frac{\partial b_y}{\partial y}$ and αb_z (as $\frac{\partial b_x}{\partial x} + \frac{\partial b_y}{\partial y} + \frac{\partial b_z}{\partial z} = 0$). Such linear dependencies can obviously reduce the inputs for control system that requires less coils. It should be noted that reducing the number of coils only works under some certain conditions, for instance the non-magnetic restoring force is required. In addition, to the study of singularity under the linearly dependencies between input terms, with some advanced control technology application to the magnetic field control, the electromagnetic field singularity problems still can be investigated and avoided[67].

3.2. Magnetic field generated in the reference workspace

Considering the EMA system composed of a set of n electromagnets, the generated magnetic field ${}^{\mathcal{F}_0}B(P)$ at any point P in the workspace Ω can be illustrated in Fig. 6. This overall magnetic field is assumed to be the sum of the contributions of

all individual electromagnets. Recall that when the current input i_e flows through the coils e, the corresponding magnetic field can be expressed as: $B_e(P) = \widetilde{B}_e(P)i_e$. A key step is thus to compute the magnetic field produced by the electromagnets e. Several models, based either on numerical or analytical approaches, have been proposed in the literature. Numerical models are commonly based on maps of the magnetic field obtained either from FEM or from experimental measurement of the field B_e. The numerical method allows a good accuracy but costs a lot of calculation time. Analytical methods are often based on dipole approximation which offers a better computation time, or even on elliptical integrals [68, 69, 70]. Hybrid approaches, using a map of the magnetic field obtained from FEM and a fitting of an analytical model can be also considered, such as in [43]. The choice of the method commonly leads to make the best trade-off between speed and accuracy. As in this work, numerous simulations are realized, we assume that the magnetic field $B_e(P)$ induced by the electromagnet e can be approximated by the *magnetic point-dipole model*. Specifically, the point-dipole model expresses the magnetic field ${}^{\mathcal{F}_e}B_e(P)$ of the coils e with respect to its own frame $\mathcal{F}_e(O_e : x_e, y_e, z_e)$, as shown in Fig. 6, and can be written as:

$$ {}^{\mathcal{F}_e}B_e(P) = \frac{\mu_0}{4\pi|P|^3}\left(\frac{3\,(M_e \cdot P)}{|P|^2} - M_e\right) \qquad (44) $$

where M_e is the equivalent magnetic dipole moment related to the magnet source e for a unit current input. Indeed, for the sake of clarity and simplicity, we assume that each electromagnet e can be approximated by its analogous dipole moment M_e. Hence, the magnetic field is generated by using the point-dipole model for computation. The electromagnet is considered as a theoretical point-dipole mapping to the unit-current contribution, thus the shape or the filled core does not affect the performance analysis of the system. Especially, the manipulability indexes, conditioning indexes and existing singularities are based on the arrangements of electromagnet instead of input current.

The magnetic field ${}^{\mathcal{F}_e}B_e(P)$ can be thus expressed in the reference frame $\mathcal{F}_0(O : x, y, z)$ linked to the workspace center using the homogeneous transformation:

$$ {}^{\mathcal{F}_0}B_e(P) = {}^{\mathcal{F}_0}\mathbf{T}_{\mathcal{F}_e} \times {}^{\mathcal{F}_e}B_e(P) \qquad (45) $$

where the homogeneous transformation matrix is basically defined as:

$$ {}^{\mathcal{F}_0}\mathbf{T}_{\mathcal{F}_e} = \left(\begin{array}{c|c} {}^{\mathcal{F}_0}\mathbf{R}_{\mathcal{F}_e} & {}^{\mathcal{F}_0}\mathbf{t}_{\mathcal{F}_e} \\ \hline \mathbf{0} & 1 \end{array}\right) \qquad (46) $$

where ${}^{\mathcal{F}_0}\mathbf{R}_{\mathcal{F}_e}$ and ${}^{\mathcal{F}_0}\mathbf{t}_{\mathcal{F}_e}$ denote the rotation and translation matrices with respect to the reference frame $\mathcal{F}_0$, respectively.

The overall magnetic field distribution in the workspace produced by a set of n electromagnetic coils can be superposed, that is:

$$ \begin{aligned} {}^{\mathcal{F}_0}B(P) &= \sum_{e=1}^{n} {}^{\mathcal{F}_0}B_e(P) = \sum_{e=1}^{n} {}^{\mathcal{F}_0}\tilde{B}_e(P)i_e \\ &= {}^{\mathcal{F}_0}\mathcal{B}(P)\mathbf{i} = \begin{pmatrix} {}^{\mathcal{F}_0}\tilde{B}_1(P) & \dots & {}^{\mathcal{F}_0}\tilde{B}_n(P) \end{pmatrix}\mathbf{i} \end{aligned} \qquad (47) $$

with the input currents $\mathbf{i} = (i_1, i_2, \dots, i_n)^\intercal$.

It can be easily shown that the total magnetic field ${}^{\mathcal{F}_0}B(P)$ in the workspace can be changed not only thanks to the currents $\mathbf{i}$, but also by varying the position and/or orientation of electromagnets. If the electromagnets are dynamically moved following a control strategy, a similar current-control approach can be designed.

4. Configurations of magnetic systems with multiple electromagnets

The arrangement of electromagnets is also a key issue for the magnetic actuation system. With the number of electromagnets computed by the proposed approach and the derived equations, the simulations of various EMA systems can be performed mathematically. The magnetic characteristics will be investigated according to different configurations of electromagnets with the various performance metrics mentioned in section. 2.3. Thus, in this section, several typical configurations of EMA systems will be quantitatively evaluated.

In a 2D space, the flat configurations of EMA systems including $n = 4, 6$ and 8 electromagnets are studied. The 3D-placement setups with $n = 6$ and 8 electromagnets are simulated for 3D space. These configurations as illustrated in Fig.7 are selected to estimate the effectiveness of different arrangements of electromagnets.

As shown in Fig.7a-Fig.7c, the considered four-electromagnet system, the six-electromagnet system and the eight-electromagnet system are organized in axisymmetric configuration around the center O of the workspace where their coils separated with an offset angle of 90°, 60° and 45°,

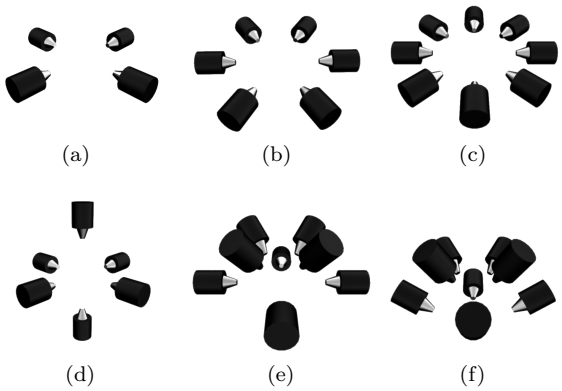

Figure 7: Representation of different basic multi-electromagnet EMA systems: (a) flat four-electromagnet system; (b) flat six-electromagnet system; (c) flat eight-electromagnet system; (b) 3D six-electromagnet system; (e) OctoMag system (eight coils) and (f) MiniMag system (eight coils).

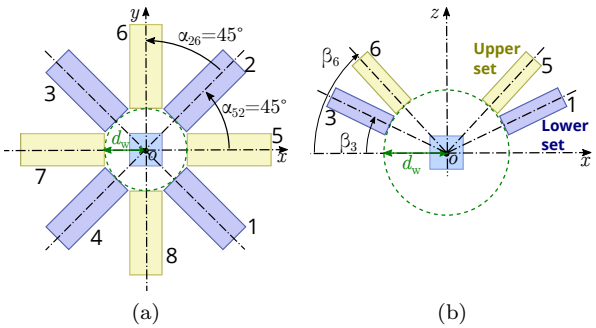

Figure 8: 3D eight coils EMA systems arrangement: (a) top view on xy-plane and the (b) side view on xz-plane.

respectively. The Fig.7d-Fig.7f illustrate the 3D-arrangement setups where the 3D six-electromagnet system, eight-electromagnet OctoMag system and eight-electromagnet MiniMag system are represented. The 3D six-electromagnet system consists of three pairs of opposing electromagnets aligned along the x, y and z-axis with same distance to the center O. The OctoMag and MiniMag systems designed and developed at the ETH Zurich [43] are both composed of $n = 8$ electromagnets. Here, the eight electromagnets have been divided into two sets of four coils referred as the upper and lower sets. As presented in Fig.8a, these two sets are equally spaced and organized around the common z-axis of rotation with $\alpha = 45°$, and are pointing at the center O of the workspace with a fixed distance. For OctoMag system, the lower set is placed in xy-plane, with $\beta_e = 0$ ($e = 1..4$) and the upper are tilted $\beta_e = 45°$ ($e = 5..8$). Whereas, the lower set of MiniMag is rotated to $\beta_e = 26°$ ($e = 1..4$) from the xy-plane, and the upper set is set to $\beta_e = 47.5°$ ($e = 5..8$).

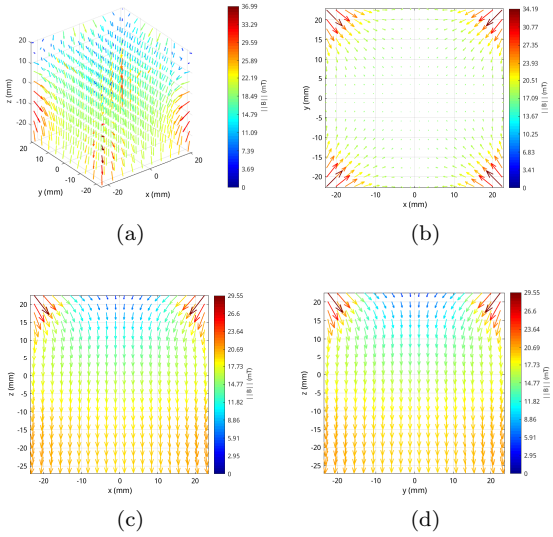

Figure 9: The magnetic field B generated by OctoMag-like EMA system with $d_w = 65$ mm: (a) a 3D view, (b) the xy-plane, (c) the xz-plane and (d) the yz-plane. The colorbar indicates the magnetic field magnitude.

In our study, the influence of the distance d_w between the workspace center O and each electromagnet regarding the performance of EMA system is assessed. Also, the impact of tilted angle of the placed electromagnets is evaluated as well to optimize the system performances.

4.1. Optimization regarding working distance d_w of electromagnets for EMA System

We consider that each coil has the equal distance d_w for the considered system as represented in Fig. 8. Different arrangements of EMA system have been investigated from numerous simulations, and different metrics have been calculated to evaluate their performances. To sum up, the values of root mean square (RMS) and uniformity indexes of the magnetic field are synthesized in Table.2, and in Table.3 for its gradient.

Commonly, long distance d_w from the workspace center O to the electromagnet leads globally to a slight more uniform magnetic field and gradient, in addition, the effective control of magnetic microrobot is improved. Nevertheless, stronger magnetic

Table 2: Metrics of the magnetic field strength: its RMS (mT) and uniformity $\gamma(B)$ metric (%)

	Distance d_w (mm)				
EMA System	60	65	70	75	80
Flat four-coil (Fig. 7a)	13.13 (71.18)	9.39 (70.97)	6.91 (70.82)	5.21 (70.81)	4.00 (70.88)
Flat six-coil (Fig. 7b)	20.55 (72.55)	14.69 (72.96)	10.80 (73.03)	8.13 (72.96)	6.24 (72.85)
Flat eight-coil (Fig. 7c)	27.41 (73.05)	19.59 (73.26)	14.41 (73.23)	10.85 (73.09)	8.33 (72.92)
3D six-coil (Fig. 7d)	10.08 (51.09)	6.48 (50.00)	4.28 (49.11)	2.90 (48.39)	2.01 (47.80)
OctoMag (Fig. 7e)	24.86 (76.97)	18.61 (79.32)	14.49 (81.32)	11.58 (82.92)	9.44 (84.19)
MiniMag (Fig. 7f)	55.73 (63.86)	42.40 (67.20)	33.21 (69.89)	26.57 (72.12)	21.63 (74.02)

Table 3: Metrics of the magnetic field gradient strength: its RMS (mT/m) and uniformity $\gamma(B)$ metric (%)

	Distance d_w (mm)				
EMA System	60	65	70	75	80
Flat four-coil (Fig. 7a	1.18 (59.89)	0.78 (64.58)	0.54 (68.95)	0.38 (72.99)	0.28 (76.78)
Flat six-coil (Fig. 7b)	1.48 (64.27)	0.97 (70.66)	0.68 (75.34)	0.50 (78.69)	0.38 (81.21)
Flat eight-coil (Fig. 7c)	1.87 (66.49)	1.27 (71.77)	0.91 (75.60)	0.67 (78.66)	0.51 (81.20)
3D six-coil (Fig. 7d)	1.32 (65.61)	0.84 (66.97)	0.55 (67.50)	0.37 (66.94)	0.26 (66.42)
OctoMag (Fig. 7e)	1.80 (36.68)	1.00 (43.02)	0.59 (49.00)	0.37 (54.40)	0.25 (59.26)
MiniMag (Fig. 7f)	2.17 (56.69)	1.31 (66.02)	0.88 (72.13)	0.63 (76.26)	0.47 (79.18)

field and gradient require a short length d_w. Thus, a compromise should be made with respect to the biomedical applications specifications. Certainly, the value of d_w will affect the size of the workspace since a great length enables larger workspace dimension.

Obviously, EMA setup with $n = 8$ coils produces stronger magnetic field and gradient than configuration with fewer magnets. Furthermore, as presented in the results of tables, MiniMag arrangement generates the strongest and the most uniform magnetic field, specially in xy-plane. From these results, it confirms that the performances of EMA systems are not only affected by the number of coils but also by their configurations.

In order to better present the effect of the shifted distance d_w of electromagnet, let us focus on the EMA system with a certain number of coils. As mentioned in section.3.1, the $n = 8$ electromagnets can be applied for the combined force and torque singular-free control with 5 DOFs (3-DOF position and 2-DOF pointing orientation) in a 3D workspace. In the following, we only keep one variable parameter. We have chosen to set the tilted angle similar to the OctoMag EMA setup [43], while working distances of $d_w = 60\,\text{mm}$, 70 mm and 80 mm are evaluated, respectively.

As presented in Fig. 9, the magnetic field B distribution is mainly oriented along the z-axis direction. As the OctoMag setup shares the same arrangement of electromagnets in the xy-plane with the flat four-electromagnet configuration, the vector field in the xy-plane is quite homogeneous. The directions of the magnetic field vectors mainly along the z-axis are basically due to the upper set of electromagnets.

Fig. 10 shows the magnetic field magnitude $\|B\|$ in the xy-plane for the different working distances. The magnetic field distribution B looks much less like a radial field and becomes stronger for the shorter distance d_w. However, if a magnetic microrobot moves outward from the center of xy-plane,

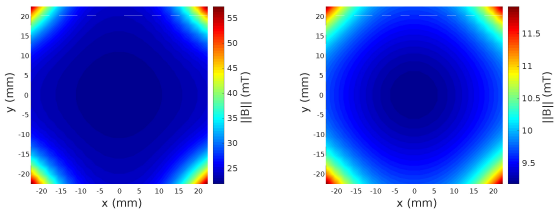

Figure 10: The magnetic field magnitude $\|B\|$ in the xy-plane for lengths of (a) $d_w = 60\,\text{mm}$, and (b) $d_w = 80\,\text{mm}$.

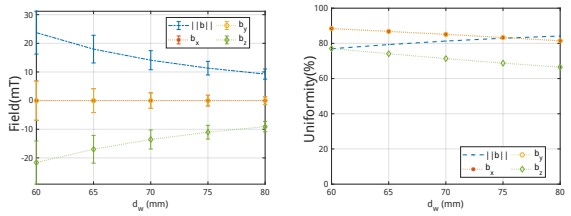

Figure 11: Magnetic field metrics over the workspace Ω for d_w ranging from 60 mm to 80 mm: (a) error-bar showing the average and STD values; and (b) the uniformity index γ.

the longer distance d_w can make magnetic field more homogeneous in each direction. This means that OctoMag system is able to actuate a magnetic microrobot to any direction with less interference in long distances d_w. For instance, when the working distance is set to $d_w = 65\,\text{mm}$, the maximum magnetic intensity decreases from 36.99 mT with the 2D configuration to 35.86 mT with the OctoMag platform.

The magnetic field metrics are shown in Fig. 11. It appears that the average value $\langle\|B\|\rangle$ of the magnetic field magnitude is equivalent to the flat eight-

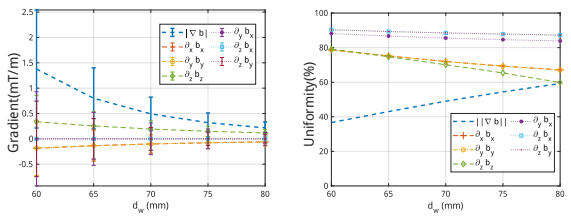

Figure 12: Magnetic field gradient metrics for distance d_w ranging from 60 mm to 80 mm: (a) the mean and STD values; and (b) the uniformity index γ.

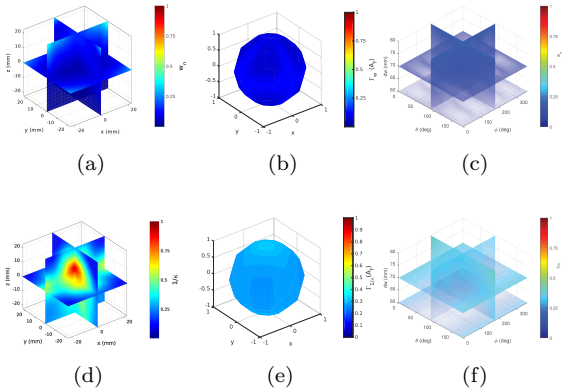

Figure 13: Performance metrics of the force actuation matrix $\mathcal{A}_\mathbf{f}$: (a) the manipulability w_n and (d) conditioning number $1/\kappa$ indexes for $P \in \Omega$ when M is aligned along the x-direction; (b) $\Gamma_{w_n}(\mathcal{A}_\mathbf{f})$ and (e) $\Gamma_{1/\kappa}(\mathcal{A}_\mathbf{f})$ for the sampled orientation of M; and (c) $\Gamma_{w_n}(\mathcal{A}_\mathbf{f})$ and (f) $\Gamma_{1/\kappa}(\mathcal{A}_\mathbf{f})$ as function of d_w.

electromagnet arrangement, however, its STD value is here improved. Furthermore, the uniformity index $\gamma(\|B\|)$ is more important and is increasing with the length d_w. Therefore, the values confirm that OctoMag-like arrangement is a promising solution to efficiently actuate a magnetic microrobot in a 3D workspace.

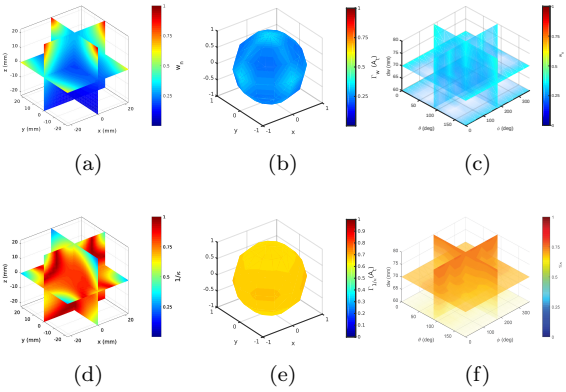

Figure 14: Performance metrics of the torque actuation matrix $\mathcal{A}_\mathbf{t}$: (a) the manipulability w_n and (d) conditioning number $1/\kappa$ indexes in $P \in \Omega$ when M is aligned along the x-direction; (b) $\Gamma_{w_n}(\mathcal{A}_\mathbf{t})$ and (e) $\Gamma_{1/\kappa}(\mathcal{A}_\mathbf{t})$ for the sampled orientation of M; and (c) $\Gamma_{w_n}(\mathcal{A}_\mathbf{t})$ and (f) $\Gamma_{1/\kappa}(\mathcal{A}_\mathbf{t})$ as function of d_w.

The metrics of the magnetic field gradient are illustrated in Fig. 12. The average of magnetic field gradient behaves equivalently to flat eight-electromagnet configuration. However, as the mag-

netic field becomes more uniform, its gradient is obviously lower. Next, it appears that the uniformity of the magnetic gradient is decreasing significantly with d_w, especially, for the component $\frac{\partial b_y}{\partial y}$ and $\frac{\partial b_z}{\partial z}$.

The performance metrics of the force and torque actuation matrices in the workspace for the sampled orientations of dipole moment M are presented in Fig. 13 and 14, respectively. The manipulability indexes w_n of the force and torque have better performance when the orientation of the microrobot magnetic moment M is in the xy-plane ($\theta = 90°$) and along z-axis ($\theta = 0°$). The conditioning indexes $1/\kappa$ of force and torque reach a high value when the dipole moment M is aligned along the z-axis. From these results, it can be seen that these global performance metrics of the both force and torque control are increasing with d_w in the given OctoMag configuration. Furthermore, the impact of changing the shifting angles of EMA system will be estimated hereafter.

4.2. Analysis with respect to the tilted angle β of electromagnets for EMA systems

Let us highlight the orientation angle β of electromagnets and fix other parameters. Once again, eight electromagnets are applied to enable reliable combined torque and force singular-free control with 5 DOFs. As it has been shown above that long distance d_w from the workspace center O to the electromagnet leads globally to a slight more uniform magnetic field and gradient, in addition, the effectiveness control of magnetic microrobot is improved. Nevertheless, stronger magnetic field and gradient require a short length d_w. With a comprehensive consideration of strength and uniformity, we have set the working distance to $d_w = 65\,\text{mm}$, that is similar to the OctoMag EMA setup [43], and a workspace of $\Omega = 45\,\text{mm} \times 45\,\text{mm} \times 45\,\text{mm}$ is considered throughout the simulations. For the sake of simplicity, the eight electromagnetic coils of the EMA platform are divided in two sets: four stationary electromagnets: $e = 1..4$; and four mobile coils: $e = 5..8$, as illustrated in Fig. 8. These two sets are arranged around a common axis of rotation with an azimuth angle $\alpha_e = 45°$ ($e = 1..8$), and are pointing to the common center O of the workspace. The mobile sets are able to rotate their polar angle $\beta_e \in [0; 90°)$ ($e = 5..8$). Two cases are considered for the stationary coils set where the polar β_e ($e = 1..4$) is fixed to:

1. $\beta_e = 0°$, that is equivalent to the OctoMag [43] configuration;
2. $\beta_e = 26°$, that is close to the MiniMag [44] arrangement.

Hence, the considered reconfigurable EMA platform can vary from one to another of these configurations by changing the orientation of the polar angle β_e in their two sets of electromagnets.

In the following sections, the influence of the mobile angle β_e on the magnetic field and gradient performance indexes, and on the magnetic actuation indexes are investigated. As previously stated, each electromagnet is computed with a point dipole moment magnitude of: $\|M_e\| = 8.178\,\text{A}\,\text{m}^2$, and the microrobot is modeled from its magnetic moment $M = (1, \theta, \varphi)$, with a unit magnitude, azimuth $\varphi \in [0; 360°)$ and polar angles $\theta \in [0; 180°]$. Let us recall that the possible collision of the coils is not taken into account in this study.

4.2.1. Case #1: reconfigurable OctoMag-like setup

This section investigates a reconfigurable EMA platform similar to the OctoMag system. Specifically, the mobile set of coils is able to rotate with the same angle $\beta = \beta_e \in [0; 90°)$ ($e = 5..8$). To analyze the performance of such reconfigurable EMA setup, different simulations are conducted, and their results are presented hereafter.

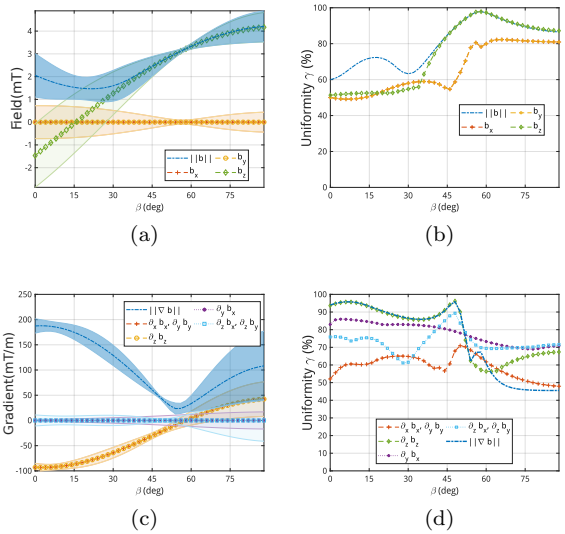

Figure 15: Performance metrics of (a)-(b) the magnetic field and (c)-(d) its gradient of reconfigurable OctoMag-like setup when the mobile coils set is rotating with $\beta \in [0; 90°)$. The markers and envelopes (a)-(c) refer to the mean and standard deviation (STD) of the fields.

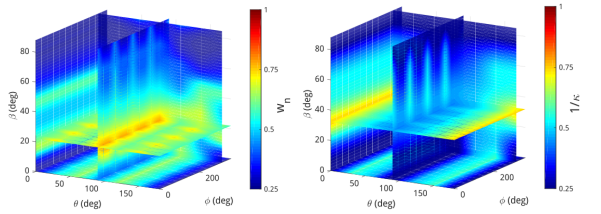

(a) Performance metrics of the force $\mathcal{A}_\mathbf{f}$

(b) Performance metrics of the force $\mathcal{A}_\mathbf{f}$

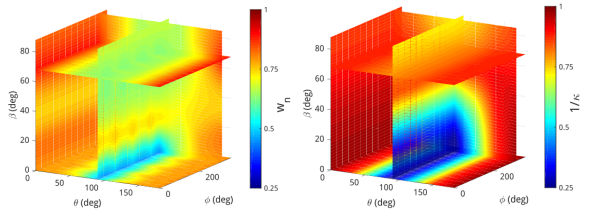

(c) Performance metrics of the torque $\mathcal{A}_\mathbf{t}$

(d) Performance metrics of the torque $\mathcal{A}_\mathbf{t}$

Figure 16: Actuation performance indexes of the (a)-(b) force and (c)-(d) torque actuation matrices for the sampled orientations of the magnetic moment of the microrobot: (a)-(c) the global normalized manipulability index Γ_{w_n}; and (b)-(d) the global conditioning index $\Gamma_{1/\kappa}$.

First, the magnetic field performance indexes are analyzed and shown in Fig. 15, for different moving angles $\beta \in [0; 90°)$. As previously analyzed, the performance indexes are axisymmetric around the z-axis, and the magnetic field and gradient behave similarly between the x and y components. In particular, the average values $\langle b_x \rangle$ and $\langle b_x \rangle$ of B, and $\left\langle \frac{\partial b_x}{\partial y} \right\rangle$, $\left\langle \frac{\partial b_x}{\partial z} \right\rangle$ and $\left\langle \frac{\partial b_y}{\partial z} \right\rangle$ of ∇B are close to zero. Moreover, from these results, two distinguishing behaviors appear: i) for low angle $\beta \lesssim 45°$, the magnetic field gradient is the strongest and more uniform; whereas ii) for higher value of β, the magnetic field becomes stronger and more uniform. Thus, the reconfigurable OctoMag-like platform exhibits a versatility to manipulate either the magnetic field or its gradient, which is only driven by simply regulating the orientation β_e of some electromagnets.

Table 4: Minimum and Maximum values of the global actuation performance indexes.

	min	(φ, θ, β)	max	(φ, θ, β)
$\Gamma_{w_n}(\mathcal{A}_\mathbf{f})$	0.241	$(0, 0, 89)$	0.772	$(0, 0, 22)$
$\Gamma_{1/\kappa}(\mathcal{A}_\mathbf{f})$	0.133	$(180, 180, 89)$	0.739	$(0, 0, 32)$
$\Gamma_{w_n}(\mathcal{A}_\mathbf{t})$	0.446	$(90, 90, 0)$	0.889	$(0, 0, 0)$
$\Gamma_{1/\kappa}(\mathcal{A}_\mathbf{t})$	0.227	$(210, 90, 0)$	0.973	$(0, 0, 68)$

Fig. 16 shows the global performance indexes for the sampled orientations of the magnetic moment M with different moving β angles. The simulation results release that if M is parallel to the xy-plane (ie. $\theta = 90°$), the global performance indexes of the torque $\mathbf{t}$ are low, whereas the force $\mathbf{f}$ is low when M is aligned along the z-axis ($\theta = 0°$or$180°$). To further investigate these results, table.4 reports the maximal and minimal values of the global performance indexes, and the corresponding angles for the sampled orientations of a unit-strength magnetic moment. It can be shown that to improve the perfromacnes of magnetic actuation, firstly, M should be globally aligned along the z-axis. Secondly, the moving angle must be set to $\beta = 32°$ in order to maximize the dexterity index $1/\kappa$ of the force, whereas a value around $\beta = 68°$ is required for the torque. In contrast, the normalized manipulability of the force and torque needs a low angle below $\beta \leq 22°$ for improvement.

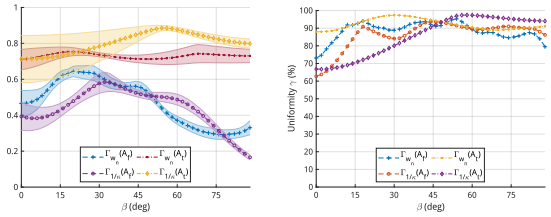

(a) (b)

Figure 17: Statistical data of the global performance indexes of the force and torque actuation matrices for $\beta \in [0; 90°)$: (a) the mean and STD, and (b) the uniformity γ metrics.

To exhibit the influence of the moving angle β on the magnetic actuation performance, Fig. 17 depicts the mean and uniformity metrics of the global performance indexes Γ_{w_n} and $\Gamma_{1/\kappa}$. The analysis of the performance indexes reveals that it is more efficient to control $\mathbf{f}$ with low angle, whereas $\mathbf{t}$ requires a higher β, especially to increase its uniformity. These simulation results demonstrate that rotating the moving angle β could make the EMA platform more flexible to control efficiently either the force $\mathbf{f}$ or the torque $\mathbf{t}$.

Finally, the impact of the moving angle β on the workspace size has been also investigated. Since the indexes are axisymmetric around the z-axis, the analysis is reported only along this direction. In particular, to evaluate the tissue penetration, the locations behind the workspace Ω could be considered. The different performance metrics are shown

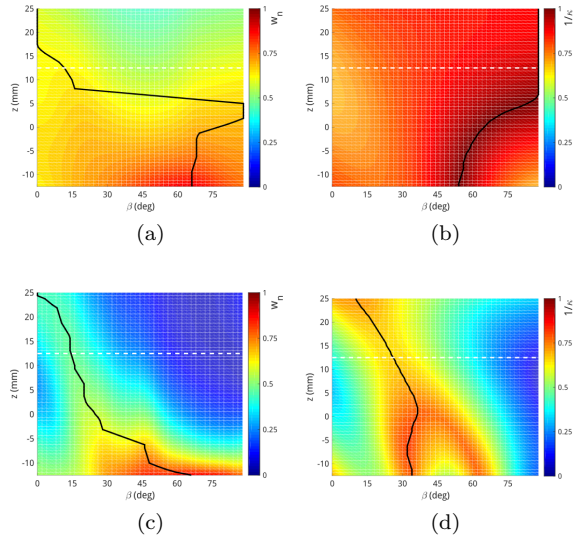

Figure 18: Performance indexes along the z-axis of (a)-(b) the torque and (c)-(d) the force actuation matrices: (a)-(c) the normalized manipulability index w_n; and (b)-(d) the dexterity index $1/\kappa$. The black line represents the maximum value of the performance indexes.

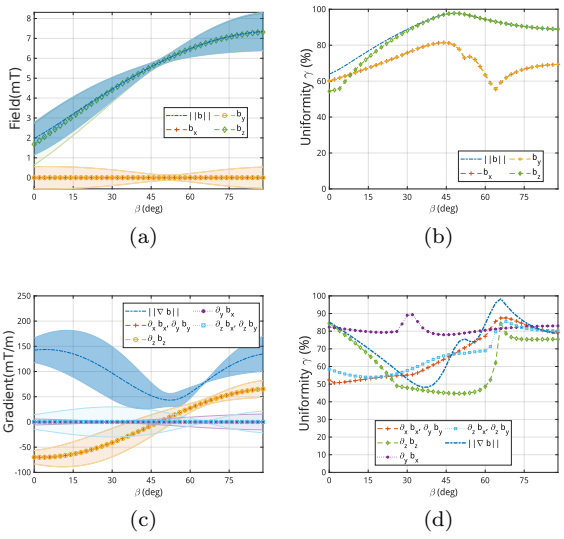

Figure 19: Performance metrics of (a)-(b) the magnetic field and (c)-(d) its gradient of reconfigurable MiniMag-like setup when the mobile coils set is rotating with $\beta \in [0; 90°)$. The markers and envelopes (a)-(c) refer to the mean and standard deviation (STD) of the fields.

in Fig. 18. Fig. 18b shows that high angle β leads to the reliable torque dexterity. Specifically, a high angle $\beta \gtrsim 50°$ allows the increasing of the value of the conditioning number $1/\kappa$. The good conditioning number of torque means that a reconfigurable EMA system is able to transmit a torque $\mathbf{t}$ along any directions more efficient. However, to enable sufficient force $\mathbf{f}$ in the high locations together with a good manipulability index w_n, a low angle $\beta \lesssim 30°$ is required. Therefore, these results exhibit that to design a versatile EMA system with both effective force and torque control, it is necessary to be able to vary the moving angle β_e of some coils. Such design objective seems a promising way to achieve optimal control of $\mathbf{f}$ and $\mathbf{t}$.

4.2.2. Case #2: reconfigurable MiniMag-like setup

The second case corresponds to EMA platform, similar to the MiniMag system. Specifically, the mobile set of coils is able to rotate with the same angle $\beta = \beta_e \in [0; 90°)$ ($e = 5..8$, as shown in Fig. 8), while the stationary set of coils is fixed to $\beta_e = 26°$ ($e = 1..4$).

Fig. 19 shows the performance metrics of the magnetic field and its gradient with a moving angle $\beta \in [0; 90°)$. Similarly, the high moving angle value $\beta \gtrsim 45°$ provides stronger and more uniform magnetic field B. Especially, the reconfigurable MiniMag-like setup induces a larger magnetic field strength along the z-axis than the OctoMag-like one (cf. Fig. 15). However, the magnetic field gradient requires a low moving angle β to be stronger and more uniform. In particular, it can be seen in Fig. 19d that their uniformity metrics γ are decreasing for $\beta < 26°$, and increasing again for $\beta > 56°$. In such case #2, it appears that it is more convenient to use high angles around $\beta \approx 50°$–$60°$ to get a suitable uniform magnetic field and gradient.

The performance indexes of the actuation matrix $\mathcal{A}(P, M)$ are evaluated for different moving β angles, and reported in Fig. 20. From these simulation results, it appears that if M is parallel to the xy-plane (ie. $\theta = 90°$), the global conditioning indexes $\Gamma_{1/\kappa}$ of both the force and torque are low, whereas the global normalized manipulability indexes Γ_{w_n} are advantageous. Moreover, when M is aligned along the z-axis ($\theta = 0° \mod 180°$), a good Γ_{w_n} is obtained and $\Gamma_{1/\kappa}$ has the greatest value. Next, the moving angle β should have a low value to enable the good global performance indexes Γ_{w_n} of the torque and the force, while their $\Gamma_{1/\kappa}$ require a value around $\beta = 60°$. These trends are clearly revealed in Fig. 21 that shows the magnetic actuation performance indexes statistical data and uniformity

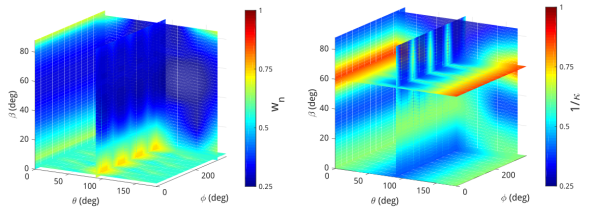

(a) Performance metrics of the force $\mathcal{A}_\mathbf{f}$ (b) Performance metrics of the force $\mathcal{A}_\mathbf{f}$

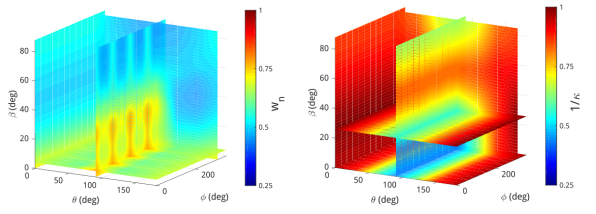

(c) Performance metrics of the torque $\mathcal{A}_\mathbf{t}$ (d) Performance metrics of the torque $\mathcal{A}_\mathbf{t}$

Figure 20: Actuation performance indexes of the (a)-(b) force and (c)-(d) torque actuation matrices for the sampled orientations of the magnetic moment of the microrobot: (a)-(c) the global normalized manipulability index Γ_{w_n}; and (b)-(d) the global conditioning index $\Gamma_{1/\kappa}$.

γ.

The influence of $\beta \in [0; 90°)$ along the z-axis has been evaluated and reported in Fig. 22. To maximize the performance indexes, the moving angle should be adjusted with respect to the z-depth position of the magnetic moment M of the microrobot. For instance, Fig. 22d shows that there are two angle routes to provide a force with a good dexterity: one with $\beta \lesssim 35°$ and the second with $\beta \gtrsim 65°$. Basically, for deep location, a low angle β enables a reliable manipulability w_n and conditioning number $1/\kappa$ metrics of both the force and torque. Therefore, the tilted angle of the applied electromagnet can be determined referring the above analysis for different applications.

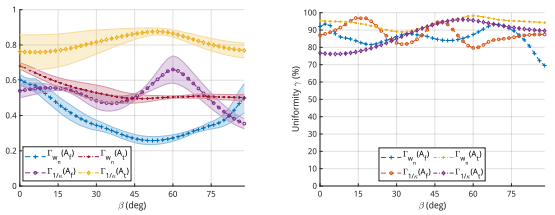

(a) (b)

Figure 21: Statistical data of the global performance indexes of the force and torque actuation matrices for $\beta \in [0; 90°)$: (a) the mean and STD, and (b) the uniformity γ metrics.

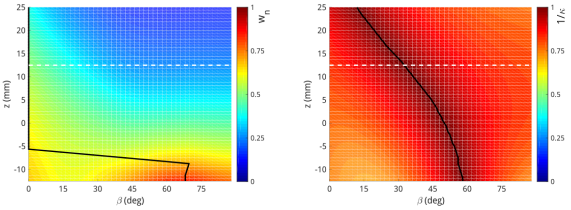

(a) (b)

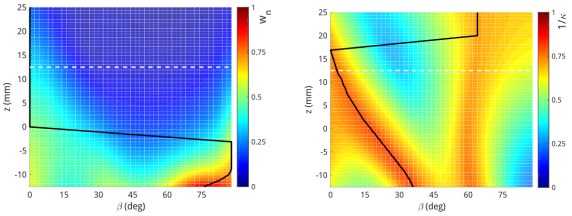

(c) (d)

Figure 22: Performance indexes along the z-axis of (a)-(b) torque and (c)-(d) the force actuation matrices: (c)-(a) the normalized manipulability index w_n; and (d)-(b) the dexterity index $1/\kappa$. The black line represents the maximum value of the performance indexes.

4.3. Discussions

Based on the numerous simulations, it appears that MiniMag-like arrangement provides the greatest magnetic field and gradient, besides, the most effective actuation performance can also be performed among the various considered configurations. However, the magnetic field distribution uniformity index Iso of MiniMag-like arrangement is less interesting than OctoMag-like arrangement, implying some difficulties to derive the control strategy. The system is capable of providing different performances by setting the positions and orientations of electromagnets. Therefore, the choice of the basic EMA configuration can be motivated based on the applications objectives and the desired manipulation tasks.

5. Design analysis

Different configurations of electromagnetic coils can produce various magnetic field distributions. The flat multi-electromagnet EMA systems are

used for 2D manipulation. For the 3D control of microrobot, the 3D configurations are applied. In this study, the six different typical systems consisting of flat four-electromagnet, flat six-electromagnet, flat eight-electromagnet, 3D six-electromagnet, OctoMag and MiniMag configurations were simulated and compared. Based on these results, an optimal configuration can be determined for the considered application.

Obviously, the investigated EMA systems all can be reconfigurable where either the distance d_w or mobile angle β is adjusted. If either the strong magnetic field or gradient is required in 2D plane, $n = 2$ and 3 coils are necessary, respectively. The flat four-electromagnet system with short distance d_w can be applied for this control with redundancy. Commonly, if 2D applications require only a weak magnetic field and its gradient, a minimum of $n = 5$ electromagnets is essential. Thus, the flat six-electromagnet or flat eight-electromagnet systems set to long distance d_w can be used to improve the field distribution and the control redundancy.

Similarly, the 3D EMA systems are also formulated with different distances d_w to achieve the desired performances. Especially, the efficiency of OctoMag-like and MiniMag-like systems has been further investigated with respect to the mobile angle β. When a strong magnetic field and gradient are of prime importance for the application, d_w has to be set to a short distance. Moreover, to enhance the magnetic field B, the tilted angle β has to be set to an high value. In contrast, to enable a proper magnetic field gradient ΔB, different specific values of β can be considered. Conversely, the long distance d_w leads to a more uniform magnetic field and gradient, higher manipulability of torque and force, and higher dexterity of torque and force. Moreover, these performance's improvements can also be realized by implementing the corresponding tilted angles β to superimpose their advantages with d_w.

From these results, various system performances can be obtained, depending on the given design parameters. All these capabilities are summarized in the chart[1] given in Fig. 23 and 24. In Fig.23, it is observed that the more electromagnets lead to the stronger magnetic field strength $\langle \|B\| \rangle$. However, the uniformity of field does not change significant by applying more coils. If the magnetic gradient

[1]For the sake of consistency between the different results, the magnetic field strength and gradient are here normalized.

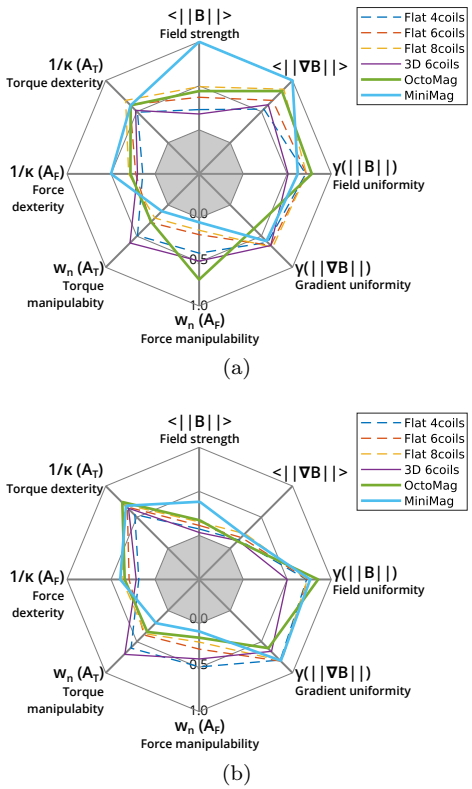

Figure 23: The optimal performances for each EMA system design for (a) short and (b) long distance d_w.

is prioritized for control, MiniMag, OctoMag and flat eight-electromagnet configurations are set to short working distance d_w. Meanwhile, MiniMag, flat eight-electromagnet and 3D six-electromagnet configurations are proposed for long distance d_w. Considering the uniformity of magnetic field and gradient, MiniMag system has the capability of generating both uniform field and gradient. OctoMag system can produce more uniform magnetic field as well, while its weakness lies in the uniformity of magnetic gradient. Besides, the flat configurations are also able to provide uniform magnetic gradient. The 3D six-electromagnet and flat four-electromagnet configurations carry the benefit of the good manipulability of torque. Especially in long distance d_w, flat four-electromagnet arrangement has significant capability of producing better manipulability of force than other configurations. With short distance d_w, OctoMag system can be used to provide good manipulability of the force. Whereas, the great dexterity of force is produced by using MiniMag system since the eight coils with such configuration could lead to more dexterous

force control. Such improved phenomenon also occurs in the term of the dexterity of torque through applying more coils.

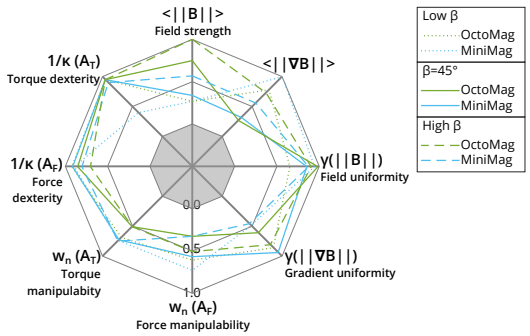

Figure 24: The optimal performances for the OctoMag-like and MiniMag-like designs regrading the mobile angle β value.

The investigation of mobile angle β is further represented in Fig. 24. It can be observed that the magnetic field generated by MiniMag-like arrangement becomes much more strong than OctoMag-like configuration when the β is set to a high angle value. Conversely, the lower mobile angle allows OctoMag-like system to produce a stronger and more uniform magnetic gradient ΔB. Comparing in Fig. 24, MiniMag-like configuration commonly presents better performance of force and torque control. When β is set to around 45°, MiniMag-like configuration has the significant capability to provide more manipulabilities of force and torque. When β is rotated to higher angle, OctoMag-like systems is able to achieve high manipulability of torque control, whereas MiniMag is good at controlling force. Therefore, for the desired application and required system performance, the optimal configuration or the design inspiration could be obtained from them.

6. CONCLUSION

In the paper, theoretical foundation of electromagnetism has been studied, especially, the point-dipole model was analyzed for magnetic field simulation. Moreover, the electromagnetic manipulation of the untethered microrobot was investigated where the motion includes translation and rotation actuated by magnetic force and torque, respectively. Furthermore, the required minimum electromagnetic coils for EMA system were estimated mathematically. Indeed, the linear dependencies regarding the applied field and gradient, and their resulting singular cases have been fully evaluated.

The various configurations of EMA systems have been studied and compared. The performance evaluation of the reconfigurable platform was thereby investigated. Several simulations were proceeded, and performance metrics of the actuated system were analyzed under different shifted distance d_w and the tilted angle β of electromagnets. Results show that the reconfigurable platform of electromagnets enables a variety of local magnetic field distribution. The evaluations of the force, torque, manipulability and the dexterity indexes demonstrate that the reconfigurable system provides more flexibility. Overall, the shorter distance d_w can be used to generate the strong magnetic field and gradient, while their uniformities require longer distance d_w. Moreover, the low angle β leads to the more efficient magnetic force control. But the magnetic torque becomes less controllable as it requires an higher angle β. Thus, when the configuration of EMA system is stationary, the system design parameters can be determined depend on the above results. If the stationary EMA platform is upgraded to a reconfigurable system by enabling the control of the distance d_w and angle β, it will be resourceful to perform various tasks. Basically, for different applications, by using the mathematical approach as we demonstrated for performant electromagnetic micromanipulation platforms, the obtained EMA system could be optimized and improved concerning the specific medical application. These would help to develop more advanced navigation control strategy of biomedical magnetic microrobot for different micromanipulation tasks. In particular, it can be used for improving the convenience of minimally invasive operation.

References

[1] F. Tendick, S. S. Sastry, R. S. Fearing, M. Cohn, Applications of micromechatronics in minimally invasive surgery, IEEE/ASME Trans. Mechatronics 3 (1) (1998) 34–42.

[2] M. J. Mack, Minimally invasive and robotic surgery, Jama 285 (5) (2001) 568–572.

[3] S. Purkayastha, T. Athanasiou, R. Casula, S. A. Darzi, Robotic surgery: a review, Hospital Medicine 65 (3) (2004) 153–159.

[4] J. Troccaz, R. Bogue, The development of medical microrobots: a review of progress, Industrial Robot: An International Journal (2008).

[5] S. Tsuda, D. Oleynikov, J. Gould, D. Azagury, B. Sandler, M. Hutter, S. Ross, E. Haas, F. Brody, R. Satava,

Sages tavac safety and effectiveness analysis: da vinci® surgical system (intuitive surgical, sunnyvale, ca), Surgical endoscopy 29 (10) (2015) 2873–2884.

[6] S.-J. Baek, S.-H. Kim, Robotics in general surgery: An evidence-based review, Asian journal of endoscopic surgery 7 (2) (2014) 117–123.

[7] L. Morelli, S. Guadagni, G. Di Franco, M. Palmeri, G. Di Candio, F. Mosca, Da vinci single site© surgical platform in clinical practice: A systematic review, The International Journal of Medical Robotics and Computer Assisted Surgery 12 (4) (2016) 724–734.

[8] J. P. Desai, R. V. Patel, A. Ferreira, S. K. Agrawal, Encyclopedia of Medical Robotics, World Scientific, 2017.

[9] G.-Z. Yang, J. Bellingham, P. E. Dupont, P. Fischer, L. Floridi, R. Full, N. Jacobstein, V. Kumar, M. McNutt, R. Merrifield, et al., The grand challenges of science robotics, Science robotics 3 (14) (2018).

[10] N. Simaan, R. M. Yasin, L. Wang, Medical technologies and challenges of robot-assisted minimally invasive intervention and diagnostics, Annual Review of Control, Robotics, and Autonomous Systems 1 (2018) 465–490.

[11] C. M. Hoang, T. K. Nguyen, V. H. Le, J. Kim, C. S. Kim, Independent electromagnetic field control for practical approach to actively locomotive wireless capsule endoscope, IEEE Transactions on Systems, Man, and Cybernetics: Systems (2019) 1–13.

[12] D. Rattner, A. Kalloo, Asge/sages working group on natural orifice translumenal endoscopic surgery, Surgical Endoscopy and Other Interventional Techniques 20 (2) (2006) 329–333.

[13] J. R. Romanelli, D. B. Earle, Single-port laparoscopic surgery: an overview, Surgical endoscopy 23 (7) (2009) 1419–1427.

[14] M. M. Tiwari, J. F. Reynoso, A. C. Lehman, A. W. Tsang, S. M. Farritor, D. Oleynikov, In vivo miniature robots for natural orifice surgery: State of the art and future perspectives, World journal of gastrointestinal surgery 2 (6) (2010) 217.

[15] D. Samarasekera, J. H. Kaouk, Robotic single port surgery: Current status and future considerations, Indian journal of urology: IJU: journal of the Urological Society of India 30 (3) (2014) 326.

[16] S. U. Bae, W. K. Jeong, S. K. Baek, Current status of robotic single-port colonic surgery, The International Journal of Medical Robotics and Computer Assisted Surgery 13 (1) (2017) e1735.

[17] F. Carpi, C. Pappone, Stereotaxis niobe® magnetic navigation system for endocardial catheter ablation and gastrointestinal capsule endoscopy, Expert review of medical devices 6 (5) (2009) 487–498.

[18] B. J. Nelson, I. K. Kaliakatsos, J. J. Abbott, Microrobots for minimally invasive medicine, Annual review of biomedical engineering 12 (2010) 55–85.

[19] M. Sitti, Voyage of the microrobots, Nature 458 (7242) (2009) 1121–1122.

[20] M. Sitti, H. Ceylan, W. Hu, J. Giltinan, M. Turan, S. Yim, E. Diller, Biomedical applications of untethered mobile milli/microrobots, Proceedings of the IEEE 103 (2) (2015) 205–224.

[21] H. Ceylan, J. Giltinan, K. Kozielski, M. Sitti, Mobile microrobots for bioengineering applications, Lab on a Chip 17 (10) (2017) 1705–1724.

[22] T. Honda, K. Arai, K. Ishiyama, Micro swimming mechanisms propelled by external magnetic fields, IEEE Transactions on Magnetics 32 (5) (1996) 5085–5087.

[23] Y. Alapan, O. Yasa, O. Schauer, J. Giltinan, A. F. Tabak, V. Sourjik, M. Sitti, Soft erythrocyte-based bacterial microswimmers for cargo delivery, Science Robotics 3 (17) (2018) eaar4423.

[24] A. Barbot, D. Decanini, G. Hwang, The rotation of microrobot simplifies 3d control inside microchannels, Scientific reports 8 (1) (2018) 1–9.

[25] R. W. Carlsen, M. R. Edwards, J. Zhuang, C. Pacoret, M. Sitti, Magnetic steering control of multi-cellular biohybrid microswimmers, Lab on a Chip 14 (19) (2014) 3850–3859.

[26] F. Carpi, N. Kastelein, M. Talcott, C. Pappone, Magnetically controllable gastrointestinal steering of video capsules, IEEE Transactions on Biomedical Engineering 58 (2) (2010) 231–234.

[27] E. Diller, M. Sitti, et al., Micro-scale mobile robotics, Foundations and Trends® in Robotics 2 (3) (2013) 143–259.

[28] A. Hosney, J. Abdalla, I. S. Amin, N. Hamdi, I. S. Khalil, In vitro validation of clearing clogged vessels using microrobots, in: 2016 6th IEEE International Conference on Biomedical Robotics and Biomechatronics (BioRob), IEEE, 2016, pp. 272–277.

[29] S. Jeon, S. Kim, S. Ha, S. Lee, E. Kim, S. Y. Kim, S. H. Park, J. H. Jeon, S. W. Kim, C. Moon, et al., Magnetically actuated microrobots as a platform for stem cell transplantation, Science Robotics 4 (30) (2019) eaav4317.

[30] V. H. Le, S. Zheng, J. Han, J.-O. Park, et al., Preparation of tumor targeting cell-based microrobots carrying nir light sensitive therapeutics manipulated by electromagnetic actuating system and chemotaxis, Journal of Micro-Bio Robotics 14 (3-4) (2018) 69–77.

[31] J. Li, B. E.-F. de Ávila, W. Gao, L. Zhang, J. Wang, Micro/nanorobots for biomedicine: Delivery, surgery, sensing, and detoxification, Science Robotics 2 (4) (2017).

[32] J. Li, X. Li, T. Luo, R. Wang, C. Liu, S. Chen, D. Li, J. Yue, S.-h. Cheng, D. Sun, Development of a magnetic microrobot for carrying and delivering targeted cells, Science Robotics 3 (19) (2018) eaat8829.

[33] S. Martel, Microrobotics in the vascular network: present status and next challenges, Journal of Micro-Bio Robotics 8 (1) (2013) 41–52.

[34] J. J. Abbott, E. Diller, A. J. Petruska, Magnetic methods in robotics, Annual Review of Control, Robotics, and Autonomous Systems 3 (2015).

[35] F. Carpi, N. Kastelein, M. Talcott, C. Pappone, Magnetically controllable gastrointestinal steering of video capsules, IEEE Trans. Biomed. Eng. 58 (2) (2011) 231–234.

[36] S. Park, K. Cha, J. Park, Development of biomedical microrobot for intravascular therapy, International Journal of Advanced Robotic Systems 7 (1) (2010) 1.

[37] K. B. Yesin, K. Vollmers, B. J. Nelson, Modeling and control of untethered biomicrorobots in a fluidic environment using electromagnetic fields, The International Journal of Robotics Research 25 (5-6) (2006) 527–536.

[38] T. W. Fountain, P. V. Kailat, J. J. Abbott, Wireless control of magnetic helical microrobots using a rotating-permanent-magnet manipulator, in: 2010 IEEE International Conference on Robotics and Automation, IEEE, 2010, pp. 576–581.

[39] A. W. Mahoney, J. J. Abbott, Five-degree-of-freedom

manipulation of an untethered magnetic device in fluid using a single permanent magnet with application in stomach capsule endoscopy, The International Journal of Robotics Research 35 (1-3) (2016) 129–147.

[40] P. Ryan, E. Diller, Magnetic actuation for full dexterity microrobotic control using rotating permanent magnets, IEEE Transactions on Robotics 33 (6) (2017) 1398–1409.

[41] W. Amokrane, K. Belharet, M. Souissi, A. B. Grayeli, A. Ferreira, Macro–micromanipulation platform for inner ear drug delivery, Robotics and Autonomous Systems 107 (2018) 10–19.

[42] S. Schuerle, S. Erni, M. Flink, B. E. Kratochvil, B. J. Nelson, Three-dimensional magnetic manipulation of micro-and nanostructures for applications in life sciences, IEEE transactions on magnetics 49 (1) (2012) 321–330.

[43] M. P. Kummer, J. J. Abbott, B. E. Kratochvil, R. Borer, A. Sengul, B. J. Nelson, Octomag: An electromagnetic system for 5-dof wireless micromanipulation, IEEE Transactions on Robotics 26 (6) (2010) 1006–1017.

[44] B. E. Kratochvil, M. P. Kummer, S. Erni, R. Borer, D. R. Frutiger, S. Schürle, B. J. Nelson, Minimag: a hemispherical electromagnetic system for 5-dof wireless micromanipulation, in: Experimental Robotics, Springer, 2014, pp. 317–329.

[45] S. Jeon, G. Jang, H. Choi, S. Park, Magnetic navigation system with gradient and uniform saddle coils for the wireless manipulation of micro-robots in human blood vessels, IEEE transactions on magnetics 46 (6) (2010) 1943–1946.

[46] H. Choi, K. Cha, J. Choi, S. Jeong, S. Jeon, G. Jang, J.-o. Park, S. Park, Ema system with gradient and uniform saddle coils for 3d locomotion of microrobot, Sensors and Actuators A: Physical 163 (1) (2010) 410–417.

[47] A. Pourkand, J. J. Abbott, A critical analysis of eight-electromagnet manipulation systems: The role of electromagnet configuration on strength, isotropy, and access, IEEE Robotics and Automation Letters 3 (4) (2018) 2957–2962.

[48] D. J. Griffiths, Introduction to Electrodynamics, 4th Edition, Cambridge University Press, 2017.

[49] D. Jiles, Introduction to magnetism and magnetic materials, CRC press, 2015.

[50] E. Diller, J. Giltinan, G. Z. Lum, Z. Ye, M. Sitti, Six-degree-of-freedom magnetic actuation for wireless microrobotics, The Int. J. Robot. Res. 35 (1-3) (2016) 114–128.

[51] E. Diller, J. Giltinan, P. Jena, M. Sitti, Three dimensional independent control of multiple magnetic microrobots, in: IEEE Int. Conf. on Intel. Robot. and Autom., 2013, pp. 2576–2581.

[52] S. Schuerle, S. Erni, M. Flink, B. E. Kratochvil, B. J. Nelson, Three-dimensional magnetic manipulation of micro-and nanostructures for applications in life sciences, IEEE Trans. Magn. 49 (1) (2013) 321–330.

[53] J. K. Salisbury, J. J. Craig, Articulated hands: Force control and kinematic issues, The International journal of Robotics research 1 (1) (1982) 4–17.

[54] T. Yoshikawa, Manipulability of robotic mechanisms, The international journal of Robotics Research 4 (2) (1985) 3–9.

[55] S. Kucuk, Z. Bingul, Comparative study of performance indices for fundamental robot manipulators, Rob. Auton. Syst. 54 (7) (2006) 567–573.

[56] J.-P. Merlet, Jacobian, manipulability, condition number, and accuracy of parallel robots, J. of Mech. Des. 128 (1) (2006) 199–206.

[57] S. Schürle, B. E. Kratochvil, S. Pané, M. A. Zeeshan, B. J. Nelson, Generating magnetic fields for controlling nanorobots in medical applications, in: Nanorobotics, Springer, 2013, pp. 275–299.

[58] K. Ishiyama, K. Arai, M. Sendoh, A. Yamazaki, Spiral-type micro-machine for medical applications, in: MHS2000. Proceedings of 2000 International Symposium on Micromechatronics and Human Science (Cat. No. 00TH8530), IEEE, 2000, pp. 65–69.

[59] R. Dreyfus, J. Baudry, M. L. Roper, M. Fermigier, H. A. Stone, J. Bibette, Microscopic artificial swimmers, Nature 437 (7060) (2005) 862–865.

[60] M. N. Faddis, W. Blume, J. Finney, A. Hall, J. Rauch, J. Sell, K. T. Bae, M. Talcott, B. Lindsay, Novel, magnetically guided catheter for endocardial mapping and radiofrequency catheter ablation, Circulation 106 (23) (2002) 2980–2985.

[61] T. Roberts, W. Hassenzahl, S. Hetts, R. Arenson, Remote control of catheter tip deflection: an opportunity for interventional mri, Magnetic Resonance in Medicine: An Official Journal of the International Society for Magnetic Resonance in Medicine 48 (6) (2002) 1091–1095.

[62] A. J. Petruska, B. J. Nelson, Minimum bounds on the number of electromagnets required for remote magnetic manipulation, IEEE Trans. Robot. 31 (3) (2015) 714–722.

[63] C. R. Thornley, L. N. Pham, J. J. Abbott, Reconsidering six-degree-of-freedom magnetic actuation across scales, IEEE Robotics and Automation Letters 4 (3) (2019) 2325–2332.

[64] J. Giltinan, M. Sitti, Simultaneous six-degree-of-freedom control of a single-body magnetic microrobot, IEEE Robotics and Automation Letters 4 (2) (2019) 508–514.

[65] E. D. Diller, J. Giltinan, G. Z. Lum, Z. Ye, M. Sitti, Six-degrees-of-freedom remote actuation of magnetic microrobots., in: Robotics: Science and Systems, 2014.

[66] Z. Nagy, B. J. Nelson, Lagrangian modeling of the magnetization and the magnetic torque on assembled soft-magnetic mems devices for fast computation and analysis, IEEE transactions on robotics 28 (4) (2012) 787–797.

[67] K. T. Nguyen, M. C. Hoang, G. Go, B. Kang, E. Choi, J.-O. Park, C.-S. Kim, Regularization-based independent control of an external electromagnetic actuator to avoid singularity in the spatial manipulation of a microrobot, Control Engineering Practice 97 (2020) 104340.

[68] D. Wong, E. B. Steager, V. Kumar, Independent control of identical magnetic robots in a plane, IEEE Robotics and Automation Letters 1 (1) (2016) 554–561.

[69] M. Etiévant, A. Bolopion, S. Régnier, N. Andreff, An improved control-oriented modeling of the magnetic field, in: 2019 International Conference on Robotics and Automation (ICRA), IEEE, 2019, pp. 6178–6184.

[70] X. Jing, W. Guo, Modeling and configuration design of electromagnetic actuation coil for a magnetically controlled microrobot, Chinese Journal of Mechanical Engineering 32 (1) (2019) 63.

Index of Terms and Notations

Notation rules

Notations	Description
x lower case	a scalar
$\mathbf{v}$ bold lower case	a vector
$\hat{\mathbf{e}}$ bold lower case	a unit vector
$\mathbf{M}$ bold upper case	a matrix or a vector field
$\mathbf{f}$	a force vector
$\mathbf{t}$	a torque vector
$\mathbf{M}^t$	the transpose of matrix $\mathbf{M}$
$\mathbf{M}^{-1}$	inverse of matrix $\mathbf{M}$
$\mathbf{M}^{+}$	pseudo-inverse of matrix $\mathbf{M}$
$\mathbb{O}_{n\times m}$	a zero matrix or null matrix of dimension $n \times m$
$\mathbb{I}_{n\times m}$	identity matrix of dimension $n \times m$
$\imath$	imaginary unit: $\imath^2 = -1$
$\boldsymbol{\nabla}$	gradient operator
$\mathbf{a} \cdot \mathbf{b}$	dot product between vector $\mathbf{a}$ and $\mathbf{b}$
$\|\mathbf{a}\|$	norm of $\mathbf{a}$
$\langle a(t) \rangle$	mean value of $a(t)$

Unless explicitly stated otherwise, throughout this document the values are stated in SI units.

List of Symbols

Symbol	Description	Units
R	Microrobot radius	m
R_v	Vessel radius	m
V	Volume	m
$\mathbf{B}$	Magnetic field flux density	T
$\boldsymbol{\nabla}\mathbf{B}$	Magnetic field flux gradient	T/m
$\mathbf{E}$	Electric field strength	V/m
$\mathbf{H}$	Magnetic field strength	A/m
$\mathbf{j}$	Electric current density	A/m^2
$\mathbf{i}$	Electric current	A
$\mathbf{m}$	Magnetic moment	A m^2
$\mathbf{M}$	Magnetization or magnetic polarization of a magnetic material that correspond to the volumetric density of magnetic moment	A/m
μ	Magnetic permeability	H/m
μ_0	Magnetic permeability of the free space: $\mu_0 = 4\pi \times 10^{-7}$	H/m
$\mathcal{A}$	Magnetic actuation matrix	NA
τ_m	Magnetic volume ratio ($\tau_m = V_m/V$)	–
$\mathbf{f}_m$	Magnetic force	N
$\mathbf{t}_m$	Magnetic torque	Nm
$\mathbf{f}_d$	Hydrodynamic drag force	N
$\mathbf{t}_d$	Hydrodynamic drag torque	Nm
κ	Dynamic shape factor	–
$\mathbf{v}$	Velocity vector	m/s
$\boldsymbol{\omega}$	Rotational velocity vector	rad/s
p	pressure vector	Pa
R_e	Reynolds number that corresponds to the ratio of inertial forces to viscous forces within a fluid	–
η	Viscosity of a fluid	Pa · s
ρ	Density of a material	kg/m^3

Lists of Acronyms

2D two-dimension
3D three-dimension
CFD computational fluid dynamics
DOF degrees of freedom
EMA electro-magnetic actuation
ENSI École Nationale Supérieur d'Ingénieurs
FMM fast marching methdod
FEM finite element methdod
GPC generalized predictive controller
HDR Habilitation à Diriger des Recherches
INSA Institut National des Sciences Appliquée
LQI linear quadratic integral
LQR linear quadratic regulator
LTI linear time-invariant system
MIS minimally invasive surgery
MNM micro/nano-motor
MPC model predictive controller
MRN magnetic resonance navigation
MRI magnetic resonance imaging
MSRL Multi-Scale Robotics Laboratory
NANOMA Nano-Actuators and Nano-Sensors for Medical Applications
NS Navier-Stokes equations
PHC Partenariats Hubert Curien
PIANHO Innovative Haptic Instrumental platform for 3D Nano-manipulation
PROTEUS Robotic Platform to facilitate transfer between Industries
PROSIT Robotic Platform for an Interactive Tele-echographic System
RBC red blood cell
RMS root mean square
SD standard deviation
SDC state dependent coefficients
SDRE state-dependent Riccati equation
SMPC state-space based model predictive controller
SPIO superparamagnetic iron oxide
TACE transcatheter arterial chemoembolization
TARE transcatheter arterial radioembolisation
TMMC therapeutic magnetic microcarriers
US (medical) ultrasound or ultrasonography

List of Terms

ANR French National Research Agency, that is to say in French "Agence Nationale de la Recherche". http://www.agence-nationale-recherche.fr

biomicromanipulation Biomicromanipulation commonly refers to the manipulation of small bioligical material such as micro-organsims, cells, tissues, DNA, etc

CNU French National Universities Council, that is to say in French "Conseil National des Universités", which comprises 57 sections covering different scientific disciplines. The 61st section involve IT engineering, automation and signal processing. https://www.conseil-national-des-universites.fr/cnu/

ETH Swiss Federal Institute of Technology in Zurich, from German "Eidgenössische Technische Hochschule". https://ethz.ch

hETD Equivalent TD hours, is the reference hour to calculate the teaching duties. The rules are as follows: 1h of course = 1.5hETD, while the others, e.g. 1h of tutorial (TD) = 1h of practical work (TP) = 1hETD

INSA CVL The INSA Centre Val de Loire was established on 1st January 2014 following the merger of the Val de Loire ENI (National Engineering School) and Bourges ENSI (Graduate Engineering School). On the Bourges campus two engineering courses are available to students with the Industrial Risk Control (MRI) and Information Technology and Cybersecurity (STI) departments, and one apprenticeship-training course, Energy Risks and the Environment (ERE), is taught together with the Cher Chamber of Commerce and Industry (CCI) Hubert Curien CFSA (Apprentice Further Training Centre) in Bourges. https://insa-centrevaldeloire.fr

AMiR Division of Microrobotics and Control Engineering, that is from German "Abteilung für Mikrorobotik und Regelungstechnik", is a department of the University of Oldenburg, Germany, headed by Prof. Dr.-Ing. Sergej Fatikov. http://www.amir.uni-oldenburg.de

medical robotics A medical robot is a robot used in the medical sciences to help the practitioner in diagnosis and treating patients. They include surgical robots, rheabilitation/assistive robotics, and so on.

microfluidic Microfluidics deals with the behaviour, precise control and manipulation of fluids that are geometrically constrained to a small scale (e.g. typically sub-millimeter) at which capillary penetration governs mass transport. It is a multidisciplinary field at the intersection of engineering, physics, chemistry, biochemistry, nanotechnology, and biotechnology, with practical applications in the design of systems in which low volumes of fluids are processed to achieve multiplexing, automation, and high-throughput screening.

micromotor Micromotor is a component of microrobot that can convert energy from various sources, such as magnetic fields, light, or chemical bonds, to do mechanical work in the form of directional motion.

microrobot Microrobot is commonly seen as a reprogrammable, microscopic machine (e.g. with dimension less than 1mm) with partly or fully self-contained capabilities entitled by on-board motion, perception, and learning.

microrobotics **Microbotics** is commonly referred to the branch of robotics, which deals with the study and application of miniature ones, such as microscale mobile robots. The term can also be used for system capable of manipulating micrometer-sized components.
While the '*micro*' prefix has been used subjectively to mean "small", standardizing on length scales should avoid confusion. A nanorobot would have characteristic dimensions at or below $L < 1$ µm, or manipulate components on the 1 to 1000 nm size range. Similarly, a millirobot would have characteristic length $L < 1$ cm; and a small-robot would have dimensions $L < 10$ cm. Anything above the milli-scale is, here, globally considered as a macroscale robot, where objects or phenomena are large enough to be visible with the naked eye.

microswimmer Microswimmer is a specific locomotion mode of a microrobot that is able to propel and do directional motion in bulk fluid.

MAE Department of Mechanical and Automation Engineering (MAE) of The Chinese University of Hong Kong (CUHK). http://www.mae.cuhk.edu.hk

MSRL Multi-Scale Robotics Lab is part of Institute of Robotics and Intelligent Systems (IRIS), ETH Zurich, Switzerland. https://msrl.ethz.ch, https://www.iris.ethz.ch

PRISME Laboratory Laboratoire Pluridisciplinaire de Recherche en Ingénierie des Systèmes, Mécanique, Énergétique. The PRISME Laboratory is from University of Orléans and INSA Centre Val de Loire (EPRES 4229). The PRISME laboratory seeks to carry out multidisciplinary research in the general domain of engineering sciences over a broad range of subject areas, including combustion in engines, energy engineering, aerodynamics, the mechanics of materials, image and signal processing, automatic control and robotics. The laboratory is split in 2 units: i) Fluids, Energy, Combustion, Propulsion (FECP) and ii) Images, Robotics, Automatic control and Signal (IRAUS). There are about 170 research professors, engineers, technicians and PhD. students working for this laboratory across several sites in Bourges, Orléans, Chartres, and Châteauroux. https://www.univ-orleans.fr/fr/prisme

Bibliography

[1] S. Hutchinson, G. D. Hager, and P. I. Corke, "A tutorial on visual servo control," *IEEE Transactions on Robotics and Automation*, vol. 12, no. 5, pp. 651–670, Oct. 1996. DOI: 10.1109/70.538972.

[2] F. Chaumette and S. Hutchinson, "Visual servo control. Part I. basic approaches," *IEEE Robotics and Automation Magazine*, vol. 13, no. 4, pp. 82–90, Nov. 2006. DOI: 10.1109/MRA.2006.250573.

[3] F. Chaumette and S. Hutchinson, "Visual servo control. Part II. advanced approaches," *IEEE Robotics and Automation Magazine*, vol. 14, no. 1, pp. 109–118, Mar. 2007. DOI: 10.1109/MRA.2007.339609.

[4] S. Fatikow and U. Rembold, *Microsystem technology and microrobotics*. Berlin Heidelberg: Springer International Publishing, 1997, ISBN: 978-3-662-03450-7. DOI: 10.1007/978-3-662-03450-7.

[5] B. J. Nelson, L. Dong, and F. Arai, "Micro/Nanorobots," in *Springer Handbook of Robotics*, B. Siciliano and O. Khatib, Eds., Berlin, Heidelberg: Springer, 2008, pp. 411–450, ISBN: 978-3-540-30301-5. DOI: 10.1007/978-3-540-30301-5_19.

[6] B. J. Nelson, I. K. Kaliakatsos, and J. J. Abbott, "Microrobots for minimally invasive medicine," *Annual Review of Biomedical Engineering*, vol. 12, no. 1, pp. 55–85, Jul. 2010. DOI: 10.1146/annurev-bioeng-010510-103409.

[7] M. Sitti, "Miniature devices: Voyage of the microrobots," *Nature*, vol. 458, no. 7242, p. 1121, 2009. DOI: 10.1038/4581121a.

[8] M. Sitti, *Mobile Microrobotics*, ser. Intelligent Robotics and Autonomous Agents. MIT Press, Jun. 2017, ISBN: 9780262036436.

[9] J. J. Abbott, Z. Nagy, F. Beyeler, and B. J. Nelson, "Robotics in the Small, Part I: Microbotics," *IEEE Robotics and Automation Magazine*, vol. 14, no. 2, pp. 92–103, Jun. 2007. DOI: 10.1109/MRA.2007.380641.

[10] M. J. Mack, "Minimally invasive and robotic surgery," *Jama*, vol. 285, no. 5, pp. 568–572, 2001. DOI: 10.1001/jama.285.5.568.

[11] P. Gomes, Ed., *Medical Robotics: Minimally Invasive Surgery*, ser. Woodhead Publishing Series in Biomaterials 51. Cambridge: Elsevier Science, Oct. 2012, ISBN: 9780857097392.

[12] J. Troccaz, Ed., *Medical Robotics*, ser. ISTE. Wiley Online Library, Mar. 2013, ISBN: 9781118563335. DOI: 10.1002/9781118562147.

[13] M. Kroh and S. Chalikonda, Eds., *Essentials of robotic surgery*. Springer International Publishing, Oct. 27, 2014, 218 pp., ISBN: 978-3-319-09564-6.

[14] H. Ryan and S. Tsuda, "History of and current systems in robotic surgery," in *Essentials of Robotic Surgery*, M. Kroh and S. Chalikonda, Eds., Springer International Publishing, 2015, pp. 1–12, ISBN: 978-3-319-09564-6. DOI: 10.1007/978-3-319-09564-6_1.

[15] G. M. Grimsby, M. E. Dwyer, M. A. Jacobs, M. C. Ost, F. X. Schneck, G. M. Cannon, and P. C. Gargollo, "Multi-institutional review of outcomes of robot-assisted laparoscopic extravesical ureteral reimplantation," *The Journal of urology*, vol. 193, no. 5, pp. 1791–1795, 2015. DOI: 10.1016/j.juro.2014.07.128.

[16] R. H. Taylor, A. Menciassi, G. Fichtinger, P. Fiorini, and P. Dario, "Medical robotics and computer-integrated surgery," in *Springer handbook of robotics*, B. Siciliano and O. Khatib, Eds., Cham: Springer International Publishing, 2016, pp. 1657–1684, ISBN: 978-3-319-32552-1. DOI: 10.1007/978-3-319-32552-1_63.

[17] J. Li, B. E.-F. de Ávila, W. Gao, L. Zhang, and J. Wang, "Micro/nanorobots for biomedicine: Delivery, surgery, sensing, and detoxification," *Science Robotics*, vol. 2, no. 4, 2017.

[18] H. Alemzadeh, J. Raman, N. Leveson, Z. Kalbarczyk, and R. K. Iyer, "Adverse events in robotic surgery: A retrospective study of 14 years of fda data," *PloS one*, vol. 11, no. 4, e0151470, 2016. DOI: 10.1371/journal.pone.0151470.

[19] N. Simaan, R. M. Yasin, and L. Wang, "Medical technologies and challenges of robot-assisted minimally invasive intervention and diagnostics," *Annual Review of Control, Robotics, and Autonomous Systems*, vol. 1, pp. 465–490, 2018.

[20] J. Hwang, J.-y. Kim, and H. Choi, "A review of magnetic actuation systems and magnetically actuated guidewire- and catheter-based microrobots for vascular interventions," *Intelligent Service Robotics*, vol. 13, no. 1, pp. 1–14, Jan. 1, 2020. DOI: 10.1007/s11370-020-00311-0.

[21] F. Tendick, S. S. Sastry, R. S. Fearing, and M. Cohn, "Applications of micromechatronics in minimally invasive surgery," *IEEE/ASME Transactions on Mechatronics*, vol. 3, no. 1, pp. 34–42, 1998.

[22] M. C. Carrozza, P. Dario, and L. P. S. Jay, "Micromechatronics in surgery," *Transactions of the Institute of Measurement and Control*, vol. 25, no. 4, pp. 309–327, 2003.

[23] S.-J. Baek and S.-H. Kim, "Robotics in general surgery: An evidence-based review," *Asian journal of endoscopic surgery*, vol. 7, no. 2, pp. 117–123, 2014.

[24] F. Courreges, P. Vieyres, and G. Poisson, "Robotized tele-echography," in *Teleradiology*, Berlin, Heidelberg: Springer International Publishing, 2008, pp. 139–154, ISBN: 978-3-540-78871-3. DOI: 10.1007/978-3-540-78871-3_13.

[25] S. Kumar and E. Krupinski, *Teleradiology*. Springer International Publishing, Jul. 25, 2008, ISBN: 9783540788713.

[26] S. Avgousti, E. G. Christoforou, A. S. Panayides, S. Voskarides, C. Novales, L. Nouaille, C. S. Pattichis, and P. Vieyres, "Medical telerobotic systems: Current status and future trends," *BioMedical Engineering OnLine*, vol. 15, no. 1, p. 96, Aug. 12, 2016. DOI: 10.1186/s12938-016-0217-7.

[27] G.-Z. Yang, J. Bellingham, P. E. Dupont, P. Fischer, L. Floridi, R. Full, N. Jacobstein, V. Kumar, M. McNutt, R. Merrifield, *et al.*, "The grand challenges of science robotics," *Science Robotics*, vol. 3, no. 14, eaar7650, 2018. DOI: 10.1126/scirobotics.aar7650.

[28] K. Ishiyama, M. Sendoh, and K. I. Arai, "Magnetic micromachines for medical applications," *Journal of Magnetism and Magnetic Materials*, Proceedings of the Joint European Magnetic Symposia (JEMS'01), vol. 242-245, pp. 41–46, Apr. 1, 2002. DOI: 10.1016/S0304-8853(01)01181-7.

[29] H. Ceylan, J. Giltinan, K. Kozielski, and M. Sitti, "Mobile microrobots for bioengineering applications," *Lab on a Chip*, vol. 17, no. 10, pp. 1705–1724, 2017. DOI: 10.1039/C7LC00064B.

[30] I. Kassim, L. Phee, W. S. Ng, F. Gong, P. Dario, and C. A. Mosse, "Locomotion techniques for robotic colonoscopy," *IEEE Engineering in Medicine and Biology Magazine*, vol. 25, no. 3, pp. 49–56, May 2006. DOI: 10.1109/MEMB.2006.1636351.

[31] G. Ciuti, A. Menciassi, and P. Dario, "Capsule endoscopy: From current achievements to open challenges," *IEEE Reviews in Biomedical Engineering*, vol. 4, pp. 59–72, 2011. DOI: 10.1109/RBME.2011.2171182.

[32] W. Gao, R. Dong, S. Thamphiwatana, J. Li, W. Gao, L. Zhang, and J. Wang, "Artificial micromotors in the mouse's stomach: A step toward in vivo use of synthetic motors," *ACS nano*, vol. 9, no. 1, pp. 117–123, 2015. DOI: 10.1021/nn507097k.

[33] A. Servant, F. Qiu, M. Mazza, K. Kostarelos, and B. J. Nelson, "Controlled in vivo swimming of a swarm of bacteria-like microrobotic flagella," *Advanced Materials*, vol. 27, no. 19, pp. 2981–2988, 2015. DOI: 10.1002/adma.201404444.

[34] O. Felfoul, M. Mohammadi, S. Taherkhani, D. de Lanauze, Y. Zhong Xu, D. Loghin, S. Essa, S. Jancik, D. Houle, M. Lafleur, L. Gaboury, M. Tabrizian, N. Kaou, M. Atkin, T. Vuong, G. Batist, N. Beauchemin, D. Radzioch, and S. Martel, "Magneto-aerotactic bacteria deliver drug-containing nanoliposomes to tumour hypoxic regions," *Nature Nanotechnology*, vol. 11, no. 11, pp. 941–947, 11 Nov. 2016. DOI: 10.1038/nnano.2016.137.

[35] S. Jeon, S. Kim, S. Ha, S. Lee, E. Kim, S. Y. Kim, S. H. Park, J. H. Jeon, S. W. Kim, C. Moon, B. J. Nelson, J.-y. Kim, S.-W. Yu, and H. Choi, "Magnetically actuated microrobots as a platform for stem cell transplantation," *Science Robotics*, vol. 4, no. 30, 2019. DOI: 10.1126/scirobotics.aav4317.

[36] J. Li and D. J. Mooney, "Designing hydrogels for controlled drug delivery," *Nature Reviews Materials*, vol. 1, no. 12, p. 16 071, 2016. DOI: 10.1038/natrevmats.2016.71.

[37] E. M. Purcell, "Life at low Reynolds number," *American Journal of Physics*, vol. 45, no. 1, pp. 3–11, 1977. DOI: 10.1119/1.10903.

[38] M. Setti, "Microscale and nanoscale robotics systems: Caracteristics, state of the art, and grand challenges," *IEEE Robotics and Automation Magazine*, vol. 14, no. 1, pp. 53–60, Mar. 2007. DOI: 10.1109/MRA.2007.339606.

[39] A. A. Solovev, Y. Mei, E. Bermúdez Ureña, G. Huang, and O. G. Schmidt, "Catalytic microtubular jet engines self-propelled by accumulated gas bubbles," *Small*, vol. 5, no. 14, pp. 1688–1692, 2009. DOI: 10.1002/smll.200900021.

[40] A. Ghosh and P. Fischer, "Controlled propulsion of artificial magnetic nanostructured propellers," *Nano letters*, vol. 9, no. 6, pp. 2243–2245, 2009. DOI: 10.1021/nl900186w.

[41] V. Garcia-Gradilla, J. Orozco, S. Sattayasamitsathit, F. Soto, F. Kuralay, A. Pourazary, A. Katzenberg, W. Gao, Y. Shen, and J. Wang, "Functionalized ultrasound-propelled magnetically guided nanomotors: Toward practical biomedical applications," *ACS nano*, vol. 7, no. 10, pp. 9232–9240, 2013. DOI: 10.1021/nn403851v.

[42] V. Magdanz, M. Medina-Sánchez, Y. Chen, M. Guix, and O. G. Schmidt, "How to improve spermbot performance," *Advanced Functional Materials*, vol. 25, no. 18, pp. 2763–2770, 2015. DOI: 10.1002/adfm.201500015.

[43] P. Dario, R. Valleggi, M. Carrozza, M. Montesi, and M. Cocco, "Microactuators for microrobots: A critical survey," *Journal of Micromechanics and microengineering*, vol. 2, no. 3, p. 141, 1992.

[44] J. J. Abbott, K. E. Peyer, L. Dong, and B. J. Nelson, "How should microrobots swim?" In *Springer Tracts in Advanced Robotics*, vol. 66, Springer Berlin Heidelberg, 2010, pp. 157–167. DOI: 10.1007/978-3-642-14743-2_14.

[45] T. Honda, K. Arai, and K. Ishiyama, "Micro swimming mechanisms propelled by external magnetic fields," *IEEE Transactions on Magnetics*, vol. 32, no. 5, pp. 5085–5087, Sep. 1996. DOI: 10.1109/20.539498.

[46] H. Zhou, C. C. Mayorga-Martinez, S. Pané, L. Zhang, and M. Pumera, "Magnetically Driven Micro and Nanorobots," *Chemical Reviews*, Mar. 31, 2021. DOI: 10.1021/acs.chemrev.0c01234.

[47] K. B. Yesin, K. Vollmers, and B. J. Nelson, "Modeling and Control of Untethered Biomicrorobots in a Fluidic Environment Using Electromagnetic Fields," *The International Journal of Robotics Research*, vol. 25, no. 5-6, pp. 527–536, May 2006. DOI: 10.1177/0278364906065389.

[48] S. Martel, J.-B. Mathieu, O. Felfoul, A. Chanu, E. Aboussouan, S. Tamaz, P. Pouponneau, L. Yahia, G. Beaudoin, G. Soulez, and M. Mankiewicz, "Automatic navigation of an untethered device in the artery of a living animal using a conventional clinical magnetic resonance imaging system," *Applied Physics Letters*, vol. 90, no. 11, pp. 11–13, 2007. DOI: 10.1063/1.2713229.

[49] T. W. Fountain, P. V. Kailat, and J. J. Abbott, "Wireless control of magnetic helical microrobots using a rotating-permanent-magnet manipulator," in *IEEE International Conference on Robotics and Automation (ICRA)*, IEEE, 2010, pp. 576–581.

[50] B. E. Kratochvil, M. P. Kummer, S. Erni, R. Borer, D. R. Frutiger, S. Schürle, and B. J. Nelson, "MiniMag: A hemispherical electromagnetic system for 5-DOF wireless micromanipulation," *Springer Tracts in Advanced Robotics*, vol. 79, pp. 317–329, 2014. DOI: 10.1007/978-3-642-28572-1_22.

[51] M. P. Kummer, J. J. Abbott, B. E. Kratochvil, R. Borer, A. Sengul, and B. J. Nelson, "Octomag: An electromagnetic system for 5-dof wireless micromanipulation," *IEEE Transactions on Robotics*, vol. 26, no. 6, pp. 1006–1017, 2010. DOI: 10.1109/TRO.2010.2073030.

[52] H. Choi, J.-o. Park, and S. Park, "Electromagnetic Actuated Micro and Nano Robots," in *The Encyclopedia of Medical Robotics*, vol. 2, World Scientific, 2018, pp. 1–32. DOI: 10.1142/9789813232280_0006.

[53] W. Amokrane, K. Belharet, M. Souissi, A. B. Grayeli, and A. Ferreira, "Macro–micromanipulation platform for inner ear drug delivery," *Robotics and Autonomous Systems*, vol. 107, pp. 10–19, 2018.

[54] D. Li, F. Niu, J. Li, X. Li, and D. Sun, "Gradient-Enhanced Electromagnetic Actuation System With a New Core Shape Design for Microrobot Manipulation," *IEEE Transactions on Industrial Electronics*, vol. 67, no. 6, pp. 4700–4710, Jun. 2020. DOI: 10.1109/TIE.2019.2928283.

[55] Z. Yang and L. Zhang, "Magnetic Actuation Systems for Miniature Robots: A Review," *Advanced Intelligent Systems*, vol. 2, no. 9, p. 2 000 082, 2020. DOI: 10.1002/aisy.202000082.

[56] O. Erin, M. Boyvat, M. E. Tiryaki, M. Phelan, and M. Sitti, "Magnetic Resonance Imaging System–Driven Medical Robotics," *Advanced Intelligent Systems*, vol. 2, no. 2, p. 1 900 110, 2020. DOI: 10.1002/aisy.201900110.

[57] J. Wang, *Nanomachines: fundamentals and applications*. Wiley Online Library, 2013.

[58] S. Pané, J. Puigmartí-Luis, C. Bergeles, X. Z. Chen, E. Pellicer, J. Sort, V. Počepcová, A. Ferreira, and B. J. Nelson, "Imaging Technologies for Biomedical Micro- and Nanoswimmers," *Advanced Materials Technologies*, vol. 1800575, pp. 1–16, 2018. DOI: 10.1002/admt.201800575.

[59] C. R. Reid, H. MacDonald, R. P. Mann, J. A. Marshall, T. Latty, and S. Garnier, "Decision-making without a brain: How an amoeboid organism solves the two-armed bandit," *Journal of The Royal Society Interface*, vol. 13, no. 119, p. 20 160 030, 2016. DOI: 10.1098/rsif.2016.0030.

[60] R. W. Carlsen and M. Sitti, "Bio-hybrid cell-based actuators for microsystems," *Small*, vol. 10, no. 19, pp. 3831–3851, 2014. DOI: 10.1002/smll.201400384.

[61] J. A. Sethian, *Level Set Methods and Fast Marching Methods: evolving interfaces in computational geometry, fluid mechanics, computer vision, and materials science*. Cambridge university press Cambridge, Jun. 1, 1999, 400 pp., ISBN: 0521645573.

[62] J.-B. Mathieu, G. Beaudoin, and S. Martel, "Method of propulsion of a ferromagnetic core in the cardiovascular system through magnetic gradients generated by an MRI system," *IEEE Transactions on Biomedical Engineering*, vol. 53, no. 2, pp. 292–299, 2006. DOI: 10.1109/TBME.2005.862570.

[63] F. Martini, *Fundamentals of Anatomy and Physiology*, 11th ed. New York: Pearson Education, Limited, 2018, 1272 pp., ISBN: 9780134396026.

[64] Y. C. Fung, *Biomechanics: Mechanical Properties of Living Tissues*, 2nd ed. Springer Science & Business Media, 1993, 585 pp., ISBN: 978-1-4757-2257-4.

[65] Y. C. Fung, *Biomechanics: Circulation*, 3rd ed. Springer Science & Business Media, 1997, 587 pp., ISBN: 978-1-4757-2696-1.

[66] W. F. Boron and E. L. Boulpaep, *Medical Physiology*. Elsevier Health Sciences, Dec. 3, 2008, 4220 pp., ISBN: 978-1-4377-2017-4.

[67] E. Gauger and H. Stark, "Numerical study of a microscopic artificial swimmer," *Physical Review E*, vol. 74, no. 2, p. 021 907, Aug. 2006. DOI: 10.1103/PhysRevE.74.021907.

[68] S. Tamaz, R. Gourdeau, A. Chanu, J.-B. Mathieu, and S. Martel, "Real-time MRI-based control of a ferromagnetic core for endovascular navigation," *IEEE Transactions on Biomedical Engineering*, vol. 55, no. 7, pp. 1854–1863, 2008. DOI: 10.1109/TBME.2008.919720.

[69] L. Arcèse, M. Fruchard, and A. Ferreira, "Endovascular Magnetically-Guided Robots: Navigation Modeling and Optimization," *IEEE Transactions on Biomedical Engineering*, vol. 54, no. 4, pp. 977–987, 2012. DOI: 10.1109/TBME.2011.2181508>.

[70] R. Dreyfus, J. Baudry, M. L. Roper, M. Fermigier, H. A. Stone, and J. Bibette, "Microscopic artificial swimmers," *Nature*, vol. 437, no. 7060, pp. 862–865, 7060 Oct. 2005. DOI: 10.1038/nature04090.

[71] A. Yamazaki, M. Sendoh, K. Ishiyama, K. Ichi Arai, R. Kato, M. Nakano, and H. Fukunaga, "Wireless micro swimming machine with magnetic thin film," *Journal of*

Magnetism and Magnetic Materials, Proceedings of the International Conference on Magnetism (ICM 2003), vol. 272-276, E1741–E1742, May 1, 2004. DOI: 10.1016/j.jmmm.2003.12.337.

[72] B. Behkam and M. Sitti, "Design Methodology for Biomimetic Propulsion of Miniature Swimming Robots," *Journal of Dynamic Systems, Measurement, and Control*, vol. 128, no. 1, pp. 36–43, Mar. 1, 2006. DOI: 10.1115/1.2171439.

[73] K. E. Peyer, L. Zhang, and B. J. Nelson, "Bio-inspired magnetic swimming microrobots for biomedical applications," *Nanoscale*, vol. 5, no. 4, pp. 1259–1272, 2013. DOI: 10.1039/C2NR32554C.

[74] A. F. Tabak and S. Yesilyurt, "Improved kinematic models for two-link helical micro/nanoswimmers," *IEEE Transactions on Robotics*, vol. 30, no. 1, pp. 14–25, 2014. DOI: 10.1109/TRO.2013.2281551.

[75] J. Nam, W. Lee, J. Kim, and G. Jang, "Magnetic Helical Robot for Targeted Drug-Delivery in Tubular Environments," *IEEE/ASME Transactions on Mechatronics*, vol. 22, no. 6, pp. 2461–2468, Dec. 2017. DOI: 10.1109/TMECH.2017.2761786.

[76] S. Palagi and P. Fischer, "Bioinspired microrobots," *Nature Reviews Materials*, vol. 3, no. 6, pp. 113–124, 2018. DOI: 10.1038/s41578-018-0016-9.

[77] L. Zhang, J. J. Abbott, L. Dong, K. E. Peyer, B. E. Kratochvil, H. Zhang, C. Bergeles, and B. J. Nelson, "Characterizing the swimming properties of artificial bacterial flagella.," *Nano letters*, vol. 9, no. 10, pp. 3663–7, 2009. DOI: 10.1021/nl901869j.

[78] S. Martel, M. Mohammadi, O. Felfoul, Zhao Lu, and P. Pouponneau, "Flagellated magnetotactic bacteria as controlled MRI-trackable propulsion and steering systems for medical nanorobots operating in the human microvasculature," *The International Journal of Robotics Research*, vol. 28, no. 4, pp. 571–582, 2009. DOI: 10.1177/0278364908100924.

[79] I. S. Khalil, V. Magdanz, S. Sánchez, O. G. Schmidt, L. Abelmann, and S. Misra, "Magnetic Control of Potential Microrobotic Drug Delivery Systems : Nanoparticles , Magnetotactic Bacteria and Self- Propelled Microjets," in *Annual International Conference of the IEEE Engineering in Medicine and Biology Society (EMBC)*, 2013, pp. 5299–5302. DOI: 10.1109/EMBC.2013.6610745.

[80] I. S. M. Khalil, V. Magdanz, S. Sanchez, O. G. Schmidt, and S. Misra, "Precise Localization and Control of Catalytic Janus Micromotors Using Weak Magnetic Fields," *International Journal of Advanced Robotic Systems*, vol. 12, no. 1, p. 2, Jan. 2015. DOI: 10.5772/58873.

[81] A. X. Lu, Y. Liu, H. Oh, A. Gargava, E. Kendall, Z. Nie, D. L. DeVoe, and S. R. Raghavan, "Catalytic Propulsion and Magnetic Steering of Soft, Patchy Microcapsules: Ability to Pick-Up and Drop-Off Microscale Cargo," *ACS Applied Materials & Interfaces*, vol. 8, no. 24, pp. 15 676–15 683, Jun. 2016. DOI: 10.1021/acsami.6b01245.

[82] D. H. Kim, P. S. S. Kim, A. A. Julius, and Min Jun Kim, "Three-dimensional control of engineered motile cellular microrobots," in *IEEE International Conference on Robotics and Automation*, May 2012, pp. 721–726. DOI: 10.1109/ICRA.2012.6225031.

[83] Y. Alapan, O. Yasa, O. Schauer, J. Giltinan, A. F. Tabak, V. Sourjik, and M. Sitti, "Soft erythrocyte-based bacterial microswimmers for cargo delivery," *Science Robotics*, vol. 3, no. 17, eaar4423, Apr. 25, 2018. DOI: 10.1126/scirobotics.aar4423.

[84] M. Aubry, W.-A. Wang, Y. Guyodo, E. Delacou, J.-M. Guigner, O. Espeli, A. Lebreton, F. Guyot, and Z. Gueroui, "Engineering E. coli for Magnetic Control and the Spatial

Localization of Functions," *ACS Synthetic Biology*, vol. 9, no. 11, pp. 3030–3041, Nov. 20, 2020. DOI: 10.1021/acssynbio.0c00286.

[85] A. Cavalcanti, B. Shirinzadeh, T. Fukuda, and S. Ikeda, "Nanorobot for Brain Aneurysm," *The International Journal of Robotics Research*, vol. 28, no. 4, pp. 558–570, Apr. 1, 2009. DOI: 10.1177/0278364908097586.

[86] L. P. Chua, J. Zhang, and T. Zhou, "Numerical study of a complete anastomosis model for the coronary artery bypass," *International Communications in Heat and Mass Transfer*, vol. 32, no. 3, pp. 473–482, Feb. 1, 2005. DOI: 10.1016/j.icheatmasstransfer.2004.03.016.

[87] A. K. Politis, G. P. Stavropoulos, M. N. Christolis, F. G. Panagopoulos, N. S. Vlachos, and N. C. Markatos, "Numerical modeling of simulated blood flow in idealized composite arterial coronary grafts: Steady state simulations," *Journal of Biomechanics*, vol. 40, no. 5, pp. 1125–1136, Jan. 1, 2007. DOI: 10.1016/j.jbiomech.2006.05.008.

[88] C. Vlachopoulos, M. O'Rourke, and W. W. Nichols, *McDonald's Blood Flow in Arteries: Theoretical, Experimental and Clinical Principles*. CRC Press, Jul. 29, 2011, 758 pp., ISBN: 978-1-4441-2878-9.

[89] M. Zamir, *The Physics of Pulsatile Flow*. Springer Science & Business Media, Dec. 6, 2012, 232 pp., ISBN: 978-1-4612-1282-9.

[90] A. Afshari, M. Akbari, D. Toghraie, and M. E. Yazdi, "Experimental investigation of rheological behavior of the hybrid nanofluid of MWCNT–alumina/water (80%)–ethylene-glycol (20%)," *Journal of Thermal Analysis and Calorimetry*, vol. 132, no. 2, pp. 1001–1015, May 1, 2018. DOI: 10.1007/s10973-018-7009-1.

[91] U. Dinnar, *Cardiovascular Fluid Dynamics*. CRC Press, Aug. 15, 2019, 241 pp., ISBN: 978-1-00-069688-2.

[92] D. Quemada, "Rheology of concentrated disperse systems II. A model for non-newtonian shear viscosity in steady flows," *Rheologica Acta*, vol. 17, no. 6, pp. 632–642, Nov. 1, 1978. DOI: 10.1007/BF01522036.

[93] A. R. Pries and T. W. Secomb, "Blood Flow in Microvascular Networks," in *Comprehensive Physiology*, American Cancer Society, 2011, pp. 3–36, ISBN: 978-0-470-65071-4. DOI: 10.1002/cphy.cp020401.

[94] A. R. Pries, D. Neuhaus, and P. Gaehtgens, "Blood viscosity in tube flow: Dependence on diameter and hematocrit," *American Journal of Physiology-Heart and Circulatory Physiology*, vol. 263, no. 6, H1770–H1778, Dec. 1, 1992. DOI: 10.1152/ajpheart.1992.263.6.H1770.

[95] A. S. Popel and P. C. Johnson, "Microcirculation and Hemorheology," *Annual Review of Fluid Mechanics*, vol. 37, pp. 43–69, Jan. 1, 2005. DOI: 10.1146/annurev.fluid.37.042604.133933.

[96] O. K. Baskurt and H. J. Meiselman, "Blood rheology and hemodynamics," *Seminars in Thrombosis and Hemostasis*, vol. 29, no. 5, pp. 435–450, Oct. 2003. DOI: 10.1055/s-2003-44551.

[97] J. Happel and H. Brenner, *Low Reynolds Number Hydrodynamics*, ser. Mechanics of Fluids and Transport Processes. Dordrecht: Springer Netherlands, 1983, vol. 1, ISBN: 978-90-247-2877-0. DOI: 10.1007/978-94-009-8352-6.

[98] E. Guyon, J. P. Hulin, L. Petit, and C. D. Mitescu, *Physical Hydrodynamics*. Oxford University Press, 2015, 547 pp., ISBN: 978-0-19-870245-0.

[99] J. R. Womersley, "Method for the calculation of velocity, rate of flow and viscous drag in arteries when the pressure gradient is known," *The Journal of Physiology*, vol. 127, no. 3, pp. 553–563, Mar. 28, 1955. DOI: 10.1113/jphysiol.1955.sp005276.

[100] D. W. Holdsworth, C. J. D. Norley, R. Frayne, D. A. Steinman, and B. K. Rutt, "Characterization of common carotid artery blood-flow waveforms in normal human subjects," *Physiological Measurement*, vol. 20, no. 3, pp. 219–240, Jan. 1999. DOI: 10.1088/0967-3334/20/3/301.

[101] T. S. Anirudhan and S. Sandeep, "Synthesis, characterization, cellular uptake and cytotoxicity of a multi-functional magnetic nanocomposite for the targeted delivery and controlled release of doxorubicin to cancer cells," *Journal of Materials Chemistry*, vol. 22, no. 25, pp. 12 888–12 899, Jun. 6, 2012. DOI: 10.1039/C2JM31794J.

[102] S. Kim, F. Qiu, S. Kim, A. Ghanbari, C. Moon, L. Zhang, B. J. Nelson, and H. Choi, "Fabrication and Characterization of Magnetic Microrobots for Three-Dimensional Cell Culture and Targeted Transportation," *Advanced Materials*, vol. 25, no. 41, pp. 5863–5868, 2013. DOI: 10.1002/adma.201301484.

[103] X. Dong and M. Sitti, "Controlling two-dimensional collective formation and cooperative behavior of magnetic microrobot swarms," *The International Journal of Robotics Research*, vol. 39, no. 5, pp. 617–638, Apr. 1, 2020. DOI: 10.1177/0278364920903107.

[104] J. J. Abbott, E. Diller, and A. J. Petruska, "Magnetic Methods in Robotics," *Annual Review of Control, Robotics, and Autonomous Systems*, vol. 3, no. 1, pp. 57–90, 2020. DOI: 10.1146/annurev-control-081219-082713.

[105] D. J. Griffiths, *Introduction to Electrodynamics*, 4th ed. Cambridge University Press, Jun. 29, 2017, 624 pp., ISBN: 978-1-108-35714-2.

[106] D. Jiles, *Introduction to Magnetism and Magnetic Materials*. CRC Press, Sep. 18, 2015, 616 pp., ISBN: 978-1-4822-3888-4.

[107] A. Sommerfeld, *Electrodynamics*, ser. Lectures on Theoretical Physics. Academic Press, 1964.

[108] E. P. Furlani, *Permanent magnet and electromechanical devices: materials, analysis, and applications*. Academic press, 2001, 540 pp., ISBN: 978-0-12-269951-1. DOI: 10.1016/B978-0-12-269951-1.X5000-1.

[109] L. D. Landau, J. Bell, M. Kearsley, L. Pitaevskii, E. Lifshitz, and J. Sykes, *Electrodynamics of continuous media*, ser. Course of Theoretical Physics. Elsevier Science, 1984, vol. 8.

[110] F. M. White, *Viscous Fluid Flow*, 3rd ed. New York: McGraw-Hill, Jan. 5, 2005.

[111] J. W. Maccoll, "Aerodynamics of a spinning sphere," *The Aeronautical Journal*, vol. 32, no. 213, pp. 777–798, Sep. 1928. DOI: 10.1017/S0368393100136260.

[112] W. L. Haberman and R. M. Sayre, "Motion of rigid and fluid spheres in stationary and moving liquds inside cylindrical tubes," 1143, 1958. [Online]. Available: http://hdl.handle.net/1721.3/48988.

[113] R. Chhabra, S. Agarwal, and K. Chaudhary, "A note on wall effect on the terminal falling velocity of a sphere in quiescent Newtonian media in cylindrical tubes," *Powder Technology*, vol. 129, no. 1-3, pp. 53–58, Jan. 8, 2003. DOI: 10.1016/S0032-5910(02)00164-X.

[114] G. Kasper, T. Niida, and M. Yang, "Measurements of viscous drag on cylinders and chains of spheres with aspect ratios between 2 and 50," *Journal of Aerosol Science*, vol. 16, no. 6, pp. 535–556, Jan. 1985. DOI: 10.1016/0021-8502(85)90006-0.

[115] G. V. Madhav and R. P. Chhabra, "Drag on non-spherical particles in viscous fluids," *International Journal of Mineral Processing*, vol. 43, no. 1-2, pp. 15–29, Apr. 1995. DOI: 10.1016/0301-7516(94)00038-2.

[116] A. V. Filippov, "Drag and torque on clusters of N arbitrary spheres at low Reynolds number," *Journal of Colloid and Interface Science*, vol. 229, no. 1, pp. 184–195, 2000. DOI: 10.1006/jcis.2000.6981.

[117] A. S. Geller, L. Mondy, D. J. Rader, and M. S. Ingber, "Boundary element method calculations of the mobility of nonspherical particles-1. Linear chains," *Journal of Aerosol Science*, vol. 24, no. 5, pp. 597–609, 1993. DOI: 10.1016/0021-8502(93)90017-4.

[118] R. Kehlenbeck and R. D. Felice, "Empirical Relationships for the Terminal Settling Velocity of Spheres in Cylindrical Columns," *Chemical Engineering & Technology*, vol. 22, no. 4, pp. 303–308, 1999. DOI: 10.1002/(sici)1521-4125(199904)22:4<303::aid-ceat303>3.0.co;2-8.

[119] N. Kishore and S. Gu, "Wall effects on flow and drag phenomena of spheroid particles at moderate Reynolds numbers," *Industrial and Engineering Chemistry Research*, vol. 49, no. 19, pp. 9486–9495, 2010. DOI: 10.1021/ie1011189.

[120] W. Wang, T.-Y. Chiang, D. Velegol, and T. E. Mallouk, "Understanding the efficiency of autonomous nano-and microscale motors," *Journal of the American Chemical Society*, vol. 135, no. 28, pp. 10 557–10 565, 2013.

[121] S. Sánchez, L. Soler, and J. Katuri, "Chemically powered micro-and nanomotors," *Angew. Chem. Int. Ed.*, vol. 54, no. 5, pp. 1414–1444, 2015.

[122] B. Jurado-Sánchez and A. Escarpa, "Milli, micro and nanomotors: Novel analytical tools for real-world applications," *TrAC Trends in Analytical Chemistry*, Recent Advances and Trends in Analytical Nanoscience and Nanotechnology, vol. 84, pp. 48–59, Nov. 1, 2016. DOI: 10.1016/j.trac.2016.03.009.

[123] J. Katuri, X. Ma, M. M. Stanton, and S. Sánchez, "Designing Micro- and Nanoswimmers for Specific Applications," *Accounts of Chemical Research*, vol. 50, no. 1, pp. 2–11, Jan. 17, 2017. DOI: 10.1021/acs.accounts.6b00386.

[124] J. Wang and W. Gao, "Nano/Microscale Motors: Biomedical Opportunities and Challenges," *ACS Nano*, vol. 6, no. 7, pp. 5745–5751, Jul. 24, 2012. DOI: 10.1021/nn3028997.

[125] S. Sanchez, A. A. Solovev, S. Schulze, and O. G. Schmidt, "Controlled manipulation of multiple cells using catalytic microbots," *Chemical Communications*, vol. 47, no. 2, pp. 698–700, Dec. 14, 2010. DOI: 10.1039/C0CC04126B.

[126] W. Gao, X. Feng, A. Pei, Y. Gu, J. Li, and J. Wang, "Seawater-driven magnesium based Janus micromotors for environmental remediation," *Nanoscale*, vol. 5, no. 11, pp. 4696–4700, May 16, 2013. DOI: 10.1039/C3NR01458D.

[127] R. Golestanian, T. B. Liverpool, and A. Ajdari, "Designing phoretic micro- and nanoswimmers," *New Journal of Physics*, vol. 9, no. 5, pp. 126–126, May 2007. DOI: 10.1088/1367-2630/9/5/126.

[128] J. Anderson, "Colloid Transport By Interfacial Forces," *Annual Review of Fluid Mechanics*, vol. 21, no. 1, pp. 61–99, 1989. DOI: 10.1146/annurev.fluid.21.1.61.

[129] Y. Solomentsev and J. L. Anderson, "Electrophoresis of slender particles," *Journal of Fluid Mechanics*, vol. 279, p. 197, Nov. 1994. DOI: 10.1017/S0022112094003885.

[130] W. F. Paxton, P. T. Baker, T. R. Kline, Y. Wang, T. E. Mallouk, and A. Sen, "Catalytically Induced Electrokinetics for Motors and Micropumps," *Journal of the*

American Chemical Society, vol. 128, no. 46, pp. 14 881–14 888, Nov. 2006. DOI: 10.1021/ja0643164.

[131] V. M. Fomin, M. Hippler, V. Magdanz, L. Soler, S. Sánchez, and O. G. Schmidt, "Propulsion mechanism of catalytic microjet engines," *IEEE Transactions on Robotics*, vol. 30, no. 1, pp. 40–48, Feb. 2014. DOI: 10.1109/TRO.2013.2283929.

[132] A. Klingner, I. S. Khalil, V. Magdanz, V. M. Fomin, O. G. Schmidt, and S. Misra, "Modeling of Unidirectional-Overloaded Transition in Catalytic Tubular Microjets," *The Journal of Physical Chemistry C*, vol. 121, no. 27, pp. 14 854–14 863, Jul. 2017. DOI: 10.1021/acs.jpcc.7b02447.

[133] L. Li, J. Wang, T. Li, W. Song, and G. Zhang, "Hydrodynamics and propulsion mechanism of self-propelled catalytic micromotors: Model and experiment," *Soft Matter*, vol. 10, no. 38, pp. 7511–7518, Jul. 2014. DOI: 10.1039/C4SM01070A.

[134] J. R. Howse, R. A. Jones, A. J. Ryan, T. Gough, R. Vafabakhsh, and R. Golestanian, "Self-Motile Colloidal Particles: From Directed Propulsion to Random Walk," *Physical Review Letters*, vol. 99, no. 4, pp. 3–6, 2007. DOI: 10.1103/PhysRevLett.99.048102.

[135] Y. Mei, A. A. Solovev, S. Sanchez, and O. G. Schmidt, "Rolled-up nanotech on polymers: From basic perception to self-propelled catalytic microengines," *Chemical Society Reviews*, vol. 40, no. 5, pp. 2109–2119, Apr. 18, 2011. DOI: 10.1039/C0CS00078G.

[136] I. S. Khalil, V. Magdanz, S. Sanchez, O. G. Schmidt, and S. Misra, "The control of self-propelled microjets inside a microchannel with time-varying flow rates," *IEEE Transactions on Robotics*, vol. 30, no. 1, pp. 49–58, Feb. 2014. DOI: 10.1109/TRO.2013.2281557.

[137] S. Sanchez, A. A. Solovev, S. M. Harazim, and O. G. Schmidt, "Microbots swimming in the flowing streams of microfluidic channels," *Journal of the American Chemical Society*, vol. 133, no. 4, pp. 701–703, 2010.

[138] J. R. Baylis, J. H. Yeon, M. H. Thomson, A. Kazerooni, X. Wang, A. E. St. John, E. B. Lim, D. Chien, A. Lee, J. Q. Zhang, J. M. Piret, L. S. Machan, T. F. Burke, N. J. White, and C. J. Kastrup, "Self-propelled particles that transport cargo through flowing blood and halt hemorrhage," *Science Advances*, vol. 1, no. 9, pp. 1–8, 2015.

[139] W. Wang, W. Duan, S. Ahmed, T. E. Mallouk, and A. Sen, "Small power: Autonomous nano- and micromotors propelled by self-generated gradients," *Nano Today*, vol. 8, no. 5, pp. 531–554, Oct. 2013. DOI: 10.1016/j.nantod.2013.08.009.

[140] B. Jang, W. Wang, S. Wiget, A. Petruska, X. Chen, C. Hu, A. Hong, D. Folio, A. Ferreira, S. Pané, and B. Nelson, "Catalytic locomotion of core-shell nanowire motors," *ACS Nano*, vol. 10, no. 11, pp. 9983–9991, Nov. 2016. DOI: 10.1021/acsnano.6b04224.

[141] J. L. Anderson, M. E. Lowell, and D. C. Prieve, "Motion of a particle generated by chemical gradients Part 1. Non-electrolytes," *Journal of Fluid Mechanics*, vol. 117, pp. 107–121, Apr. 1982. DOI: 10.1017/s0022112082001542.

[142] D. C. Prieve, J. L. Anderson, J. P. Ebel, and M. E. Lowell, "Motion of a particle generated by chemical gradients. Part 2. Electrolytes," *Journal of Fluid Mechanics*, vol. 148, pp. 247–269, Nov. 1984. DOI: 10.1017/S0022112084002330.

[143] S. Jeong, H. Choi, J. Choi, C. Yu, J.-o. Park, and S. Park, "Novel electromagnetic actuation (EMA) method for 3-dimensional locomotion of intravascular microrobot," *Sensors and Actuators A: Physical*, vol. 157, no. 1, pp. 118–125, Jan. 1, 2010. DOI: 10.1016/j.sna.2009.11.011.

[144] Y. Ganji \ ast$ and F. Janabi-Sharifi, "Catheter Kinematics for Intracardiac Navigation," *IEEE Transactions on Biomedical Engineering*, vol. 56, no. 3, pp. 621–632, Mar. 2009. DOI: 10.1109/TBME.2009.2013134.

[145] F. Carpi, N. Kastelein, M. Talcott, and C. Pappone, "Magnetically Controllable Gastrointestinal Steering of Video Capsules," *IEEE Transactions on Biomedical Engineering*, vol. 58, no. 2, pp. 231–234, Feb. 2011. DOI: 10.1109/TBME.2010.2087332.

[146] F. Kirbas C. Quek, "A review of vessel extraction techniques and algorithms," *Computing Surveys*, vol. 36, no. 2, pp. 81–121, 2004. DOI: 10.1145/1031120.1031121.

[147] O. Felfoul, J.-B. Mathieu, G. Beaudoin, and S. Martel, "In Vivo MR-Tracking Based on Magnetic Signature Selective Excitation," *IEEE Transactions on Medical Imaging*, vol. 27, no. 1, pp. 28–35, 2008. DOI: 10.1109/TMI.2007.897375.

[148] J. Tokuda, G. S. Fischer, S. P. DiMaio, D. G. Gobbi, C. Csoma, P. W. Mewes, G. Fichtinger, C. M. Tempany, and N. Hata, "Integrated navigation and control software system for mri-guided robotic prostate interventions," *Computerized Medical Imaging and Graphics*, vol. 34, no. 1, pp. 3–8, 2010, Image-Guided Surgical Planning and Therapy. DOI: DOI:10.1016/j.compmedimag.2009.07.004.

[149] T. Deschamps and L. D. Cohen, "Fast extraction of minimal paths in 3D images and applications to virtual endoscopy," *Medical Image Analysis*, vol. 5, no. 4, pp. 281–299, Dec. 2001. DOI: 10.1016/S1361-8415(01)00046-9.

[150] O. Wink, A. F. Frangi, B. Verdonck, M. A. Viergever, and W. J. Niessen, "3D MRA coronary axis determination using a minimum cost path approach," *Magnetic Resonance in Medicine*, vol. 47, no. 6, pp. 1169–1175, 2002. DOI: 10.1002/mrm.10164.

[151] W. Sabra, M. Khouzam, A. Chanu, and S. Martel, "Use of 3D Potential Field and an Enhanced Breadth-first Search Algorithms for the Path Planning of Microdevices Propelled in the Cardiovascular System," in *IEEE Engineering in Medicine and Biology*, Jan. 2005, pp. 3916–3920. DOI: 10.1109/IEMBS.2005.1615318.

[152] C. Petres, Y. Pailhas, P. Patron, Y. Petillot, J. Evans, and D. Lane, "Path Planning for Autonomous Underwater Vehicles," *IEEE Transactions on Robotics*, vol. 23, no. 2, pp. 331–341, Apr. 2007. DOI: 10.1109/TRO.2007.895057.

[153] A. F. Frangi, W. J. Niessen, K. L. Vincken, and M. A. Viergever, "Multiscale vessel enhancement filtering," in *Medical Image Computing and Computer-Assisted Intervention (MICCAI)*, W. M. Wells, A. Colchester, and S. Delp, Eds., ser. Lecture Notes in Computer Science, Berlin, Heidelberg: Springer International Publishing, 1998, pp. 130–137, ISBN: 978-3-540-49563-5. DOI: 10.1007/BFb0056195.

[154] Y. Sato, S. Nakajima, H. Atsumi, T. Koller, G. Gerig, S. Yoshida, and R. Kikinis, "3D multi-scale line filter for segmentation and visualization of curvilinear structures in medical images," in *International Conference on Computer Vision, Virtual Reality, and Robotics in Medicine-International Conference on Medical Robotics and Computer-Assisted Surgery*, J. Troccaz, E. Grimson, and R. Mösges, Eds., ser. Lecture Notes in Computer Science, Berlin, Heidelberg: Springer International Publishing, 1997, pp. 213–222, ISBN: 978-3-540-68499-2. DOI: 10.1007/BFb0029240.

[155] J. A. Sethian and A. Vladimirsky, "Ordered Upwind Methods for Static Hamilton–Jacobi Equations: Theory and Algorithms," *SIAM Journal on Numerical Analysis*, vol. 41, no. 1, pp. 325–363, Jan. 1, 2003. DOI: 10.1137/S0036142901392742.

[156] E. Konukoglu, M. Sermesant, O. Clatz, J.-M. Peyrat, H. Delingette, and N. Ayache, "A Recursive Anisotropic Fast Marching Approach to Reaction Diffusion Equation: Application to Tumor Growth Modeling," in *Information Processing in Medical*

Imaging, N. Karssemeijer and B. Lelieveldt, Eds., ser. Lecture Notes in Computer Science, Berlin, Heidelberg: Springer International Publishing, 2007, pp. 687–699, ISBN: 978-3-540-73273-0. DOI: 10.1007/978-3-540-73273-0_57.

[157] F. Bornemann and C. Rasch, "Finite-element Discretization of Static Hamilton-Jacobi Equations based on a Local Variational Principle," *Computing and Visualization in Science*, vol. 9, no. 2, pp. 57–69, Jun. 1, 2006. DOI: 10.1007/s00791-006-0016-y.

[158] R. Marler and J. Arora, "Survey of multi-objective optimization methods for engineering," *Structural and Multidisciplinary Optimization*, vol. 26, no. 6, pp. 369–395, Apr. 1, 2004. DOI: 10.1007/s00158-003-0368-6.

[159] H. Li, J. Tan, and M. Zhang, "Dynamics Modeling and Analysis of a Swimming Microrobot for Controlled Drug Delivery," *IEEE Transactions on Automation Science and Engineering*, vol. 6, no. 2, pp. 220–227, Apr. 2009. DOI: 10.1109/TASE.2008.917137.

[160] C. Pawashe, S. Floyd, and M. Sitti, "Modeling and Experimental Characterization of an Untethered Magnetic Micro-Robot," *The International Journal of Robotics Research*, vol. 28, no. 8, pp. 1077–1094, Aug. 1, 2009. DOI: 10.1177/0278364909341413.

[161] Y. Bailly, Y. Amirat, and G. Fried, "Modeling and Control of a Continuum Style Microrobot for Endovascular Surgery," *IEEE Transactions on Robotics*, vol. 27, no. 5, pp. 1024–1030, Oct. 2011. DOI: 10.1109/TRO.2011.2151350.

[162] H. Marino, C. Bergeles, and B. J. Nelson, "Robust Electromagnetic Control of Microrobots Under Force and Localization Uncertainties," *IEEE Transactions on Automation Science and Engineering*, vol. 11, no. 1, pp. 310–316, Jan. 2014. DOI: 10.1109/TASE.2013.2265135.

[163] M. J. Pourmand, S. Taghvaei, R. Vatankhah, and M. M. Arefi, "An Underactuated Bio-Inspired Helical Swimming Microrobot Using Fuzzy-PI Controller with Novel Error Detection Method for 5-DOF Micromanipulation," *Designs*, vol. 2, no. 2, p. 18, 2 Jun. 2018. DOI: 10.3390/designs2020018.

[164] S. P. BANKS and K. J. MHANA, "Optimal control and stabilization for nonlinear systems," *IMA Journal of Mathematical Control and Information*, vol. 9, no. 2, pp. 179–196, Jan. 1, 1992. DOI: 10.1093/imamci/9.2.179.

[165] B. Friedland, *Advanced Control System Design*. Prentice Hall, 1996, 368 pp., ISBN: 978-0-13-014010-4.

[166] C. P. Mracek and J. R. Cloutier, "Control designs for the nonlinear benchmark problem via the state-dependent Riccati equation method," *International Journal of Robust and Nonlinear Control*, vol. 8, no. 4-5, pp. 401–433, 1998. DOI: 10.1002/(sici)1099-1239(19980415/30)8:4/5<401::aid-rnc361>3.0.co;2-u.

[167] T. Çimen, "Survey of State-Dependent Riccati Equation in Nonlinear Optimal Feedback Control Synthesis," *Journal of Guidance, Control, and Dynamics*, vol. 35, no. 4, pp. 1025–1047, 2012. DOI: 10.2514/1.55821.

[168] D. W. Clarke, C. Mohtadi, and P. Tuffs, "Generalized predictive control—Part I. The basic algorithm," *Automatica*, vol. 23, no. 2, pp. 137–148, Mar. 1987. DOI: 10.1016/0005-1098(87)90087-2.

[169] D. W. Clarke, C. Mohtadi, and P. Tuffs, "Generalized Predictive Control—Part II Extensions and interpretations," *Automatica*, vol. 23, no. 2, pp. 149–160, Mar. 1987. DOI: 10.1016/0005-1098(87)90088-4.

[170] L. Grüne and J. Pannek, *Nonlinear Model Predictive Control: Theory and Algorithms*, 2nd ed., ser. Communications and Control Engineering. Springer International Publishing, 2017, ISBN: 978-3-319-46023-9. DOI: 10.1007/978-3-319-46024-6.

[171] P. Ru and K. Subbarao, "Nonlinear Model Predictive Control for Unmanned Aerial Vehicles," *Aerospace*, vol. 4, no. 2, p. 31, 2 Jun. 2017. DOI: 10.3390/aerospace4020031.

[172] P. Hahnfeldt, D. Panigrahy, J. Folkman, and L. Hlatky, "Tumor development under angiogenic signaling: A dynamical theory of tumor growth, treatment response, and postvascular dormancy," *Cancer Research*, vol. 59, no. 19, pp. 4770–4775, Oct. 1, 1999.

[173] E. Diller and M. Sitti, "Three-Dimensional Programmable Assembly by Untethered Magnetic Robotic Micro-Grippers," *Advanced Functional Materials*, vol. 24, no. 28, pp. 4397–4404, 2014. DOI: 10.1002/adfm.201400275.

[174] A. Eqtami, O. Felfoul, and P. E. Dupont, "MRI-powered closed-loop control for multiple magnetic capsules," in *IEEE International Conference on Intelligent Robots and Systems*, 2014, pp. 3536–3542. DOI: 10.1109/IROS.2014.6943056.

[175] M. Salehizadeh, S. Salmanipour, J. Zhang, and E. Diller, "Controlling Multiple Microrobots using Homogeneous Magnetic Fields," in *IEEE Conference on Robotics and Automation*, 2018.

[176] K. W. Yung, P. B. Landecker, and D. D. Villani, "An Analytic Solution for the Force Between Two Magnetic Dipoles," *Magnetic and Electrical Separation*, vol. 9, no. 1, pp. 39–52, 1998. DOI: 10.1155/1998/79537.

[177] I. S. M. Khalil, I. E. O. Gomaa, and R. M. A.-K. a. S. Misra, "Magnetic-Based Contact and Non-Contact Manipulation of Cell Mockups and MCF-7 Human Breast Cancer Cells," *Smart Drug Delivery System*, Feb. 10, 2016. DOI: 10.5772/61686.

[178] A. Chanu, O. Felfoul, G. Beaudoin, and S. Martel, "Adapting the clinical MRI software environment for real-time navigation of an endovascular untethered ferromagnetic bead for future endovascular interventions," *Magnetic Resonance in Medicine*, vol. 59, no. 6, pp. 1287–1297, 2008. DOI: 10.1002/mrm.21638.

[179] N.-S. Cheng, "Formula for the viscosity of a glycerol-water mixture," *Industrial & engineering chemistry research*, vol. 47, no. 9, pp. 3285–3288, 2008. DOI: 10.1021/ie071349z.

[180] Y.-L. Park, S. Elayaperumal, B. Daniel, S. C. Ryu, M. Shin, J. Savall, R. J. Black, B. Moslehi, and M. R. Cutkosky, "Real-Time Estimation of 3-D Needle Shape and Deflection for MRI-Guided Interventions," *IEEE/ASME Transactions on Mechatronics*, vol. 15, no. 6, pp. 906–915, Dec. 2010. DOI: 10.1109/TMECH.2010.2080360.

[181] M. Rea, D. McRobbie, H. Elhawary, Z. T. H. Tse, M. Lampérth, and I. Young, "System for 3-D real-time tracking of MRI-compatible devices by image processing," *IEEE/ASME Transactions on Mechatronics*, vol. 13, no. 3, pp. 379–382, 2008. DOI: 10.1109/TMECH.2008.924132.

[182] J.-H. Park, G. von Maltzahn, L. Zhang, M. P. Schwartz, E. Ruoslahti, S. N. Bhatia, and M. J. Sailor, "Magnetic Iron Oxide Nanoworms for Tumor Targeting and Imaging," *Advanced Materials*, vol. 20, no. 9, pp. 1630–1635, 2008. DOI: 10.1002/adma.200800004.

[183] K. Zhang, F. Maier, A. J. Krafft, R. Umathum, W. Semmler, and M. Bock, "Tracking of an interventional catheter with a ferromagnetic tip using dual-echo projections," *Journal of Magnetic Resonance*, vol. 234, pp. 176–183, Sep. 1, 2013. DOI: 10.1016/j.jmr.2013.06.020.

[184] O. Felfoul, A. Becker, C. Bergeles, and P. E. Dupont, "Achieving Commutation Control of an MRI-Powered Robot Actuator," *IEEE Transactions on Robotics*, vol. 31, no. 2, pp. 387–399, Apr. 2015. DOI: 10.1109/TRO.2015.2407795.

[185] R. Bitter, T. Mohiuddin, and M. Nawrocki, *LabVIEW: Advanced Programming Techniques*, 2nd ed. CRC Press, 2017, ISBN: 9781420004915. [Online]. Available: http://www.ni.com/labview/.

Magnetic Microrobotics for Biomedical Applications

This research work mainly focuses on the study of the modeling and control of microrobotic systems in a biomedical context. So far, the use of magnetic actuation has been regarded as the most convenient approach for such achievements. Besides, the cardiovascular system allows to reach most parts of the human body and is then chosen as the main navigation route. This original topic is a rapidly expanding field whose ambition is to modernize current therapies by trying to improve therapeutic targeting while improving patient comfort. To achieve this goal, a good understanding of how microrobots evolve in the human body is an important step. The theoretical foundations and the physical laws that make it possible to describe the various phenomena which act on magnetic microrobots in vascular-like environments have thus been deeply studied. Methodologies for dealing with multiphysics approaches combining different sources of hypotheses and uncertainties have been developed. Great care has been taken in their validations by experimentation when possible, otherwise by numerical analysis. This helps to better understand the dominant dynamics, as well as the predominant parameters in the description of magnetic microrobots in a vascular-like environment. This makes it possible to efficiently characterize and predict their behaviors in a viscous flow and their responses to magnetic fields. On this basis, advanced navigation strategies have been developed. The navigation process can be divided into two stages. First, safe and efficient navigation paths are planned (off-line) based on the fast marching method (FMM). With the proposed navigation planning framework, different constraints and objectives can then be taken into account to obtain a truly feasible reference path. Second, control schemes that drive the magnetic microrobots along the planned reference path to the targeted location are synthesized. To do so, predictive and optimal control laws have been implemented. All the proposed models and navigation strategies have been evaluated through various experiments under different conditions with the platforms developed at the PRISME Laboratory.

Microrobots magnétiques pour des applications biomédicales

Ce travail traite principalement l'étude de la modélisation et du contrôle de systèmes microrobotiques dans un contexte biomédical. Jusqu'à présent, l'utilisation de l'actionnement magnétique est considérée comme l'approche la plus prometteuse pour de telles réalisations. Par ailleurs, le système cardiovasculaire permet d'atteindre la plupart des parties du corps humain et est alors choisi comme voie de navigation principale. Cette thématique originale est un domaine en pleine expansion dont l'ambition est de moderniser les thérapies actuelles en essayant d'améliorer le ciblage thérapeutique tout en améliorant le confort des patients. Pour atteindre cet objectif, une bonne compréhension du comportement des microrobots dans le corps humain est une étape importante. Les fondements théoriques et les lois de la physique permettant de décrire les différents phénomènes qui agissent sur les microrobots magnétiques dans des environnements de type vasculaire ont ainsi été étudiés en détails. Des méthodologies pour traiter des approches multiphysiques combinant différentes sources d'hypothèses et d'incertitudes ont été développées. Un grand soin a été apporté à leurs validations par l'expérimentation lorsque cela était possible, le cas échéant par des analyses numériques. Cela permet de mieux comprendre la dynamique dominante, ainsi que les paramètres prédominants dans la description des microrobots magnétiques. Cela permet de caractériser et de prédire efficacement leurs comportements dans un écoulement visqueux et leurs réponses aux champs magnétiques. Sur cette base, des stratégies de navigation avancées ont été développées. Le processus de navigation peut être divisé en deux étapes. Premièrement, des chemins de navigation sûrs et efficaces sont planifiés (hors ligne) sur la base de la méthode du *fast marching* (FMM). Dans le cadre de la méthode de planification de la navigation proposée, différentes contraintes et objectifs peuvent être pris en compte pour obtenir un chemin de référence véritablement réalisable. Deuxièmement, des stratégies de commande guidant les microrobots magnétiques le long du chemin de référence jusqu'à l'emplacement ciblé sont synthétisées. Pour ce faire, des lois de commande prédictives et optimales ont été mises en œuvre. Tous les modèles et stratégies de navigation proposés ont été évalués à travers diverses expérimentations dans différentes conditions sur les plateformes développées au Laboratoire PRISME.